

**MAGNETIC RESONANCE IMAGING (MRI) AND
ELECTROMECHANICAL STUDY OF ELECTRO-ACTIVE
POLYMERS FOR APPLICATION IN SOFT ACTUATORS**

Leila Naji

**A Thesis Submitted for the Degree of PhD
at the
University of St Andrews**



2007

**Full metadata for this item is available in
St Andrews Research Repository
at:**

<http://research-repository.st-andrews.ac.uk/>

Please use this identifier to cite or link to this item:

<http://hdl.handle.net/10023/367>

This item is protected by original copyright

**Magnetic Resonance Imaging (MRI) and
Electromechanical Study of
Electro-Active Polymers for Application in Soft
Actuators**

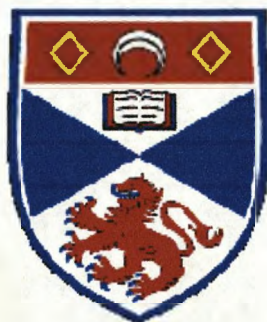
A thesis submitted for the degree of PhD.

by

Leila Naji

University of St. Andrews

Supervised by Dr. Richard T. Baker
Co-supervised by Dr. Sandy Chudek



Submitted May 2007



Declaration

I, Leila Naji, hereby certify that this thesis, which is approximately 61812 words in length, has been written by me, that it is the record of work carried out by me and that it has not been submitted in any previous application for a higher degree.

Date 03.05.07 signature of candidate

I was admitted as a research student in August 2003 and as a candidate for the degree of Ph.D in August 2003: the higher study for which this is a record was carried out in the University of Dundee between 2003 and 2005 and then in the University of St Andrews between 2005 and 2007.

Date 3.05.07 signature of candidate

I hereby certify that the candidate has fulfilled the conditions of the Resolution and Regulations appropriate for the degree of Doctor of Philosophy in the University of St Andrews and that the candidate is qualified to submit this thesis in application for that degree.

Date 3/5/07 signature of supervisor

In submitting this thesis to the University of St Andrews I wish it to be subject to the following conditions: for a period of 1 year from the date of submission, this shall be withheld from use. I understand however, that the title and abstract of the thesis will be published during this period of restricted access: and that after the expiry of this period the thesis will be made available for use in accordance with the regulations of the University Library for the time being in force, subject to and copyright in the work not being affected thereby, and a copy of the work may be made available to any bona fide library or research worker, that my thesis will be electronically accessible for personal or research use, and that the library has the right to migrate my thesis into new electronic forms as required to ensure continued access to the thesis. I have obtained any third-party copyright permission that may be required in order to allow such access and migration.

Date 03.05.07 signature of candidate

Acknowledgment

I would like to express my sincere gratitude and appreciation to my first supervisor Dr. Richard T. Baker for providing useful advice during my studies and through the writing of this thesis. I really appreciate his experience and acute observations. Also, I am deeply indebted to my second supervisor Dr. Sandy Chudek, University of Dundee, for his valuable suggestions, assistance and criticism to this work.

I would like to thank Prof. Eric Abel, University of Dundee, for his great help on electromechanical tests on IPMC materials and for allowing me to take benefit from facilities available at his lab; Dr. Sean Rigby, University of Bath, for his help with diffusion data; Mr. Martin Kierans, University of Dundee, for training me SEM techniques and Mrs Julie Nairn for helping me with SEM sample preparation.

My sincere thanks go to my parents, Mahin and Abdolmajid, and family for their prayers, support and encouragement. My deepest thanks go to my dearest husband, Mahmoud, and my darling daughter, Hasti, without whose support, patience and love I could not have finished this thesis. Mahmoud has always been there to encourage me, support me, and share my tears and laughter.

Additional thanks goes to Nicholl Lindsay Award for funding my study over the past 3 years.

Abstract

It is more than a decade that Ionic Polymer-Metal Composites (IPMCs) have been known as an exciting class of smart materials and attracted growing worldwide attention. IPMCs are soft and flexible, and can generate large and reversible strains in response to electrical stimulus. Thus, they have potential applications in industrial and biomedical fields, as actuators. Before these applications can be realized, however, the performance of IPMCs must be understood and improved through improvement of component characteristics and of preparation methods. In general, the aim of this thesis is to gain a fundamental understanding of the chemical and structural factors that affect the electromechanical performance of IPMCs. To this end, a multi-technique investigation is applied to correlate the electrochemical and electromechanical behavior of IPMCs, during operation, with their chemistry, microstructure and nanostructure. Researchers have suggested several plausible mechanical and mathematical models to reveal that ion transport occurs within IPMCs and that it is an important factor in their actuation performance. However, there is still a need for further experimental studies to help refine our understanding of the actuation mechanism of these materials. In this work, the powerful, non-invasive and non-destructive technique of Magnetic Resonance Imaging (MRI) is employed to study the internal structure and water content distribution in Nafion membranes and also IPMCs. Moreover, MRI is also applied to image electrically-induced diffusion of ions with their associated water molecules in real time, in operating IPMC actuators. This forms the major part of this project and, to the best of our knowledge, it is the first recorded electrochemical experiment of this kind. The size and dimensions of IPMCs can affect their actuation performance. Thus, in this work, model IPMC actuators are prepared based on the available commercial Nafion membrane and fabricated cast Nafion membrane and their electromechanical behaviors are compared. The effect of parameters such as electrode composition and Nafion thickness on actuation behavior is also studied by measuring displacement and force generation of the IPMC actuators during actuation cycles. Simultaneous current and electromechanical measurements are made to correlate electrochemical processes with actuation behavior directly. Scanning electron microscopy (SEM) is also used to study the internal and surface structure of IPMCs.

Overview of Thesis

The thesis consists of ten chapters; an introduction, a conclusion and eight substantive chapters. It begins with an introductory chapter which reviews the most important aspect of Ionic Polymer-Metal Composites (IPMCs) and their actuation mechanism. Chapter Two provides fundamental information about NMR, MRI and SEM, which have been applied to characterize the IPMC samples. Chapter Three discusses the general experimental protocol followed during this research and explains experimental procedures used to obtain the MRI and SEM images. It also gives a detailed description about the techniques that have been used to measure the generated force and actuation performances of IPMC samples. Chapter Four presents preliminary results about the samples that are used in the subsequent experiments. It also presents the SEM results of all IPMC samples. Chapter Five gives experimental details about multi-echo MRI imaging of electrically-induced diffusion of water molecules within the commercial Nafion samples. It also presents the MRI experimental results as spin-spin relaxation time, T_2 , and proton density, PD , maps. Chapter Six presents experimental results of multi-echo MRI imaging of electrically-induced diffusion of water within a working IPMC sample. Chapter Seven discusses the use of the diffusion-weighted imaging (DWI) method to obtain the diffusion coefficient, D , for water molecules within a cast Nafion membrane and a working IPMC sample. Chapter Eight presents the results obtained from electromechanical tests; displacement and force measurements that were performed on various commercial and cast Nafion-based IPMC samples. It also provides the waveform analysis results. Chapter Nine compares and discusses the results presented in the chapters Four to Eight. Chapter Ten is the concluding chapter of the study. It summarizes and highlights the major findings from the previous chapters and draws some general conclusions.

Table of Contents

CHAPTER ONE: INTRODUCTION

1.1. Introduction	1
1.2. Ionic Polymer-Metal Composites (IPMCs)	3
1.2.1. Introduction	3
1.2.2. The IPMC Polymers	4
1.2.2.1. Nafion Properties	5
1.2.2.2. Ion Exchange Capacity	9
1.2.2.3. Equivalent Weight, EW	9
1.2.2.4. Swelling and Water Content	10
1.2.2.5. Determination of Ion Transport in Nafion Membrane	11
1.2.3. Actuation Mechanism of IPMCs	14
1.2.4. Factors Effecting Actuation Response of IPMCs	19
1.2.4.1. Cations	19
1.2.4.2. Solvents	21
1.2.4.3. Electrodes	22
1.2.4.4. Level of Hydration	23
1.2.4.5. Sample Dimension	24
1.2.5. Measurement of Actuation	25
1.2.6. Comparison with Other Smart Actuator Materials	27
1.2.7. Applications of IPMC Actuators	28
1.2.7.1. Industrial Applications	29
(a) Mechanical Robot Grippers	29
(b) Metering Valves	29
(c) Diaphragm Pumps	30
(d) Microelectromechanical Systems (MEMS)	30
1.2.7.2. Biomedical Applications	30
(a) Artificial Ventricular or Cardiac-Assist Muscles	30
(b) Surgical Tools	31
(c) Incontinence Assist Device	31
(d) Active Tactile Display Devices	31
1.3. References	31

CHAPTER TWO: TECHNIQUES

2.1. Introduction	37
2.2. Magnetic Resonance Imaging (MRI)	37
2.2.1. Introduction	37
2.2.2. The Nuclear Magnetic Resonance (NMR) Phenomenon	39
2.2.2.1. Excitation	42
2.2.2.2. Relaxation	44
(a) Spin-Lattice Relaxation Time, T_1	44
(b) Spin-Spin Relaxation Time, T_2	45
(c) Effective Spin-Spin Relaxation Time, T_2^*	46

(d) Bloch Equations	46
2.2.2.3. Relaxation and Molecular Motion	47
2.2.2.4. Pulsed NMR Methods	49
(a) Free Induction Decay (FID)	49
(b) Simple Hahn Spin Echo Pulse Sequence	50
(c) Carr-Purcell-Meiboom-Gill (CPMG) Pulse Sequence	51
2.2.3. MRI Principles	53
2.2.3.1. Influence of Magnetic Field Gradient	54
2.2.3.2. Selective Excitation	55
2.2.3.3. One-Dimensional Imaging	56
2.2.3.4. Two-Dimensional Imaging	57
2.2.3.5. Sensitivity and Resolution	58
2.2.3.6. Experimental Methods of MRI	58
(a) Spin Echo Method	59
i) Multi-Echo Imaging	59
ii) Contrast Determining Parameters	60
b) Pulsed Gradient Spin Echo (PGSE) Method	62
i) Diffusion-Weighted Imaging (DWI)	64
ii) Contrast and Diffusion Maps	65
iii) Anisotropic Diffusion	66
2.2.3.7. Applications of MRI	67
2.3. Scanning Electron Microscopy (SEM)	71
2.3.1. Effects useful for Imaging in the SEM	72
2.3.1.1. Secondary Electrons	73
2.3.1.2. Backscattered Electrons	73
2.3.1.3. X-Ray Emission	73
2.3.2. Sample Preparation for SEM	74
2.3.3. Chemical Analysis in SEM	75
2.3.3.1. Energy-Dispersive Analysis	75
2.3.3.2. Line Scanning	75
2.3.3.3. X-Ray Mapping	76
2.4. References	76

CHAPTER THREE: GENERAL EXPERIMENTAL

3.1. Introduction	80
3.2. Materials	80
3.3. Commercial Nafion-117 Membrane	80
3.4. Preparation of Thick Nafion Membrane	81
3.5. IPMC Manufacturing Technique	82
3.5.1. Pre-treatment	83
3.5.1.1. Surface Roughening	83
3.5.1.2. Cleaning Procedure	83
3.5.2. Compositing Process (Electroless Platinum Electroding)	84
3.5.2.1. Ion Exchange (Absorption)	84
3.5.2.2. Plating (Reduction)	85
3.5.3. Surface Electroding	86

3.6. IPMC Samples	87
3.7. Experimental Set-up	88
3.7.1. Scanning Electron Microscopy (SEM)	88
3.7.1.1. Instrumentation	88
3.7.1.2. Sample Preparation	89
3.7.2. MRI	90
3.7.2.1. Instrumentation	90
3.7.2.2. Experimental Set-up	90
3.7.2.3. Construction of T ₂ and PD Images	91
3.7.2.4. Construction of Diffusion Maps	92
3.7.3. Displacement Measurements	93
3.7.3.1. Instrumentation	93
3.7.3.2. Experimental Set-up	94
3.7.4. Force Measurements	95
3.7.4.1. Instrumentation	95
3.7.4.2. Experimental Set-up	95
3.8. Summary	97
3.9. References	98

CHAPTER FOUR: PRELIMINARY RESULTS

4.1. Introduction	101
4.2. NMR Spectroscopy	101
4.2.1. Experimental	101
4.2.2. Results and Discussion	102
4.3. Magnetic Resonance Imaging (MRI)	103
4.3.1. Comparative MRI of Cast and Commercial Nafion Membranes	103
4.3.1.1. Experimental	103
4.3.1.2. Results and Discussion	104
4.3.2. MRI of Dry Nafion Membranes	109
4.3.2.1. Experimental	109
4.3.2.2. Results and Discussion	110
4.4. Determination of Water Content	110
4.4.1. Experimental	110
4.4.2. Results and Discussion	111
4.5. SEM	112
4.5.1. Experimental	112
4.5.2. Results and Discussion	113
4.6. Summary	128
4.7. References	129

CHAPTER FIVE: MRI STUDY OF COMMERCIAL NAFION MEMBRANE

5.1. Introduction	132
5.2. Experimental	133
5.3. Results and Analysis	135

5.4. Discussion	150
5.5. Summary	157
5.6. References	158
CHAPTER SIX: MRI STUDY OF IPMCS	
6.1. Introduction	160
6.2. Experimental	161
6.3. Results and Analysis	163
6.4. Discussion	172
6.5. Summary	179
6.6. References	181
CHAPTER SEVEN: DIFFUSION STUDIES	
7.1. Introduction	183
7.2. Experimental	184
7.2.1. Diffusion Study of Cast Nafion Membranes	184
7.2.3. Diffusion Study of IPMCS	185
7.3. Results and Analysis	188
7.3.1. Self-Diffusion of Water in Cast Nafion Membrane	188
7.3.2. Self-Diffusion of Water in an IPMC Actuator	194
7.3.3. Electrically-Induced Diffusion of Water in an IPMC Actuator	201
7.4. Discussion	220
7.5. Summary	228
7.6. References	229
CHAPTER EIGHT: ELECTROMECHANICAL TESTS	
8.1. Introduction	231
8.2. Experimental	231
8.3. Results and Analysis	232
8.3.1. Displacement Measurements	232
8.3.1.1. Commercial IPMC Samples	232
8.3.1.2. Cast IPMC Samples	240
8.3.1.3. Comparison of Commercial and Cast IPMC samples	245
8.3.2. Force Measurements	248
8.3.2.1. Commercial IPMC Samples	248
8.3.2.3. Comparison of Commercial and Cast IPMC samples	255
8.3.3. Waveform Analysis	258
8.4. Discussion	263
8.5. Summary	273
8.6. References	274
CHAPTER NINE: CONCLUSION AND FUTURE WORK	
9.1. Conclusion	277
9.1.1. Structural Characterization of Nafion Membranes	277

9.1.2. Structural Characterization of IPMCs	279
9.1.3. MRI Study of Electrically-Induced Distribution of Water in the Commercial Nafion Membrane and IPMC Actuator	283
9.1.4. Modeling of the Structure of Nafion Membrane and Electrically-Induced Diffusion of Hydrated Li^+ Ions within the Membrane	287
9.1.5. Characterization of Electromechanical Performance of IPMCs	288
9.2. Future Work	290
9.3. References	291
APPENDIX 1	292
APPENDIX 2	294
APPENDIX 3	303

Chapter One

Introduction

1.1. Introduction

In recent years, Electro-active polymers (EAPs) have been intensively studied because of their unique properties and wide range of potential applications in medical, mechanical, electrical and aerospace engineering.¹ EAPs are classified as “smart materials” and can sense external stimuli and respond accordingly in real or near real time.¹ There are many types of such polymers and they may be activated by several mechanisms and many different stimulants. Some of these polymers show reversible changes while others achieve permanent changes. They possess many advantageous characteristics: they are low-mass, soft, fracture tolerant, flexible and relatively inexpensive. They can be cut and formed into almost any size and shape. EAPs can be used as sensors and actuators in medicine, industry and robotics. As sensors they can produce an electrical response, which can be sensed by a low power amplifier, when they are subjected to dynamic impact or shock.² As actuators they are characterised by the fact that they can undergo a large amount of deformation and produce large forces in response to an external stimulus. Therefore, they have the potential for application in the field of robotics, where large displacements are often needed. Due to their similarities with biological muscles, achieving stress and force, they are often called “artificial muscles”. The first basic artificial muscle was produced by McKibben in the 1950s and so it is referred to as McKibben muscle.¹ This muscle consists of an internal rubber hose surrounded by a jacket of nylon weave (with flexible but non-extensible threads) clamped off at either end to fittings or to some tendon-like structure. When the internal rubber hose is pressurized, the high pressure gas pushes against its inner surface and also against the nylon weave jacket at external surfaces, and tends to increase its

volume. The non-extensibility of the threads in the nylon weave jacket however constrain the swelling of the rubber and so causes the muscle to contract along its axis.

Based on their activation mechanism, EAPs can be divided into two categories; electrically and non-electrically activated polymers. Non-electrically activated EAPs include light, chemically, magnetically and thermally activated polymers.¹ Electrically activated EAPs in turn are categorized into two principle classes based on their response to electrical stimulation; electronic EAPs and ionic EAPs. Ionic materials are actuated by the movement of ions, and electronic materials by the movement of electrons, in response to an applied electric field.

Electronic EAPs require very high voltage, of the order of thousands of volts, to change shape or dimensions and this is one of their disadvantages. As an example of electronic EAPs one can refer to dielectric EAPs, in which actuation is caused by electrostatic forces between two electrodes, which squeeze the polymer.

In contrast to electronic EAPs, ionic EAPs need only a few volts (1-5 V) to be activated and to exhibit shape change or bending deformation. However, these polymers must be kept wet and their ionic content play a key role in the intensity of their response. The most interesting example of the application of ionic EAPs is Ionic Polymer-Metal Composites (IPMCs)¹ which forms the main focus of this thesis. IPMCs can act as large motion actuators and sensors. They are suitable candidates for the preparation of sensors and artificial actuators in the micro to macro size range³ for medical, mechanical and industrial use.

1.2. Ionic Polymer-Metal Composites (IPMCs)

1.2.1. Introduction

IPMCs are considered as novel electrochemical actuator devices as they undergo large bending deformation and flapping displacements in response to a small electrical stimulus (1-5 V). They were first developed in 1939 by precipitating colloidal silver on prepared substrates¹. The metal overlayer on the substrates however did not have sufficient mechanical stability so they could not be used in a wide range of applications. Bergman⁴ in 1970 and McCallum and Pletcher⁵ in 1975 employed sputtering methods to metalize polymer surfaces. They also considered the delamination of the metal overlayer as well. Researchers in Dow Chemical⁶ used the permselective properties of ionomeric resins to facilitate selective reduction of metal salts in ion exchange membranes, using sodium borohydride or hydrazine as the reducing agent. Japanese researchers⁷ applied the fore-mentioned method to Nafion membranes. Further development in the preparation of IPMCs was done in 1989 to 1995 by Millet et al.^{8,9} They studied the morphology of the metal deposition process in IPMCs. In 1992, Shahinpoor¹⁰ and Sadeghipour et al.¹¹ in the United State and Oguro et al.¹² in Japan discovered separately the actuation response of IPMCs. Mojarad and Shahinpoor¹³ have also improved the performance of IPMCs as soft actuators since 1996.

Currently, a typical IPMC is prepared from a thin ion exchange polymer membrane with metal electrodes deposited chemically at both faces.¹⁴ The electrodes are made up of small, interconnected metal particles, generally platinum or gold, which penetrate into the ion exchange polymer membrane through an absorption/reduction process. This results in formation of dendritic type of electrodes at sub-surfaces of the polymer membrane. In order

to achieve a high performance IPMC, the metal chemical deposition process may be repeated several times to increase the thickness and electrical conductivity of electrodes at both surfaces. A further metal layer of gold or platinum may also be deposited onto each electrode by Physical Vapour Deposition (PVD), to improve the electrical conductivity at the polymer surfaces. When an adequate potential is applied across the thickness of hydrated and ion-exchanged IPMC at the frequency of no more than a few Hertz, it bends dramatically and reversibly toward the positively charged surface of the polymer. The magnitude and speed of the bending deformation may depend on the nature and the ionic conductivity of the ion exchange polymer, the thickness of the ion exchange polymer, the structure and capacitance of the electrodes, the level of hydration (solvent saturation), the charge on the cations, the mobility of the cations, and the specific interactions between the electrode and the cations.

1.2.2. The IPMC Polymers

IPMCs are often manufactured from ion exchange polymers which are designed to selectively pass ions of single or multiple charges, either cations or anions. This means that ions are mobile within these polymers. Nafion^{*}, Aciplex[†] and Flemion[‡] are perfluorinated alkenes with short side chains terminated by ionic groups for cation exchange and can be used as base ion exchange polymer to produce IPMC actuators.¹ These polymers have linear backbones with no crosslinking and relatively few fixed ionic groups located at the end of side chains which are able to position themselves in their preferred orientation.

^{*} Trademark of Du Pont de Nemours and Co.

[†] Trademark of Asahi Chemical Company

[‡] Trademark of Asahi Glass Company

These polymers differ in the length and number of side chains and also in the nature of the ionic side group. The anions in Aciplex and Nafion are sulfonate whereas those in Flemion are carboxylate. The microstructure of Nafion and Flemion and the potential micro-mechanism of the actuation of the IPMCs based on these ion exchange polymers have been extensively studied by Nemat-Nasser.¹⁵ Among these known polymers, a great deal of research is still performed on IPMC based on perfluorinated sulphonic acid cation exchange membrane, Nafion, manufactured by Du Pont de Nemours and Co. in 1972. Nafion was also used in the work described in this thesis.

1.2.2.1. Nafion Properties

Nafion membrane is a copolymer of tetrafluoroethylene and perfluorinated vinyl ether containing terminal sulfonyl fluoride groups. A typical chemical structure of Li⁺-exchanged Nafion membrane used in this research is depicted in Figure 1.1.

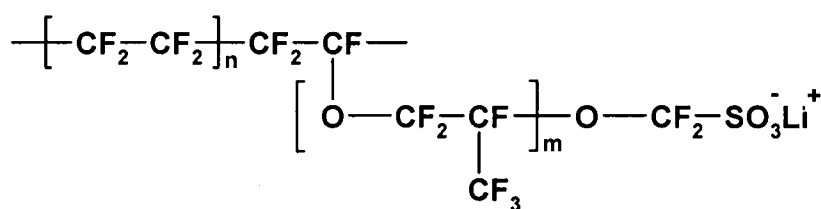


Figure 1.1. Chemical structure of Li⁺-exchanged Nafion.

Because of its PTFE-like structure this ion exchange polymer has many desirable properties including good chemical stability when immersed in the required electrolyte solution,¹⁶ remarkable mechanical strength,¹⁵ good thermal stability,¹⁷ high electrical conductivity^{18,19} and high selectivity to the desired ionic species, even in high salt concentration.^{20,21} These interesting properties of Nafion have attracted the attention of researchers in life sciences and technological engineering for numerous applications, including water electrolyzers,²² reaction catalysts,²³ batteries,^{24,25} fuel cells,²⁶ and electrochemical sensors.²⁷

The exact secondary structure of Nafion is not known. However several models have been proposed since the early 1970s to describe the ionic groups within the Nafion polymer. The secondary structure of Nafion focuses on the cluster-network model proposed by Gierke²⁸ who described the membrane as a series of clusters or inverted micelles, interconnected by narrow pores. In this model, the term clusters refers to the tightly packed regions formed by aggregation of ionic groups ($-\text{SO}_3^-\text{Li}^+$, in Figure 1.1) in Nafion, as a result of electrostatic interactions. In 1982, Yeager and Eisenberg carried out experiments on Nafion using small angle x-ray scattering (SAXS) and neutron scattering which indicated that clusters are present in Nafion.²⁹ Yeager then proposed a model based on a three-phase clustered system with interconnecting channels within Nafion.²⁹ The three phases consisted of (a) a region of perfluorinated molecular backbones, (b) an interfacial region containing some pendant side chains, water, and ionic groups which are not in clusters, and (c) the clustered regions where the majority of the ionic groups, cations, and water molecules are aggregated. In 1989, TEM analysis of hydrated Nafion membranes revealed that there is an essentially regular spacing, in the order of 30-50 Å, between the clusters which increases with increasing water content of Nafion membrane.³⁰ Meresi and co-workers³¹ have studied the

morphology of dry and swollen Nafion ionomer using MAS, ^{19}F , and ^{129}Xe NMR. According to their ^{19}F spin diffusion measurements, Nafion membrane in acid (protonated) form displayed a predominantly two-phase morphology.³¹ They suggested that the morphology of Nafion comprised of two domains; a minor domain, containing the ionic groups, pendant side chains and water molecules, and a major domain, composed of perfluorinated molecular backbones. Their findings was also consistent with the two resonances – corresponding to two sorption environments – observed in ^{129}Xe NMR spectrum of the Nafion membrane. In dry Nafion, the thickness of the minor domain was found to be 3.8 nm with an overall periodicity of about 10 nm. This thickness increased to 6.5 nm when Nafion membrane was hydrated at a level of 20 wt% (water), however, the overall periodicity hardly changed. On the other hand, upon the addition of ethanol, both the overall periodicity and the thickness of the minor domain increased significantly in which, at 20 wt% ethanol, the thickness of the minor domain was 11 nm and the overall periodicity was 19 nm. These results suggested that the addition of ethanol induces a larger morphological rearrangement in the Nafion membrane. In another study, Heitner-Wirguin³² suggested that the chemical structure of Nafion contains two different regions; hydrophobic and hydrophilic. The perfluorinated molecular backbones aggregate to form hydrophobic semicrystalline regions in Nafion. While, as a result of electrostatic interactions, ionic groups tends to aggregate and form extremely hydrophilic clusters in the polymer.³² Cluster diameters are estimated to be about 3-6 nm, depending on the water content (hydration level) of the Nafion membrane.^{33,34} It has also been deduced that clusters contain up to 100 pairs of sulfonate groups, with up to 20 water molecules around each sulfonate group.^{33,34}

The schematic diagram in Figure 1.2 shows the presence of the clusters (hydrophilic regions) within the semicrystalline perfluorinated molecular backbone.

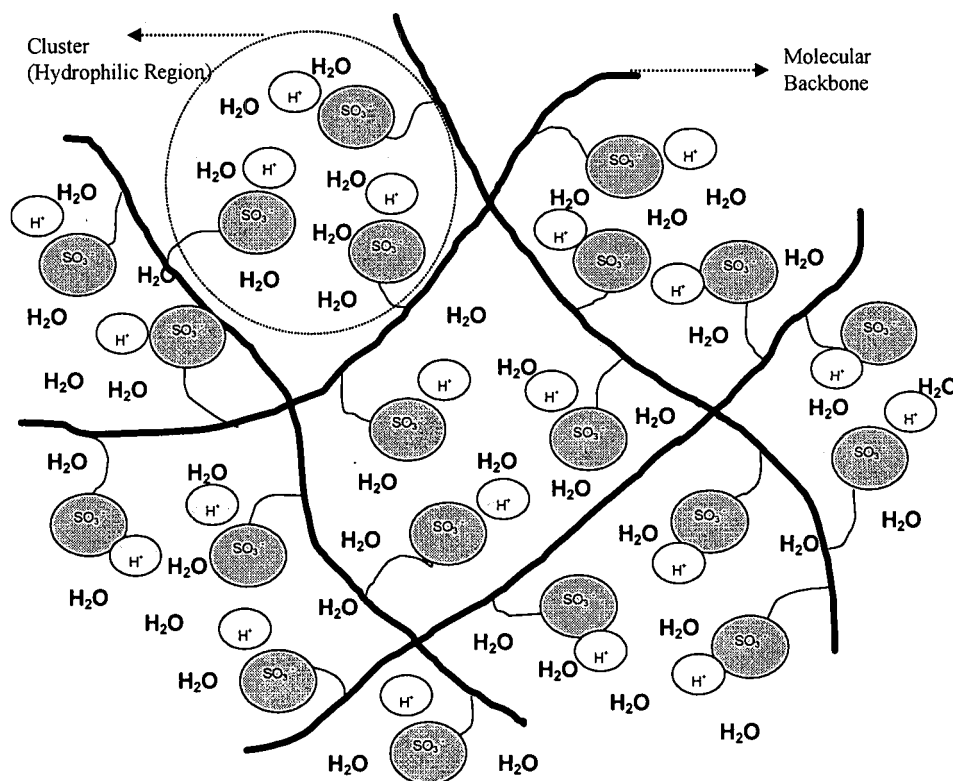


Figure 1.2. Schematic depiction of the hydrated form of Nafion.

The mentioned interesting properties of Nafion are strongly influenced by the presence of hydrophobic perfluorinated molecular backbones and hydrophilic clusters in this polymer. For example, high chemical stability of Nafion in all solvents, at temperature below 200°C, is explained by the presence of semicrystalline hydrophobic regions (consisting of perfluorinated molecular backbones) in this polymer.²⁹ The ability of the Nafion polymer to

take up ions and solvents when in contact with external electrolytes is also attributed to the presence of hydrophilic clusters within this polymer.¹

1.2.2.2. Ion Exchange Capacity

The ion exchange capacity of Nafion indicates the number of sulfonate groups within a fixed volume of this ion exchange polymer. This should be equivalent to the number of moles of exchanged (monovalent) cations within the polymer. The ion exchange capacity can be experimentally calculated from the weight difference of the Nafion membrane containing different cations.¹⁵

1.2.2.3. Equivalent Weight, EW

Equivalent weight, EW , of Nafion is equal to the mass of the dry protonated Nafion polymer divided by moles of sulfonate groups in this polymer, which is measured in grams per mole (gmol^{-1}). EW can therefore change according to the type of charge balancing cations on the sulfonate groups. The equivalent weight for Nafion containing ions other than protons is given by:¹⁵

$$EW_{ion} = \frac{EW_{H^+} - 1.008 + FW_{ion}}{SF} \quad (1.1)$$

where EW_{H^+} is the equivalent weight of the dry protonated Nafion (1100 gmol^{-1} for Nafion-117), 1.008 is the formula weight of the proton (gmol^{-1}), FW_{ion} is the formula weight of the charge balancing cations on the sulfonate groups in gmol^{-1} , and SF is a scaling factor that takes account of the mass of the added metal electrodes in a dry IPMC sample. For a

Nafion membrane without metal electrode, SF is equal to one and for an IPMC sample, SF is the weight fraction of Nafion within the sample.¹⁵

1.2.2.4. Swelling and Water Content

All the H⁺ on the sulfonate groups in the hydrophilic region of the (protonated) Nafion membrane can be exchanged for other cations such as Li⁺, Na⁺, K⁺, Cs⁺, Tl⁺, TBA⁺, Ca²⁺, Mg²⁺ and Ba²⁺. However, the nature of the charge balancing cations on the sulfonate groups can influence the degree of swelling³⁵ and also stiffness of Nafion membrane. The ability of the Nafion membrane to uptake water rises as the hydration capacity of the cation increases.³⁵ Using cations with small ionic radius, such as Li⁺, has been reported to enhance the interaction forces between cations and the fixed sulfonate groups in polymer, so making the membrane stiffer and stronger.³⁵

A Nafion membrane is able to absorb large amounts of water and other protic liquids and changes volume and length. When Nafion is placed in a polar solvent like water, the solvent penetrates towards the ionic groups inducing swelling of the hydrophilic regions (clusters) so that the spacing between these regions increases and their number density falls.³⁶ However, the extent of swelling and expansion of the polymer changes as the nature of the solvent is altered.¹⁸ In this respect, Hobson and his colleagues³⁷ have shown that Nafion swells and expands more in an acidic solvent than in a water treatment and that the swelling and hydration of a strip of Nafion membrane is different along the length (x-axis) and width (y-axis). Considering the Nafion membrane in two dimensions, they observed that the Nafion membrane expanded 11% to 16% along the x-axis and y-axis, after an

aqueous treatment (1h /100°C), while it expanded 13% to 22%, along these same axes after an acid treatment.

In Nafion, a swelling equilibrium results from the balance between the elastic forces of the polymeric matrix and the water's affinity for the fixed sulfonate groups and the moving cations.³⁸ Several studies have been done on the swelling properties and also modelling of clustering in ion exchange membranes. The results emphasise that the degree of swelling depends on the hydrophilic properties of the cations inside the membrane,³⁹ the degree of crystallinity of the polymeric membrane, which depends on the preparation method of the membrane,⁴⁰ and the polarity of the solvent.^{39,41}

The uptake of water from a dried Nafion membrane can be calculated as the weight difference between dry and hydrated samples.

1.2.2.5. Determination of Ion Transport in Nafion Membrane

The transport of ions through the Nafion membrane has been widely studied because of its highly attractive properties for application in ion selective membranes and fuel cells. A rather extensive literature exists on the determination of ionic, charge and water transport in Nafion membrane and the most general methods are impedance spectroscopy,⁴² Fourier Transform Infra-red Spectroscopy (FTIR),⁴³ electrophoretic measurements,⁴⁴ NMR spectroscopy,^{45,46} and electrophoretic NMR.⁴⁷

Attenuated Total Reflection (ATR) FTIR spectroscopy has been used to monitor, *in situ*, the penetration and diffusion of water into thin sulfonated poly (ether sulfone) films as a function of membrane thickness and the preparation solvent.⁴³ They found dual mode diffusion in all cases with diffusion coefficients D_1 and D_2 and weighting factor X_1 , which

varied depending on the conditions. They concluded that the variations in diffusion coefficient D with preparation solvent were due to the degree of ion solvation, cluster formation and subsequent ability to interact with water. In this study, a variation with the membrane thickness was observed, which was assumed to be due to the way in which information was weighted towards the D_1 and D_2 modes. The overall transport characteristics of different cationic species in Nafion-117 membrane have been measured by researchers, using conductivity and electrophoresis experiments.⁴⁴ They have studied the influence of the external sodium chloride concentration on the conductivity and the electrophoretic mobilities of sodium ions in the Nafion membrane. In this work, electrophoretic mobilities of sodium ions were determined by measuring the shifting of different radioactive tracers on the Nafion membrane samples, under the application of an electric field. The results from this study showed that conductivity of the Nafion membrane and also the mobility of sodium ions in the membrane increased as a function of the concentration of the external sodium chloride solutions. Wintersgill and Fontanella⁴² have discussed some aspects of complex impedance studies of Nafion. Their research has shown how dielectric relaxation and the results of complex impedance spectroscopy of Nafion at various concentrations of water can be used to gain insight into electrical conductivity in Nafion. Complex impedance measurements on dried Nafion samples revealed that this ion exchange polymer is a good insulator at low temperatures, below 400 K, and that its dielectric constant increases as a function of EW of Nafion membrane, due to an increased fraction of amorphous phase. The results from electrical conductivity measurements also showed that conductivity of the hydrated Nafion membranes can be comparatively very high, depending on the amount of water present in the membrane. Their findings also

revealed that even in the dry Nafion membrane there is still significant ion mobility, possibly due to the presence of residual ions or traces of water or impurities in the polymer.⁴² Furthermore, the electrical conductivity in Nafion samples containing different mixtures of methanol and water were studied by this research group. This study revealed that at low water content the electrical conductivity of the Nafion membrane was higher than the electrical conductivity of the individual constituents, water and methanol, while the reverse was true at high water concentration.⁴² In another study, Fontanella¹⁹ and co-workers applied impedance spectroscopy, and deuterium NMR spectroscopy to measure the electrical conductivity of protonated Nafion membranes of three different molecular weights, conditioned at various levels of hydration. The results obtained from this study showed that the higher molecular weight Nafion membranes exhibit lower electrical conductivity, which was explained by the segmental motions of the polymer. That is, the segmental motions show less flexibility in the higher molecular weight materials, resulting in a lower conductivity. Further, a good agreement between the results obtained from NMR and electrical conductivity was observed which suggested that the proton transport and the rotational motion of the water molecules are correlated in the Nafion membranes. MacMillan and co-workers⁴⁵ utilised proton and deuterium spin-lattice (T_1), spin-spin (T_2) and rotating frame spin-lattice ($T_{1\rho}$) relaxation times and fluorine T_1 and T_2 in an NMR investigation of the molecular dynamics of water molecules absorbed in Nafion membrane. They found an apparent dynamical transition which they attributed to a change in the degree of the order within the aqueous phase.⁴⁵ The temperature at which this transition occurred, T_b , decreased with increasing hydration level of the Nafion polymer. At temperatures above T_b , relaxation times were generally longer and the relaxation processes

were similar to those taking place in bulk water.⁴⁵ The NMR data presented in Meresi's work³¹ suggested that the domain which supports the rapid and long range transport of water and low molecular weight alcohols within the Nafion membrane must be a relatively amorphous phase and with rather little tortuosity. Kreuer and colleagues⁴⁷ applied electrophoretic NMR to measure electro-osmotic drag coefficients (K_{drag}) in a Nafion membrane. They showed that K_{drag} increased with increasing water content and with increasing temperature. However, no such studies have followed the spatial distribution of water in real time in an ion exchange polymer during application of a potential. In another study,⁴⁸ pulsed field gradient NMR was applied to measure the self-diffusion constants of water and ethanol in Nafion membrane. The NMR line shape data gave mobility information, which was used to define amorphous and more ordered (crystalline) regions. The resultant data suggested that the perfluorinated molecular backbone could be considered to be an immobile component of the polymer associated with ordered regions, and that the latter are crystalline or nearly crystalline.⁴⁸

1.2.3. Actuation Mechanism of IPMCs

The novel future applications of IPMCs require our best knowledge of the actuation mechanism of these materials. Shahinpoor and Kim⁴⁹ have collected several models that have been proposed since 1950 for the actuation mechanism of IPMC in an extensive review on ionic polymer metal composites. There, it has been mentioned that the first attempt to analytically understand the IPMCs dates back to 1950 when Kuhn⁵⁰ and his co-workers studied the degree of ionization of the network of an ion-containing polyelectrolyte

and the effect of that on the swelling and contraction of the network. His efforts were followed by others till the early 1990s, when Shahinpoor⁵¹ discussed the conceptual design, kinematics, and dynamics of a swimming robotic structure containing an electroactive polymer gel. In 1995, a theory on electrically induced dynamic contraction of ionic polymeric gels was introduced which was based on electro-capillary and electro-osmotic forces.⁵² Asaka and Oguro⁵³ also presented a theory on actuation mechanisms in IPMC, considering the electro-osmotic drag term in transport equations and how this flow might generate swelling stresses for driven actuation. The first phenomenological theory for sensing and actuation in IPMCs was developed by De Gennes.⁵⁴ In the same year, Nemat-Nasser and Li⁵⁵ discussed the electromechanical response of IPMCs according to electrostatic attraction/repulsion forces. This model include ion and water transport, electric field, and elastic deformation and it emphasized that ion transport may control the initial fast motion of IPMC actuation. In this model, the hydrophobic molecular backbone of the polymer is separated from the hydrophilic clusters, as displayed in Figure 1.2. The sulfonate groups within the hydrophilic clusters are covalently attached to the perfluorinated molecular backbone and the associated cations may move within the water that fills the interconnected clusters. Once an electric field is applied, cations with their solvation shell of water molecules are redistributed and migrate toward the cathode (negatively charged face of IPMC) which results in a fast bending deformation of IPMC toward the anode (positively charged face of IPMC). Figure 1.3 displays a schematic diagram of bending deformation of an IPMC. Once the two metal electrodes (see Section 1.2.4.3) are shorted, the fast motion is followed by a slow relaxation of the IPMC in the opposite direction, toward the initial state of the sample.

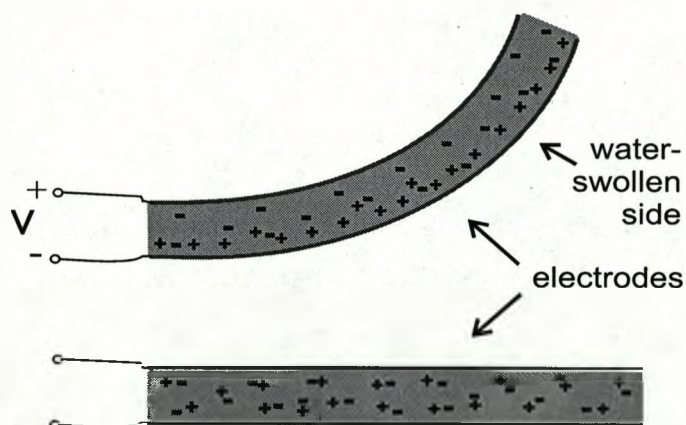


Figure 1.3. Schematic diagram of bending action in an IPMC actuator.

Bar-Cohen¹ has presented a detailed description of the actuation mechanism of an IPMC according to the Nemat-Nasser and Li⁵⁵ model. He also provided an outline of the possible changes that might happen in the local properties of IPMC near the cathode and the anode, on application of a 1V d.c. potential. These changes are explained as follows.

When a 1V d.c. potential is applied across the thickness of an IPMC sample the charge balancing cations on the sulfonate groups start to migrate and redistribute themselves. At the anode, a thin anode boundary layer is proposed in which clusters experienced a reduction in cation concentration. The depletion of cations from their clusters may result in any of the following effects within the anode boundary layer:¹

- a) A decrease in the effective stiffness of the polymer, due to the decrease in the interaction forces between the cations and the fixed anions within the clusters.

- b) An increase in the associated entropy and a decrease in the elastic energy of the polymer, as a result of the repulsive electrostatic force between the fixed anions within each cluster.
- c) Reorientation of the free water in the clusters to increase the effective electric permittivity of the clusters and reduce the repulsive electrostatic forces among the fixed anions within each cluster.
- d) Removal of some of the hydration water of the clusters which would tend to reduce their average volume:
- e) A decrease in the osmotic pressure inside the clusters, due to the reduced ion concentration.

At the cathode, the application of 1V d.c. potential results in cation enrichment within the clusters and so formation of a thin cathode boundary layer. The excess cations in this layer may cause the following effects within the cathode boundary layer:¹

- a) An increase in the effective stiffness of the polymer due to the increase in the interaction forces between the cations and the fixed anions within the clusters.
- b) A decrease in the associated entropy and an increase in the elastic energy of the polymer, as a result of the attractive electrostatic force, which tends to hold the fixed anions more tightly within the clusters.
- c) A reduction in the effective electric permittivity of the clusters causing an increase in the electrostatic forces between cations and the fixed anions within each cluster.
- d) An increase in the water content of the clusters, which tends to increase their volume.
- e) An increase in the osmotic pressure within the clusters, due to the increased ion concentration.

According to this model, the anode and cathode boundary layers with their corresponding charged electrodes form two double layers and shield the remaining part of the IPMC from the effect of the electric field.¹ Thus, the bending deformation of the IPMC occurs as a result of the combination of the above-mentioned five effects (a-e) occurring at these two double layers. Under application of a d.c. potential, the initial fast bending deformation of the IPMC sample towards the anode is followed by a slow relaxation of the sample in the opposite direction, towards the cathode. Bar-Cohen¹ has suggested that this behaviour of the sample is controlled by the slow diffusion of water into the shrunken anode boundary layer, and out of the swollen cathode boundary layer.

In general, most of the models proposed for the actuation mechanism of IPMCs emphasize the strong influence of electrostatic and hydraulic effects in describing the bending deformation of IPMCs. These effects have been extensively described by Bar-Cohen¹. The hydraulic model declares that ions in the ion exchange polymers are hydrated and so the migration of these ions with their associated solvation shell of water molecules in an applied electric field contributes to volumetric swelling stresses of IPMCs. The electrostatic model, however, declares that, on application of an electric field, the locally imbalanced net charge density in the ion exchange polymer causes the relaxation of the polymer chains near the anode and further extends the chains near the cathode. The mixed model¹ states that both the hydraulic and electrostatic effects play key roles in the bending response of IPMCs, although, depending on the cation and solvent type only one of these effects may control the bending response of IPMCs.

Shahinpoor and co-workers² have presented a number of plausible models for the micro-electromechanics of ionic polymer gels as electrically controllable artificial muscles in

different environments. In order to understand the underlying mechanism of sensing and actuation of IPMCs, plots of blocked force and displacement versus time have been prepared for IPMCs, when they are subjected to applied potential of sinusoidal, triangular, square, and sawtooth waveforms.⁵⁶

1.2.4. Factors Effecting Actuation Response of IPMCs

The investigation on the actuation mechanism of IPMC actuators indicated that their bending performance is influenced by the type of charge balancing cations on the sulfonate groups, the material and the structure of the electrodes, the solvent, the level of hydration, thickness of the ionic IPMC polymer and the dimension of IPMCs.¹ The effects of these factors on the actuation response of IPMCs are briefly described in the following sections.

1.2.4.1. Cations

Several investigations indicate the strong influence of cation species on the actuation and sensing performance of IPMCs.^{55,57,58} These studies show the effect of the monovalent cations such as alkali metal salts (e.g. Li^+ , Na^+ , K^+) and tetraalkylammonium salts (e.g. tetrabutylammonium (TBA^+), tetramethylammonium (TMA^+)) on the behaviour of IPMCs: the level of hydration, the magnitude of bending, stiffness and their surface conductivity. When a hydrated strip of Nafion-based IPMC in an alkali metal cation form is subjected to a small d.c. potential, it undergoes fast bending deformation towards the anode, followed by a slow relaxation in the opposite direction (towards the cathode). The results from studies cited here indicate that the Li^+ -exchanged IPMCs produce the greatest tip

displacement and smallest slow relaxation and is superior to those containing the other alkali metals.¹ Also, the TBA⁺-exchanged IPMCs exhibit a very slow motion and much smaller bending deformation towards the anode, without any slow relaxation in the opposite direction.⁵⁹ The observed differences are attributed to the hydration phenomenon and the mobility of the cations. The Li⁺ ion is the smallest bare ion and has the highest hydration level. However, the TBA⁺ ion has a relatively large diameter and due to its hydrophobic structure it has negligible hydration. It has been suggested that large ions may sterically entrain free water molecules, forcing them to move towards the cathode. These factors may explain why the actuation behaviour of IPMC varies depending upon the nature of cations.¹

The stiffness of Nafion membrane is primarily due to the presence or absence of water (solvent) however the nature of the cation present also has a significant effect on stiffness, especially in a dry sample. Since the ion and solvent uptake of IPMCs is dependent on the method of solvation and also the cation activity and mobility, the stiffness of samples also depends on the radius of the cations and the charge they are carrying.¹

The surface conductivity is another important electrical property which can influence the actuation behaviour of IPMC samples. In a study conducted by Nemat-Nasser and Wu⁵⁹, it has been shown that the surface conductivity of a Nafion-based IPMC sample is also significantly influenced by the nature of the neutralizing cations on the sulfonate groups of Nafion polymer. They observed a decrease in the surface conductivity of the IPMC sample on going from the Na⁺- to the TBA⁺-exchanged form. This is thought to be due to the greater microscopic swelling of the polymer in the TBA⁺-exchanged form, which introduces microcracks in the electroded metal layers at the surface.⁵⁹

1.2.4.2. Solvents

As was mentioned earlier in this Chapter, the chemical structure of Nafion consists of a perfluorinated molecular backbone with sulfonic acid side groups arranged at intervals along the chain. The swelling behaviour of this ion exchange polymer, therefore, depends strongly on the interactions of the hydrophobic perfluorinated molecular backbone and the hydrophilic ionic groups of the polymer with different solvents. Elliot and colleagues⁴¹ have studied the microscopic and bulk swelling of Nafion membrane in a mixture of ethanol and water using x-ray diffraction and optical microscopy. The results showed that the polymer expands or contracts as the solvent was changed and that the degree of macroscopic swelling increased with increasing ethanol content in the solvent. They suggested the more polar solvent (water) interacts preferentially with the ionic groups, whereas the less polar solvent (ethanol) mainly affects the behaviour of the perfluorinated molecular backbones and causes the molecular backbone chain to expand and form a highly stretched random structure in the solvent.⁴¹ In another study, the effect of methanol, ethanol, 2-propanol and water on the proton conductivity and surface properties of Nafion membrane were investigated using impedance spectroscopy and atomic force microscopy.¹⁸ The authors established that both conductivity and surface roughness of Nafion membranes decreased in an alcohol environment whereas they increased in an aqueous environment. Nemat-Nasser and Zamani⁶⁰ have studied the effect of different types of solvents on the actuation behaviour of IPMCs. They presented the results of a series of tests on both Nafion- and Flemion-based IPMCs with ethylene glycol as the solvent, and compared these with the results obtained using water (as the solvent). The results indicated that the IPMCs

with ethylene glycol as their solvent have greater solvent uptake, less stiffness and can be subjected to higher voltages without electrolysis. However, the actuation of an IPMC sample with water as solvent is faster and the sample possesses higher overall electrical capacitance than with ethylene glycol.

1.2.4.3. Electrodes

As was mentioned earlier, the electrodes in IPMCs are made up of small, interconnected metal particles, generally platinum or gold, which penetrate into the sub-surfaces of the ion exchange polymer membrane through an absorption/reduction process. Concentration and size distribution of platinum particles within the polymer matrix is an important issue that can directly affect the actuation performance and generated force of IPMCs. It has been established that increased platinum concentration within the polymer, using the repetitive platinum absorption/reduction process, leads to achievement of an IPMC with much higher electrical capacitance.⁵⁸ The platinum particles penetrate the polymer to a depth of $\sim 10 \mu\text{m}$ and provide a porous electrode structure at both surfaces of the IPMC. This has the advantage of allowing effective water transport within the electrode regions and the disadvantage of water leakage, in the form of ion-driven water molecules, out of the porous electrode surface.⁵⁸ This phenomenon reduces the effectiveness of the IPMCs and reduces the forces they can generate. Shahinpoor and Kim⁶¹ have discussed a successfully developed technique to prevent such solvent leakage out of the porous electrode. They recognised that the coagulation of platinum particles within the polymer during the chemical reduction process could be the main reason for obtaining large platinum particles ($\sim 50 \text{ nm}$) compared to those associated with ion clusters ($\sim 5 \text{ nm}$). In order to enhance the

dispersion of platinum particles within the material and reduce the coagulation of platinum particles they introduced an effective dispersing agent (polyvinylpyrrolidone) during the chemical reduction process. This process resulted in the formation of platinum particles with more uniform sizes at the electroded polymer surfaces. They also found that, by using a stretching technique, the particle penetration within the polymer was much more effective and a much denser platinum particle phase was formed which significantly improved the forces generated in the IPMCs.

1.2.4.4. Level of Hydration

The hydration of IPMCs plays a key role in their actuation performance. The bending deformation of IPMC actuators depends on the migration of cation species within the Nafion membrane. The solvent (water) provides a medium for ions to be transported towards their desired charged electrode in an applied electric field. Without a solvent, the ion transport inside the polymer will stop, reducing or eliminating the actuation behaviour of IPMCs. Therefore, an IPMC sample needs to obtain the maximum hydration level in order to show its highest actuation performance. It has been shown that the amount of solvent uptake (level of hydration) at full saturation depends on the cation used, being a maximum for hydrogen.¹

The work of Nemat-Nasser and Wu⁵⁹ shows that the stiffness of the Nafion polymer (without electrode) and the Nafion-based IPMCs is strongly affected by their hydration level. A dry sample may have stiffness 10 times greater than when it is water saturated. They have also shown that, in open air, the hydration level and the cross-sectional area of both dry and hydrated samples does not remain constant because samples in the dry form

absorb moisture and swell, whereas samples in the hydrated form lose water by evaporation and shrink. Furthermore, during the bending actuation of IPMC, the extent of hydration and thus the power and force generated change continuously.

1.2.4.5. Sample Dimension

Investigations concerning the optimization of the performance of IPMC actuators have revealed that the size and dimension of these materials can also affect the magnitude of their output power and generated force. Commercially available Nafion membranes have a typical thickness in the range of approximately 100-300 μm and can be used to prepare IPMCs with fixed thickness. However, other thicknesses may be required in different fields of application. In this regard, Kim and Shahinpoor⁶² reported a newly developed fabrication method that can scale up or down the IPMC samples to give strips of μm to cm thicknesses. Using this recently developed technique, they prepared a number of samples having different thicknesses (more than 2 mm) and showed that thicker IPMC samples generate much greater forces but smaller displacement.⁶² They also carried out mechanical tests on the commercial and prepared thick Nafion samples and the results revealed that prepared thick samples have a weaker electrostatic crosslinking and crystallinity in comparison with commercially available Nafion samples.

Also, the results from the research of Nemat-Nasser and Wu⁵⁹ show that the longitudinal resistance (along the length, x-axis) of IPMC samples, which influences their actuation behaviour, is significantly controlled by the dimensions of the sample. The resistance of a sample increases with increasing length, L , and decreasing width, W . The specific resistance, R_s (in Ω/cm), is obtained from:

$$R_s = R \frac{W}{L} \quad (1.2)$$

In the transverse direction (along the membrane thickness, z-axis), it has also been shown that, the conductivity of Nafion increases almost linearly with membrane thickness.^{63,64} The membrane conductivity can be calculated from the membrane resistance, R , according to Equation 1.3, where t is the membrane thickness and A is the surface of the electrode (in cm^2).

$$\sigma = \frac{t}{RA} \quad (1.3)$$

1.2.5. Measurement of Actuation

As mentioned before, IPMC actuators can operate under a small applied potential. On application of a small d.c potential, the IPMC sample bends towards the anode as a result of ion migration within the polymer and on application of a small alternating voltage, the sample undergoes a swinging movement as a consequence of the changes in the polarity of the applied potential. The development of these actuators requires a better understanding of the parameters that control the bending deformation and the force generated in IPMCs. In this regard, the mechanical and electrical characteristics of the bending response of IPMCs are studied, using reliable characterization methods. The factors that affect the mechanical performance of IPMCs can be examined by performing an accurate and systematic study of the inter-relationship between the composition and the preparation procedures of IPMCs and their electrochemical and electromechanical behaviour.

In order to study the mechanical characteristics of IPMC, strips of these materials have been used to investigate the magnitude of displacement and force response. Shahinpoor⁶⁵ has shown that by applying a low alternating voltage to a strip of Nafion-based IPMC sample, placed in a fixed platform, the swinging movement of the free end of the strip could be calibrated and its response measured accordingly. The results from his study exhibited that the displacement level depends on the voltage magnitude and the frequency. For 0.5cm×2cm×0.2mm thick IPMC samples, the highest displacement, up to 15 mm, was observed for lower frequencies, down to 0.1 Hz or 0.01 Hz. He also investigated the frequency-dependence of the amplitude of bending deformation of the IPMC samples when they were subjected to alternating voltages of various forms such as sinusoidal, rectangular, saw tooth or pulsed at frequencies up to 100 Hz and amplitudes up to 10 V. On application of a 2 V sinusoidal voltage, at a frequency range of 0.1 Hz to 35 Hz, a resonance was observed at about 20 Hz where the associated displacement was 7.5 mm.⁶⁵ The generated force of the IPMC samples in response to a 2 V sinusoidal voltage at frequency of 0.5 Hz was also studied. The results indicated that the IPMC behaviour is similar to a piecewise linear spring with large deformation.⁶⁵ In another similar study, the plots of measured displacement of IPMC samples versus frequency have also been presented, for a 2 V sinusoidal applied potential.⁵⁶ The electrical properties of the IPMC can be assessed using impedance spectroscopy and cyclic voltametry. A typical measured impedance plot, provided in the literature,⁶¹ shows the frequency dependency of impedance of the IPMC. It also shows that the IPMC is nearly completely resistive in the high frequency range while it is fairly capacitive in the low frequency range.⁶¹ The cyclic current/voltage response in a

cyclic voltammogram of a typical IPMC can give information about whether or not any distinct reduction or oxidation processes have occurred in the system.¹

1.2.6. Comparison with Other Smart Actuator Materials

Many different smart actuator materials such as piezoelectrics, electroceramics (EACs) and shape memory alloys (SMAs) are known. The reason why most of the current researches have been done on ionic EAPs, especially IPMCs, is that these materials are relatively inexpensive, low-mass, compact, flexible and can be cut to any size and shape. IPMCs show a large deformation in response to a low applied voltage (1-5 V) and their response is relatively quick (μsec -sec). It is interesting to note that the bending deformation of IPMCs, under applied voltages is not associated with generation of heat or electromagnetic waves.¹ This property of IPMCs has attracted the attention of researchers in biomechanical and biomimetic areas. A comparison between IPMCs, EACs and SMAs shows that the level of induced strain for IPMCs can be as high as two orders of magnitude greater than the rigid and fragile EAC.³⁸ Unlike ionic EAPs (e.g. IPMCs), EACs require a high potential and large electrical power supplies to move in the micro-strain regime so their applications are limited by this and also by their high mass compared to IPMCs. According to a study by Hunter and Lafontaine,⁶⁶ SMAs and hydraulic actuators are able to exhibit large stress and strain. However, poor conversion of thermal energy to mechanical energy affects the mechanical efficiency of SMAs.⁶⁶ The efficiency is higher and response speed is shorter for ionic EAPs than for SMAs. Hydraulic actuators show high efficiency but the large operating equipment cost influences their applications for small scale devices.⁶⁶ Unlike

hydraulic actuators, IPMCs can be produced at low cost and easily formed in various shapes. However, IPMCs must to be kept hydrated to show their high performance as actuators, which may be disadvantageous in many applications. According to Table 1.1,¹ which compares the properties of EAPs, SMAs and EACs, the other disadvantages of EAPs are their low force output and slow response time which can limit their applications where higher force output and faster response for a given actuation signal is required.¹

Table 1.1. Comparison of the properties of Electro-active Polymers (EAPs), Shape Memory Alloys (SMAs) and electroceramics (EACs).¹

Property	EAP	SMA	EAC
Actuation strain	>10%	<8%	0.1-0.3%
Force (MPa)	0.1-3	about 700	30-40
Reaction speed	μ s-min	s-min	μ s-s
Density (g/cm ³)	1-2.5	5-6	6-8
Drive voltage	2-7 V	not applicable	50-800 V
Consumed power	mW	W	W
Fracture toughness	resilient, elastic	short fatigue life, elastic	fragile

1.2.7. Applications of IPMC Actuators

A number of potential applications of IPMCs that have been proven to be a possible alternative to conventional methods have been gathered and presented in a review paper.⁶⁷

There are various industrial and biomedical potential applications using IPMCs as sensors

and actuators. It is beyond the scope of this thesis to mention or explain all such applications, however, a brief description of the most important and interesting applications of IPMCs will be given in this section.

1.2.7.1. Industrial Applications

(a) Mechanical Robot Grippers

Soft micro- to macro-grippers could be fabricated from IPMC membranes when two IPMC actuators are placed parallel to each other and wired in such a way that they bend in opposing directions. Grippers can be activated by a low voltage (~5 V) and are able to lift an object such as a small stone. NASA claims that such grippers could work in outer space environments of pressures of a few mBar and temperatures of the order of -140°C. Since NASA's investigations in space require light weight, low cost compact grippers and actuators which consume little energy they have considered the IPMCs as a possible class of materials for space actuators.⁶⁷

(b) Metering Valves

Metering valves, which are applied to control the aqueous fluid flow in tubes, could also be manufactured from IPMC actuators. In this case, an undulating strip of IPMC is placed in a pipe flow as metering valve. By applying a calibrated amount of direct voltage to the IPMC metering valve attached to the tubes, and so varying the magnitude of bending displacement of the IPMC actuator, the amount of fluid flow through the tube could be controlled.⁶⁷

(c) Diaphragm Pumps

Diaphragm pumps can be fabricated by attaching two different size IPMC planar sections and sandwiching them between two circular or rectangular gold plated ring electrodes. Variations of the curvature of the planar sections permits modulation of the volume trapped between the IPMCs. The flow and volume of fluid being pumped could be controlled by adjusting the applied voltage amplitude and frequency.⁶⁷

(d) Microelectromechanical Systems (MEMS)

IPMC sensors and actuators could be manufactured using MEMS technology since they are easily processable and can be made as small as desired and in any geometry. MEMS is a new way of making complex electromechanical systems similar to the way integrated circuits are made, using a batch fabrication technique.⁶⁷ This technology is generally utilised to fabricate sensor and actuator microarrays, disposable microbiosensors for real time medical applications, and a variety of microfabrication processes requiring the manipulation of small objects. Some examples of such IPMC MEMS devices include micro-pumps, micro-valves, micro-actuators, micro propulsion engines for material transport in liquid media and biomedical applications such as active microsurgical tools.⁶⁷

1.2.7.2. Biomedical Applications

(a) Artificial Ventricular or Cardiac-Assist Muscles

Artificial ventricular assist type muscle could be made from IPMC actuators and implanted external to a patients' heart. This assist muscle is partly sutured to the heart to act as a heart compression device without contacting or interfering with the internal blood circulation.⁶⁷

(b) Surgical Tools

Small strip or fiber-like IPMC actuators could be used as a guide wire or a micro-catheter in biomedical applications for intra-cavity endoscopic surgery and diagnostics. Using these soft and flexible actuators, small internal cavities in the body can be navigated.⁶⁷

(c) Incontinence Assist Device

Various configurations of IPMCs may be used in medical applications involving incontinence. In this system, a patient can activate the muscle, by means of a battery operated switch, to prevent leakage and control discharge.⁶⁷

(d) Active Tactile Display Devices

IPMC actuators could be used to produce tactile display devices. These devices can present textual and graphical information to the blind. The display medium can be constructed as a planar array of small cones called 'reading pins'⁶⁸

1.3. References

-
- [1]. Y. Bar-Cohen, "Electroactive Polymer (EAP) Actuators as Artificial Muscles – Reality, Potential & Challenges", *SPIE Press*, Bellingham WA, 2001.
 - [2]. M. Shahinpoor, Y. Bar-Cohen, J. O. Simpson, J. Smith, *Smart Structures & Materials, Proc. SPIE*, 1998, 7, R15.
 - [3]. M. Shahinpoor, *Electrochimica Acta*, 2003, 48, 2343.
 - [4]. I. Bergman, *GB Patent*, 1970, 1200595.

-
- [5]. C. McCollum, D. Pletcher, *Electrochim. Acta*, 1975, 20(11), 811.
- [6]. C. A. Levine, A. L. Prevost, Dow Chemical Co., *FR Patent*, 1968, 1536414.
- [7]. T. Hitachi, *JP Patent*, 1983, 58185790.
- [8]. P. Millet, R. Durand, M. Pineri, *Int. J. Hydrogen Energy*, 1990, 15(4), 245.
- [9]. Millet, R. Durand, E. Dartyge, G. Tourillon, A. Fontaine, *J. Electrochem. Soc.*, 1993, 140(5), 1373.
- [10]. M. Shahinpoor, *ACT. Mater. Adapt. Struct.*, 1992, 91.
- [11]. K. Sadeghipour, R. Salomon, S. Neogi, *Smart Mater. Struct.*, 1992, 1(2), 172.
- [12]. K. Oguro, Y. Kawami, H. Takenaka, *Osaka Kogyo Gijutsu Shikensho kiho*, 1992, 43(1), 21.
- [13]. M. Mojarrad, M. Shahinpoor, *3rd Inter. Conf. Intel. Mater. Proc. SPIE*, 1996, 2779, 1012.
- [14]. M. Shahinpoor, M. Mojarrad, *US Patent*, 2000, 6109852.
- [15]. S. Nemat-Nasser, S. Zamani, *Smart Structures & Materials, Proc. SPIE*, 2003, 5051.
- [16]. H. L. Yeager, A. Steck, *Anal. Chem.*, 1979, 51, 862.
- [17]. A. Eisenberg, M. King, R. S. Stein, "Polymer Physics", *Academic Press*, New York, 1977, Chap 4.
- [18]. M. Abed Affoune, A. Yamada, M. Umeda, *J. Power Sources*, 2005, 148(9), 17.
- [19]. J. J. Fontanella, M. C. Wintersgrill, R. S. Chen, Y. Wu, S. G. Greenbaum, *Electrochimica Acta*, 1995, 40(13-14), 2321.
- [20]. H. L. Yeager, B. O'Dell, Z. Twardowski, *J. Electrochem. Soc.*, 1982, 129(1), 85.
- [21]. A. A. Grownowski, H. L. Yeager, *J. Electrochem. Soc.*, 1991, 138(9), 2690.
- [22]. T. Yamamoto, C. Hindeshima, G. Prakash, G. A. Olah, *J. Organ. Chem.*, 1991, 56(6), 2089.
- [23]. G. Xie, T. Okada, *J. chem. Soc. Farad. Trans.*, 1996, 92(4), 663.
- [24]. W. T. Grubb, *J. Electrochem. Soc.*, 1959, 106(4), 275.

-
- [25]. F. G. Will, H. S. Spacil, *J. Power Sources*, 1980, 5, 173.
- [26]. S. Tsushima, K. Teranishi, K. Nishida, S. Hirai, *Magnetic Resonance Imaging*, 2005, 23, 255.
- [27]. M. Konyo, Y. Konishi, S. Tadokoro, T. Kishina, *Smart Structures & Materials, Proc. SPIE*, 2004, 5385, 307.
- [28]. T. D. Gierke, *The electrochemical Society Extended Abstracts*, 1977, 77(2), 438, 1139.
- [29]. H. J. Yeager, A. Eisenberg, *American Chem. Soc.*, 1982, 180(1), 41.
- [30]. T. Xue, S. Trent, K. Osseo-Asare, "*J. Membr. Sci.*", 1989, 45(3), 261.
- [31]. G. Meresi, Y. Wang, A. Bandis, P. T. Inglefield, A. A. Jones, W. Y. Wen, *Polymer*, 2001, 42, 6153.
- [32]. C. Heinter-Wirguin, *J. Membr. Sci.*, 1996, 120(1), 1.
- [33]. R. Dulessix, M. Escoubes, B. Rodmacq, F. Volino, E. Roche, A. Eisenberg, M. Pineri, *American Chem. Soc.*, 1980, 127, 469.
- [34]. W. Y. Hsu, T. D. Gierke, *J. Membr. Sci.*, 1983, 13, 307.
- [35]. G. Pourcelly, A. Oikonomou, C. Gavach, *J. Electroanal. Chem.*, 1990, 287, 43.
- [36]. J. A. Elliot, S. Hanna, A. M. S. Elliot, G. E. Cooley, *Macromolecules*, 2000, 33, 4161.
- [37]. L. J. Hobson, H. Ozu, M. Yamaguchi, M. Muramatsua, S. Hayase, *J. Mater. Chem.*, 2002, 12, 1650.
- [38]. Y. Bar-Cohn, S. Leary, M. Shahinpoor, J. O. Harrison, J. Smith, *Smart Structures & Materials, Proc. SPIE*, 1999, 3669, 57.
- [39]. M. D. Bennet and Donald J. Leo, *Smart Structures & Materials, Proc. SPIE*, 2004, 5385, 210.
- [40]. R. B. Moore, K. M. Cable, T. L. Croley, *J. Membrane Sci.*, 1992, 75, 7.
- [41]. J. A. Elliot, S. Hanna, A. M. S. Elliot, G. E. Cooley, *Polymer*, 2001, 42, 2251.
- [42]. M. C. Wintersgill, J. J. Fontanella, *Electrochim. Acta*, 1998, 43(10-11), 1533.

-
- [43]. M. R. Pereira, J. Yarwood, *J. Chem. Soc. Faraday Trans.*, 1996, 92(15), 2737.
- [44]. A. Lehmani, P. Turq, M. Perie, J. Perie, J. P. Simonin, *J. Electroanal. Chem.*, 1997, 428, 81.
- [45]. B. MacMillan, A. R. Sharp, R. L. Armstrong, *Polymer*, 1999, 40, 2471.
- [46]. K. Winfried, *Angewandte Chemie Int. Ed. Engl.*, 1990, 29, 1.
- [47]. M. Ise, K. D. Kreuer, J. Maier, *Solid state Ionic*, 1999, 125, 213.
- [48]. X. Gong, A. Bandis, A. Tao, G. Meresi, Y. Wang, P. T. Inglefield, A. A. Jones, W. Y. Wen, *Polymer*, 2001, 42, 6485.
- [49]. M. Shahinpoor, K. J. Kim, *Smart Mater. Struct.*, 2004, 13, 1362.
- [50]. W. Kuhn, B. Hargitay, A. Katchalsky and H. Eisenberge, *Nature*, 1950, 165, 514.
- [51]. M. Shahinpoor, *Smart Mater. Struct., Proc. SPIE*, 1992, 1, 91.
- [52]. M. Shahinpoor, Y. Osada, , *Smart Structures & Materials, Proc. SPIE*, 1995, 2441, 91.
- [53]. K. Asaka and K. Oguro, *J. Electroanal. Chem.*, 2000, 480, 186.
- [54]. P. G. De Gennes, K. Okumura, M. Shahinpoor, K. J. Kim, *Europhys. Lett.*, 2000, 50, 513.
- [55]. S. Nemat-Nasser, J. Y. Li, *J. Appl. Phys.*, 2000, 87, 3321.
- [56]. M. Shahinpoor, M. Mojarad, *Smart Structures & Materials, Proc. SPIE* , 1997, 3040, 294.
- [57]. Y. Abe, A. Mochizuki, T. Kawashima, S. Yamashita, K. Asaka, K. Oguro, *Polym. Adv. Technol.*, 1998, 9(8), 520.
- [58]. K. J. Kim, M. Shahinpoor, *Smart Mater. Struct.*, 2003, 12, 65.
- [59]. S. Nemat-Nasser, Y. Wu, *J. Appl. Phys.*, 2003, 93(9), 5255.
- [60]. S. Nemat-Nasser, S. Zamani, *Smart Structures & Materials*, 2003, 5051, 233.
- [61]. M. Shahinpoor, K. J. Kim, *Smart Mater. Struct.*, 2001, 10, 819.
- [62]. K. J. Kim, M. Shahinpoor, *Polymer*, 2002, 43, 797.

-
- [63]. M. N. Tsampas, A. Pikos, S. Brosda, A. Katsaounis, C. G. Vayenas, *Electrochimica Acta*, 2006, 51(13), 2743.
- [64]. P. Dimitrova, K. A. Friedrich, B. Vogt, U. Stimming, *J. Electroanal. Chem.*, 2002, 532, 75.
- [65]. M. Shahinpoor, *Smart Structures & Materials, Proc. SPIE*, 1999, 3669, 109.
- [66]. I. W. Hunter, S. Lafontaine, *Solid-State Sensor and Actuator Workshop, 5th Technical Digest, IEEE*, 1992, 22-25 June, 178.
- [67]. M. Shahinpoor, K. J. Kim, *Smart Mater. Struct.*, 2005, 14, 197.
- [68]. Y. Bar-Cohen, C. Mavroidis, M. Bouzit, B. Dolgin, L. Deborah, *8th Ann. Inter. Symp. on Smart Structures & Materials, Smart Structures & Materials, Proc. SPIE*, 2001, Paper No. 4329-47.

Chapter Two

Techniques

2.1. Introduction

The theory of MRI and SEM that will be reviewed in this chapter will be necessary to understand the experiments described in chapters Four, Five, Six, and Seven. Theoretical descriptions of the particular techniques used in those studies will be addressed as well. The discussion in this chapter is restricted to a general outline of the basic principles of the techniques and contains no original contribution by the author.

2.2. Magnetic Resonance Imaging (MRI)

2.2.1. Introduction

Magnetic resonance imaging (MRI) microscopy is a technique based on the principles of nuclear magnetic resonance (NMR), which has the ability to provide microscopic chemical and physical information about molecules. Clinical MRI scanners with horizontal bore magnets (between 60 and 100 cm diameter) had been available since the 1980s in hospitals for clinical diagnosis. These scanners operate at magnetic field strengths between 0.23 T and 2.4 T and achieve spatial resolution of the order of 5 mm^3 . Subsequently, MRI scanners were developed with a vertical bore, magnetic fields of 4.7-14.1 T, and image resolution of the order of 10^{-5} mm^3 to image smaller objects. This type of scanner is widely applied as a supportive technique for imaging of small material samples and for *in-vivo* imaging of development processes in biological systems such as plants.

The resolution of MRI is lower than that of other microscopic techniques such as atomic force microscopy, electron microscopy or even light microscopy but it offers several major advantages as an imaging technique:¹

1. MRI is a non-invasive and non-destructive imaging technique. Therefore, unlike other imaging preparative methods like optical or electron microscopy, samples may be studied several times under the same or changed conditions, which is a great advantage.

2. This technique can provide two- and three-dimensional images of a sample with scale resolution of $\leq 40 \mu\text{m}$.

3. Unlike other imaging techniques where a probe beam is directed at a specific angle through the sample, in MRI, image projections are possible in any direction.

4. It is nucleus-specific and allows the total density of a molecule of interest to be determined.

5. It is highly sensitive to the rotational and translational mobility of molecules in samples. Therefore, it is an attractive technique in materials science to study the structure, characterize the composition and quantify the mobility of fluid transport processes. These data are not achievable with other measuring techniques.

These fascinating properties has made MRI a powerful technique for monitoring the static and dynamic structural changes and processes in plant and animal tissues, polymers, food products and non-biological materials. In the next chapters, it will be shown that IPMC actuators are able to function effectively within the MRI scanner without degrading their imaging performance and how this technique yields information on molecular structure and water transport phenomena in IPMC samples.

Numerous classic texts^{1,2,3,4} give thorough descriptions of NMR and MRI. In the following sections, only an outline of the basic NMR and MRI principles, the pulse sequences used for imaging in this study and theoretical descriptions of the particular techniques used here will be presented.

2.2.2. The Nuclear Magnetic Resonance (NMR) Phenomenon

The phenomenon of nuclear magnetic resonance (NMR) is observed in any nucleus possessing non-zero spin when it is placed in a static magnetic field and exposed to a second oscillating magnetic field. Nuclear spin is a form of angular momentum which is quantized in integral or half-integral units, I , of $\hbar = h/2\pi$ (h is the Plank constant), depending on whether the number of constituent nucleons is even or odd.¹ I is known as the spin quantum number and is a fixed quantity characterizing a nucleus in its stable ground state. For $I \geq 1/2$, the nucleus will possess an inherent magnetic dipole moment, μ , proportional to the angular momentum, P . The proportionality constant is known as the gyromagnetic ratio, γ . Equation 2.1 shows the relationship between these two vectors. Gyromagnetic ratio is a constant for any particular nucleus.

$$\mu = \gamma P \tag{2.1}$$

For reasons of simplicity, the following discussion will be limited to nuclei with $I=1/2$ since most of the experiments performed in this work involved observation of the ^1H nucleus which has half-spin, $I=1/2$.

NMR arises from the interaction between the magnetic dipole moments of atomic nuclei and imposed strong magnetic fields, B_0 . This form of magnetic interaction is known as a

Zeeman interaction and the energy resulting from this interaction is written as $-\mu \cdot B_0$. For a half-spin nucleus the Zeeman interaction gives rise to the energy level structure shown in Figure 2.1.

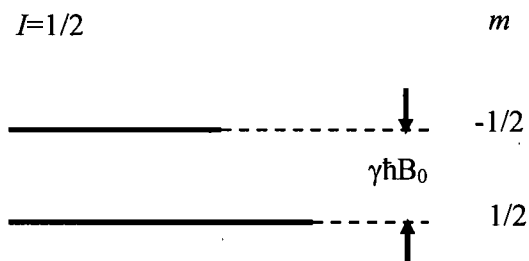


Figure 2.1. Energy level diagram for half-spin nuclei experiencing a Zeeman interaction.¹

The energy separation between levels is $\hbar\gamma B_0$. The $1/2$ and $-1/2$ energy levels are labeled as m . These two energy levels will be unequally populated when the nucleus is in a magnetic field. It means that the lower level, $1/2$, will contain slightly more nuclei than the higher level, $-1/2$. The ratio of the nuclei population is given by the Boltzmann equation:

$$\frac{N_{-1/2}}{N_{1/2}} = \exp\left(\frac{-\hbar\gamma B_0}{KT}\right) \quad (2.2)$$

where $N_{1/2}$ is the population on the lower state and $N_{-1/2}$ is the population on the upper state. K is the Boltzmann constant ($1.3806503 \times 10^{-23} \text{ m}^2 \text{ Kg S}^{-2} \text{ K}^{-1}$).

It is possible to excite nuclei into the higher energy level with electromagnetic radiation. Transitions between states are controlled by the selection rule $\Delta m = \pm 1$. The energy transferred in a single transition is equal to $\hbar\nu$, where ν is the frequency of the transition involved. Thus in the NMR experiment:

$$\nu = \left| \frac{\gamma}{2\pi} \right| B_0 \quad (2.3)$$

where, ν and γ are respectively the resonant frequency and the gyromagnetic ratio of the nucleus placed in a magnetic field B_0 . For protons, γ is $26.75720 \times 10^7 \text{ rad T}^{-1}\text{s}^{-1}$ and in a typical field of the order of 1 to 10 T, the frequency required for transition is of the order of 10^2 MHz which is in the radio frequency region.

In any NMR experiment there are a large number of nuclear spins in the sample and the NMR signal arises from the response of groups of spins (spin packets)⁵ experiencing the same magnetic field strength. Therefore, it is convenient to adopt a classical view of the spin system using the Vector Model. In this model, the magnetic field due to the spins in each spin packet can be represented by a magnetization vector. The vector sum of the magnetization vector from all of the spin packets is the bulk magnetization vector M . Figure 2.2 describes the behavior of the bulk magnetization in a conventional NMR coordinate system, using vector diagrams. At equilibrium, Figure 2.2(a), the external magnetic field, B_0 , and the bulk magnetization vector M are both along the z-axis. When this equilibrium is somehow disturbed, the bulk magnetization will experience a twisting force. This force however is applied to an already existing angular momentum and leads to the precessional motion of the bulk magnetization around the magnetic field, Figure 2.2(b). The frequency of precession is known as the Larmor frequency, $\omega_0 = \gamma B_0$, which is constant for any particular nucleus. The displacement of the bulk magnetization M from its equilibrium state produces a detectable NMR signal.

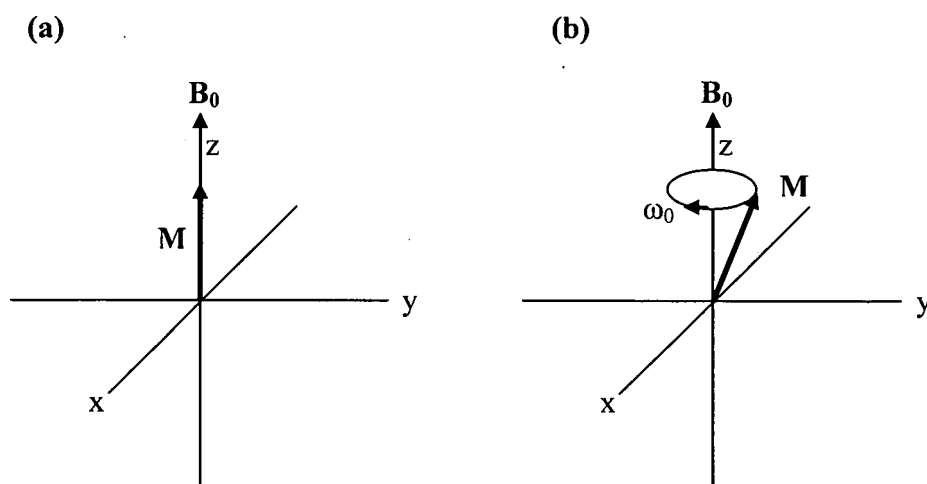


Figure 2.2. The behavior of the bulk magnetization, M (a) at equilibrium and (b) after perturbation.

The behavior of a net magnetization, M , in a magnetic field, B , is described by the Larmor theorem:

$$\frac{dM}{dt} = \gamma M \times B \quad (2.4)$$

where B is a magnetic field of amplitude B_0 corresponding to a precession of the magnetization about the field at rate $\omega_0 = \gamma B_0$.

2.2.2.1. Excitation

In pulse NMR, the excitation of the magnetization from equilibrium is caused by occasional application of a second smaller magnetic field, B_1 , perpendicular to the permanent B_0 field. B_1 is provided by a short resonant radio frequency (r.f) pulse. The linearly oscillating

pulsed field, $2B_1\cos\omega t$, is applied in the laboratory frame and can be deconvoluted into two magnetic fields rotating at angular rate ω in opposite directions (Figure 2.3).

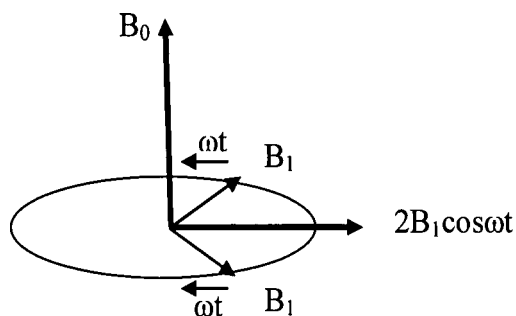


Figure 2.3. Linearly polarized, oscillatory transverse field $2B_1\cos\omega t$, represented as two counter-rotating circularly polarized fields.¹

One of these components will rotate in the same direction as the nuclear spin precession and will be responsible for the excitation phenomenon. The other rotating component will rotate at the opposite sense and can be ignored since $B_1 \ll B_0$.

Now if we consider a rotating frame of reference which rotates at the Larmor frequency about the z-axis of the laboratory frame the apparent precessional speed is reduced by ω and so, the magnetic field is reduced by ω/γ . In on resonance condition the pulse frequency is equal to the Larmor frequency, $\omega = \omega_0$, and the apparent magnetic field B_0 takes the value zero and leaves the applied field B_1 as the effective field along the rotating frame x-axis. In this case the r.f pulse rotates the bulk magnetization from its equilibrium position (along z-axis) through an angle $\Theta = \omega t$ and lays it along the x-axis.

In the off resonance condition the pulse frequency is not equal to the Larmor frequency, $\omega \neq \omega_0$, and the apparent field B_0 in the rotating frame takes the value $(B_0 - \omega/\gamma)$. In this case, the resultant effective field, B_{eff} , in the rotating frame is given by:

$$B_{eff} = (B_0 - \omega/\gamma)k + B_1i \quad (2.5)$$

where k and i are the unit vectors along the z and x axes of rotating frame, respectively.

Under these circumstances the precession of the bulk magnetization occurs about B_{eff} .

2.2.2.2. Relaxation

(a) Spin-Lattice Relaxation Time, T_1

The effect of a resonant r.f pulse is to disturb the spin system from its equilibrium state. The equilibrium is restored by a process known as spin-lattice relaxation, T_1 . This process involves an exchange of energy between the spin system and the surrounding thermal reservoir known as the lattice.¹ Because at equilibrium the bulk magnetization is directed along the longitudinal applied magnetic field, T_1 , relaxation is also macroscopically characterized by the longitudinal return of the bulk magnetization to its ground state of maximum length in the direction of the main magnetic field. The description of this process is given by the equation:

$$\frac{dM_z}{dt} = -\frac{(M_z - M_0)}{T_1} \quad (2.6)$$

with solution:

$$M_z(t) = M_z(0)\exp\left(-\frac{t}{T_1}\right) + M_0\left(1 - \exp\left(-\frac{t}{T_1}\right)\right). \quad (2.7)$$

where M_z and M_0 are referred to as the longitudinal and equilibrium magnetization, respectively.

According to the above equations, the rate of return of the net magnetization to its ground state is an exponential growth process (Figure 2.4).

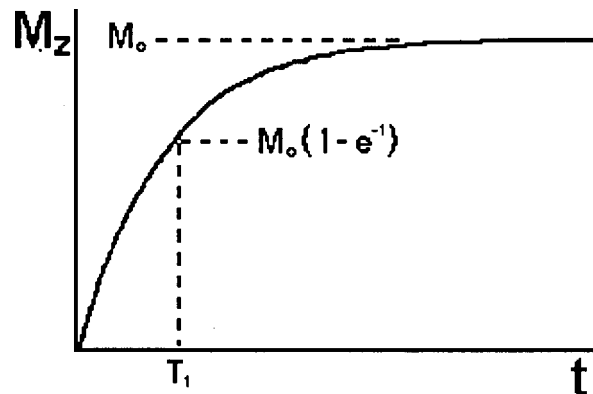


Figure 2.4. The exponential process of return of the net magnetization to its ground state.⁵

(b) Spin-Spin Relaxation Time, T_2

The second mechanism of the relaxation is known as spin-spin (or transverse) relaxation time, T_2 . This is the process by which nuclear spins come to thermal equilibrium among themselves but do not lose energy to the surrounding lattice. This mechanism of relaxation applies to the transverse component of the magnetization, M_{xy} , and similarly is described by the equation:

$$\frac{dM_{x,y}}{dt} = -\frac{M_{x,y}}{T_2} \quad (2.8)$$

with solution:

$$M_{x,y}(t) = M_{x,y}(0) \exp\left(-\frac{t}{T_2}\right). \quad (2.9)$$

This results macroscopically in loss of the transverse magnetization. The rate of loss of the transverse magnetization is an exponential decay process (Figure 2.5).

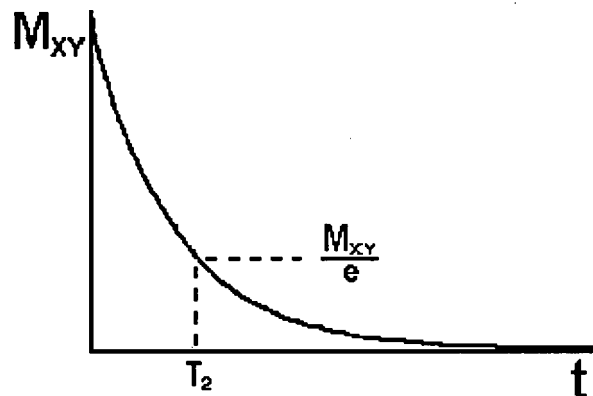


Figure 2.5. The exponential decay process of the return to equilibrium of the transverse magnetization, M_{xy} .

(c) Effective Spin-Spin Relaxation Time, T_2^*

Effective spin-spin relaxation time, T_2^* , is the loss of signal seen with dephasing of individual magnetizations. It is caused by magnetic field inhomogeneities which can occur in all magnets. T_2^* is not equal to T_2 and $T_2^* < T_2$. The 180 degree r.f. pulse used in a spin echo sequence (described in Section 2.2.2.4(b)) can rephase the spins that have undergone T_2^* decay.

(d) Bloch Equations

Combining Equations 2.4, 2.6 and 2.8 yields a set of relationships known as the Bloch equations:¹

$$\frac{dM_x}{dt} = \gamma(M_y B_0 + M_z B_1 \sin \omega t) - \frac{M_x}{T_2} \quad (2.10)$$

$$\frac{dM_y}{dt} = \gamma(M_z B_1 \cos \omega t - M_x B_0) - \frac{M_y}{T_2} \quad (2.11)$$

$$\frac{dM_z}{dt} = \gamma(M_x B_1 \sin \omega t - M_y B_1 \cos \omega t) - \frac{M_z - M_0}{T_1} \quad (2.12)$$

These equations provide a valuable reference in describing many important phenomena in NMR imaging. In practice these equations are quite accurate for spins in rapidly tumbling molecules however they are not applicable when the molecular motion becomes slow. The rapid motion regime is applicable to most molecules in the liquid state where dipolar interactions fluctuate because of molecular tumbling.

2.2.2.3. Relaxation and Molecular Motion

The nuclear spin relaxation process is caused by field fluctuation due to molecular motion since the local field experienced by a molecule changes when the molecule reorients. The rate of spin relaxation is sensitive to the magnitude of local interactions, experienced by the nuclear spins, and also to the rate of spin fluctuation. This is the regime of Bloembergen, Purcell, and Pound (BPP) theory, the first theory proposed to describe NMR relaxation and molecular motion.⁶ BPP showed that the spins need to interact with surrounding molecules to release their energy, and for relaxation the spin must interact with a fluctuating field on the molecular level.⁶

For protons with half-spin nuclei, the dominant interaction causing spin relaxation arises from the dipolar Hamiltonian, H_D . In liquids, H_D fluctuates due to molecular tumbling, leading to a time-averaged H_D of zero. For small molecules in liquid state (such as water),

the time it takes a molecule to tumble by one degree (correlation time, τ_c) is of order 10^{-12} s to 10^{-14} s and is very much smaller than the Larmor period. In this case, T_1 and T_2 relaxation appear identical and independent of Larmor frequency. The slowing of rotational motion leads to a reduction of T_1 and T_2 until the correlation time, τ_c , is of order of the Larmor period (about 10^{-9} s). This is the characteristic T_1 minimum, and for a pair of protons undergoing isotropic motion the relaxation values at this point are of the order 10-100 ms. However, as the rotational tumbling continues to become slower and more restricted in highly viscous liquids, concentrated flexible polymers and semi-rigid polymers, the correlation time, τ_c , decreases significantly, leading to the divergence of T_1 and T_2 relaxations in which T_2 continues to fall while T_1 increases. In other words, in the case of solids or rigid macromolecules, where H_D fluctuates very slowly, T_2 relaxation is much faster than T_1 relaxation. It should also be emphasized that the phenomenological description for T_2 given in Equation 2.9 is only applicable for spins existing in liquid state molecules. For solids and macromolecules, the decay process is more complicated than that shown by Equation 2.9.

Both T_2 and T_1 of the nuclear spins are dependent upon the molecular correlation time, τ_c , of the molecule.¹ However, the dependence of T_2 upon the magnetic field strength is significantly less than T_1 and therefore T_2 values measured at different frequencies may still be compared with each other. This, thus, makes the T_2 value an ideal parameter for the characterization of molecular dynamic properties.⁴

2.2.2.4. Pulsed NMR Methods

A set of r.f. pulses applied to a sample to produce a specific form of NMR signal is called a pulse sequence.⁵ There are different pulse sequences which are used in modern NMR, such as the inversion recovery sequence, the simple Hahn echo, the Carr-Purcell echo train, and the stimulated echo. Usually, each application of a particular pulse sequence to the NMR spin system is performed in rapid succession and the resulting signal from each experiment is successively added.

The following sections present a brief description of pulse sequences which are used in MRI imaging experiments in this thesis.

(a) Free Induction Decay (FID)

The NMR signal which is primarily measured in all experiments is called the Free Induction Decay (FID). In the FID pulse sequence, the bulk magnetization is rotated down into the xy plane with a 90° pulse.

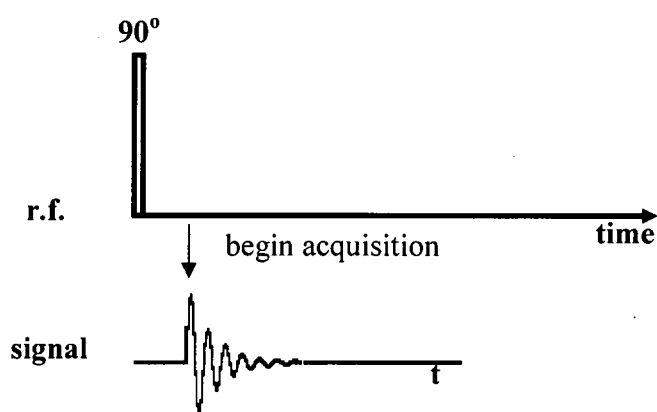


Figure 2.6. Free Induction Decay (FID) following a single 90° pulse.

It is measured in the time domain as an oscillating and decaying e.m.f. induced by the magnetization in free precession (Figure 2.6).

By Fourier transformation, the signal in time domain may be presented in the frequency domain. In this transformation no information is created or lost and therefore the original signal can be recovered from the Fourier transform, and *vice versa*.

When the FID sequence is repeated, the amplitude of signal in the frequency domain, S , will depend on T_I and the time between repetitions, T_R , of the sequence. In Equation 2.13, signal intensity, S , is related to k and ρ , which are respectively the proportionality constant and the spin density in the sample.

$$S = k\rho(1 - e^{-T_R/T_1}) \quad (2.13)$$

(b) Simple Hahn Spin Echo Pulse Sequence

Another commonly used pulse sequence is the Hahn spin echo pulse sequence⁷ which involves application of a 90° pulse followed by a 180° pulse. Application of a 90° pulse results in the rotation of the bulk magnetization down into the xy plane. The transverse magnetization then starts to dephase due to field inhomogeneity. Magnetic inhomogeneity causes nuclear spins to precess at differing Larmor Frequencies according to their location in the sample. In order to rephase the transverse magnetization Hahn⁷ applied a 180° pulse at some point in time after the 90° pulse. This pulse rotates the magnetization by 180° about the x-axis and causes the magnetization to rephase and to produce a signal called a 'spin-echo'.

$$S = k\rho(1 - e^{-T_R/T_1})e^{-T_E/T_2} \quad (2.14)$$

According to the signal equation for a repeated spin echo pulse sequence (Equation 2.14) the amplitude of signal, S , is a function of the repetition time, T_R , and the spin echo time T_E . Spin echo time is defined as the time between the 90° pulse and the maximum amplitude in the echo.

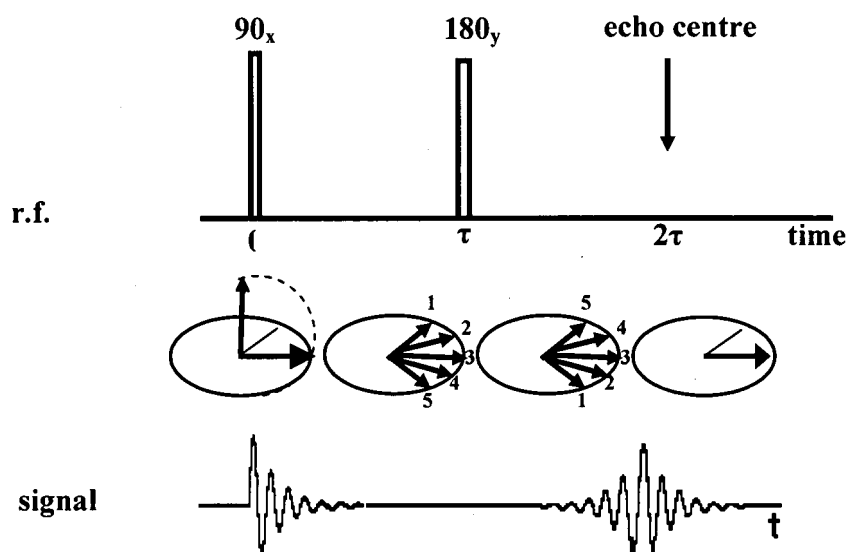


Figure 2.7. Spin echo pulse sequence showing the echo signal. τ is the length of time that the pulse is on and is assumed to be much smaller than the T_1 and T_2 .

(c) Carr-Purcell-Meiboom-Gill (CPMG) Pulse Sequence

The phase coherence recovered in the nuclear spin echo is subsequently lost at some point in time after the formation of spin-echo, $t > 2\tau$ (Figure 2.7). However, if a train of additional 180° r.f. pulses is used as suggested by Carr and Purcell⁸ successive recoveries are possible. When a train of 180° pulses is used after an initial 90° pulse, multiple echoes

are produced. That is, a 180° pulse following an echo can cause the echo to re-focus and form a new echo. If the pulse rotations differ from 180° , echoes do not refocus perfectly. Meiboom and Gill⁹ developed a sequence in which the imperfections in successive echoes became self-correcting. This sequence is called Carr-Purcell-Meiboom-Gill (CPMG) and introduces a 90° phase shift into the radio frequency field between the initial 90° pulse and the subsequent 180° pulses. The envelope of the echoes in a CPMG sequence is determined by T_2 decay processes and so it is possible to determine T_2 in a single experiment (Figure 2.8).¹

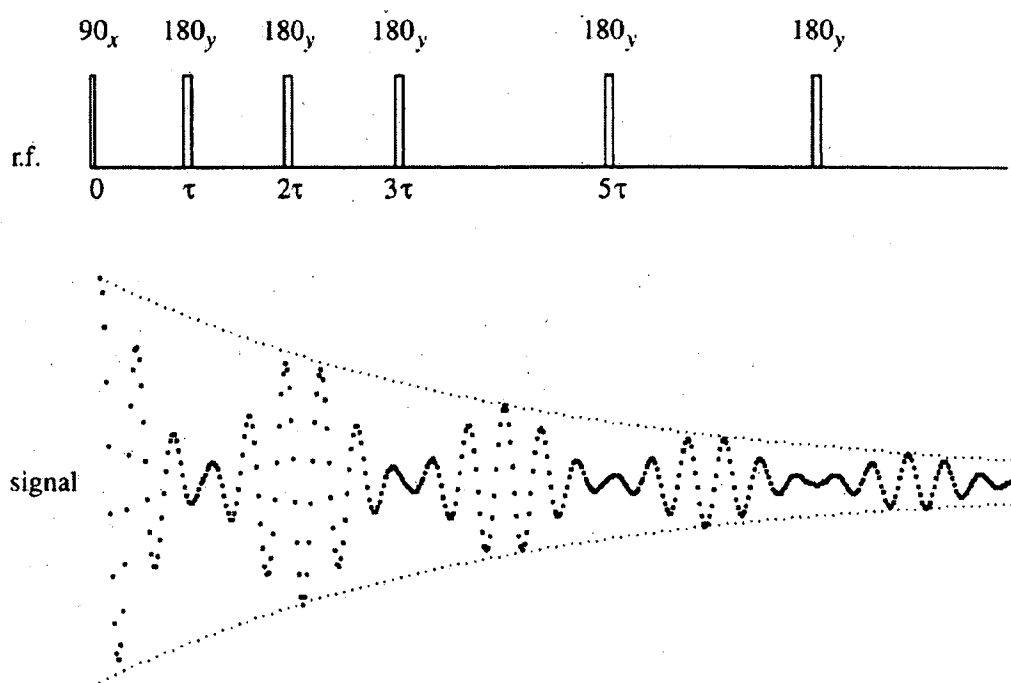


Figure 2.8. CPMG pulse sequence exhibiting multiple spin echoes modulated by a T_2 relaxation envelope.¹

2.2.3. MRI Principles

In conventional NMR spectroscopy, the resultant spectrum of nuclear precession frequencies gives no information about spatial localization of the spins or molecules within the sample since each nuclear species experiences a field independent of its position. At the beginning of the 1970s, Damadian¹⁰ and Lauterbur¹¹ described independently the way to achieve spatially resolved NMR spectroscopy.⁴ Their idea was to superimpose a time dependent linear gradient field $G(r, t)$ onto the spatially uniform static magnetic field B_0 (Equation 2.15). This gradient field has a linear dependence on the position, r , and produces additional constant fields (about 0.001 T) which are much smaller than B_0 (of the order of 8 T).

$$B(r, t) = B_0 + G(r, t) \quad (2.15)$$

As the nuclear resonance frequency is proportional to the magnetic field (Equation 2.16) and the gradient field has a linear dependence upon the position, r , there is then a linear relationship between the resonance frequency, ω , and the spatial position, r (Equation 2.17). This means that the Larmor frequencies of the spins will show similar spatial dependence. The simple relationship between the Larmor frequency and the nuclear spin position, r , is the base of the imaging principles.

$$\omega = \gamma B \quad (2.16)$$

$$\omega(r, t) = \gamma B(r, t) \quad (2.17)$$

The Larmor frequency is affected only by any component of gradient field which is parallel to B_0 since the gradients that are much smaller than B_0 and the components perpendicular to B_0 may be neglected. Hence, the local Larmor frequency is defined as:

$$\omega(r) = \gamma B_0 + \gamma G \cdot r \quad (2.18)$$

where G is defined as the gradient of the pulsed gradient field component parallel to B_0 . In practice the only components having any influence on the resonance frequency in the sample are;⁴

$$g_x = \left(\frac{\partial B_z}{\partial x} \right), g_y = \left(\frac{\partial B_z}{\partial y} \right), g_z = \left(\frac{\partial B_z}{\partial z} \right). \quad (2.19)$$

2.2.3.1. Influence of Magnetic Field Gradient

To describe the influence of the magnetic field gradient on a spin system, the nuclear spins are considered at position r in the sample, occupying a small element of volume (voxel) dV . If the local spin density is $\rho(r)$ the number of spins in this voxel will be $\rho(r)dV$. The NMR signal from this voxel may be written as:

$$dS(G, t) = \rho(r)dV \exp[i(\gamma B_0 + \gamma G \cdot r)t] \quad (2.20)$$

According to Equation 2.20, the decay of the signal due to spin-spin relaxation time, T_2 , is not allowed. In other words, we can say that the dephasing of the transverse magnetization due to the spread in $\gamma G \cdot r$ is very much more rapid than that due to T_2 .

In on-resonance condition, where the reference frequency is γB_0 , the signal finally obtained oscillates at $\gamma G \cdot r$ and so the γB_0 term in Equation 2.20 may be neglected. Under this circumstance, after integrating the Equation 2.20 it may be rewritten as:

$$S(t) = \iiint \rho(r) \exp[i\gamma G \cdot r t] dr \quad (2.21)$$

where the symbol dr is used to represent volume integration. This equation has the form of a Fourier transformation and it becomes more obvious when the definition of the general concept of a reciprocal space vector, k , is introduced:¹²

$$k = (2\pi)^{-1} \gamma G t. \quad (2.22)$$

where the k vector has the dimensions, m^{-1} . As Equation 2.22 shows, k is dependent upon time and gradient magnitude. Therefore, the use of the concept of the Fourier transform and its inverse leads to the following fundamental Equations in MRI:

$$S(k) = \iiint \rho(r) \exp[i2\pi k \cdot r] dr \quad (2.23)$$

$$\rho(r) = \iiint S(k) \exp[-i2\pi k \cdot r] dk \quad (2.24)$$

These equations show that the signal, $S(k)$, and the spin density, $\rho(r)$, are equally conjugate. Since in practice the sampling of k -space takes place as the NMR signal at successive time intervals is sampled $S(k)$ is measured in the time domain, while $\rho(r)$ is measured in the frequency domain. Therefore, $\rho(r)$ is some sort of three-dimensional spectrum of $S(k)$.¹

2.2.3.2. *Selective Excitation*

Selective excitation in MRI is the excitation of spins within a predetermined and well-defined region of the sample. Generally the region of interest will be a plane through the sample, known as a slice. It is usually important to have a well-defined slice since a long tail on the frequency response is not desirable.¹ In general, the bandwidth of frequencies contained in an excitation pulse is inversely proportional to the pulse duration. Also, the bandwidth of the pulse is simply related to the r.f. amplitude. Thus, a selective (soft) 90° pulse will have a very much smaller magnitude and longer duration than a non-selective (hard) 90° pulse.

The selective excitation process involves applying a r.f pulse in conjunction with a magnetic field gradient to excite only those spins which are located in a slice or plane through the sample. This process creates a two-dimensional image which is a projection of

$\rho(r)$ onto the plane in which the slice lies (see also Section 2.2.3.4). It is possible to choose any desired slice within the sample by applying a one-dimensional linear magnetic field gradient during the period that the r.f pulse is applied. By choosing an appropriate direction for the slice selection gradient, the orientation of this plane may be chosen at will. The names axial, coronal and saggittal are used to describe the slice orientation.

For the purpose of this description, the read-out direction is defined as parallel to the field, B_0 , the plane in which transverse magnetization is described in the rotating frame and the slice direction is defined as perpendicular to B_0 , which is called the slice plane. For convenience, the slice plane is described by coordinates (x, y) which means that we shall represent the slice gradient by G_z and the read-out gradient by G_x . The strength of G_x is given by:

$$G_x = \frac{2\pi BW_x}{\gamma FOV} MS \quad (2.25)$$

where BW_x is the read-out gradient bandwidth, FOV is the field of view, a square-shaped area that contains the object of interest to be measured, and MS matrix size. Matrix size defines the number of rows multiplied by the number of columns in a selected slice of sample. A similar equation also holds for the strength of G_z , except that the FOV in Equation 2.25 is replaced by the slice thickness.

2.2.3.3. One-Dimensional Imaging

The simplest imaging experiment involves selectively exciting a thin strip of spins along the z-direction and the projection of the spin density $\rho(r)$ against this axis. The Fourier transform of the acquired signal yields a one-dimensional profile of spin density.

2.2.3.4. Two-Dimensional Imaging

When the equilibrium magnetization in a sample is excited by a selective pulse, the projection of the spin density $\rho(r)$ (image reconstruction) is performed in the two dimensions of the slice plane. The reconstruction involves k -space sampling and performance of Fourier transformation. The k -space sampling requires the application of gradients in the plane of the slice. The reconstructed image is an average of contributions from across the layer. The depth dimension of the volume element is determined by the slice thickness.¹

When in the presence of an imaging gradient, G , the FID is acquired a series of signal points are obtained along a single line in k -space. In two-dimensional imaging this line is orientated along the x -axis (read-out direction) and as was mentioned the associated gradient is called as the 'read-out' gradient, G_x . If a gradient is applied in the y -direction, G_y , for a fixed period before FID sampling begins, it can impart a phase modulation to the signal, depending on the position of the volume element along the y -axis.¹ In practice this is performed by simultaneous application of G_x and G_y and adjusting their relative magnitudes. This allows the reconstruction of spin density according to:

$$\rho(x, y) = \iint S(x, y) \exp[-i2\pi(K_x x + K_y y)] dx dy \quad (2.26)$$

If a series of signals are acquired with G_y incremented over a range of values corresponding to the desired image space, then two-dimensional Fourier transformation of $\rho(x, y)$ will give rise to a two-dimensional image of the spin density.

2.2.3.5. Sensitivity and Resolution

The quality of an MRI image is controlled by the signal-to-noise ratio (SNR). The noise is caused by random thermal motion of electrons in the receiver coil wire or small differences in the measurement electronics, which depend on the size of the r.f. coil and the bandwidth of the pulse sequence. The size of the coil must be just large enough to contain the sample. The SNR also increases with increases in the strength of the magnetic field, slice thickness, voxel volume, the square root of the number of acquisitions, and the square root of the number of scans. The improvement of SNR however limits the resolution of MRI images. Therefore, there is a technical challenge to increase the resolution of MRI images by optimization of the parameters such as slice thickness, field of view (*FOV*), and matrix size. For instance, the spectral resolution increases in proportion with the *FOV*. However, as the *FOV* increases the voxel size decreases which leads to a decrease in SNR. Similarly, the increase in slice thickness increases the SNR while it decreases the spatial resolution of the image. It is however possible to overcome the loss of SNR in high resolution imaging by increasing the repetition time, T_R , and the number of acquisitions. Matrix size also affects the time required for imaging (image acquisition time), SNR and resolution. In high resolution imaging, a large matrix size (128×128 or 256×256) is used which increases the acquisition time.

2.2.3.6. Experimental Methods of MRI

Commonly used pulse sequences in MRI include spin-echo, inversion recovery, gradient echo, diffusion, saturation recovery, echo-planar and spiral pulse sequences. These methods

of MRI imaging are thoroughly described in excellent texts.^{1,4,5} Here, the method used in this study will be introduced very briefly.

(a) Spin Echo Method

Spin echo methods are based on Hahn's spin echo pulse sequence (Section 2.2.2.4(b)). These methods include pulse sequences such as multi-slice, multi-echo, inversion recovery and chemical shift selective imaging, which produce spin echoes using a 90° pulse sequence followed by a 180° refocusing pulse. These methods are very insensitive to inhomogeneities in the static magnetic field and thus provide images with a good SNR. An advantage of using spin echo pulse sequence is that it produces signals which are dependent on spin-spin relaxation time, T_2 . This pulse sequence can also be adjusted to give T_1 -weighted, proton or spin density, and T_2 -weighted images.

Since multi-echo imaging is widely exploited in our study to measure the spatially resolved T_2 , it will be described in more detail in the following paragraphs.

i) Multi-Echo Imaging

Multi-echo imaging is based on the CPMG pulse sequence and produces simultaneously multiple echoes with the same phase encoding (Section 2.2.2.4(c)). In this method, the generated multi-echoes (produced by repeated application of selective 180° r.f. pulses) are detected and stored in separate data sets. Therefore, a series of base images are produced which are different in spin echo time, T_E . The amplitude of the spin echoes and so the intensity of these images decreases exponentially at a rate determined by the spin-spin relaxation time, T_2 , (Equation 2.27).

$$M_{x,y}(T_E) = M_0 \exp\left(-\frac{T_E}{T_2}\right) \quad (2.27)$$

The two variables of interest in the spin echo sequence are the repetition time, T_R , and the spin echo time, T_E . In this method, T_R is selected to be preferably in the order of 3-5 times T_1 in order to provide sufficient time for the magnetization to relax almost completely prior to each fresh repetition of 90° - 180° pulse sequence.

ii) Contrast Determining Parameters

In this work, the contrast of the images obtained from spin echo imaging is determined by the spin density and the spin-spin relaxation time, T_2 , within the sample. The images of T_2 and spin density can be obtained by appropriate choice of the parameters T_E and T_R . These images are important since they can provide information about the local state and physical properties of the sample.

Spin-Spin Relaxation Time, T_2

As was mentioned earlier, the result of multi-echo imaging is a series of base images which are different in spin echo time, T_E . It is possible to construct a ' T_2 image' from the images of a multi-echo sequence. These images contribute to the reconstruction of a T_2 image. Since T_2 contrast varies depending on the spin echo time, T_E , it is possible to obtain heavily or minimally T_2 -weighted images (T_2 image) of a sample by respectively increasing or decreasing T_E . The intensity of the T_2 image is proportional to T_2 and so it provides an insight into the homogeneity of the T_2 in the sample.

Pure T_2 images are obtained by choosing $T_R=5T_1$. The signal intensity is hereby a function of T_E and T_2 :

$$S(T_E, T_2) = \rho e^{-\frac{T_E}{T_2}} \quad (2.28)$$

The spin-spin relaxation time, T_2 , of the species of interest, *i.e.* the proton, is constant in a sample with homogenous structure, while in a sample with heterogeneous structure, the spin-spin relaxation time, T_2 , varies depending on the location of proton in the sample. For protons located in a region where they can freely tumble, high rotational mobility, (*e.g.*, low viscosity or less macromolecules with which to interact) T_2 tends to be longer. However, for protons located in a region where their rotational mobility is significantly restricted, T_2 tends to be shorter. Regions in the sample that have longer T_2 show up brighter in a T_2 image, while the regions that have shorter T_2 appear darker.

Spin Density

The spin density is the number of nuclei of interest in a selected slice of a sample. Spin density images can be obtained with a spin echo pulse sequence by choosing the parameters $T_R \gg T_1$ and $T_E \ll T_2$.⁴ In practice these parameters lead to a long image acquisition time, due to delays of the order of seconds between repetitions of spin echo pulse sequence. It is possible to reduce the acquisition time by choosing a shorter T_R , generally $T_R = T_1$, and $T_1 \gg T_E \ll T_2$. In this case, the signal strength S is only a function of the spin density and is independent of other parameters. From the integral of the spin density image, it is possible to obtain the relative, or by calibration, the absolute nuclei concentration.

The visual image contrast of a spin (proton) density image is determined by the concentration of proton-containing species (for example water) in the sample; the more water in a selected region, the brighter the region will appear in the proton density (*PD*) image, and *vice versa*.

b) Pulsed Gradient Spin Echo (PGSE) Method

In pure liquids such as water, individual molecules are in constant translational motion in every possible direction, due to random motion initiated by thermal energy. This phenomenon is commonly referred to as Brownian motion. It is well-known that the Brownian motion of water molecules under the influence of steady strong magnetic field gradients leads to random fluctuation in the Larmor frequency and hence causes an attenuation of the NMR signal.⁸ The translational motion of molecules is an important issue in MRI, because, on the one hand, it limits the resolution of the images and on the other, the effect of these motions on amplitude of spin echo can provide a contrast mechanism to image the molecular displacements. Hahn⁷ recognized that by applying an additional gradient to the sample, the spin echo pulse sequence could be made sensitive to translational motion of spins and hence be used to measure molecular displacement (self-diffusion). Stejskal and Tanner¹³ extended the method proposed by Hahn in which they applied pulsed gradients instead of steady gradients. This method is called the pulsed gradient spin echo (PGSE) sequence. As is shown in the Figure 2.9, PGSE is a spin echo pulse sequence with a pair of pulsed gradients, g , applied before and after the 180° refocusing pulse. The first gradient pulse induces a phase shift to the system which is a function of position (Equation 2.15). The second identical gradient pulse, which is applied after the 180° pulse, reverses this phase shift.

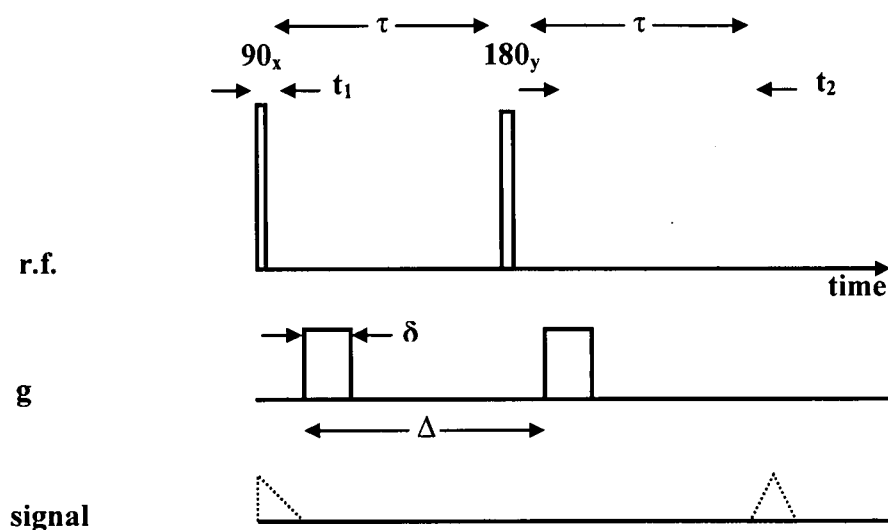


Figure 2.9. Pulsed gradient spin echo (PGSE) sequence with gradient amplitude, g , gradient pulse duration, δ , and gradient pulse spacing, Δ . τ is the time between the 90_x and 180_y r.f. pulses and corresponds to half the spin echo formation time, T_E .

If diffusion occurs between the application of this pair of pulsed-gradients then the phase shift is partly reversed and the spin echo intensity is attenuated. This sequence yields an echo amplitude and phase dependant on the nuclear spin self-correlation function, $P_s(r' - r, \Delta)$. The self-correlation function indicates the conditional probability that a spin initially at r has migrated to r' over the time Δ . The difference $(r' - r)$ is labeled the dynamic displacement.¹⁴ Thus, unlike in multi-echo imaging, in PGSE the phase shifts acquired arises from the spin translational motions, not spin positions, over a well-defined time scale, Δ . In practice, PGSE is limited to imaging the translational displacements between 100 Å and 100 μm over time scale of a few milliseconds to a few seconds.¹

The attenuation of signal, R , due to diffusion is described by the well-known Stejskal-Tanner¹³ equation (Equation 2.29) where $S(g)$ is the spin echo intensity in the presence of

gradient g , $S(0)$ is the spin echo intensity in the absence of gradient, δ is the pulse duration, Δ is the time interval separating the pulse gradients, and D is the diffusion coefficient. The gradient magnitude is labeled g to be distinguished from the capital symbol used to represent the imaging gradients.

$$R = \frac{S(g)}{S(0)} = \exp^{-bD}; \text{ b-factor} = \gamma^2 g^2 \delta^2 (\Delta - \delta/3) \quad (2.29)$$

Equation (2.29) indicates that the attenuation of signal increases in proportion with the increases in b -factor and diffusion constant. That is, the larger the time interval separating the pulse gradients, Δ , the strength of gradient, g , the pulse duration, δ , and the diffusion coefficient, D , the larger is the signal attenuation.

i) Diffusion-Weighted Imaging (DWI)

Diffusion-weighted imaging (DWI) is based on the PGSE sequence. As was mentioned in Section 2.2.3.6(b), the PGSE sequence makes the resultant image sensitive to translational motion (diffusion) processes in the sample. Therefore, the signal intensity of the resultant images of DWI illustrates the diffusion of sample protons. The signal intensity of a DWI image is defined by the following equation:

$$S = S_0 e^{-bD}; \text{ b-factor} = \gamma^2 g^2 \delta^2 (\Delta - \delta/3) \quad (2.30)$$

where S and S_0 are the measured signals in the presence and absence of diffusion gradient field, respectively. The signal intensity of DWI images decays as gradient strength, g , and the diffusion constant, D , of protons in the sample increases. To obtain images with various amount of the diffusion-weighting it is mostly common to vary the strength of the gradient, g .

DWI is potentially very useful since it offers the possibility of probing the microstructure of sample. This is based on the fact that the molecules can have different diffusion coefficients depending on the microstructure of samples they have been absorbed in. The most convenient way to understand the diffusion of molecules is to imagine it as a series of separate jumps along one dimension, the direction of the pulsed field gradients. Unlike in samples with homogenous structure, the diffusion of molecules is restricted by interfaces in samples with heterogeneous structure. Therefore, molecules obtain different diffusion coefficients, D , depending on the magnitude of the restriction. This results in DWI images with varying signal intensity over the sample. That is, regions containing highly mobile molecules appear dark on the resultant DWI images, implying high signal attenuation. While the regions containing molecules with restricted diffusion appear bright in these images. This image contrast can therefore be used to probe the microstructure of the sample.

ii) Contrast and Diffusion Maps

It should be emphasized that the absolute intensity or contrast of DWI images can not be directly considered as an indicator of diffusion coefficient, D , in each pixel of the image because the intensity of these images contains contributions of spin density, T_E , T_R , T_1 and T_2 . That is, the bright regions on a DWI image may reflect a long T_2 instead of (restricted) low diffusion.

In the case of isotropic diffusion in bulk water or any other protic solvents, the degree of signal decay is more important than the absolute intensity of the images. In this case, the

diffusion coefficient at each pixel can be obtained from the slope of the plot of natural logarithm of signal decay against b -factor.¹⁵

In the case of anisotropic diffusion (see Section 2.2.3.6(b(iii))), in samples with heterogeneous structure, the calculation of diffusion coefficients at each pixel is more complicated since diffusion of molecules varies over the sample. In this case, a diffusion map is calculated by combining at least two DWI images which are differently sensitized to diffusion but are still identical with respect to the other parameters, spin density, T_E , T_R , T_1 and T_2 . For instance, by combining two DWI images; one obtained using b -factor=0 (without diffusion-weighting) and other obtained using b -factor>0, diffusion coefficient, D , can be calculated at each pixel according to Equation 2.30. D values obtained with this procedure depend only on the DWI experimental conditions, direction of sensitization gradient and pulse duration time, δ . The calculated D at each pixel can then be mapped to create a diffusion map for sample.

iii) Anisotropic Diffusion

In an isotropic environment molecules are freely diffusing and their measured diffusion coefficient does not depend on the direction of applied gradient. However, in samples with heterogeneous structure the measured diffusion coefficient depends on the direction of the measurements since the diffusion of molecules is interrupted by interfaces and it may be fast along one direction while it is slow along other directions. Therefore, the diffusion coefficient of these materials can not be represented by one diffusion coefficient. This behavior is called anisotropic diffusion.^{15,16} The anisotropic diffusion can be measured in any desired direction by applying the PGSE sequence in three independent gradient

directions (x, y and z) that are orthogonal to each other. Diffusion maps of a sample with heterogeneous structure will present different contrast and diffusion coefficients depending on the orientation of the applied PGSE sequence. This strong contrast due to anisotropy effect carries very interesting information about the object microstructure.¹⁵

For an anisotropic diffusion process, the simple Equation 2.30 is replaced by:

$$S = S_0 e^{-\sum b_{ij} D_{ij}} \quad (2.31)$$

where i and j can be any of the three spatial directions, x, y, z, b_{ij} characterizes the sensitizing gradients along i and j directions and the D_{ij} represents the anisotropic diffusion constant.

2.2.3.7. Applications of MRI

Numerous possible applications of MRI in biological and non-biological research have been reported.⁴ Biomedical applications of MRI include the study of biochemical process at the cellular level and monitoring the development biology of very small animals and insects. Gassner and Lahman¹⁷ have shown how this technique of imaging can be applied to *in vivo* monitoring of locust embryo development and tobacco horn worm. An interesting feature of these studies was the separate imaging of water and lipid distributions in the same object. In pharmaceutical research, MRI is applied to investigate the effect of new treatments for human diseases. These applications concern the radiology of small mammalian animals such as mice and rats. In plants biological research, since 1986, MRI is applied as a powerful tool to investigate the morphology and physiological changes in plant systems. MRI study of plant stems (with cell size of order 50 μm) showed that this method of imaging is able to provide images with high resolution, in which the region of

parenchyma tissue is clearly distinguished from the surrounding vascular tissue and epidermal layer.¹⁸ One of the most interesting applications of MRI to plants concerns the monitoring of structural changes in a developing plant system. It has also been shown that the bulk movement of water in plants can be imaged using MRI, especially when the rate of this movement occurs much slower than the imaging acquisition time.¹⁹ MRI can also be used to examine the distribution of water in wood in order to distinguish earlywood and latewood components.²⁰

In non-biological research, since 1984, MRI is used to image small molecules (in the liquid state) absorbed into a solid object in order to investigate the porosity of object and also following mutual diffusion processes. This type of study is applied to polymer composites²¹ and especially porous materials to obtain useful information about the morphology of these materials and also the diameters of pores. In the petrochemical industry, MRI has been applied to the variety of sandstones to provide information about the relative distribution of oil and water in the multiple fluid phases contained in the pores.²² These studies have shown that water molecules in small pores possess short T_2 of a few tens of milliseconds, which is much shorter than the T_2 of bulk water. MRI study of polymers has revealed that the local mobility of polymer segments (and so T_2 values) depends especially on the chemical structure of the polymer and it varies from one material to another.¹ These studies have also shown that the process of curing and solidification leads to reduction in the relaxation times of the liquid components in the solid object.²³ In a study conducted by Rothwell and co-workers²⁴ MRI was used to observe the penetration of water molecules at high temperature into different epoxy resin composites. Their study showed that the rate of water ingress depends on the thermal shrinkage cracks of the resins. They also monitored

the distribution and mutual diffusion of fluid such as water or other solvents into resins and other similar materials. Since then a variety of investigations were carried out using MRI as a powerful analysis technique to study and map physical and chemical heterogeneity in composite materials,²¹ porosity in minerals,²² mutual diffusion of solvents into solid matrices,²⁵ and the transition from liquid to solid state in ceramics, glues, and epoxies.²⁴ MRI is also a well-established technique for *in situ* studies of surface chemistry and of chemical processes occurring during catalytic reactions.²⁶ Here, however, we concentrate on describing several applications of MRI in the field of polymer research which have been reported in literature.

In general, the applications of MRI in the field of polymer research include measuring and sensing the distribution of solvents such as water in polymers²⁴ and studying the cross-linking of polymers as a function of relaxation time values.²⁷ Rothwell and co-workers²⁸ have used MRI to monitor the mutual diffusion of solvent into solid polymer, with a series of images obtained successively for a 19 mm diameter polystyrene rod immersed in toluene. This study revealed that protons of solid polystyrene had sufficiently short T_2 , resulting in effective reduction of image intensity, and that the proton density maps was obtained from the toluene molecules which have a very much longer T_2 . A similar set of proton density maps has been obtained by Samoilenko et al. for the diffusion of acetone into poly-methylmethacrylate (PMMA).²⁹

The sensitivity of the PGSE sequence to molecular diffusion means that DWI can be useful to measure and monitor the transport (diffusion) processes in biology and material science. In plant physiological studies, the possibility of measuring vascular diffusion at various positions in stems and petioles, during various plant development stages, can provide

unique insight on active transport processes.¹ In the human body the non-invasive measurements of vascular blood flow can be applied to detect and monitor the effect of disease and drug treatments.¹⁵ Also, in the field of materials, DWI plays a key role in porous materials, catalysts and polymers investigations. One of the effects of solvent adsorption in amorphous polymers is to induce a swelling disordering transition. Marechi et al.²⁵ have obtained a series of images following the diffusion of chloroform into a bar of PMMA. In one series of measurements they used normal chloroform and in the other deuterio-chloroform. The latter case is particularly interesting since the deutro-chloroform contributes no proton NMR signal and so the regions of high intensity in the images result from increased segmental mobility in PMMA molecules swollen by solvent. A remarkable example of solvent imaging in a swollen polymer has been provided by Kuhn and Mattingley³⁰ where water molecules were imaged in hygroscopic polymer beads. The images of this polymer were obtained at differing T_E values in a spin echo imaging experiment to investigate the influence of T_2 on the images. MRI has also been used to monitor the temperature-induced volume-phase-transition of a polymer gel that responds to temperature stimuli through one-dimensional proton images.³¹ The resultant images derived from this experiment provided insights on the water content and motional state of the polymer in the fully swollen and collapsed states of the gel. In a similar study, Yung³² has reported the changes of the relaxation times T_1 , T_2 and the diffusion coefficient, D , of the PMMA gel, and D for the N-isopropylacrylamide (NIPA) gel during volume-phase-transition.

In the following Chapters, a novel application of MRI in detecting and monitoring the changes of spin-spin relaxation time, T_2 , and diffusion coefficient, D , of water molecules

absorbed in Nafion and IPMC samples, during application of a small d.c potential, is reported. The results will be derived from a complete set of MRI measurements *in situ*: the samples in their equilibrium state and during application of potential.

2.3. Scanning Electron Microscopy (SEM)

The main content of this section has been adapted from *Electron Microscopy and Analysis* written by Goodhew, Humphreys and Beanland.³³

The Scanning Electron Microscopy (SEM) employs a beam of electrons directed at the specimen to provide images of the external morphology of an object. This technique is primarily used to study the surface or near surface and structure of bulk specimens. The main components of a simple SEM are the electron source, condenser, lenses and vacuum system. The electron source is usually of the tungsten thermionic emission filament, although field emission gun (FEG) sources are increasingly being used for higher resolution.

The electrons are accelerated to an energy which is usually between 1 keV and 30 keV. Two or three condenser lenses then demagnify the electron beam until it may have a diameter of only 2-10 nm. In older SEM instruments, this fine beam of electrons is scanned across the specimen by the scan coils, while a detector counts the number of low energy secondary electrons, or other radiation, given off from each point on the surface. In modern digital SEM, the same effect is achieved by digitally controlling the beam position on the sample and the resultant image is displayed on a computer screen.

In SEM, the electron beam enters the specimen and the same or different electrons leave it again to form the image. When an electron is incident on a thick specimen it will be scattered many times until it effectively comes to rest. The strength of the scattering by an atom depends on its atomic number.

The electron scattering can be elastic or inelastic. Elastic scattering is defined as a process which, although it might change the direction of the primary electron, does not change its energy detectably. Elastic scattering is important since it is a major mechanism by which electrons are deflected and also because elastically scattered electrons are the main contributors to diffraction patterns.

Inelastic scattering is a very general term which refers to any process which causes the primary electron to lose a detectable amount of energy, ΔE . Almost all of the kinetic energy which was carried by the primary electron will end up as heat in the specimen. A small proportion of the energy may escape as x-rays, light or secondary electrons, which are called secondary effects. These effects are detectable in SEM and may prove extremely useful for both imaging and analysis.

2.3.1. Effects useful for Imaging in the SEM

The effects with which we are mainly concerned are secondary and backscattered electron emission and x-ray emission.

2.3.1.1. Secondary Electrons

Secondary electrons (SE) are those electrons which escape from near the surface of a specimen with energies below about 50 eV. The yield of secondary electrons, which is the number of emitted secondary electrons per primary electron, can be as high as, or higher than, 1. Therefore, secondary electrons are the most commonly used imaging signal in scanning electron microscopy which provide us with good surface images.

2.3.1.2. Backscattered Electrons

Backscattered electrons (BSE) are those electrons which escape from the surface of the specimen while they still have a large fraction of their incident energy. Backscattered electrons are not usually as numerous as secondary electrons. These electrons originate near the incident beam and are capable of giving information at high spatial resolution. The intensity of a BSE image is strongly dependent on the atomic number (Z) of the specimen. Backscattered electrons are used for imaging, diffraction and analysis in the SEM.

2.2.3.3. X-Ray Emission

If an electron is knocked out of an inner shell of an atom, at some later time the empty electron shell will be filled and the atom will relax, giving off a large excess of energy as an x-ray. The x-rays provide us with a great deal of information about the composition of the specimen. This was realized in the 1950s and since then it has been increasingly used for qualitative analysis, by measuring the wavelength of each characteristic x-ray emitted by elements present in the sample, and quantitative analysis, by measuring of how many x-rays of any type are emitted per second.

The signal from the specimen is capable of yielding information about the surface topography and composition. The contrast of an SEM image does not depend very much on the composition of the sample, although it may be sensitive to the surface condition and electronic structure of the material. However, the contrast of a BSE image varies monotonically with atomic number Z .

2.3.2. Sample Preparation for SEM

Since the SEM in most cases is used to study the surface morphology, bulk and thick specimens are normally used. For effective viewing of a specimen in the SEM, it is usually necessary for the surface of the specimen to be electrically conducting. The surface conductivity of specimen is important in order to prevent the build up of excess electrons on the specimen surface. If they are not conducted away to earth, the specimen surface will become negatively charged until the incoming primary electrons are repelled and deviated from their normal path, and a distorted image will be formed.

Clearly, there is no difficulty in studying clean metal specimens as they are mounted so as to provide a conducting path to earth. However, non-conducting materials, such as ceramics, polymers and biological materials present a problem. In this case it is usual to coat the specimen with a thin (~10 nm) conducting layer of gold or carbon. This is done easily and rapidly by sputter coating.

2.3.3. Chemical Analysis in SEM

The method of presentation of qualitative analytical information depends on the types of information which is required. These methods include energy-dispersive analysis, line-scanning and x-ray mapping.

2.3.3.1. Energy-Dispersive Analysis

SEMs are often equipped with an energy dispersive spectrometer or EDS detection system which is able to detect and display most of the x-ray spectrum, but with some loss of precision and resolution. The EDS system is controlled by a computer which also stores a library of the energies of the x-ray radiation for all the elements. So, it is a simple matter for the software to identify the element giving rise to a line in the spectrum. Alternatively, it can indicate on the screen the positions on the spectrum at which lines for any chosen element would appear. Thus qualitative analysis is extremely rapid with such a system.

2.3.3.2. Line Scanning

In line scanning the variation of chemical composition within a sample is examined by selecting the x-ray signal from an element of interest, collecting x-rays of this frequency and so displaying the concentration of the element as the beam is scanned across the sample. For ease of recognition, the 'line' of the analysis is shown superimposed on a micrograph of the specimen. An accurate analysis is difficult, as the electron beam spends only a short time on each spot, and the counting statistics are poor.

2.3.3.3. X-Ray Mapping

X-ray mapping is another way of displaying information about the distribution of a single element. This is essentially an extension of the linescan method discussed above, to two dimensional scanning. The x-ray map consists of bright dots, the dot intensity being an indication of the concentration of the element of interest. The quality of such dot maps is often not very good, primarily because the counting statistics are sometimes poor, even for exposures of more than 1000s.

2.4. References

-
- [1]. P. T. Callaghan, "Principles of Nuclear Magnetic Resonance Microscopy", *Clarendon Press. Oxford*, New York, 1991.
 - [2]. Z. P. Liang, P. C. Lauterbur, "Principles of Magnetic Resonance Imaging: A Signal Processing Perspective", *IEEE Press*, 1999.
 - [3]. J. R. Ballinger, "Introduction to MRI", <http://www.mritutor.org/mritutor>, (Last visited 29 April 2007).
 - [4]. W. Kuhn, *Angewandte Chemie, Int. Ed. Engl.*, 1990, 29, 1.
 - [5]. J. P. Hornak, "The Basic of MRI", <http://www.cis.rit.edu/htbooks/mri>, (Last visited 29 April 2007).
 - [6]. N. Blombergen, E. M. Purcell, R. V. Pound, *Phys. Rev.*, 1948, 73, 679.
 - [7]. E. L. Hahn, *Phys. Rev.*, 1950, 80, 580.
 - [8]. H. Y. Carr, E. M. Purcell, *Phys. Rev.*, 1954, 94, 630.
 - [9]. S. Meiboom, D. Gill, *Rev. Sci. Instr.*, 1959, 29, 688.
 - [10]. R. Damadian, *Science* (Washington), 1971, 171, 1151.

-
- [11]. P. C. Lauterbur, *Nature* (London), 1973, 242, 190.
- [12]. P. Mansfield, P. K. Grannel, *Phys. Rev.*, 1975, 12, 3618.
- [13]. E. O. Stejskal, J. E. Tanner, *J. Chem. Phys.*, 1965, 42, 288.
- [14]. P. T. Callaghan, C. D. Eccles, Y. Xia, *J. Phys. E; Sci. Instrum.*, 1988, 21, 820.
- [15]. S. Mori, P. B. Barker, *The Anatomical Record (New ANAT.)*, 1999, 257, 102.
- [16]. P. T. Callaghan, O. Soderman, *J. Phys. Chem.*, 1983, 87, 1737.
- [17]. J. A. B. Lohman, G. Gassner, *Ann. of N. Y. Acad. Sci.*, 1988, 508, 435.
- [18]. A. Connely, J. A. B. Lohman, B. C. Loughman, H. Quiquampoix, R. G. Ratcliffe, *J. Exp. Bot.*, 1987, 38, 1713.
- [19]. T. Tamiya, T. Miyazaki, H. Ishikawa, A. Iriguchi, T. Maki, J. Matsumoto, T. Tsuchiya, *J. Biochem.*, 1988, 104, 5.
- [20]. R. S. Menon, A. L. Mackay, S. Flibotte, J. R. T. Hailey, *J. Magn. Reson.*, 1989, 82, 205.
- [21]. K. P. Hoh, B. Perry, G. Rotter, H. Ishida, J. L. Koenig, *J. Adhesion*, 1989, 27, 245.
- [22]. W. P. Rothwell, H. J. Vinegar, *Applied Optics*, 1985, 24, 3969.
- [23]. A. O. K. Nieminen, J. Liu, J. L. Koenig, *J. Adhesion Sci. Technol.*, 1989, 3, 455.
- [24]. W. P. Rothwell, D. R. Holecek, J. A. Kershaw, *J. Polymer Sci., Polym. Lett. Ed*, 1984, 22, 241.
- [25]. T. H. Marechi, S. Donstrup, A. Rigamonti, *J. Mol. Liquids*, 1988, 38, 185.
- [26]. D. E. Demco, B. Blümich, *Current Opinion in Solid State and Materials Sciences*, 2001, 5, 195.
- [27]. P. O. Frickland, *Int. SAMPE Tech. Conf.*, 1986, 18, 876.
- [28]. W. P. Rothwell, P. P. Gentempo, *Bruker Reports*, 1985, 1, 46.
- [29]. A. A. Samoilenko, D. Yu. Artemov, L. A. Sobeldina, *Bruker Reports*, 1987, 2, 30.
- [30]. W. Kuhn, M. Mattingley, *Special Bruker Report on NMR Microscopy*, 1988.

[31]. S. Ganapathy, P. R. Rajamohannan, M. V. Badiger, A. B. Mandhare, R. A. Mashelkar, *Polymer*, 2000, 41, 4543.

[32]. K. T. Yung, *Magnetic Resonance Imaging*, 2003, 21, 135.

[33]. P. J. Goodhew, J. Humphreys, R. Beanland, "Electron Microscopy and Analysis", *Taylor & Francis*, 2001.

Chapter Three

General Experimental

3.1. Introduction

This Chapter describes manufacturing techniques used to fabricate cast Nafion and IPMC actuators. It also gives specific description of the range of cast and commercial Nafion-based IPMC samples which have been prepared in the thesis for the purpose of investigating their electrochemical and electromechanical behaviour. The chapter will also define the general experimental set-up employed in MRI imaging, SEM and electromechanical measurement of IPMCs.

3.2. Materials

DuPont Nafion with an equivalent weight of 1100 was purchased from Aldrich in two forms: a sheet of Nafion-117 perfluorinated membrane with a thickness of 0.007 inch (0.2 mm) in acid form and 5 wt% liquid Nafion solution, in a mixture of lower aliphatic alcohols and water (45 wt%). The liquid Nafion solution was used in the preparation of thick cast Nafion membrane, described in Section 3.4.

3.3. Commercial Nafion-117 Membrane

Prior to the use of Nafion-117 membrane, it was cleaned through a purification method, which is described in Section 3.5.1.2, to remove all impurities introduced into the polymer during the manufacturing process. The cleaned Nafion membrane was then stored in

deionised (DI) water to be kept hydrated for future applications. In the thesis, samples prepared from Nafion-117 membrane are referred to as “commercial Nafion”.

3.4. Preparation of Thick Nafion Membrane

Preparation of a thicker Nafion membrane was essential for use in the MRI imaging of diffusion of hydrated ions across the thickness of a working IPMC actuator since the small thickness of commercial Nafion made it unsuitable for this study. It was also required for investigating the effect of Nafion thickness on the electromechanical behaviour of the IPMCs.

Preparation of thick Nafion membrane was achieved by casting liquid Nafion solution.¹ The process of casting Nafion membrane consists of three stages; molding the prepared cast solution, drying of solvents, and finally thermal treatment. In the first step, to increase the percentage of Nafion in the liquid Nafion solution, a portion of water and alcohols was removed. This was performed by carefully heating 120 ml of Nafion solution in a water bath and reducing the volume to one half, 60 ml. In order to prevent the formation of cracks on the surface of the cast Nafion membrane during the drying stage, 15 ml of 98 wt% dimethylformamide, DMF, (Aldrich) was added to the modified Nafion solution, in an amount of 20% by weight of the polymer.² DMF was applied as an additive to make the mixture of water and alcohol act as an azeotrope.¹ The prepared mixture was carefully poured into a Teflon mold of size 5 cm×5 cm×5 cm and the formation of bubbles was avoided. The mixture in the mold was left at room temperature for five days to dry. It was

then placed in a furnace at 70°C for 24 h to promote crystallinity in the cast membrane. Finally to improve the physical, chemical and mechanical stability of the cast membrane the temperature was gradually increased to 150°C (above the glass transition temperature), left at this temperature for 2 h and allowed to cool down slowly. This annealing process was performed in order to increase the ionic charge density of the cast membrane by decreasing the unoccupied spaces in hydrophobic regions of the polymer.³ This has been reported to also expand the size of ion clusters in the hydrophilic regions.⁴ The product of the above process was a 5 cm×5 cm sheet of Nafion membrane with yellowish colour and translucent appearance and dry thickness of 1.65 mm. The yellowish colour of prepared Nafion was removed during the cleaning process which is described in Section 3.5.1.2. This membrane was stored in DI water to be kept hydrated for future applications. Samples prepared from this thick membrane are referred to as “cast Nafion” in the thesis.

3.5. IPMC Manufacturing Technique

Fabrication of cast and commercial Nafion-based IPMC samples was performed using a manufacturing technique presented by Pak and colleagues.⁵ This technique involves three exclusive stages: pre-treatment, compositing process and surface electroding.

3.5.1. Pre-treatment

3.5.1.1. Surface Roughening

As was explained in Chapter One, a typical IPMC consists of a Nafion membrane with metal electrodes, chemically plated on both faces. In order to enhance the interfacial area between these electrodes and the polymer, the Nafion membrane (in acid form) was roughened at both surfaces using a fine silicon carbide abrasive paper.

3.5.1.2. Cleaning Procedure

The roughened membrane was then decontaminated through the following cleaning method suggested by MacMillan and colleagues.⁶

- a) The membrane was boiled in 2 M HNO₃ (Fisher scientific) solution at a temperature of 80°C for 2 h to exchange all cations on the sulfonate groups, for protons.
- b) Since the presence of paramagnetic impurities in the membrane could affect the NMR results and the quality of MRI images, they were removed by immersing the membrane in a 0.01 M solution of oxalic acid (M&B Ltd.) at room temperature for 24 h.
- c) Finally, to remove organic impurities and small polymer fragments, the sample was immersed in a mixture of 50% ethanol-50% DI water in an ultrasonic bath for 2 h. This step eliminated the cloudy and yellowish appearance of the membrane.

It should be noted that the membrane was repeatedly boiled in fresh DI water for 1 h to remove any residual HNO₃, oxalic acid and ethanol following each of steps (a), (b) and (c).

3.5.2. Compositing Process (Electroless Platinum Electroding)

The compositing process is the most important stage in the manufacture of the IPMCs. The purpose of this process is to metallize the sub-surface regions of the Nafion membrane via a chemical absorption/reduction process.⁷ The metallization of the surfaces is necessary to be able to use the Nafion membrane as an IPMC actuator. The metallized surfaces are called the electrodes. The process of compositing consists of two stages: ion exchange and plating. These two stages may be repeated several times to achieve extra layers of deposited metal on the surfaces of the membrane to improve the conductivity of the IPMC.

IPMC samples discussed in this work were chemically metallized using platinum precursors since these are known to be able to penetrate the Nafion surface and give rise to a porous-structured electrode.⁸

3.5.2.1. Ion Exchange (Absorption)

The prepared Nafion membrane was soaked in an appropriate solution of tetraamineplatinum (II) chloride, $[\text{Pt}(\text{NH}_3)_4]\text{Cl}_2$ (Alfa Aesar), for 24 h and a small amount of ammonium hydroxide solution (Aldrich) was added to neutralize the solution. This allowed platinum complex cations, $[\text{Pt}(\text{NH}_3)_4]^{2+}$, to diffuse through the Nafion membrane via the ion exchange process and populate all ion exchange sites (the $-\text{SO}_3^-$ groups). The required amount of $[\text{Pt}(\text{NH}_3)_4]\text{Cl}_2$ was calculated to correspond to the number of ion exchange sites available in the dry mass of the Nafion membrane. For example, it was estimated that a Nafion membrane with dry weight of 0.575 g and EW of 1100 contained 5.23×10^{-4} mole ionic sites. Since one mole of $[\text{Pt}(\text{NH}_3)_4]^{2+}$ cation reacts with two moles of ion exchange sites, $-\text{SO}_3^-$, according to the stoichiometric calculation, the required amount

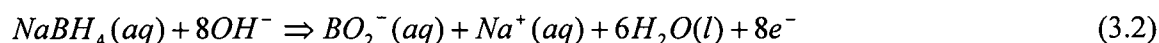
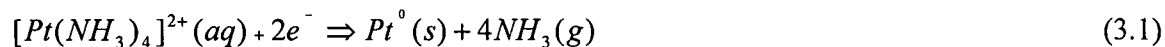
of $[\text{Pt}(\text{NH}_3)_4]\text{Cl}_2$ (MW = 352.1 g/mol) is 92 mg. This amount of platinum salt was dissolved in the minimum volume of water to obtain a solution with relatively high molarity and to maximize the speed of diffusion of $[\text{Pt}(\text{NH}_3)_4]^{2+}$ into the membrane, 58 ml in this example.

3.5.2.2. *Plating (Reduction)*

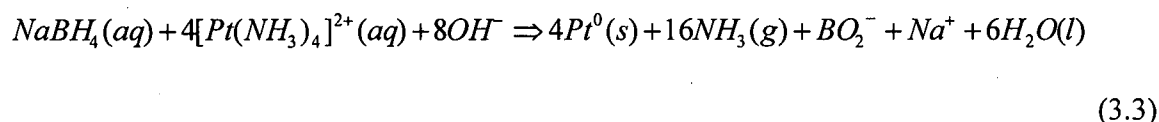
In this stage, $[\text{Pt}(\text{NH}_3)_4]^{2+}$ cations absorbed in the Nafion membrane were reduced to the metallic state using a solution of sodium borohydride, NaBH_4 , (Aldrich). The sodium borohydride reacts with the $[\text{Pt}(\text{NH}_3)_4]^{2+}$ at the surface of the Nafion membrane to form fine Pt particles. When the membrane is contacted with this solution the $[\text{Pt}(\text{NH}_3)_4]^{2+}$ cations diffuse out of the membrane and are reduced at the surface. This reduction process creates a layer of nano-size platinum particles at the surfaces of the membrane to a depth of 10 to 20 μm .⁹ The layer of platinum particles acts as an electrode at the surface of the Nafion membrane.

The $[\text{Pt}(\text{NH}_3)_4]^{2+}$ -exchanged Nafion membrane was rinsed with DI water to remove the excess platinum salt solution from the surfaces. The membrane was placed in a 250 ml crystallization dish containing a small amount of DI water under stirring. An aqueous solution (>100 ml) of 5 wt% NaBH_4 was added gradually to the membrane, 5 ml of NaBH_4 solution every 30 min, ten times. The remainder of the NaBH_4 solution was added after a further 30 min and stirred for 4 hrs. At the end of this process, a black layer of platinum particles was formed at the surfaces of the Nafion membrane. The membrane was rinsed with DI water and immersed in 0.1 M HCl (Aldrich) solution for 30 min to neutralize the residual ammonium. Finally, the membrane was rinsed with and stored in DI water.

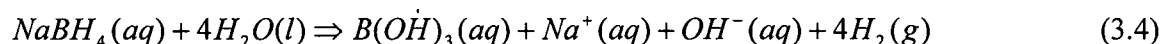
The reduction process is assumed to take place according to the following chemical reactions:¹⁰



From Equation (3.1) and (3.2):



Equation (3.4) is thought to be the source of hydroxyl ions for above equations.¹⁰



3.5.3. Surface Electroding

The deposition of platinum as small particles on the surface of the membranes, where the particles stay in a dense form, introduces a significant level of surface-electrode resistance.⁸

In order to improve the surface conductivity and consequently the actuation performance of the prepared IPMC sample, a thin layer of gold was deposited over the platinum-plated surfaces by physical vapour deposition (PVD). In the PVD process the sample was subjected to plasma bombardment of gold and was coated entirely and uniformly with a 10 nm thick gold over layer.

3.6. IPMC Samples

One of the objectives of the thesis is to study how the thickness of the applied Nafion membrane and also the thickness of the electrodes on the surfaces can influence the actuation performance and electromechanical behaviour of IPMCs. Accordingly, six commercial and five cast Nafion-based IPMC samples with the same dimension of 8 mm width and 38 mm length were fabricated using the manufacturing technique described in Section 3.5. As was mentioned earlier, the compositing process can be repeated several times to achieve thicker platinum electrodes. Therefore, the thickness of platinum electrodes in six commercial Nafion-based IPMC samples were varied by varying the number of repeats of the electroless platinum electroding process from 1 to 4 plating cycles. Certain samples were treated by PVD to deposit a thin layer of gold in order to study the effect of surface conductivity on their performance. Five cast Nafion-based IPMC samples were also prepared by performing from 1 to 4 plating cycles and some of these were also further coated with a gold layer. All the prepared samples were given a name according to the type of Nafion membrane and the number of plating cycles. Table 3.1 gives the names and the detailed process information for all samples. After preparation, to exchange all protons on $-\text{SO}_3^-$ groups for Li^+ cations, samples were soaked and stored in a saturated solution of LiOH at room temperature for four weeks, before application in electromechanical tests.

In addition to these samples, several square cast Nafion-based IPMC samples of size 8×8 mm were prepared for use in MRI experiments. These samples were named AuPt_1Cast since only one plating cycle was performed on each cast Nafion sample and a layer of gold was deposited on the plated surfaces of each.

Table 3.1. Naming system of IPMC test samples.

Sample Name	Cast Nafion	Commercial Nafion	Number of plating cycles	Surface electroding	Cation type
Pt ₁ Com	-	✓	1	-	Li ⁺
Pt ₂ Com	-	✓	2	-	Li ⁺
Pt ₃ Com	-	✓	3	-	Li ⁺
Pt ₄ Com	-	✓	4	-	Li ⁺
AuPt ₂ Com	-	✓	2	✓	Li ⁺
AuPt ₄ Com	-	✓	4	✓	Li ⁺
Pt ₁ Cast	✓	-	1	-	Li ⁺
Pt ₂ Cast	✓	-	2	-	Li ⁺
Pt ₄ Cast	✓	-	4	-	Li ⁺
AuPt ₂ Cast	✓	-	2	✓	Li ⁺
AuPt ₄ Cast	✓	-	4	✓	Li ⁺

3.7. Experimental Set-up

General descriptions of the instruments and experimental set-up used to perform SEM, MRI and electromechanical measurements on the Nafion membranes and the prepared IPMC samples are given in this section.

3.7.1. Scanning Electron Microscopy (SEM)

3.7.1.1. Instrumentation

SEM study of the IPMC samples was performed on a Philips XL30 ESEM which had a high signal-to-noise ratio and maximum resolution of 2 nm, at 30 KeV accelerating voltage.

This instrument was equipped with an EDX (x-ray microanalysis) system with a sufficient sensitivity to detect elements with low atomic numbers.

3.7.1.2. Sample Preparation

In order to study cross sections of IPMC samples, these soft and flexible samples must be embedded in a resin block composed of a liquid resin and a hardener. This mixture adhered very well to the samples and required to be left overnight for hardening. A small piece of IPMC sample was cut and placed in a stainless steel clip so that the cross section could be seen. The clip holding the sample was put in a round Teflon mold. A mixture of an epoxy resin and a hardener (Kemet) in a 7:1 ratio was prepared and poured over the sample. The mixture containing the sample was left overnight and a hard pellet was produced. The pellet was removed from the mold, ground and polished. The grinding and polishing of the pellet was necessary to minimize topographic contrast and to obtain SEM images which give more information about the depth of the penetration of platinum particles through the IPMC samples. The pellet was ground using silicon carbide papers ranging from 60-grit to 1200-grit on an automated 12-inch grinder unit (Leco). Polishing was carried out using Kemet polishing cloth (14 micron and finer) and diamond paste on the same unit.

Finally, to increase the surface conductivity of the sample, to reduce charging of the sample, and improve accordingly, the resolution and quality of the SEM images, the pellet containing the sample was coated with a thin layer of carbon (~10 nm) using an automated carbon sputter coater. This was followed by application of carbon paste to the sides of the pellet to further aid charge conduction.

3.7.2. MRI

3.7.2.1. Instrumentation

MRI data was acquired on a Bruker AVANCE FT NMR spectrometer with a 38 cm bore and 7.1 Tesla superconducting magnet resonating at 300.15 MHz for ^1H . This spectrometer possesses a gradient system, which produces linear magnetic field gradients in three orthogonal directions, and a 25 mm diameter birdcage radio frequency (r.f.) resonator probe, which is an antenna for the application and reception of the r.f. field pulses to the sample. The computing system for acquisition and reconstruction of images is operated by Bruker Paravision[®] software which provides the pulse sequences required to encode the spatial information about the protons in the samples.

3.7.2.2. Experimental Set-up

The same general experimental set-up was used to perform all of the MRI experiments. Once the sample was placed in the r.f. resonator probe, shown in Figure 3.1, and mounted in the magnet, the proton signal from the sample was initially detected by application of the Paravision[®] One-Pulse sequence. This was performed to calibrate the r.f. of the probe to the Larmor frequency of the protons within the sample. Then, a cross section image of each plane of the 3D sample was obtained using the Paravision[®] Tri-Pilot sequence. These initial images were used to adjust the angle and geometry of the slice or slices of interest through the sample. Finally, the best possible combination of effective imaging parameters such as matrix size, field of view, FOV , echo time, T_E , and repetition time, T_R , were selected to obtain MRI images with high resolution and signal-to-noise ratio, SNR.

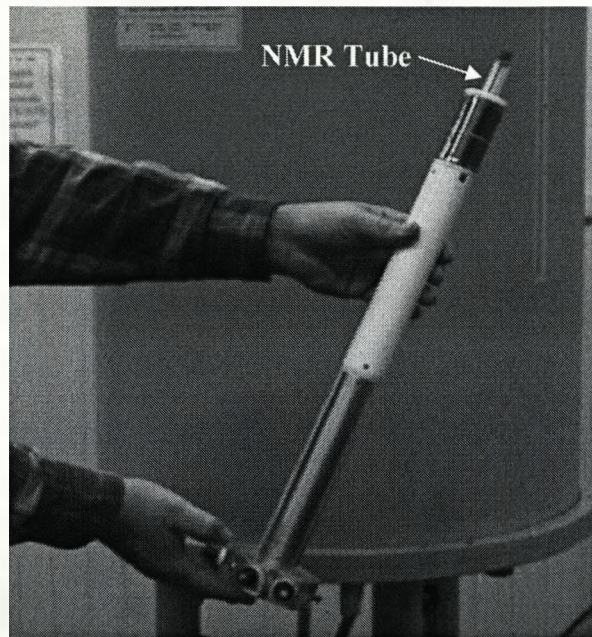


Figure 3.1. Resonator probe of the Bruker AVANCE 300 FT NMR scanner

3.7.2.3. Construction of T_2 and PD Images

T_2 images were constructed on the MRI scanner using the Paravision[®] software. To construct a T_2 image the spin-spin relaxation time, T_2 , for each individual voxel of an MRI image must be calculated. This was performed by fitting the signal intensity versus the echo time, T_E , for each voxel. For example, when a train of 64 echoes with T_E of 5 ms was applied, 64 images were acquired which showed a signal intensity corresponding to a T_E of $n \times 5$ ms, n being the echo number. The intensity of the voxels in these images decreased exponentially according to Equation 2.28. The signal intensity for all individual voxels in all of these 64 images was acquired and plotted versus T_E . By calculating the least square fit to these data points, the T_2 value for each voxel was calculated. The calculated T_2 values

were then mapped in certain coordinates to form the T_2 image. For all the MRI experiments the T_2 images were constructed on MRI instrument using the fitting process described above. This fitting process also resulted in the construction of the proton density, PD , images. The three-dimensional numerical plots of the intensity of T_2 and PD values were prepared using Microsoft Excel[®]. These three-dimensional plots are referred to as T_2 and PD maps, respectively, in this thesis.

3.7.2.4. Construction of Diffusion Maps

The diffusion maps were prepared using the batch computing software, Force[®]. The diffusion maps were constructed by combining diffusion-weighted images that were different in the magnitude of applied pulse gradient, g , but were identical with respect to the other parameters such as T_E , T_2 and PD . For instance, the result of a diffusion-weighted imaging (DWI) experiment with gradient pulse range of 0.1, 0.2, 0.3, ..., to 0.9 (T/mm²) is 9 images which each have a signal intensity corresponding to the applied gradient pulse, g . The signal intensity of the voxels in these images decreases exponentially according to Equation 2.29. A computer program was designed in Force[®] to acquire the signal intensity for individual voxels in all of these images and calculate the diffusion coefficient, D , in certain coordinates for each voxel.[§] The calculated diffusion coefficients at each voxel were then mapped to create a D -map. The three-dimensional numerical plot of the intensity of D values was also prepared using Microsoft Excel[®].

[§] This program was designed in the University of Bath by Dr Sean Rigby.

3.7.3. Displacement Measurements

3.7.3.1. Instrumentation

Figure 3.2 illustrates the experimental set-up used for displacement measurement of IPMC samples. This consists of a function generator (supplying voltage range of 0-10 V over a frequency range of 0-1000 Hz), an amplifier (output of 2-60 V), an oscilloscope (100 MHz), a sample holder and a Sony digital camera. These components were arranged to allow the capture of 2D images of the deformation of bending IPMC samples in side views, as they were subjected to sinusoidal voltages at different frequencies.

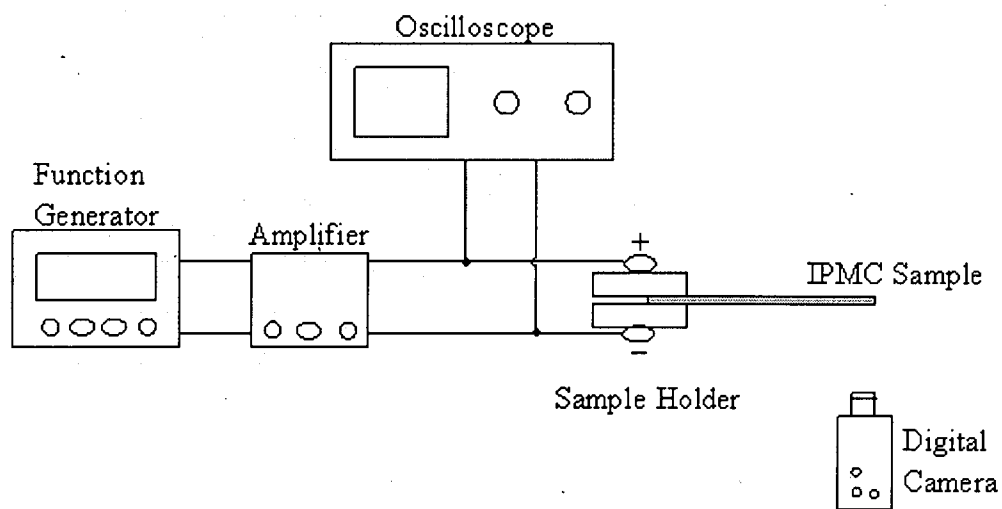


Figure 3.2. Experimental set-up for displacement measurement of IPMC samples.

3.7.3.2. Experimental Set-up

In order to measure the tip displacement of fabricated IPMC samples of standard length of 38 mm and width of 8 mm, one end of an IPMC strip sample was placed horizontally in a sample holder consisting of a pair of platinum contacts within an insulating clamp. These contacts had the same surface area as the IPMC sample in order to avoid a short circuit of the system. A photographic view of this sample holder can be seen in Figure 3.5. The platinum contacts in turn were connected to the two terminals of the function generator using thin platinum wires. 2D images of the swinging bending deformation of the free end of the sample were captured by the digital camera as the electrical signal was applied across the thickness of the sample. The images were transferred to a computer and the average tip displacement (Figure 3.3) of the free end of the IPMC sample was measured employing Scion[®] image analysis software.

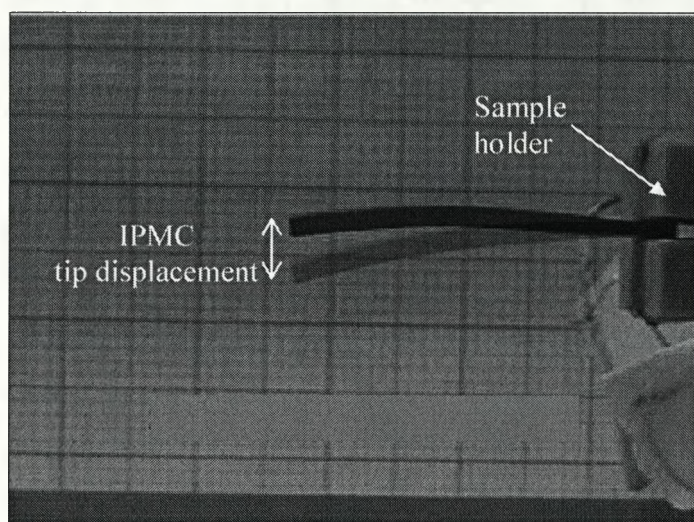


Figure 3.3. Photographic view of tip displacement of an IPMC sample.

3.7.4. Force Measurements

3.7.4.1. Instrumentation

The generated force of IPMC samples were measured using a load cell. Figure 3.4 shows a schematic diagram (a) of the experimental set-up and (b) a photographic view of the system used to measure the generative force at the tip of the bending IPMC samples. This system consists of the same components described in the displacement measurement set-up. In addition, it contained a precision 0-100 mN load cell sensor (National instrument, NI-GS0), an amplifier/signal conditioner (NI-TM-2), a resistor, R, (0.02 Ω), a NI-PXI-1031 data acquisition board and a computer. The TM-2 amplifier/conditioner provided the regulated excitation voltage, balance, and gain control necessary to couple the load cell to the system. These instruments were set in an arrangement to measure and digitize the generated force at the tip of the bending IPMC samples when they were subjected to an electrical signal. The system was also able to record simultaneously the applied voltage, the current and the generated force and store these on the computer disk drive.

3.7.4.2. Experimental Set-up

In order to measure the generative force, one end of the IPMC strip sample was clamped horizontally in the sample holder, described in Section 3.7.3.2 and connected to the two terminals of the function generator. The free end of the sample was placed on the load cell, shown in Figure 3.5, and the force generated by the sample was measured as an electrical signal was applied across the thickness of the sample by the function generator. The analogue signal from the load cell, resistor and the function generator were then digitized through the data acquisition board and transferred to the computer by using

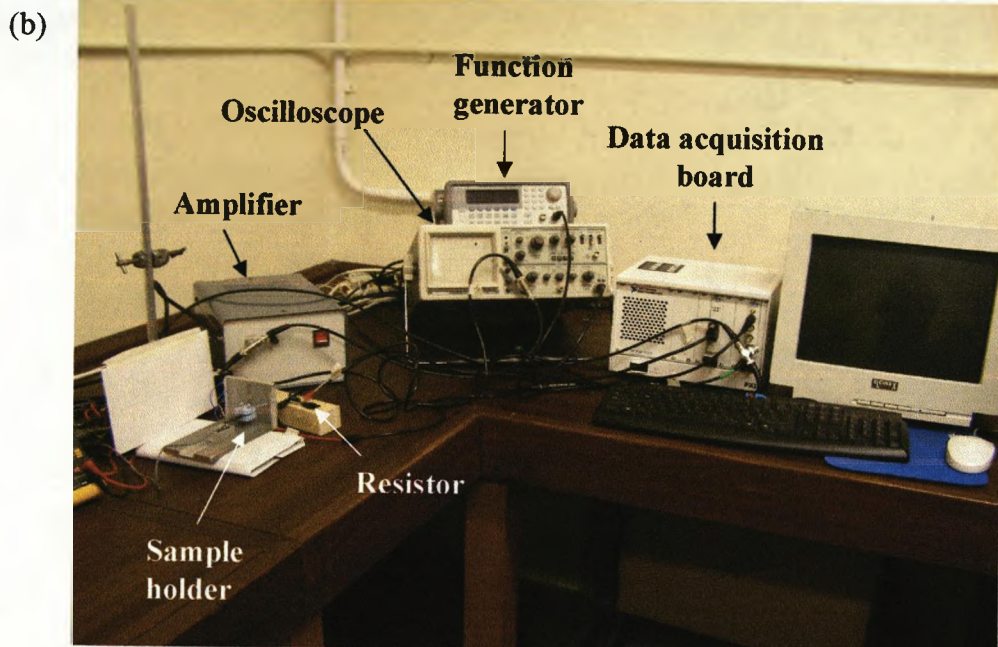
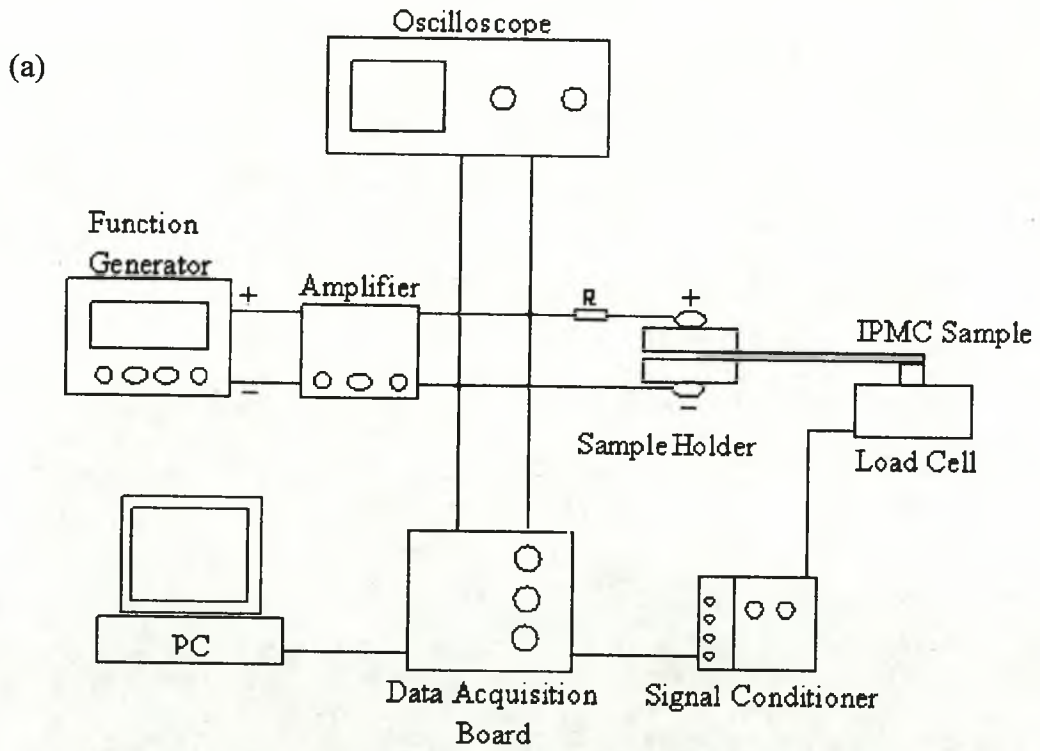


Figure 3.4. (a) Schematic diagram and (b) photographic view of experimental set-up for force measurements on IPMC samples.

LabView[®] 7.0 software. The applied voltage, current and force as a function of time were extracted from these data.

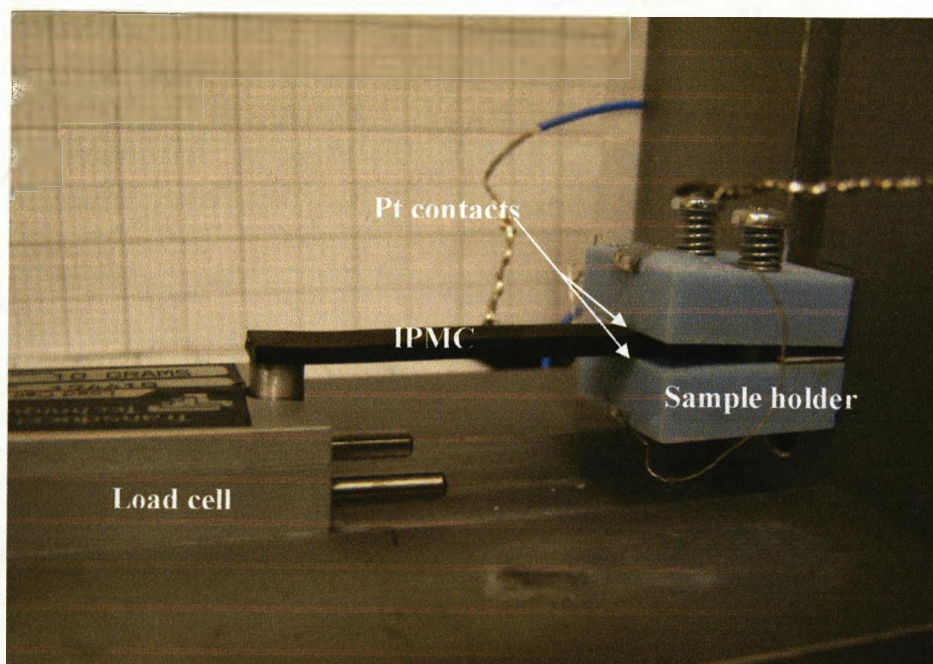


Figure 3.5. Sample holder (right) and load cell (left) used in electromechanical measurements of IPMC samples.

3.8. Summary

A specific guideline for the fabrication of the cast Nafion membrane with dry thickness of 1.65 mm and also preparation of IPMC samples with different thickness of platinum electrodes was introduced. The method of fabrication of the IPMC samples was described

through the three stages of pre-treatment, compositing and surface electroding. IPMC samples based on the commercial and cast Nafion membranes were prepared. By increasing the number of repeats of the platinum electroding process the thickness of the platinum layer in these samples was varied. All the prepared samples were given a name according to the type of the Nafion membrane and the number of plating cycles. The characterization techniques employed to investigate the surface structure and composition of the IPMC samples and their electrochemical and electromechanical behaviour were introduced. This was followed by a description of the general experimental set-up used in these techniques.

3.9. References

-
- [1]. K. J. Kim, M. Shahinpoor, *Polymer*, 2002, 43, 797.
- [2]. R. F. Kovar, N. Landrau, R. M. Formato, L. S. Rubin, P. Osenar, *US Patent*, 2001, 6248469.
- [3]. T. J. Thomas, K. E. Ponnusamy, N. M. Chang, K. Galmore, S. D. Minteer, *J. Mem. Science*, 2003, 213, 55.
- [4]. K. Asaka, N. Fujiwara, K. Oguro, K. Onishi, S. Sewa, *Smart Structure & Materials, Proc. SPIE*, 2002, 4695, 191.
- [5]. (a) J. J. Pak, S. E. Cha, H. J. Ahn, , S. K. Lee, *Proc. of the 32nd Intl. Symp. on Robotics (ISR)*, April 2001. (b) S. E. Cha, J. J. Park, S. K. Lee, "*Trans. of KIEE*, 2002, 51(9), 455.
- [6]. B. MacMillan, A. R. Sharp, R. L. Armstrong, *Polymer*, 1999, 40, 2471.
- [7]. P. Millet, M. Pineri, R. Durand, *J. Appl. Electrochem.*, 1989, 19, 162.
- [8]. M. Shahinpoor, K. J. Kim, *Smart Material Structure*, 2000, 9, 543.
- [9]. J. W. Paquette, K. J. Kim, D. Kim, W. Yim, *Smart Structure & Materials, Proc. SPIE*, 2004, 5385, 199.

[10]. M. Shahinpoor, Y. Bar-Cohen, J. O. Simpson, J. Smith, J. Smart Materials, 1998, <http://www.unm.edu/~amri/paper.html>, (Last visited 29 April 2007)

Chapter Four

Preliminary Results

4.1. Introduction

This chapter describes several preliminary experiments undertaken to compare the chemical structure and physical properties of the commercial and cast Nafion membrane using NMR spectroscopy and MRI imaging. It also discusses SEM analysis of the surface structure, composition and morphology of the fabricated IPMC samples, introduced in Chapter Three.

4.2. NMR Spectroscopy

Before investigating the distribution of absorbed water molecules in the commercial and cast Nafion membranes using Magnetic Resonance Imaging (MRI), ^1H NMR measurements were carried out to make sure that these membranes had the same chemical composition and that no proton-containing contaminant had been introduced into the cast membrane during the preparation process.

4.2.1. Experimental

Small pieces of clean commercial and cast Nafion membranes in acid form were swollen with deionized (DI) water for ^1H NMR measurements. The excess of the solvents was wiped from the water-swollen samples, they were placed in 5 mm o.d. NMR tubes and D_2O was added as a reference. The measurements were performed on a 300 MHz liquid state NMR scanner (Bruker Avance).

4.2.2. Results and Discussion

Very similar ^1H NMR spectra were acquired from cast and commercial Nafion membranes. These revealed that both membranes have a similar chemical composition and that the cast Nafion membrane contains no significant quantity of proton-containing contaminants. The ^1H NMR spectrum of the membranes presented an intense resonance at a chemical shift of 4.7 ppm with two small resonance lines located symmetrically at both sides (see Appendix 1). The large resonance at 4.7 ppm can be attributed to a large amount of water molecules absorbed in the hydrophilic regions (clusters) of the membranes. The small line width of this signal in both presented spectra also reveals that the water molecules absorbed in the Nafion membrane experience a homogeneous chemical environment and that the chemical exchange among them is fast.¹ The mentioned peak appeared narrower in the spectra of the cast sample which suggests that this sample allows more molecular mobility, probably due to its having a less dense physical structure. The broader NMR line widths seen for the commercial Nafion represent stronger dipole-dipole interactions* between the nuclei in this polymer, than in the cast Nafion. Since the solid state interactions are affected by the degree of ordering and motion present in the solid this implies that the molecular structure of the commercial Nafion membrane contains more ordered and crystalline regions.^{2,3}

The two small resonance lines observed at both sides of the large signal are almost certainly sidebands, due to dipolar-dipolar interactions.

* In contrast to the high-resolution spectra observed for solutions and liquids, NMR spectra of solid materials show very broad and featureless absorptions. This indicates clearly that there are interactions present in the solids which are orders of magnitude larger than those in solutions. A solution NMR spectrum shows spin-spin couplings and chemical shifts while in solid state the interactions which give rise to the broad absorption for abundant nuclei are the dipole-dipole interactions between the nuclei. In the solid state the chemical shifts and spin-spin coupling interactions are much smaller than those in solutions.²

4.3. Magnetic Resonance Imaging (MRI)

4.3.1. Comparative MRI of Cast and Commercial Nafion Membranes

Simultaneous MRI images of hydrated Li^+ -exchanged cast and commercial Nafion membranes, held in the same NMR tube, were obtained using a spin echo pulse sequence. This was performed first, to examine the possibility of imaging of these types of materials and second, to reveal any possible differences between their physical structures. To attain the latter goal, T_2 images of the absorbed water molecules in the two membranes were obtained.

4.3.1.1. Experimental

8×8 mm square samples of Li^+ -exchanged cast and commercial Nafion membranes (pre-soaked in a saturated solution of LiOH) were prepared and sandwiched between two similar sized pre-cleaned glass plates of the same size as the samples. A glass plate was also placed between the two samples to avoid physical contact. This assembly was put horizontally into a 25 mm o.d. NMR tube. A constant saturated water vapour pressure was maintained inside the tube by enclosing a water-soaked paper plug within it and using a gas-tight cap to avoid the dehydration of the samples during the experiment. The images were accumulated using the standard multi-echo pulse sequence, MSME, from the Bruker Paravision library. This involved a 90° pulse followed by n 180° acquisition cycles, $n=64$, with a minimum echo time, T_E , of 5 ms and repetition time, T_R , of 5 s. Twelve numbers of scans (averages) were used along with these 64 echoes. The MRI, T_2 and PD images were generated with a matrix

size of 128×128 pixels. The slice thickness was 1 mm while the field of view, *FOV*, was $15 \text{ mm} \times 15 \text{ mm}$. This resulted in a spatial resolution of $117 \mu\text{m}/\text{pixel}$.

4.3.1.2. Results and Discussion

Figure 4.1(a) shows the spin echo image obtained from a cross-sectional slice through both hydrated Li^+ -exchanged cast and commercial Nafion samples.

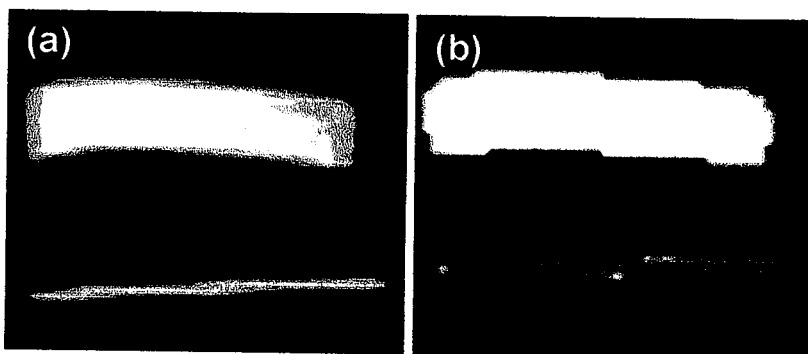


Figure 4.1. (a) Spin echo image of the Li^+ -exchanged cast (top) and commercial (bottom) Nafion samples. (b) corresponding T_2 image.

This image exhibits a fairly uniform distribution of intensity over each of these samples, which can be related to the proton density in these samples. A higher proton density is observed in the cast membrane (top) compared to that of the commercial membrane (bottom). Figure 4.1(b) exhibits the corresponding T_2 image. As can be seen, the cast sample appears much brighter than the commercial sample. This indicates that the water

molecules absorbed in the cast Nafion possess much higher spin-spin relaxation time, T_2 , than in the commercial Nafion.

The membranes were also imaged separately using the same imaging parameters and pulse sequence in order to achieve individual T_2 and PD images for each sample. Figure 4.2 shows the three-dimensional numerical plots of intensity of T_2 values over both samples. These plots display a relatively even distribution of T_2 values over the cast (4.2 (a)) and the commercial (4.2 (b)) Nafion samples which implies that both samples have a homogeneous physical structure. However, the protons of water molecules absorbed in the cast membrane show much higher (~ 250 ms) spin-spin relaxation time, T_2 , than those in the commercial membrane (~ 40 ms). Since the magnitude of T_2 for protons is largely dependent on the motion of water molecules, this dissimilarity in the T_2 values indicates that the mobility of the water molecules absorbed in the commercial membrane is by far the lesser. It should be noted that the degree of crystallinity of a polymeric membrane depends on its preparation method.⁴ Unlike the thick cast membrane, the thin commercial membrane is cast under vacuum conditions, high temperature and is passed through a rolling procedure⁵ which has been reported to cause an increase in the degree of crystallinity in the membrane.^{4,6} Thus, in the commercial membrane the molecular backbones (main chains) and also the side chains may be relatively immobile and so their reorientation would be less easy. This in turn may decrease the size of the hydrophilic regions formed within this membrane, once it is contacted with a polar solvent. The smaller hydrophilic regions may act to limit the rotational freedom of the water molecules absorbed in these regions and since the magnitude of T_2 is highly motion dependent a significantly shorter T_2 value would be seen for the water molecules absorbed in this membrane. On the other hand, according to the

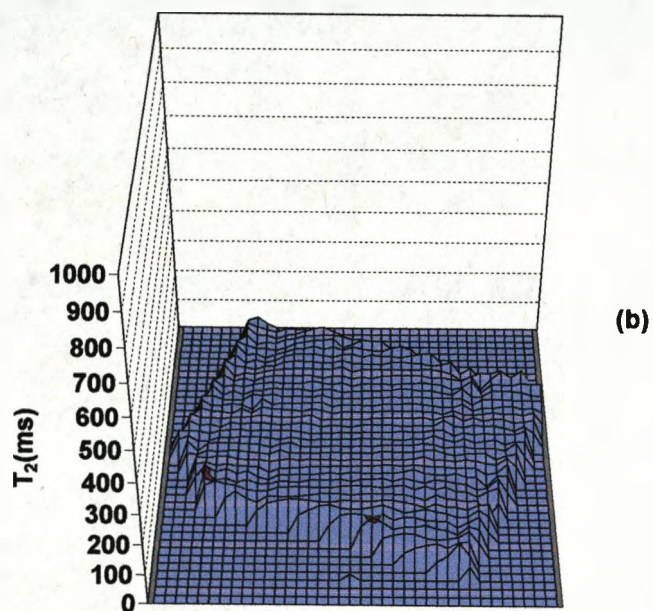
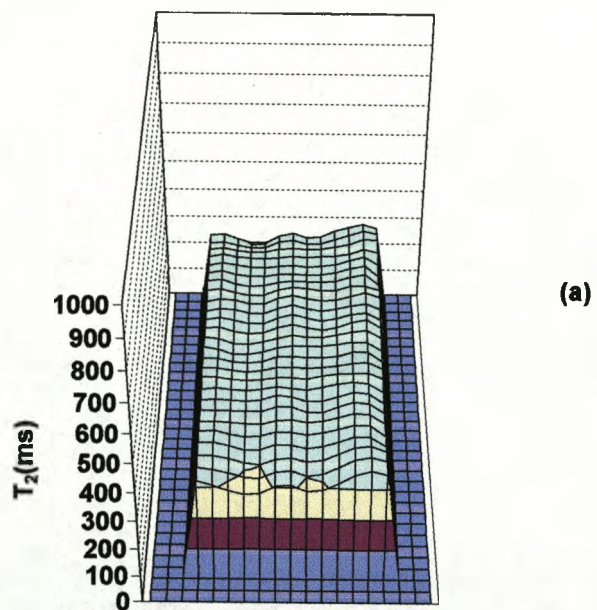


Figure 4.2. Three-dimensional plots of T_2 (ms) intensity values of hydrated Li^+ -exchanged (a) cast and (b) commercial Nafion membrane.

NMR findings, the physical structure of the cast membrane seems to be less crystalline and less dense. Therefore, it would be expected that a larger proportion of hydrophilic regions would be formed within the cast membrane since the molecular backbones and the side chains are freer to reorientate in this membrane. This could result in the hydrophilic regions being larger, or more numerous or both, in the cast membrane. This would provide further space for the absorbed water molecules in this membrane to move and rotate more freely, which consequently would result in the observation of longer T_2 values in the cast membrane.

Corresponding proton density *PD* maps were also prepared for the cast and commercial Nafion samples to obtain information about the relative concentration of water molecules absorbed in these samples. These maps are presented as three-dimensional numerical plots of proton density values in Figure 4.3. As can be seen, the cast Nafion sample (Figure 4.3(a)) contains a higher concentration of protons (~2100 a.u) than the commercial sample (~600 a.u, in Figure 4.3(b)). This can be attributed to a less dense physical structure for the cast membrane, allowing a larger amount of water molecules to be absorbed into its hydrophilic regions. The crystalline regions in the polymers are thought to increase the barrier to water-induced swelling.⁶ Because commercial Nafion membrane seems to be more crystalline (according to the NMR findings) it is not surprising that it takes up less water than the cast membrane. Comparison of these *PD* maps also reveals that the distribution of protons over the commercial Nafion membrane is slightly uneven whereas it is relatively homogenous for the cast sample. As mentioned earlier, the commercial Nafion membrane is produced under high temperature, vacuum conditions and through a rolling process which in turn would result in mechanical stresses and strains in the membrane.⁵ These

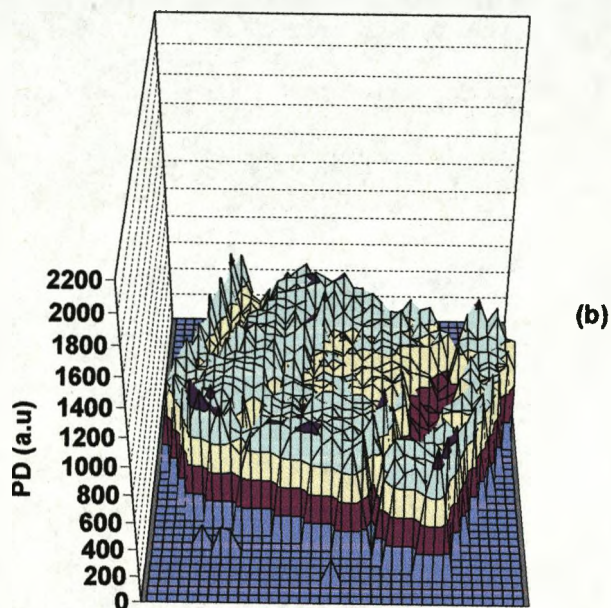
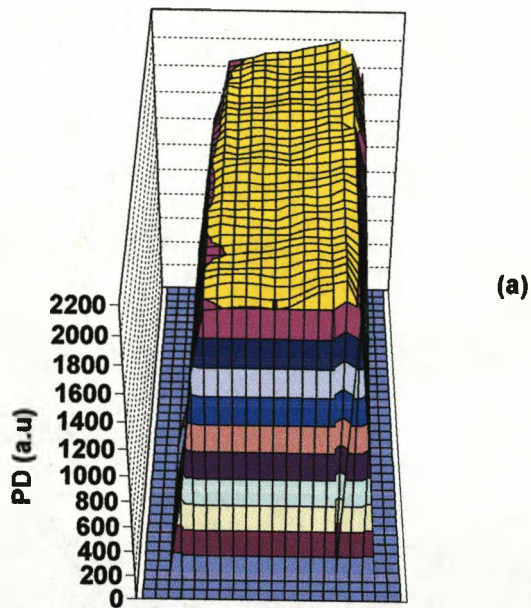


Figure 4.3. Three-dimensional plots of *PD* intensity values of hydrated Li^+ -exchanged (a) cast and (b) commercial Nafion membrane.

stresses may cause inconsistency in the physical structure of the membrane which leads to an uneven hydration of the polymer.⁵ Another explanation may be that the membrane was unevenly compressed during handling at some point after manufacture.

4.3.2. MRI of Dry Nafion Membranes

An experiment was carried out to take simultaneous spin echo images of fully dehydrated (dried) Li⁺-exchanged cast and commercial Nafion samples. This experiment was performed to ensure that the protons observed in the MRI images of the hydrated samples, shown in Section 4.3.1, are uniquely related to the absorbed water molecules in these membranes, and not to any other H-containing contaminants.

4.3.2.1. Experimental

The hydrated Li⁺-exchanged cast and commercial Nafion samples used in the experiment described in Section 4.3.1 were completely dehydrated in a furnace at 70°C for 24 h. The dried samples were sandwiched together and put in the NMR tube as explained above. The NMR tube was sealed with a dry paper plug and covered with a gas-tight cap, to prevent the samples absorbing moisture from the surrounding environment, and then placed in the resonator probe of the MRI scanner. The same multi-echo imaging technique was applied to image these samples as for the water-containing (fully hydrated) samples.

4.3.2.2. Results and Discussion

Multi-echo imaging of the fully dehydrated Li^+ -exchanged cast and commercial Nafion samples failed because no ^1H NMR signal was detected from these samples by the MRI scanner. This proved that the protons seen in the MRI image of the hydrated samples were uniquely related to the water molecules absorbed within the Nafion membranes. The failure of this imaging experiment also confirmed the results obtained from the ^1H NMR spectroscopy of these samples, shown in Section 4.2, that is, that the samples contained no mobile H-containing contaminants.

4.4. Determination of Water Content

Determination of water content of the hydrated Li^+ -exchanged commercial and cast Nafion membranes was carried out to achieve a better understanding of the results obtained from the NMR measurements and MRI imaging of the commercial and cast Nafion membranes. The results obtained can also help to explain the electromechanical performance of the IPMC samples fabricated from these two membrane types.

4.4.1. Experimental

8×8 mm square samples of fully hydrated cast and commercial Nafion membranes (in acid form) were soaked in a saturated solution of lithium hydroxide, LiOH , at room temperature for two weeks to exchange all protons on the sulfonate groups for Li^+ ions. The Li^+ -exchanged samples were then rinsed with DI water and put in a furnace at a temperature of

70°C for 24 h to become completely dehydrated (dried). These samples were weighed before and after the drying process. To calculate the water content of the samples, the mass of the dried sample was subtracted from the mass of the hydrated sample and the result was divided by the hydrated mass of the sample.

4.4.2. Results and Discussion

The results presented in Table 4.1 reveal that the cast Nafion membrane, with thickness of about nine times more than the commercial Nafion membrane, had higher water content – approximately 2 times – than the commercial membrane. This suggests once again that the cast Nafion is less dense and less crystalline, and so it is able to imbibe a larger amount of water. This may have also arisen due to the presence of a higher number of the hydrophilic regions in this membrane, which would increase the ability of the membrane to absorb a larger amount of water.⁶

The result gained from this experiment is consistent with the results obtained from the comparison of the *PD* maps of both samples in Section 4.3.1.2 in which a higher concentration of protons – approximately 3.5 times – was observed in the *PD* map of the cast Nafion sample (~2100 a.u., in Figure 4.3(a)) than the commercial Nafion sample (~600 a.u., in Figure 4.3(b)).

Table 4.1. Properties of the samples.

Samples	Li ⁺ -exchange commercial Nafion	Li ⁺ -exchanged cast Nafion
Thickness of sample (mm)	0.2	1.65
Equivalent Weight (amu)	1100	1100
Hydrated weight (g)	0.020	0.180
Dried weight (g)	0.010	0.032
Water content (%)	50	82

4.5. SEM

SEM analysis coupled with EDX elemental detection and mapping was employed to study the thickness, structure and morphology of the plated surfaces of the IPMC samples fabricated from the commercial and cast Nafion membranes. These samples were described in Table 3.1.

4.5.1. Experimental

Using the technique described in the Section 3.7.1.2, the IPMC samples were embedded in the mixture of liquid resin and hardener, to be examined in the SEM. Backscattered electron imaging (BSE) of these samples was performed with a 20 keV beam at a working distance of 10 mm and at a magnification of between 29× and 41400× on the Philips XL30 ESEM. BSE imaging was preferred to secondary electron (SE) imaging since the

contrast of BSE images varies monotonically with the atomic number (Z) of the elements in the beam.⁷ Elemental maps and line scans were collected using a 20 keV electron beam on the same instrument. All the images were captured digitally and saved as bit-map images to a computer.

4.5.2. Results and Discussion

Figure 4.4 – parts (a)-(h) presents cross-sectional BSE images of the sample, Pt₁Com, from low to high magnification. In the low magnification images of this sample, shown in Figure 4.4(a) and (b), two parallel, bright layers running along the surfaces of the Nafion membrane are observed. These layers can be assigned as the platinum-plated regions of the membrane, *i.e.* the electrodes. The thickness of the platinum electrodes at both surfaces is similar, revealing that the plating process gives a uniform coverage. The images captured at higher magnification (Figure 4.4, parts (c)-(h)) show that there is a gradient in the concentration of platinum in the electrode regions. The concentration of platinum particles is very high at the very outer surfaces and decreases gradually towards the center of the membrane. The high concentration of platinum particles at the outer surface is seen as a layer of dense appearance and relatively uniform thickness ($\sim 0.10 \mu\text{m}$) along the surface of the membrane. In the near-surface region, the platinum particles form a layer with a porous structure with a thickness of approximately $5\text{-}6 \mu\text{m}$. Thus, it can be said that the platinum electrode region is formed of two distinct layers: a thin dense layer at the top surface and a broad porous layer extending into the membrane. In the images shown in Figure 4.4(g) and (h) it can be seen that the size of the platinum particles decreases significantly across the

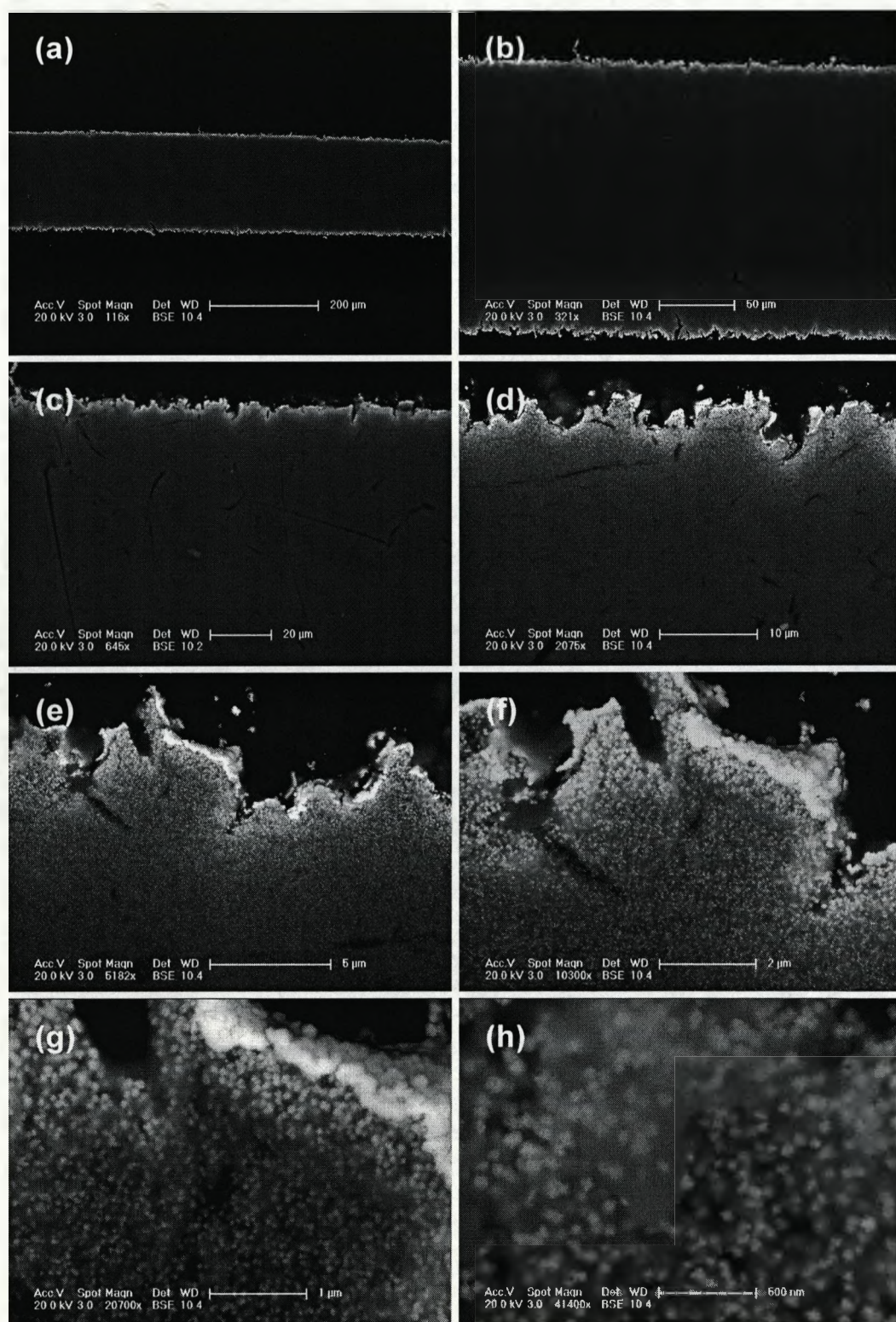


Figure 4.4. Cross-sectional BSE images of Pt₁Com at increasing magnifications (a)-(h).

porous layer towards the center of the membrane. The coagulation of platinum particles in the vicinity of the surface,⁸ where the concentration of platinum is very high, during the chemical reduction process could be the main reason for obtaining large platinum particles (~40 nm) compared to those seen in the deeper region (~10 nm).

In order to study the effect of the repetitive platinum electroding on the electrode structure and thickness, cross-sectional BSE imaging of the Nafion/platinum electrode region of the commercial and cast Nafion-based IPMC samples was performed. The images obtained are presented in Figures 4.5 to 4.8 – parts (a)-(f) at nominal magnification of $645\times$ to $207500\times$ respectively. In these figures, images of the samples (a) Pt₁Com, (b) Pt₂Com and (c) Pt₄Com are shown in the left column and, to facilitate the comparison, the images of the matching cast Nafion-based IPMC samples, (d) Pt₁Cast, (e) Pt₂Cast and (f) Pt₄Cast, are presented in the right column.

Figure 4.5, parts (a)-(f), shows the low magnification BSE images of the mentioned samples. The Nafion membrane in all these images appears rougher and brighter in the electrode region than in the centre of the membrane. Comparison of the samples in each column reveals the effect of the repetitive platinum electroding on the thickness of the electrode region. As the images show, the thinnest platinum-impregnated region (electrode) is observed in the samples with one plating cycle. That is, Pt₁Com (~5-6 μm) and Pt₁Cast (10-20 μm) shown in Figure 4.5(a) and (d), respectively. The thickness of this region increases with the increase in the number of repetitions of the plating cycle. The thickest electrodes are formed in the samples that have been through the electroding process for four cycles, Pt₄Com (Figure 4.5(c)) and Pt₄Cast (Figure 4.5(f)). Thus, the repetition of the

platinum electroding process affects the thickness of the electrode regions in the commercial and cast Nafion-based samples in the same way.

However, comparison of the samples in each row reveals that applying the same number of plating cycles to the commercial and to the cast Nafion membranes results in a thicker electrode region in the cast IPMC samples. In other words, a much thinner electrode region is always obtained in the commercial Nafion-based IPMC samples than in the matching cast IPMC samples. This can be observed more clearly in the higher magnification images of the IPMC samples presented in the Figures 4.6, 4.7 and 4.8.

For the commercial IPMC samples, it seems that the repetition of the plating process increases the thickness of the solid layer at the surface more than that of the porous layer within the membrane. This can be seen in the sample Pt₄Com which has the thickest solid layer (~0.60 μm) at the surface. For the cast IPMC samples, however, the repetitive platinum electroding results in the penetration of a higher concentration of the platinum particles into the membrane, rather than precipitation at the surface. Thus, the thickness of the porous layer is affected much more than the outer dense layer in the cast samples. The thickest porous layer is obtained in the Pt₄Cast sample (~40-50 μm), and it is much higher than that observed in the Pt₄Com (~10-20 μm). It should also be mentioned that by increasing the number of plating cycles, the thickness of the dense layer in the cast IPMC samples increases in the small range of 0.1-0.25 μm, while it increases over the larger range of ~0.15-0.60 μm in the commercial IPMC samples. The penetration of a higher concentration of platinum into the cast IPMC samples leads to the formation of larger coagulated platinum particles (in the range of 50-100 nm, depending on the number of plating cycles) compared to those in the commercial IPMC samples (40-70 nm) in the sub-surface regions.

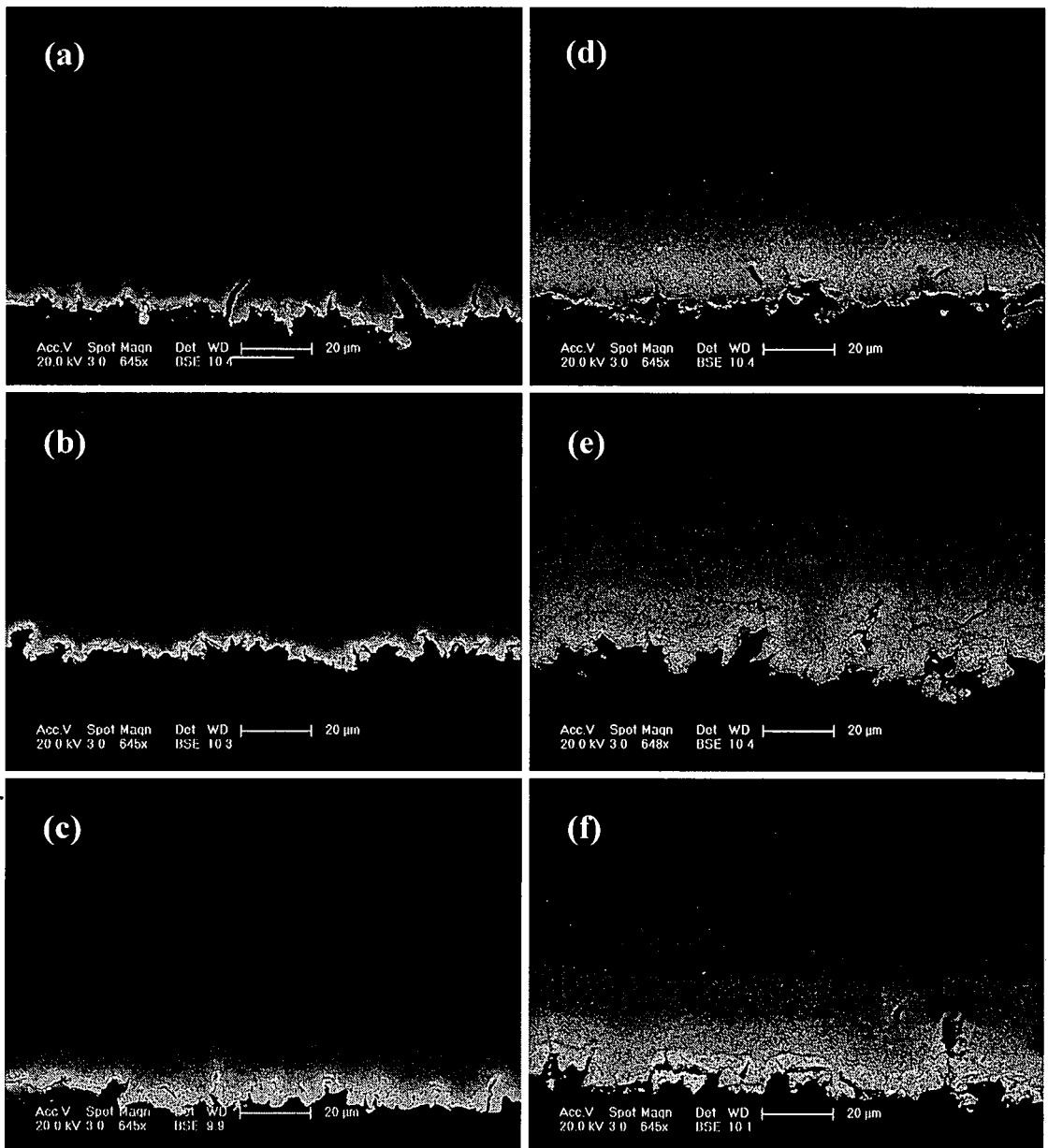


Figure 4.5. Cross-section BSE image of (a) Pt₁Com, (b) Pt₂Com, (c) Pt₄Com, (d) Pt₁Cast, (e) Pt₂Cast, and (f) Pt₄Cast with nominal magnification of 645 \times .

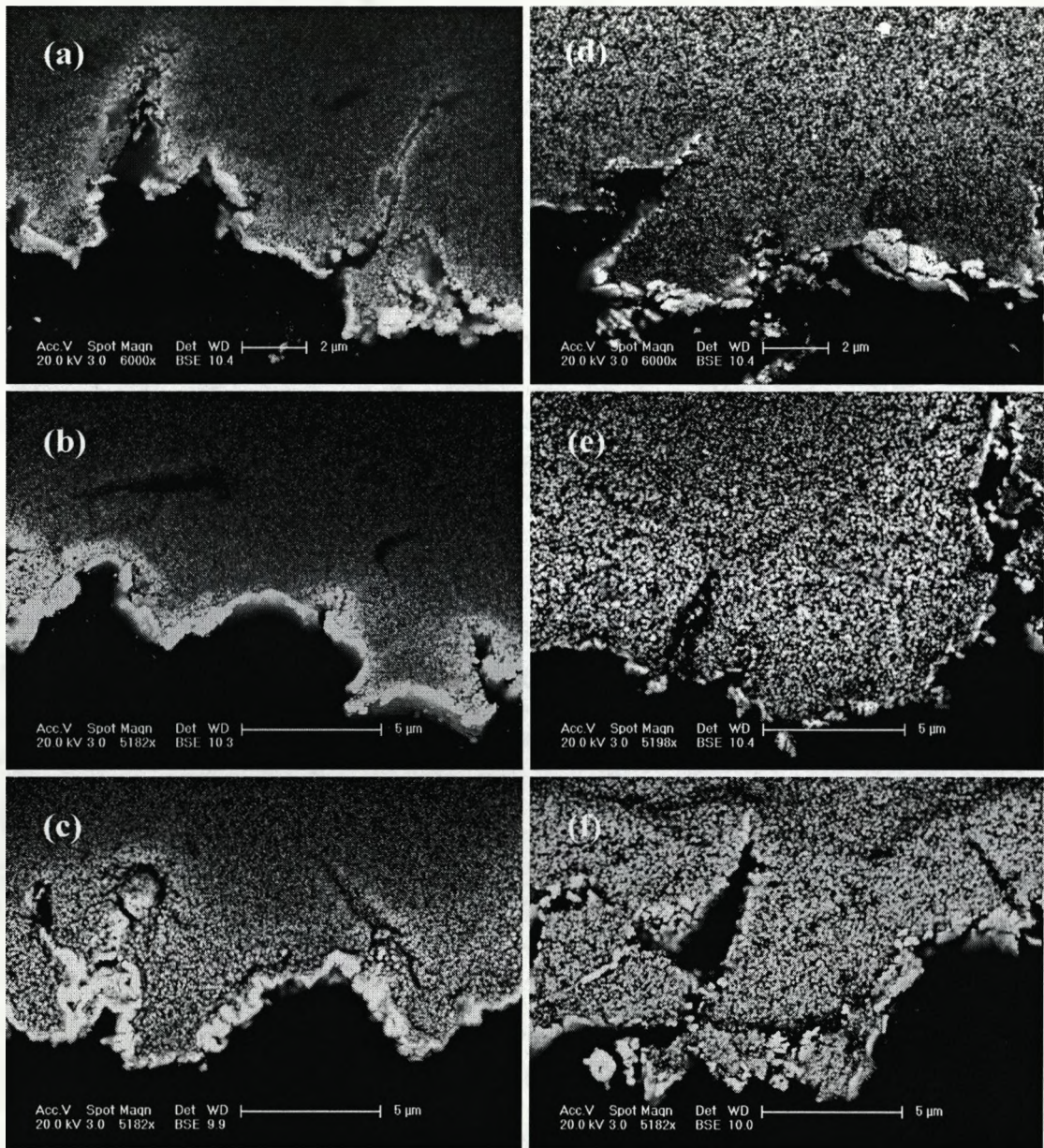


Figure 4.6. Cross-section BSE image of (a) Pt₁Com, (b) Pt₂Com, (c) Pt₄Com, (d) Pt₁Cast, (e) Pt₂Cast, and (f) Pt₄Cast with nominal magnification of 5182 \times .

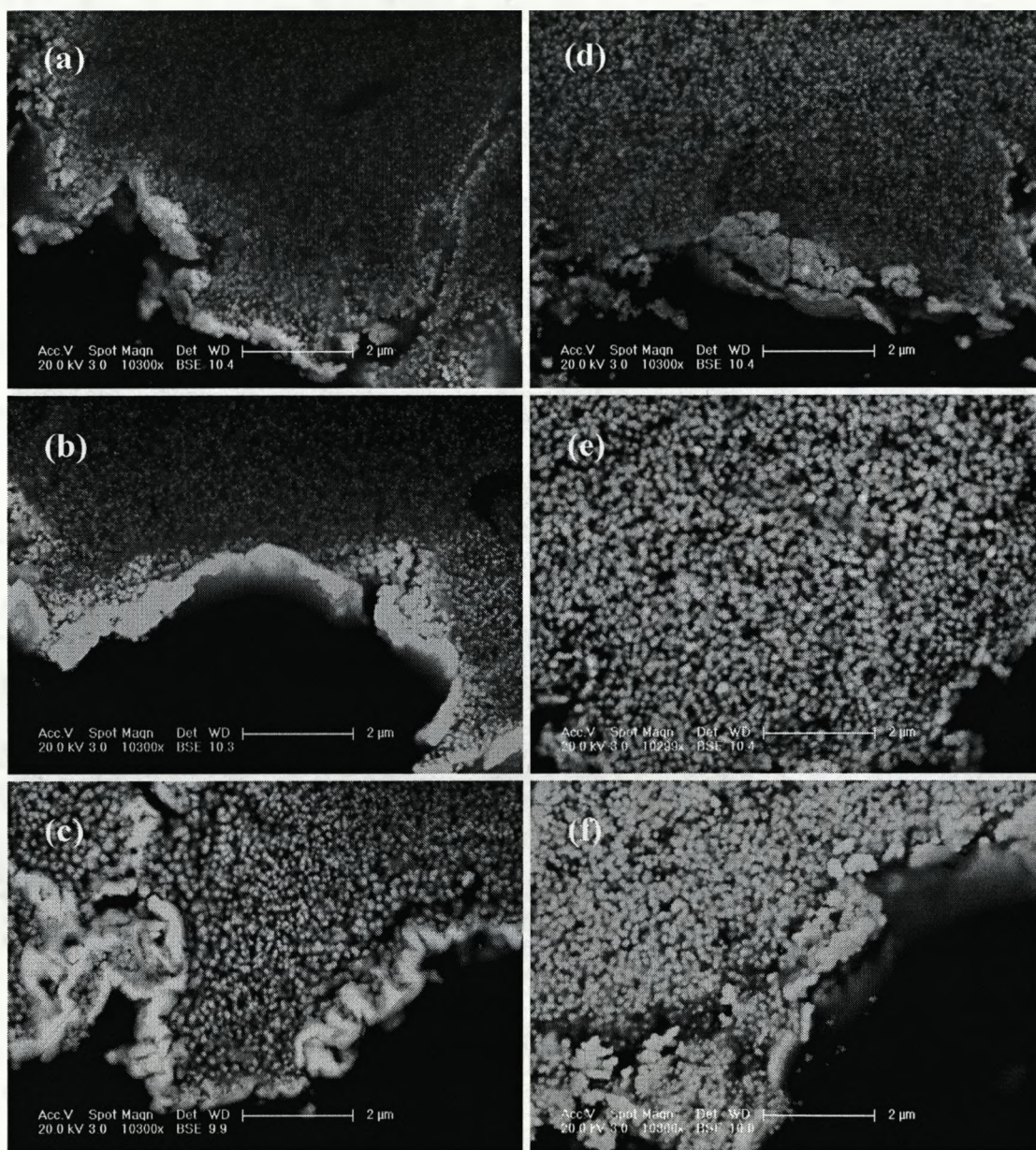


Figure 4.7. Cross-section BSE images of (a) Pt₁Com, (b) Pt₂Com, (c) Pt₄Com, (d) Pt₁Cast, (e) Pt₂Cast, and (f) Pt₄Cast with nominal magnification of 10300×.

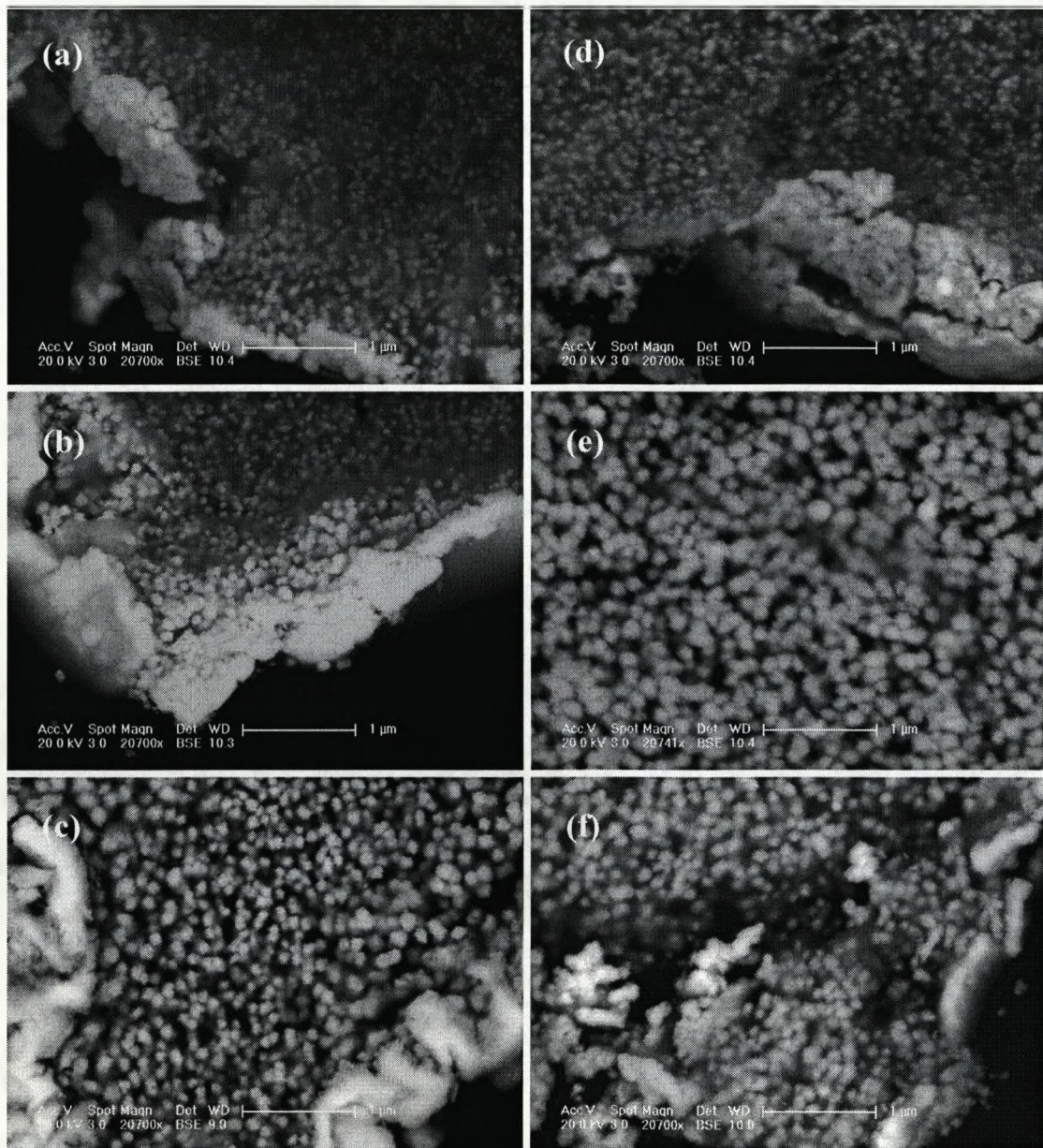


Figure 4.8. Cross-section BSE images of (a) Pt₁Com, (b) Pt₂Com, (c) Pt₄Com, (d) Pt₁Cast, (e) Pt₂Cast, and (f) Pt₄Cast with nominal magnification of 20700 \times .

The presence of the larger platinum particles in these samples is seen as a rougher region in the images.

The EDX line scans of the commercial and cast samples agree with the results obtained from the BSE imaging. The EDX line scans performed across the cross-sectional thickness of the samples are shown in Figure 4.9 and 4.10. These figures present the plots of the normalized EDX signal intensity of platinum and the other elements of interest, C, F and S, versus distance, for commercial and cast samples, respectively. Each plot is accompanied by a SEM image of the corresponding sample. The white dotted line shown in these SEM images indicates the pathway of the line scan. The raw data acquired from the line scanning experiments were normalized by dividing the intensity of all the elements by the average intensity of F at the centre of the sample.

All the line scans show an abrupt drop in intensity of C where the intensity of Pt increases. This reveals the interfacial area between the samples and the resin. A relatively constant ratio of signal intensity for elements C, S and F is observed in all the line scans. However, the ratio of the signal intensity of Pt to the rest of the elements is not constant and changes according to the number of plating cycles. A symmetrical variation in the ratio of Pt is also seen at both extremes of the line scans. This implies that the distributions of Pt at the two faces of the sample are equivalent. The figures illustrate that the samples Pt₁Com and Pt₁Cast have the lowest level of Pt. The height and width of the Pt trace further grows significantly in each series of the samples as the number of plating cycles is increased.

The comparison of the EDX line scans of the commercial and cast IPMC samples, presented in Figure 4.9 and 4.10, shows that the signal intensity of Pt appears very much sharper and narrower in the commercial IPMC samples. This reveals once again that the

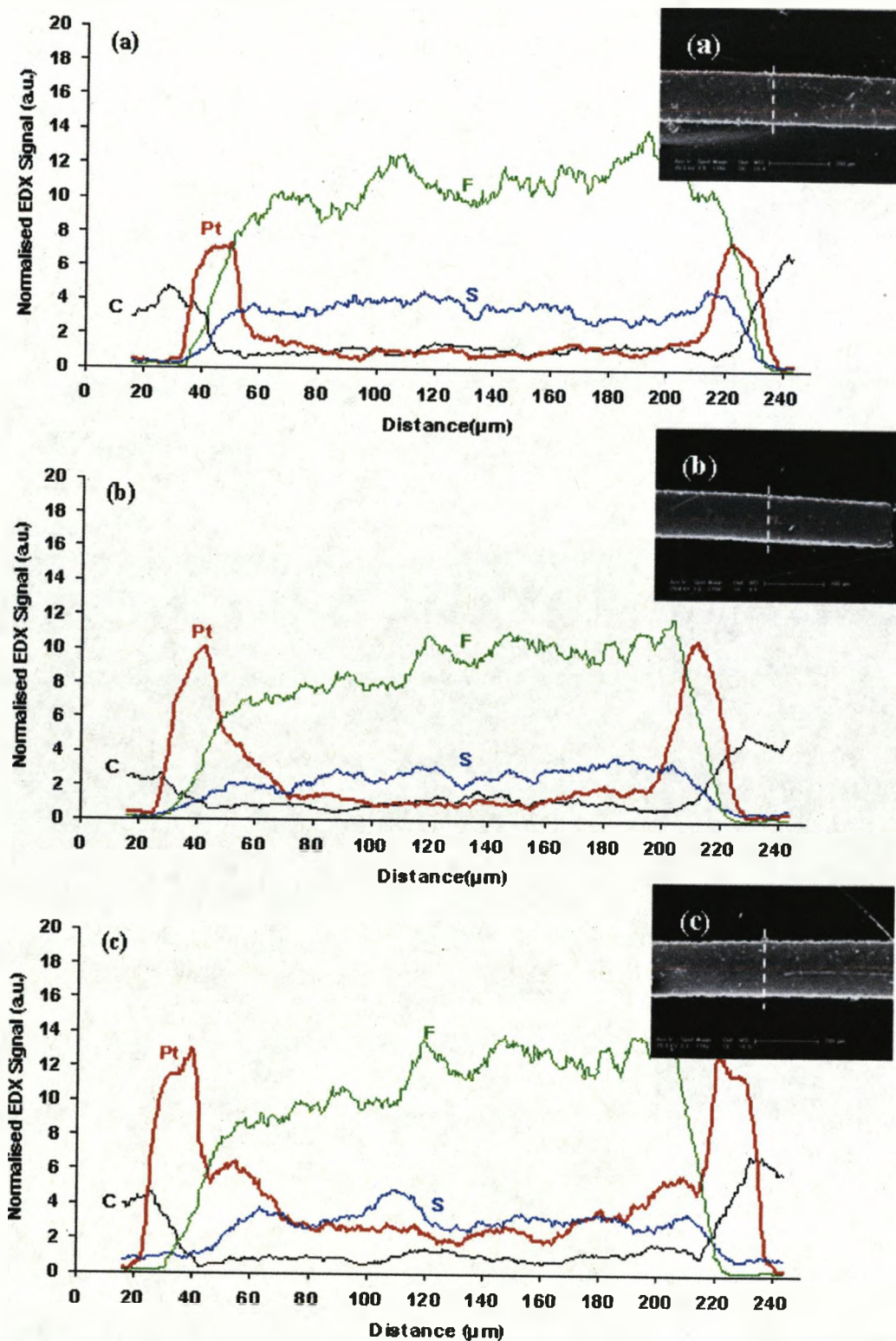


Figure 4.9. EDX line scans of the (a) Pt₁Com, (b) Pt₂Com and (c) Pt₄Com accompanied by the corresponding SEM image (insets).

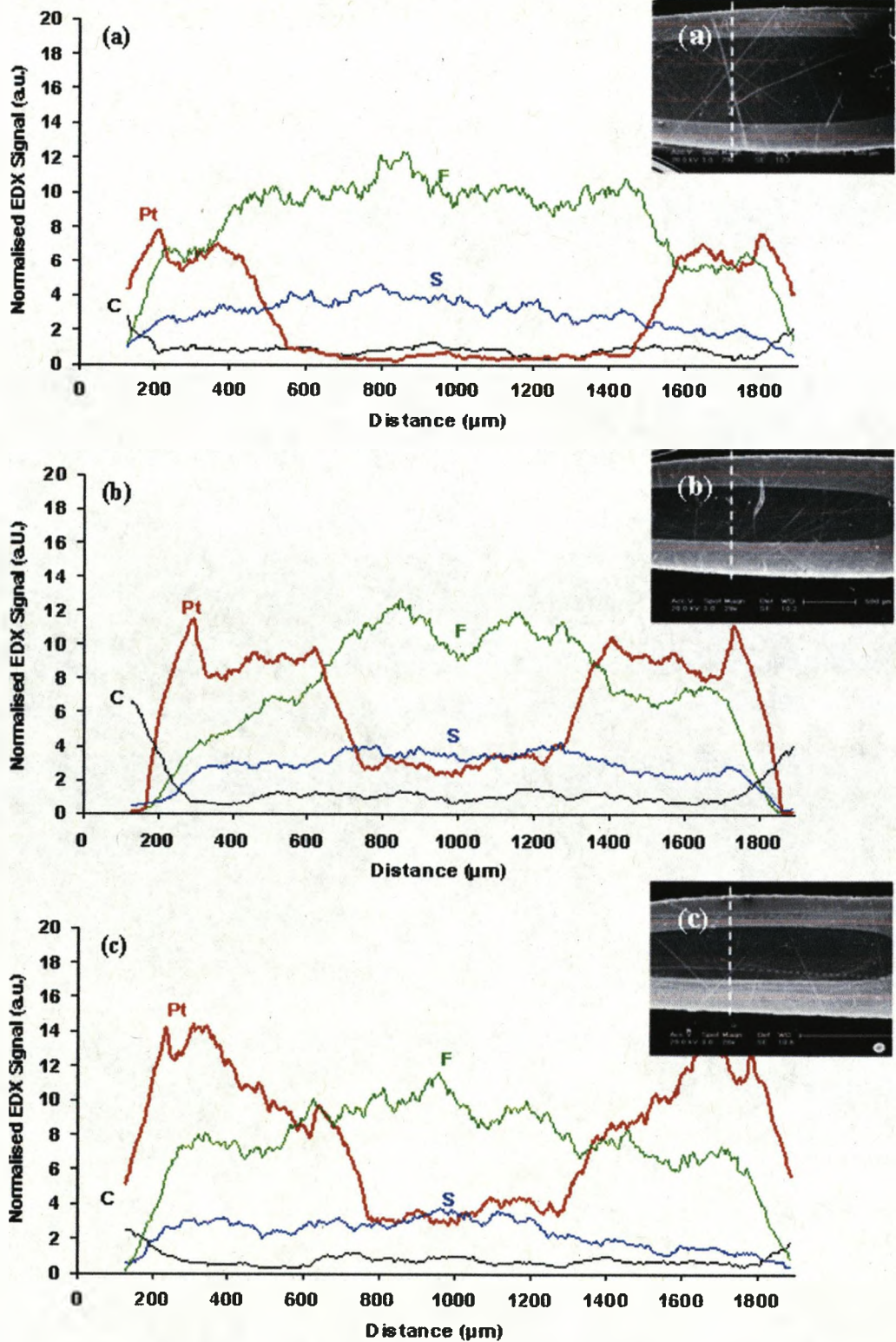


Figure 4.10. EDX line scans of the (a) Pt_1Cast , (b) Pt_2Cast and (c) Pt_4Cast accompanied by the corresponding SEM image (inset).

platinum penetrates to greater depth in the cast samples, forming a thicker electrode region compared to the equivalent commercial sample. The EDX platinum maps of the commercial and cast samples, shown in Figures 4.11 and 4.12 respectively, confirm that, with the same number of plating cycles, a higher concentration of Pt in the electrode region of the cast IPMC samples is observed.

Figure 4.13 shows cross-sectional BSE images of the AuPt₂Com sample at different magnifications. The gold layer deposited physically on top of the platinum layer of the sample can be seen as a second layer at the surface. This gold layer is slightly brighter than the platinum layer.

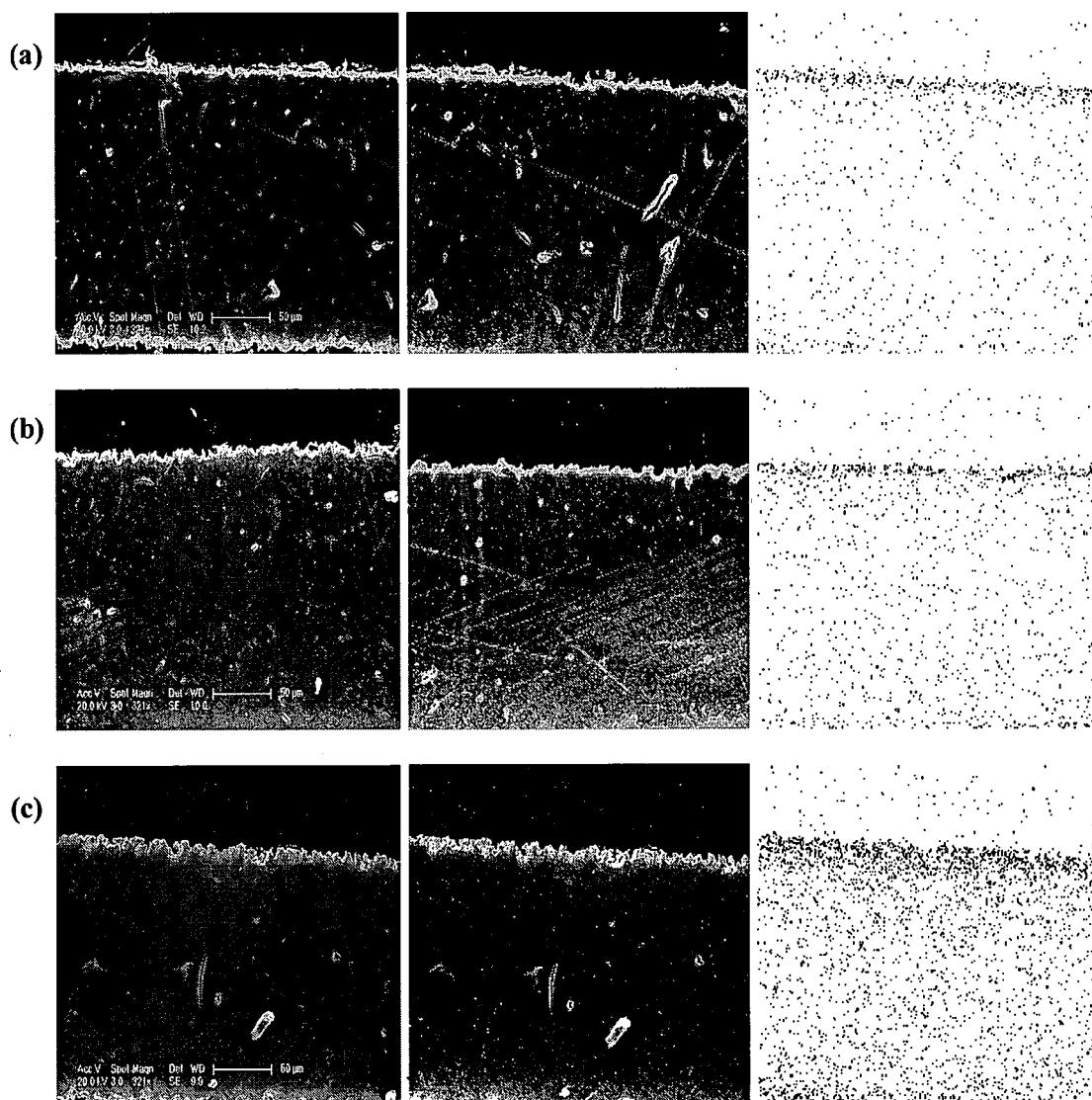


Figure 4.11. SEM image (left), EDX image (centre) and corresponding EDX platinum map (right) of (a) Pt_1Com , (b) Pt_2Com and (c) Pt_4Com , performed with a 20 keV beam at a working distance of 10 mm and at nominal magnification of $321\times$.

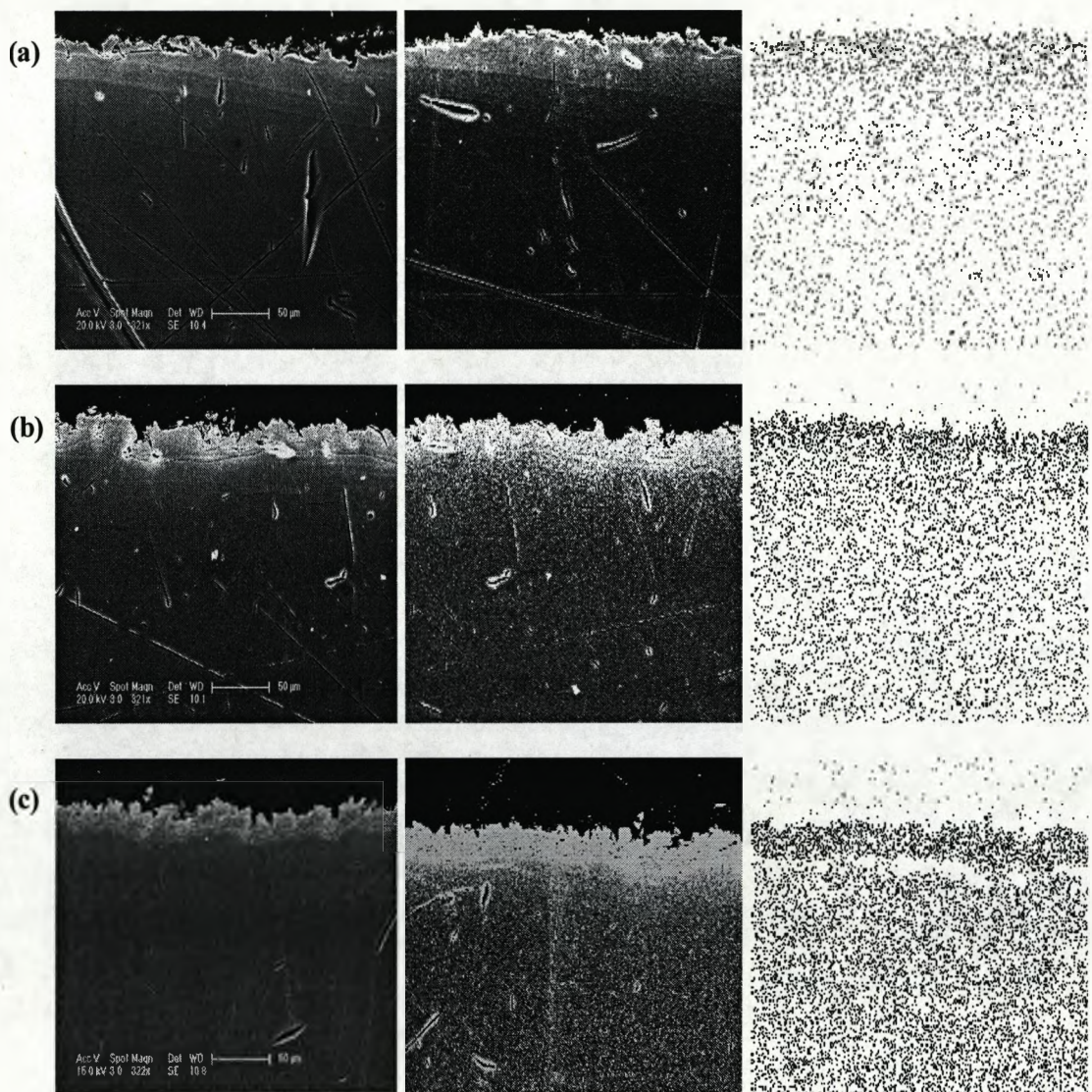


Figure 4.12. SEM image (left), EDX image (centre) and corresponding EDX platinum map (right) of (a) Pt₁Cast, (b) Pt₂Cast and (c) Pt₄Cast, performed with a 20 keV beam at a working distance of 10 mm and nominal magnification of 321×.

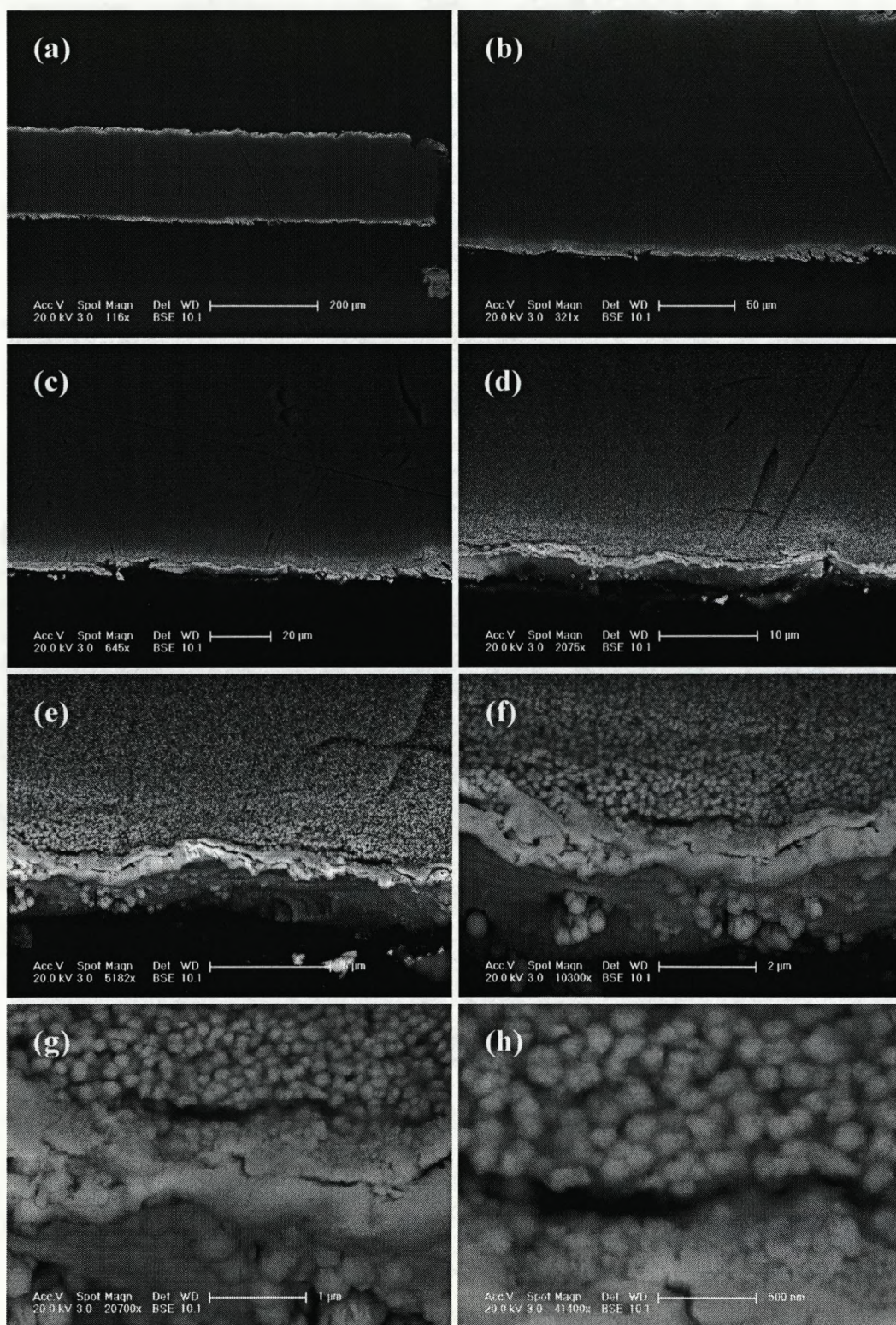


Figure 4.13. Cross-sectional BSE images of AuPt₂Com at increasing magnification (a)-(h).

4.6. Summary

This chapter presented the results obtained from several preliminary experiments performed to evaluate the chemical structure and physical properties of the cast and commercial Nafion membranes, using NMR spectroscopy and MRI imaging. ^1H NMR measurements revealed that these membranes had the same chemical composition and that no proton-containing contaminant such as alcohol or DMF had been introduced to the cast membrane during the preparation process. The broader line widths of the signals observed in the ^1H NMR spectrum of the commercial Nafion membrane also implied that this membrane has a more ordered and crystalline structure. MRI imaging of the membranes showed that the water molecules absorbed in the cast membrane have higher spin-spin relaxation time, T_2 , compared to that of the commercial membrane. This indicated that the mobility of the water molecules absorbed in the commercial membrane is more restricted. The PD maps constructed for the membranes showed that the cast membrane contains a higher concentration of protons compared to the commercial membrane. This was attributed to the less dense physical structure of the cast membrane which allows a larger amount of water molecules to be absorbed. The failure of the MRI imaging of the fully dehydrated cast and commercial membranes proved that the protons seen in the MRI and T_2 images of the hydrated Li^+ -exchanged membranes are uniquely related to the water molecules absorbed in the polymers. The result obtained from the determination of the water content of the membranes also revealed that the cast membrane contains a much higher concentration of water and confirmed the results obtained from the PD maps of the membranes. SEM study of the IPMC samples showed that in the platinum electroding process, two similar platinum electrodes are plated at each face of the Nafion membrane and that these electrodes consist

of two distinct layers: a thin dense layer at the top surface and a broad porous layer in the sub-surface region of the membrane. The results obtained from SEM analysis also revealed that the repetition of the plating process increases the thickness of the electrode regions in the commercial and cast Nafion-based samples. It showed that applying the same number of plating cycles to the commercial and cast Nafion membranes always resulted in a thicker electrode region in the cast IPMC samples. For the commercial IPMC samples, the repetition of the plating process increased the thickness of the dense layer at the surface more than the porous layer within the membrane, sub-surface region, while for the cast samples it was *vice versa*. Repetition of the plating cycle in the case of the cast IPMC samples leads to the formation of larger platinum particles, due to the coagulation in the sub-surface region of these samples, than in the commercial IPMC samples.

4.7. References

-
- [1]. A. Y. Nosaka, S. Watanabe, I. Toyoda, Y. Nosaka, *Macromolecules*, 2006, 39, 4425.
 - [2]. C. A. Fyfe, "Solid State NMR for Chemists", *C.F.C Press*, 1983.
 - [3]. D. W. McCall, D. C. Doulass, D. R. Falcone, *J. Phys. Chem.*, 1967, 71, 998.
 - [4]. R. B. Moore, K. M. Cable, T. L. Croley, *J. Membrane Sci.*, 1992, 75(1-2), 7.
 - [5]. W. Liu, K. Ruth, G. Rusch, *J. New Materials for Electrochemical System*, 2001, 4, 227.
 - [6]. R. B. Moore, III, and C. R. Martin, "chemical and morphological properties of Solution-cast perfluorinate ionomers", *Macromolecules*, 1988, 21, 1334-1339.
 - [7]. P. J. Goodhew, J. Humphreys, R. Beanland, "Electron Microscopy and Analysis", *Taylor & Francis*, 2001.

[8]. M. Shahinpoor, K.J. Kim, *Smart Mater. Struct.*, 2001, 10, 819.

Chapter Five

MRI Study of Commercial Nafion Membrane

5.1. Introduction

As mentioned in Chapter One, the underlying mechanism of actuation of IPMCs involves the electrically-induced diffusion of hydrated cations in the Nafion membrane. In this chapter, this is investigated by deploying a functioning electrochemical cell inside the MRI scanner and imaging the water distribution in a commercial Nafion membrane in real time during application of a continuous electrical potential. To the best of our knowledge, this study is the first recorded electrochemical experiment of this kind. Multi-echo imaging, based on the CPMG pulse sequence, is exploited in this experiment because it produces a signal which is dependent on spin-spin (or transverse) relaxation time, T_2 .^{1,2} T_2 is an important factor for our understanding of imaging because it is highly dependent on molecular motion and, thus, is highly sensitive to the physicochemical environment of the water molecule in the sample. Therefore, T_2 can be considered as a probe of the strength of interaction between the proton-containing molecules, in this case water, and their immediate surroundings. Thus, the multi-echo imaging allows a quantitative evaluation of the interaction of water molecules with the polymer chain and the mobility of water molecules through the polymer to be achieved. Using this method with appropriate acquisition parameters allows us to obtain images from which T_2 and proton density, PD , maps can be extracted. These can be related to the physical and structural properties of the Nafion membrane. These are presented in this chapter in the form of two and three-dimensional images and maps, respectively, of proton density, PD , and spin-spin relaxation time, T_2 , and changes in these over time and with respect to changes made to the applied potential are followed. It should also be mentioned that PD gives a measure of the number

of nuclei of interest in a selected slice of the sample and from the integral of the image profile it is possible to obtain the relative concentrations of the nuclei.¹

5.2. Experimental

8×8 mm square samples of 0.2 mm thick sheet of the pre-cleaned (see Section 3.5.1.2) commercial Nafion membrane in the acid form were cut and soaked in a saturated solution of LiOH at a temperature of 60°C for 1h to exchange protons on the sulfonate groups in the ionomer for Li⁺ cations. The samples were then briefly boiled in DI water to remove the residual LiOH and were stored in a fresh solution of saturated LiOH at room temperature until use.

To enable a suitable potential to be applied to the samples once they were inside the MRI scanner, a sample holder was arranged so that electrical contact was made to each face of the polymer square at opposite edges, such that the electrical current would pass through the width of the polymer square rather than merely through its thickness. (0.2mm). Figure 5.1 depicts the electrochemical assembly used in the *in situ* MRI studies. The sample holder consisted of two foil-coated glass plates which were painted with silver paint in order to increase the interfacial area between polymer and metal contact. The square commercial Nafion sample (Li⁺-exchanged) was sandwiched between these two foil-coated plates and wires were attached to the foil. The sample holder was then placed into an adapted 25 mm o.d. quartz NMR tube which had two holes at the bottom through which the wires to the sample were passed. The holes were sealed with quick-drying epoxy resin adhesive.

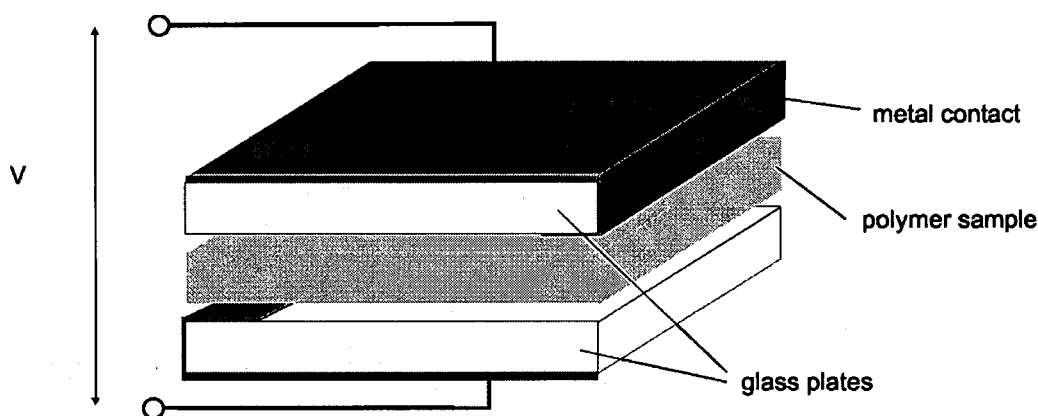


Figure 5.1. Electrochemical assembly used in the *in situ* MRI studies.

A constant saturated water vapour pressure was maintained inside the tube by enclosing a water-soaked paper plug within it and using a gas-tight cap. The NMR tube was then inserted into the resonator probe of the MRI scanner and the wires from the sample holder were connected to a variable 0-10V d.c. power supply. After initial calibration (see Section 3.7.2.2) the standard multi-echo pulse sequence, MSME (Multi Slice Multi Echo), from the Bruker Paravision[®] library, was used to collect a train of 64 echoes, each after a 180° pulse, with a minimum echo time, T_E , of 3 ms and repetition time, T_R , of 3 s. To study the electrically-induced diffusion of water in the Nafion samples, T_2 and PD images were extracted, as described in Section 3.7.2.3, from MRI images recorded during an extended experimental run on a single sample. Four electrical regimes were imposed on the sample in sequence. In chronological order these were: (a) no potential applied; (b) application of a continuous 5V d.c. potential; (c) application of a continuous 5V d.c. potential of reversed polarity and (d) application of a continuous 5V d.c. potential after a second reversal of polarity. In each case, T_2 and PD images were extracted from the same raw data set. The

field of view, *FOV*, in the images was 18×18 mm, the slice thickness was 2.0 mm, the number of scans was 2 and the acquisition time for each dataset with matrix size of 128×128 pixels was approximately 21 min. This experimental sequence was repeated several times with similar samples to confirm the repeatability of the results.

5.3. Results and Analysis

As seen in Chapter Four the Nafion membrane should contain no protons itself, except for the H⁺ in the -SO₃H groups in the acid form. Once these have been exchanged for Li⁺, as in this work, the *PD* and *T*₂ images of the Nafion samples can be considered to relate uniquely to the protons present in the water molecules absorbed in the polymer.

The *T*₂ and *PD* images extracted from the raw MRI images of the commercial Nafion sample (Li⁺-exchanged) with no potential applied are shown in Figure 5.2(a(i)) and (a' (i)), respectively. As can be seen, the *T*₂ image (Figure 5.2(a(i))) is quite dark, representing a short *T*₂ for water molecules within the sample. Unlike the *T*₂ image, the corresponding *PD* image appears with high intensity (brightness) in Figure 5.2(a'(i)). The intensity in the *PD* images is proportional to the concentration of water molecules within the Nafion membrane. Figure 5.2(b) – parts (i)-(v) present *T*₂ images of the sample 29, 60, 89 and 122 min., respectively, after application of the continuous 5V d.c. potential. As soon as the potential is applied to the Nafion film, *T*₂ considerably increases over the whole sample and particularly in the area near the cathode (labelled with a negative sign in the *T*₂ images). This increase in *T*₂ over the whole polymer sample implies an increase in the freedom of rotation of water molecules within the polymer since the *T*₂ (spin-spin relaxation time) is

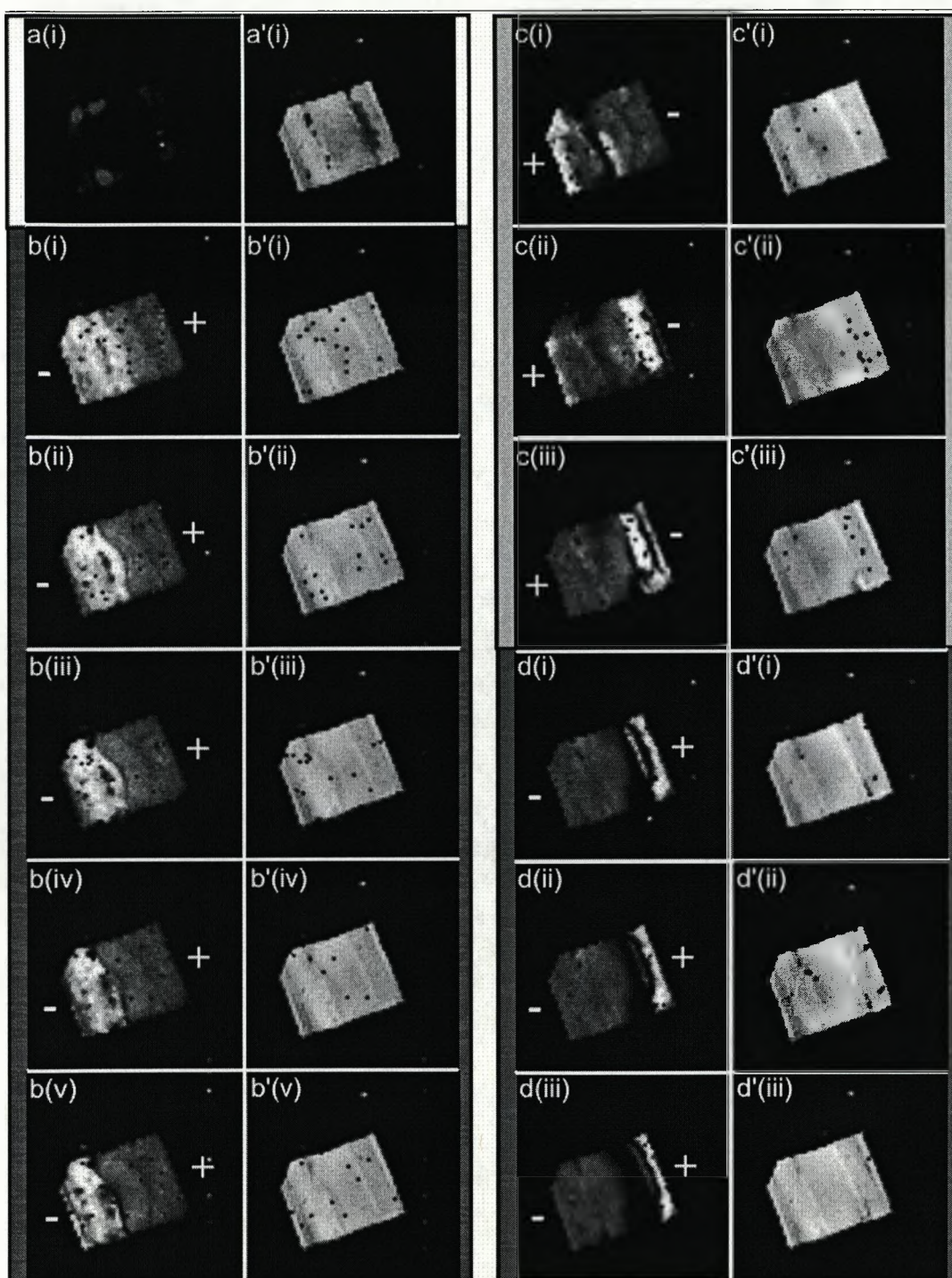


Figure 5.2. T_2 (left images) and PD (right images, primed labels) images: (a, a') with no potential applied; (b, b') (i) 0; (ii) 29; (iii) 60; (iv) 89 and (v) 122 min. after application of a 5V d.c. continuous potential in the sense indicated. (c, c') (i) 29; (ii) 60; (iii) 89 min. after reversal of the polarity of the 5V d.c. potential; (d, d') (i) 29; (ii) 89 min. after the second reversal of the polarity of the 5V d.c. potential. The negative “-” and positive “+” signs in these images show the cathode and anode side of the membrane, respectively.

dependent strongly upon the mobility of the molecules.¹ As can be seen, over time, the region of high T_2 s becomes further concentrated near the cathode, at the left of the image. Figure 5.2(b') – parts (i)-(v) reveals that the changes observed in the T_2 images are accompanied by simultaneous increases in the intensities in the corresponding PD images, mainly near the cathode. In these images higher intensities (brightness), indicating higher concentration of water molecules, are observed exactly in the same area as the high T_2 s seen in the corresponding T_2 images. The changes occurring in the PD images, however, are less obvious than those in the T_2 images, due to a high background in the PD images. Figure 5.2(c) and (c') – parts (i)-(iii) show the changes in T_2 and PD distribution in the sample 29, 60 and 89 min., respectively, after the polarity of the applied potential is reversed. The T_2 images show that the distribution of long T_2 s related to protons in mobile water is reversed by reversing the polarity of the applied potential and that T_2 near the new cathode, on the right of the image, increases over time. Accordingly, on the reversal of the polarity of the applied potential, the intensity of the PD images also increases near the new cathode. The T_2 and PD images presented in Figure 5.2(d) and (d') – parts (i)-(iii) show the effect of second reversal of the polarity of the applied potential on the electrically-induced distribution of water in the Nafion membrane. The changes in these images are less dramatic. Nevertheless, the region of high T_2 s again becomes more localised near the new cathode at the left of the T_2 images, and also the intensity in the PD images is increased in this region. The area of high T_2 which remained near the new anode (Figure 5.2(d) parts (i)-(iii)) is thought to be an artefact due to the trapping of water beyond the electrical contact and, therefore, outside the potential gradient.

Since the changes in the *PD* images were less obvious, three-dimensional numerical plots of the intensity values in these images were prepared to allow a more detailed insight into the distribution of water molecules in the polymer in the four potential regimes. Companion plots for the corresponding T_2 results were also prepared. Figure 5.3 shows one *PD* and one T_2 plot for the sample in each of the four different potential regimes (see also Appendix 2). There is a dip at the right side of the proton intensity graph when no potential was applied (Figure 5.3(a')) which disappears once the potential is applied (Figure 5.3(b')). As can be seen, the proton density increases near the cathode (at the left of the *PD* map) and undergoes qualitatively similar changes to those seen in the corresponding T_2 maps, although these are less dramatic. The plots corresponding to the first, Figure 5.3(c'), and second, Figure 5.3(d'), reversal of polarity illustrate clear increases in proton density near the cathode, despite the high proton density background. These changes also broadly mirror those seen in the corresponding T_2 plots.

Figures 5.4 to 5.7 illustrate a plot of (i) average *PD* and a plot of (ii) average T_2 over the sample, with no potential applied, 122 min after application of 5V d.c. continuous potential, 89 min after the polarity of the applied potential was reversed for the first time and 89 min. after the second reversal of the polarity, respectively. These figures provide a more clear comparison between the changes that occurred in the T_2 and the corresponding *PD* maps throughout the four imposed electrical regimes (regimes (a) to (d)). Figure 5.5(i) shows that 122 min. after application of the continuous potential, average *PD* becomes more uniform across the sample and that it increases near the cathode (extreme left) compared to what is seen in Figure 5.4(i) with no potential applied. Comparison between Figures 5.5(i) and 5.5(ii) also shows that average *PD* increases exactly where an increase in average T_2 is

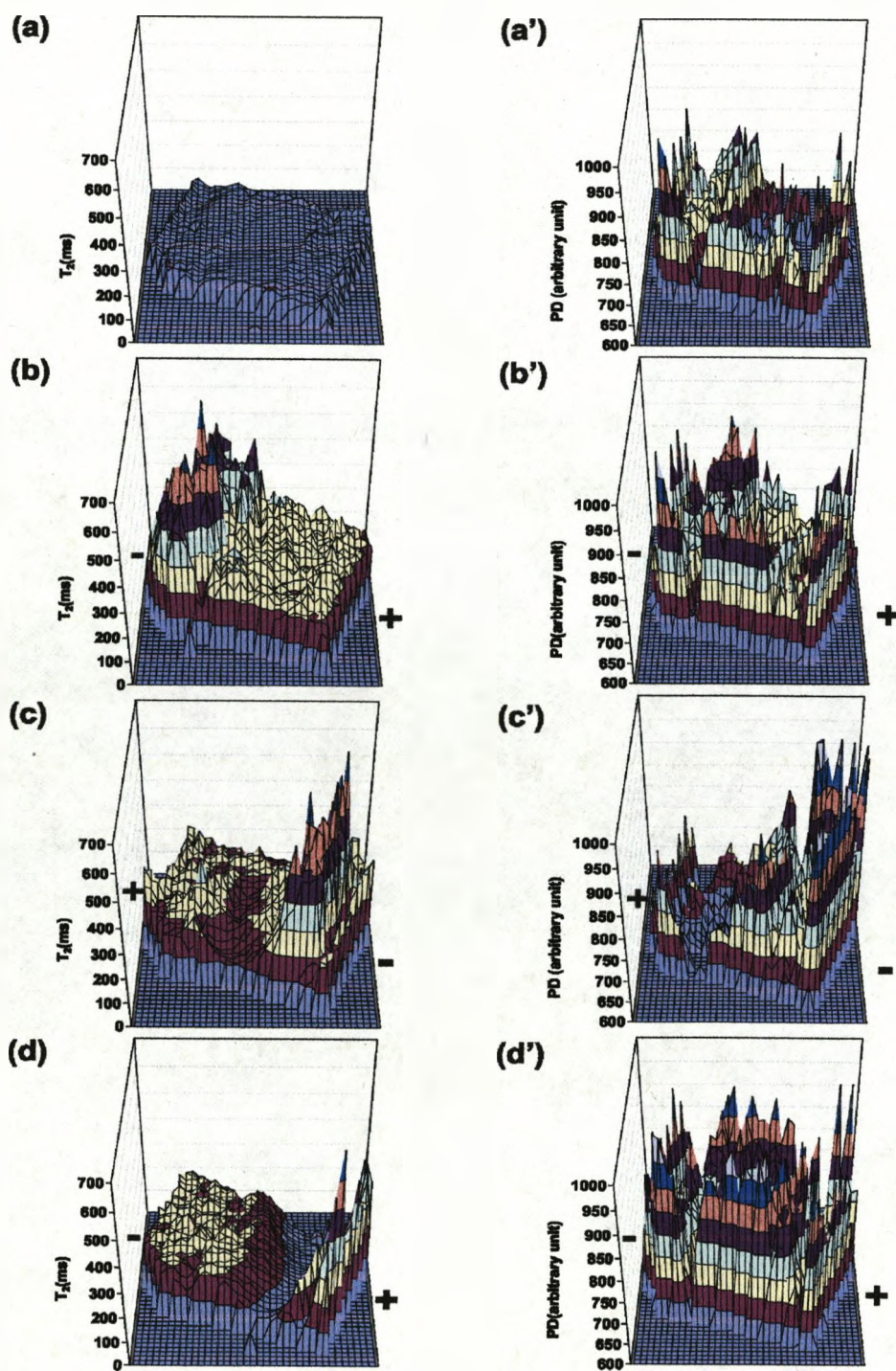


Figure 5.3. Three-dimensional plots of T_2 , T_2 maps, (left) and proton density, PD maps, (right, primed) across the whole Nafion sample: (a, a') with no potential applied. (b, b') 122 min after application of 5V d.c potential; (c, c') 89 min after first reversal of the 5V d.c potential; (d, d') 89 min after second reversal of the polarity of 5V d.c potential. The positions of the anode (+) and cathode (-) are indicated in each case.

observed. Figure 5.6 and 5.7 present very similar scenarios 89 min. after the first and 89 min. after the second reversal of the polarity of the applied potential, respectively.

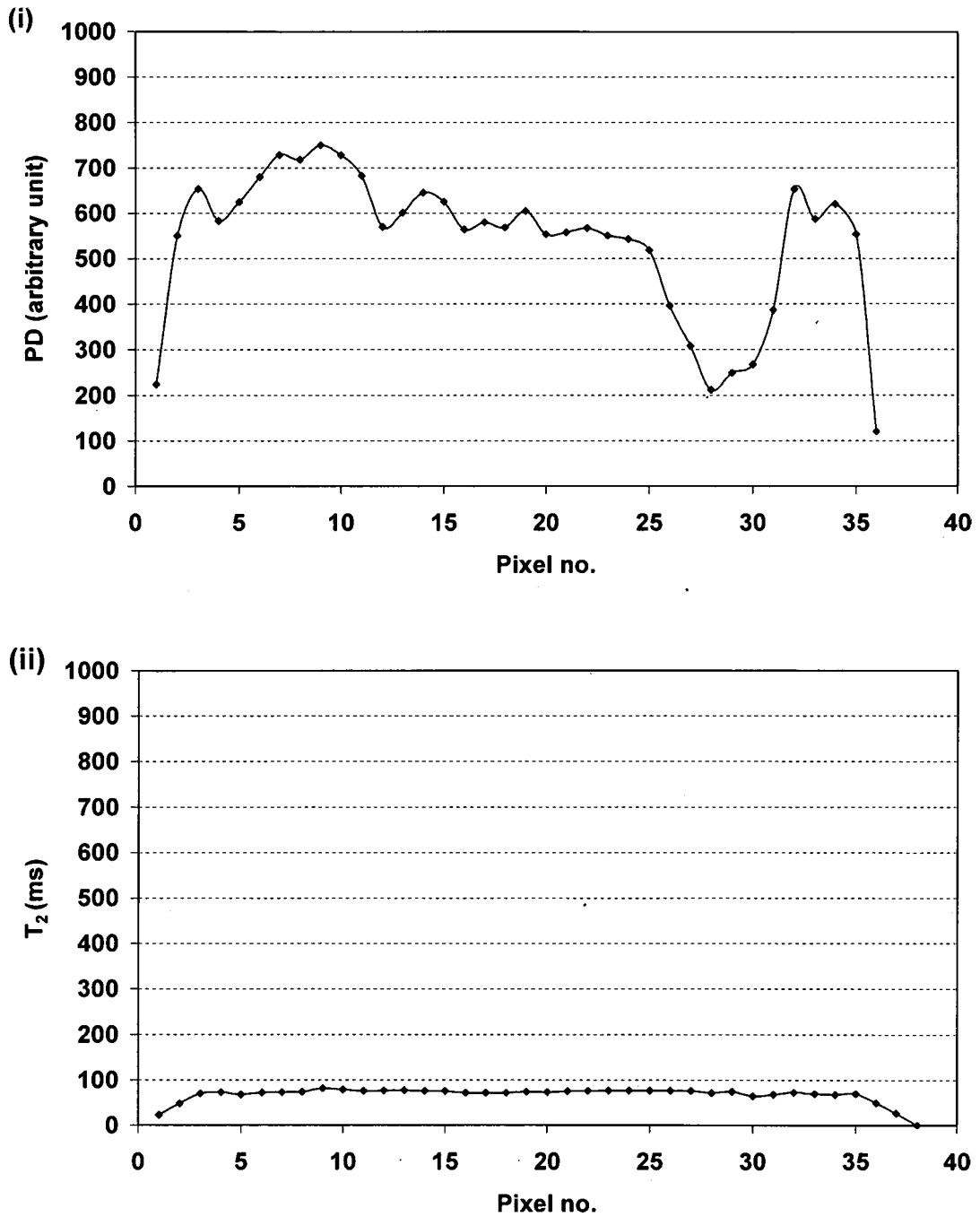


Figure 5.4. Plots of average values of (i) proton density, PD , and (ii) spin-spin relaxation time, T_2 , over the whole sample with no potential applied (regime (a)).

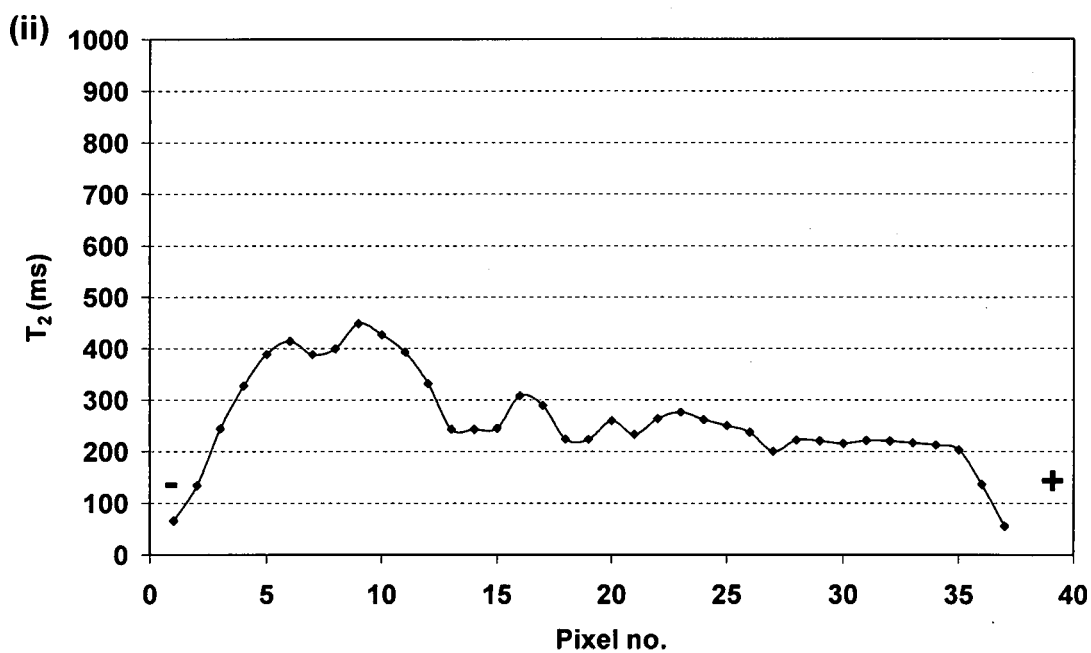
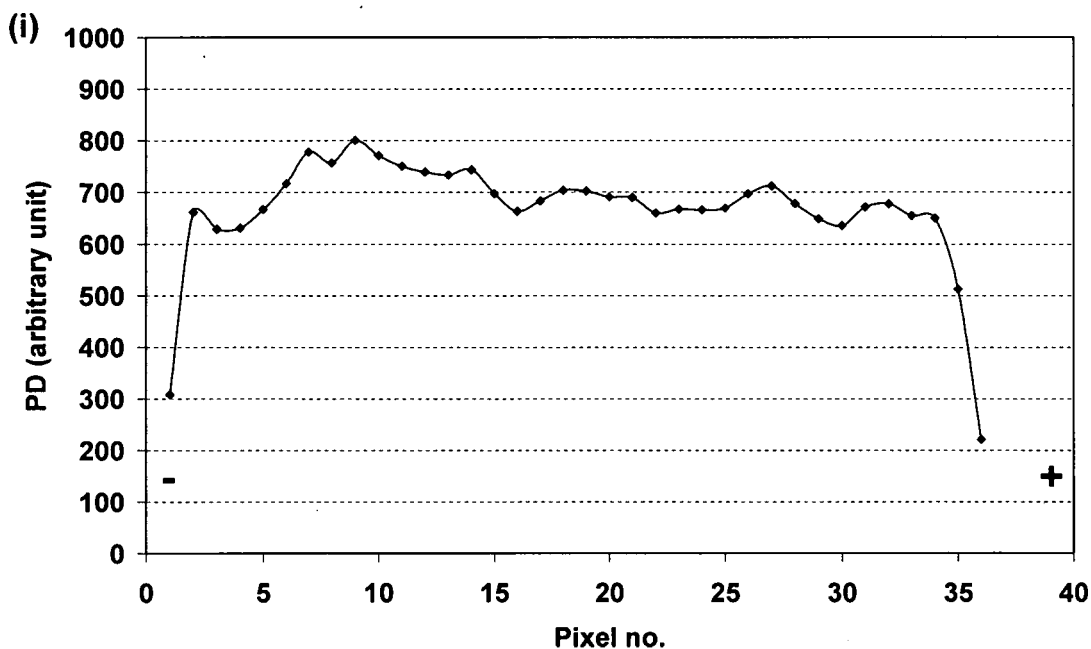


Figure 5.5. Plots of average values of (i) proton density, PD , and (ii) spin-spin relaxation time, T_2 , over the whole sample, 122 min. after application of 5V d.c. potential (regime (b)). The positions of the anode (+) and cathode (-) are indicated in each case.

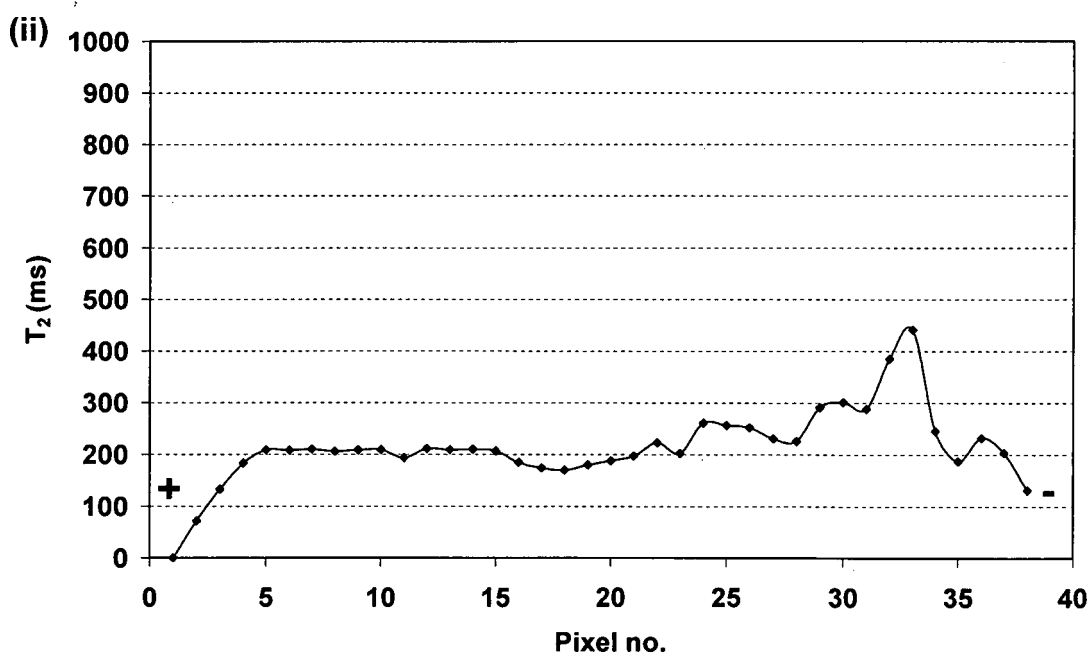
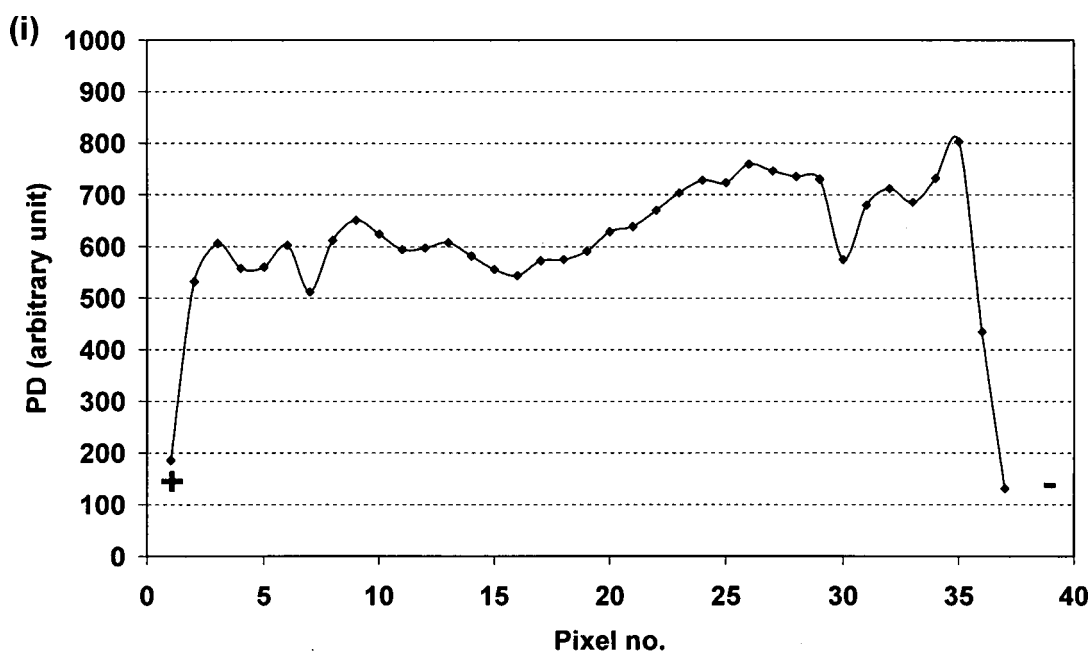


Figure 5.6. Plots of average values of (i) proton density, PD , and (ii) spin-spin relaxation time, T_2 , over the whole sample, 89 min. after the polarity of applied potential, 5V d.c., was reversed for first time (regime (c)). The positions of the anode (+) and cathode (-) are indicated in each case.

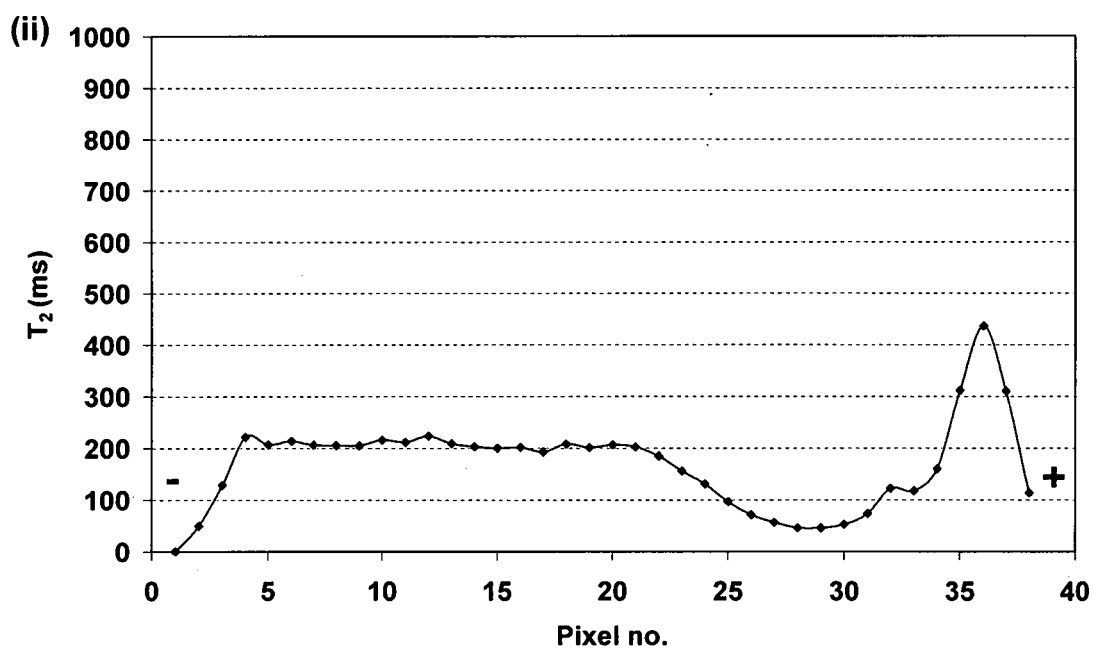
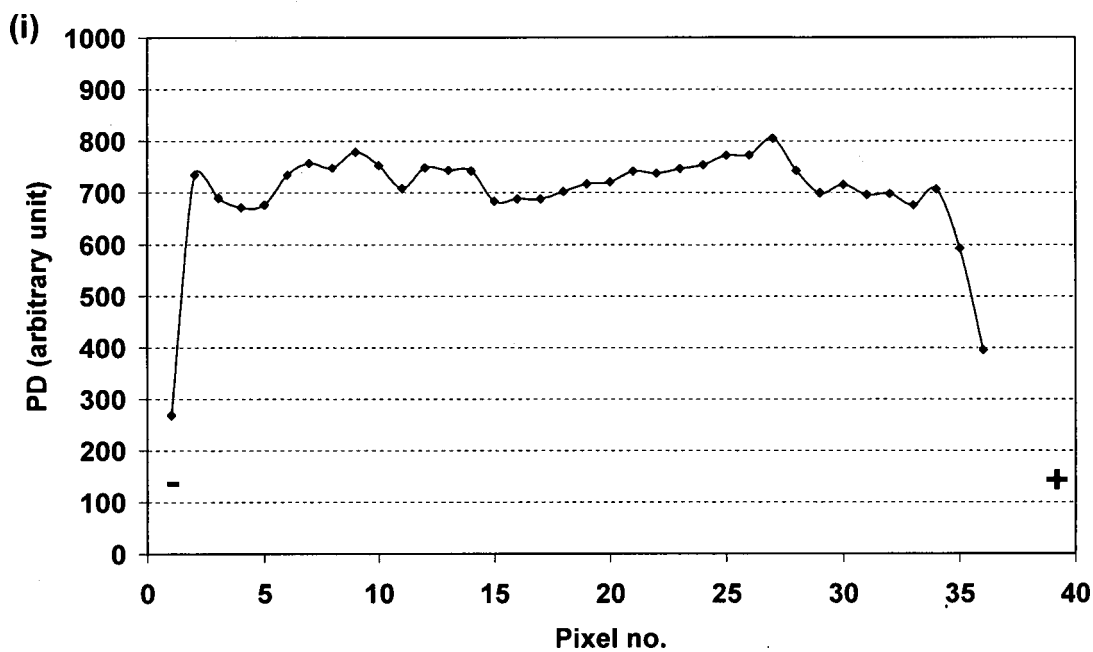


Figure 5.7. Plots of average values of (i) proton density, PD , and (ii) spin-spin relaxation time, T_2 , over the whole sample, 89 min. after the polarity of the applied potential, 5V d.c., was reversed for the second time (regime (d)). The positions of the anode (+) and cathode (-) are indicated in each case.

Values of the average apparent T_2 were extracted from the same small regions of the T_2 images in the three different potential regimes (Table 5.1) to evaluate quantitatively the changes that occurred in T_2 . In the absence of an applied potential, the average T_2 over the sample was uniform and was 40 ms. On application of the 5 V potential, the T_2 increased significantly over the whole sample and particularly near the cathode. On reversal of the polarity of the applied potential, this trend was reversed.

Table 5.1. Average T_2 values from three selected small regions of the T_2 images, on the left side, in the centre and on the right side of the sample.

T_2 (ms) at:	Left	Centre	Right
No power	40	40	40
Power on + 122 min.	364 ^c	247	218 ^a
Reversal of polarity + 89 min.	209 ^a (new anode)	219	357 ^c (new cathode)

^aactive anode; ^cactive cathode

As was seen in Figure 5.2, the evolution in the PD images over the three potential regimes is less obvious than that seen in the T_2 images. However, increases in proton density near the cathode can be recognized against a high background level. It appears that only a fraction of the water in the polymer undergoes long-range diffusion under the influence of the applied potential field and that the remainder remains largely unaffected by the application of the potential.

In order to investigate this further, the proton density map obtained before application of the potential was subtracted numerically from all subsequent proton density maps in the

same potential regime. The difference was used to estimate the percentage of water molecules that had moved after the potential was applied. In Figure 5.8, the changes in percentage of mobile water over the whole sample during the first potential regime are presented. The columns represent the percentage of mobile water in the sample after the first application of the potential. The percentage of water molecules that have moved (diffused) over large (*i.e.* measurable, on the scale of this experiment) distances was estimated to be about 10%. A large increase occurred within the first 29 min., followed by a modest increase over the rest of the experiment. This suggests a rapid initial flow of hydrated Li^+ ions, followed by much smaller subsequent increases to a continued flow over time.

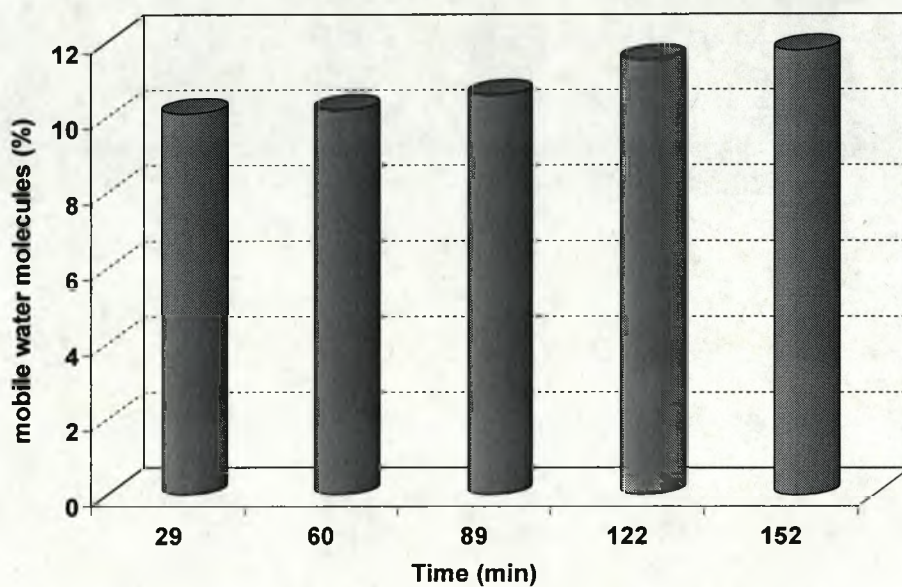


Figure 5.8. Estimation of percentage of mobile water in the Nafion membrane during regime (b).

In order to obtain a better insight into the homogeneity of T_2 and also the changes occurring in T_2 of water molecules within the sample throughout the regimes (a), (b) and (c), three-dimensional numerical plots of intensity of the corresponding T_2 images were prepared. These plots were extracted from an equivalent strip region (a 10 pixel region) across the width of each of the T_2 maps. Figure 5.9(a(i)) shows the T_2 map of the sample in regime (a), with no potential applied. As can be seen, in the absence of the applied potential, T_2 across the sample is quite homogenous and, thus, it can be said that the water molecules at all points in the sample enjoy a similar average degree of freedom to rotate. Once the potential is applied (Figure 5.9(b(i))) the homogeneous distribution of T_2 is disturbed and an increase in the intensity of T_2 is observed near the anode (positively charged side) and the cathode (negatively charged side). This indicates an increase in the rotational motion of the water molecules at these regions, which can be attributed to the electrically-induced diffusion of the hydrated Li^+ ions in these regions (see Discussion section). Figure 5.9(b), parts (ii)-(iv) show the changes in intensity of T_2 in the sample 29, 60 and 122 min., respectively, after application of the continuous 5V d.c. potential. It seems that over time a higher number of hydrated Li^+ ions are influenced by continued application of the electrical field and start their journey towards the cathode. This is observed as an increase in the intensity of T_2 over the whole sample and particularly near the cathode. As can be seen, on continuous application of the electrical field considerable changes occur in T_2 and in the concentration of high T_2 s near the cathode. However, the values of T_2 near the anode remain almost at the same level. The T_2 maps presented in Figure 5.9(c), parts (i)-(iv) illustrate the influence of the first reversal of the polarity of the applied potential on the intensity of T_2 over the whole sample. Figure 5.9(c(i)) shows that as the polarity is reversed the area of high T_2 s concentrated

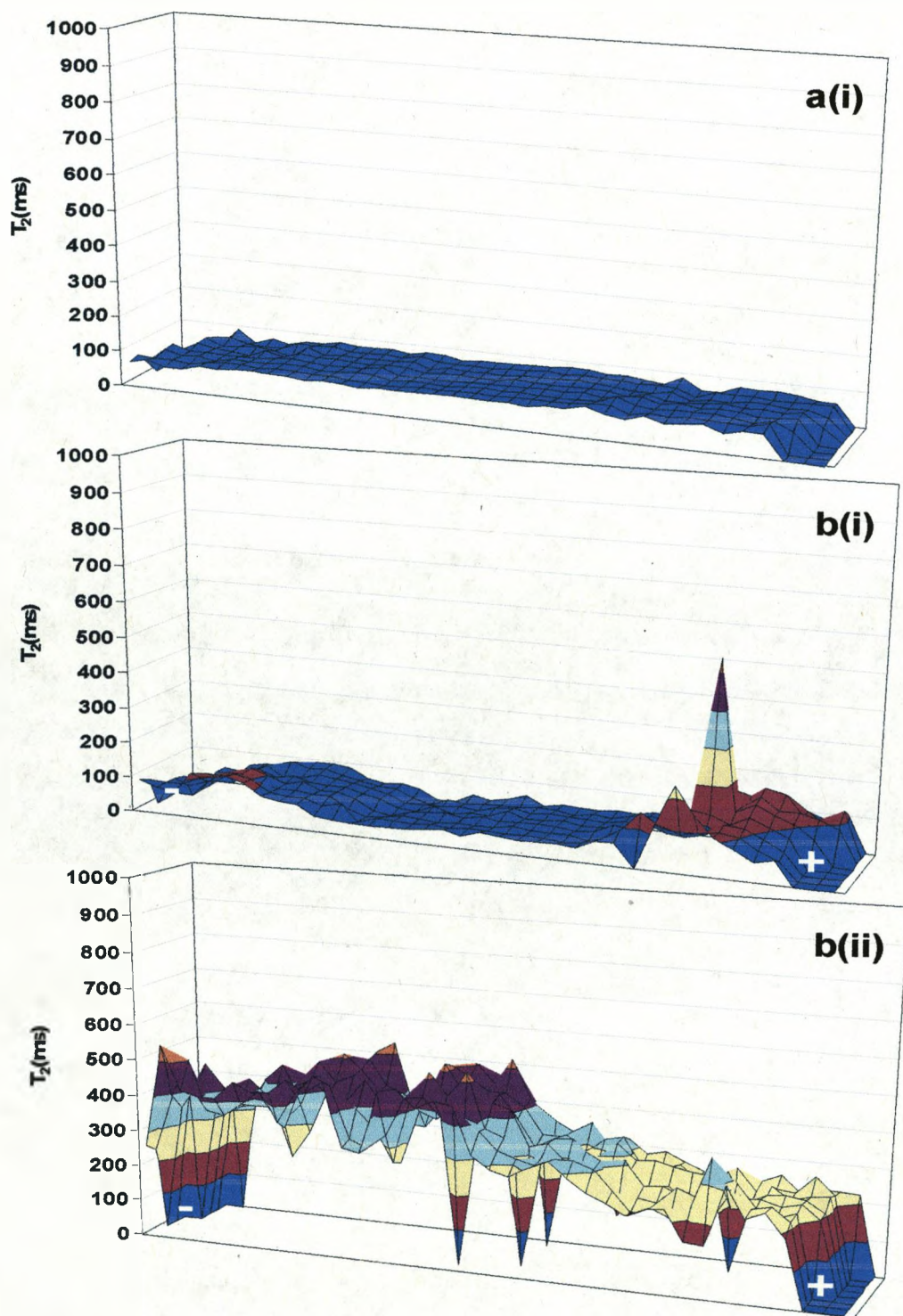


Figure 5.9. Three-dimensional plots of T_2 (T_2 map) (a(i)) with no potential applied; (b) (i) 0; (ii) 29; (iii) 60; (iv) 122 min. after application of a 5V d.c. continuous potential in the sense indicated. (c) (i) 0; (ii) 29; (iii) 60; (iv) 122 min. after first reversal of the polarity of the 5 V d.c. potential. The negative “-” and positive “+” signs in these maps show the cathode and anode side of the membrane, respectively.

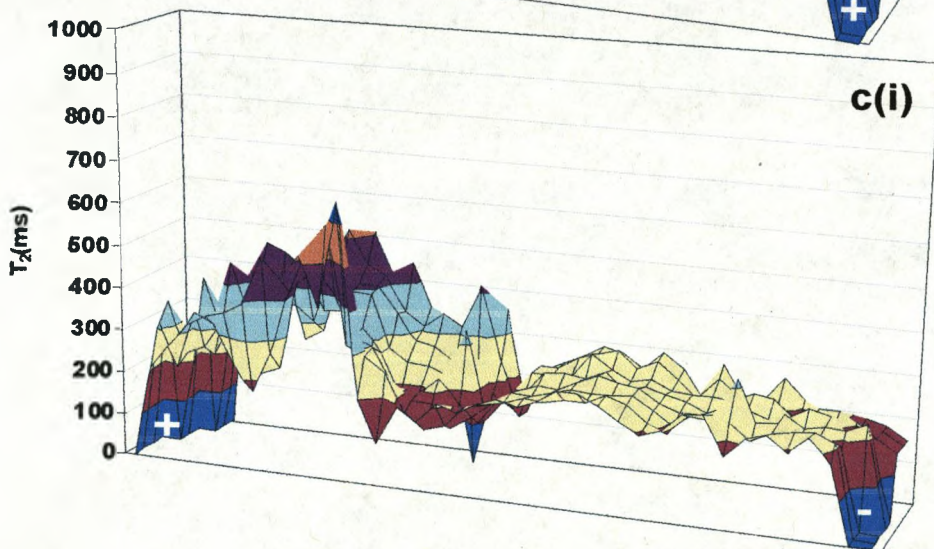
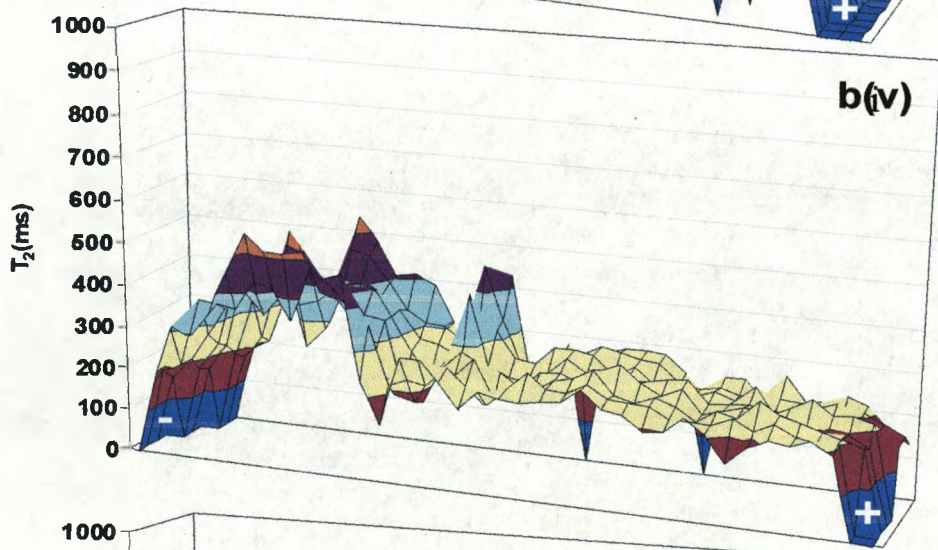
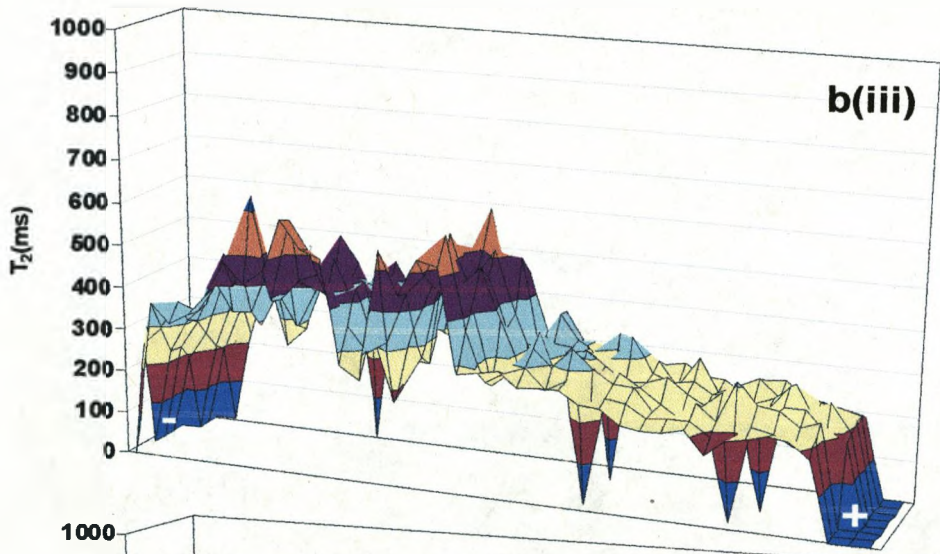


Figure 5.9. Continued.

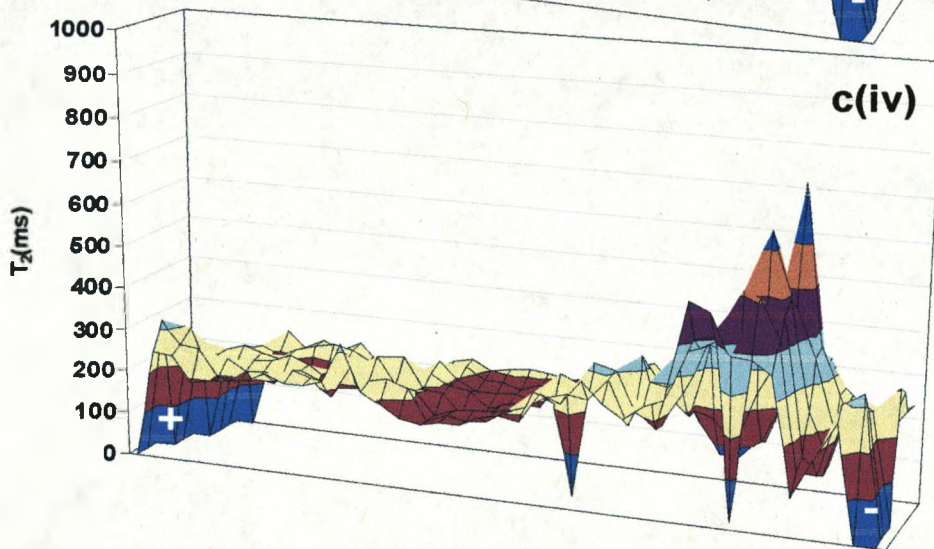
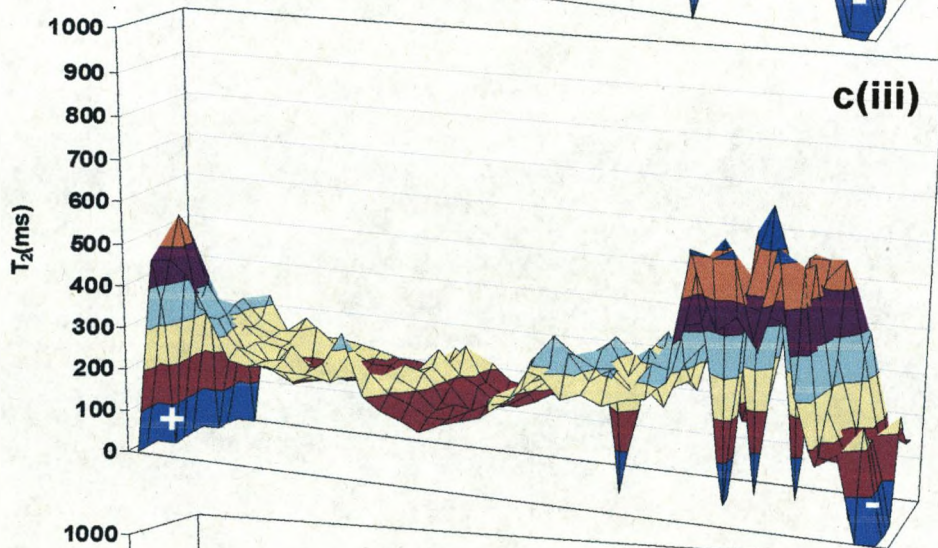
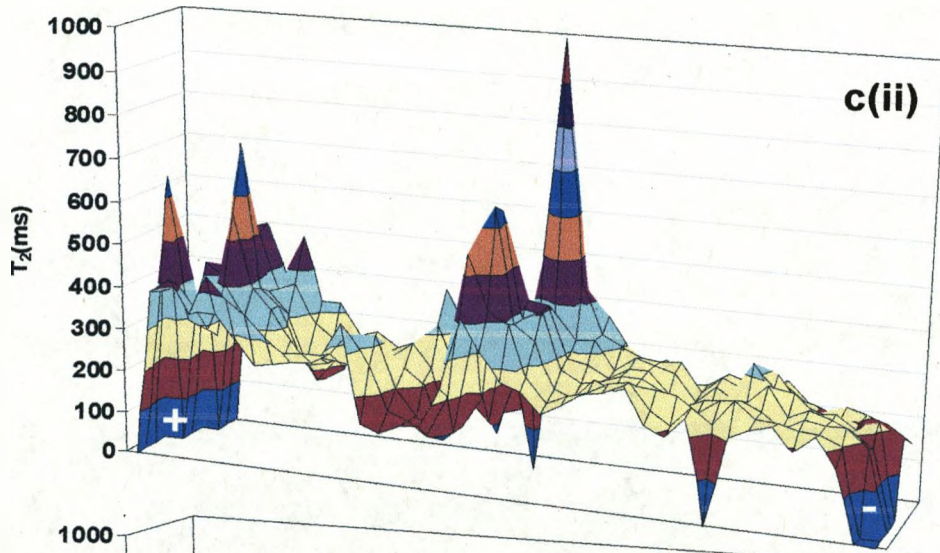


Figure 5.9. Continued.

near the new anode (previous cathode) shrinks slightly and a small increase in the values of T_2 occurs near the new cathode (previous anode). After 29 min (Figure 5.9(c(ii))) a relatively large increase in T_2 , similar to that which was seen in Figure 5.9(b(i)), is observed near the anode. A sharp peak also appears at the centre, representing the simultaneous migration of hydrated Li^+ ions, which were concentrated near the previous cathode, towards the new cathode. However, still no significant change is observed in the intensity of T_2 near the new cathode. Over time, the area of high T_2 becomes again more concentrated near the new cathode and the values of T_2 decrease significantly near the new anode, Figure 5.9(c(iv)).

5.4. Discussion

In the following sections the effects of the four imposed electrical regimes ((a) to (d)) on the variation of T_2 and PD over the commercial Nafion sample are separately discussed.

Regime (a): No Potential Applied

The T_2 image of the Nafion sample with no potential applied revealed that the water molecules within this sample possess very similar and short T_2 values of about 40 ms. This is much smaller than the T_2 values observed for bulk deionized water (450 ms)* and even saturated solution of LiOH (390 ms)*. As mentioned earlier, this shows that the rotational

* These T_2 values were obtained on MRI scanner by simultaneous spin echo imaging of an equal amount (2 ml) of deionised water and saturated solution of LiOH (in two separate 5 mm o.d. NMR tubes).

motion of water molecules within this sample is restricted since T_2 is strongly dependent upon the mobility of the molecules.¹ According to an early model proposed by Gierke^{3,4} and a recent study conducted by Heitner-Wirguin,⁵ the chemical structure of Nafion contains two different regions; hydrophobic and hydrophilic. The aggregation of the perfluorinated molecular backbone forms a semi-crystalline matrix in the polymer which is highly hydrophobic, and the aggregation of the ionic groups, as a result of electrostatic interactions, forms extremely hydrophilic regions in the polymer, known as clusters. Cluster diameters were estimated to be about 3-6 nm, depending on the water content of the polymer, to contain up to 100 ion pairs with up to 20 water molecules associated with each site and to occur at a periodicity of 6-8 nm.⁴

The observed short T_2 of water molecules within the Nafion membrane can therefore be attributed to the confinement of most or all of these molecules to the hydrophilic regions of the polymer, where their rotational motion is restricted by the strong electrostatic interactions with the ionic groups and also with the other water molecules, through hydrogen bonding.

Regime (b): Application of a Continuous 5V d.c. Potential

Immediately after the application of the continuous 5V d.c. potential, the values of T_2 over the whole sample and particularly in the area near the charged sides (cathode and anode) increased, as was observed in Figures 5.2(b(i)) and 5.9(b(i)).

The general increase in T_2 over the whole sample implies that application of the potential causes hydrated Li^+ ions to begin to move through the polymer in the direction of the

applied field. To do this, they must move between hydrophilic regions (the clusters) and so spend some time in more hydrophobic environments. Since these hydrophobic regions are made up of the perfluorinated molecular backbone of the polymer, this is expected to interact much less strongly with the water molecules. This causes much less restriction of the molecular rotation of the water molecules in these regions and so gives rise to longer T_2 over the whole sample.²

The particular increases in T_2 near both electrodes immediately after application of the potential may be explained according to the model proposed by Nemat-Nasser and Li.⁶ According to this model, as the electrical field is applied, the hydrated Li^+ ions present in the hydrophilic regions experience an electrostatic repulsive force from the anode and an attractive electrostatic force from the cathode. This leads to migration of these cations towards the cathode. The influence of these forces, however, seems to be initially much stronger at the charged sides of the membrane since the largest initial changes in T_2 occurred in these region (Figure 5.9(b(i))). It seems that, at the anode, as the electrical field is applied, the electrostatic repulsive force between the hydrated Li^+ ions within the hydrophilic regions and the positively charged surface causes the forced diffusion of hydrated Li^+ ions via the more hydrophobic region of the polymer. The presence of the hydrated Li^+ ions in the more hydrophobic region of the polymer give rise to a long T_2 observed near the anode. At the cathode, however, the negative surface charge attracts excess concentration of hydrated Li^+ ions from the neighbouring hydrophilic regions. As described above, this causes the forced diffusion of hydrated Li^+ ions out of the neighbouring hydrophilic regions through the more hydrophobic region of the polymer, and so gives rise to a long T_2 relaxation at the cathode also.

Over time, (Figure 5.9(b), parts (ii)-(iv)) it was observed that the values of T_2 continued to increase over the whole sample and that the region of high T_2 s became further concentrated near the cathode. Since these changes were accompanied by similar and simultaneous changes occurring in the corresponding *PD* maps, it can be said that over time a larger number of hydrated Li^+ ions are influenced by the continued application of the electrical field (see also Figure 5.8) and inevitably diffuse towards the cathode by jumping between neighbouring hydrophilic regions, and passing through the more hydrophobic regions as they went. Again, significant amounts of water molecules would be expected to exist in the more hydrophobic regions of the Nafion sample, between the hydrophilic regions, which would cause an overall increase in T_2 over the whole sample.

The increasing values of T_2 , over time, near the cathode can be explained in three ways. All of these are consequences of the increase in water content near the cathode by electro-induced diffusion of the hydrated Li^+ ions. Indeed, this phenomenon is observed directly in the *PD* maps.

Firstly, by definition, there is an accumulation of the more mobile hydrated Li^+ ions near the cathode (and less near the anode). As discussed, these pass through the hydrophobic regions of the materials and so contribute to higher time-averaged T_2 s.

Secondly, as a consequence of the forced increase in water content near the cathode, water will increasingly be accommodated in less and less ionic (or hydrophilic) regions. That is, as fewer of the more energetically favourable ionic sites are available, the water will begin to occupy less favourable, less ionic regions. Since the value of T_2 is related to the hydrophobic nature of the local chemical environment, this will lead to an increase in T_2 , as is seen.

Thirdly, as more water enters the area near the cathode, the hydrophilic regions would be expected to increase in size in general. As they expanded, one might expect more interaction between the water within the hydrophilic region and the surrounding polymer chains as well as less interaction between the water molecules and the ions within the hydrophilic region. Both these effects may also result in an increase in T_2 .

It is interesting that, during the continuous application of the potential, T_2 near the anode remains above the level measured before the potential was applied. This implies that some of the hydrated Li^+ ions are still moving between hydrophilic regions via the hydrophobic regions near the anode. Some may also become physically trapped in the more hydrophobic regions of the polymer.

Another possible explanation based on the Nemat-Nasser and Li model⁶ suggests that the migration of hydrated Li^+ ions out of the hydrophilic regions, at the anode, leads to a decrease in the size of the hydrophilic regions and an increase in the repulsive electrostatic forces among the anionic groups ($-\text{SO}_3^-$) within these regions. To overcome these forces, water molecules from neighbouring hydrophilic regions are absorbed. This movement of water molecules between hydrophilic regions may also explain the level of T_2 near the anode.

Regime (c): Application of a Continuous 5V d.c. Potential of Reversed Polarity

As was seen in Figure 5.9(c(i)), as the polarity of the applied potential was reversed the area of high T_2 s concentrated near the new anode (previous cathode) shrank slightly and a

small increase in T_2 occurred near the new cathode (previous anode). The migration of a significant number of hydrated Li^+ ions from the new cathode region (previous anode region) during imposition of the previous electrical regime, (b), is thought to be the reason for the observation of insignificant increases in the intensity of T_2 near the new cathode. In other words, since the hydrophilic regions near the new cathode have become depleted of Li^+ ions and water molecules throughout regime (b) the change in the polarity of the applied potential can not affect this region significantly, even after 29 min. (Figure 5.9(c(ii))). However, over time, the region of high T_2 s became concentrated again near the new cathode and the values of T_2 decreased significantly near the new anode (Figure 5.9(c(iv))), as the hydrated Li^+ ions moved back to the new cathode region.

Regime (d): Application of a Continuous 5V d.c. Potential after a Second Reversal of Polarity

The changes that occurred in the T_2 and PD of the sample after the second reversal of the polarity were less dramatic. This might be explained by the forced evaporation of a part of the water molecules, which exist in the solvation shell of hydrated Li^+ ions, from the sample by the applied electrical field. As was mentioned before, on application of the potential the hydrated Li^+ ions are concentrated near the cathode, where the metal contact possesses negative charges. Thus, it would be expected that evaporation of water molecules from the surface of the polymer would be accelerated.

Attempts to investigate the chemical structure of the Nafion membrane and also to explain the water diffusion through this polymer have yielded several models. These models were described in Section 1.2.2.1. To explain diffusion of water through Nafion membrane, pores⁴ and channels⁷ between clusters were suggested. In a recent study, Meresi et al.⁸ have proposed a modified structural model for the water-swollen unexchanged Nafion consisting of two domains: a minor hydrophilic domain and a major hydrophobic domain. They suggested that the water diffusion through the Nafion membrane occurs through the minor and continuous hydrophilic domain consisting of water, ionic sulfonate groups and the pendant side-chains to which they are attached, and that the water is not able to diffuse through the major domain containing the perfluorinated polymer backbone. From our results we propose a more disordered model than that of Gierke et al.⁴ and Meresi et al.⁸ in which highly hydrophilic regions exist within a highly hydrophobic major domain but which are connected to each other by regions of a range of thickness and a range of intermediate hydrophilicities.⁹ In this model, self-diffusion of water in the absence of an applied potential would be expected to take place via low activation energy routes through hydrophilic regions of the polymer. On application of the continuous potential, however, forced diffusion of hydrated Li^+ ions is expected to occur through higher activation energy routes. In other words, the hydrated Li^+ ions move towards the cathode by jumping consecutively from one to another cluster while passing through the more hydrophobic regions of the polymer. Therefore, more water molecules would be present for longer in the less hydrophilic regions of the polymer. This would result in a decrease in the efficiency of T_2 processes and explain the observed increase in T_2 values. The results presented above are unlikely to be explained only by the changes in T_2 values of protons within the highly ionic

regions alone since there is evidence that the T_2 values in this environment are short and uniform due to rapid exchange with a small fraction of protons on the sulfonate ($-\text{SO}_3^-$) groups.⁹ Figure 5.8 showed that only 10% of water molecules had moved toward the cathode. Thus, it can be said that the majority of water molecules stay in the highly hydrophilic regions of the polymer (remain unaffected by the application of the potential) and contribute to the high background intensity observed in the *PD* maps.

5.5. Summary

The electrically-induced distribution of water molecules in the Nafion membrane was investigated by placing a functioning electrochemical cell inside the MRI scanner and imaging the water distribution in real time during application of a continuous potential. The results were presented as two dimensional images and three-dimensional plots (maps) of proton density, *PD*, and spin-spin relaxation time, T_2 . The changes in these images and maps over time and with respect to changes made to the applied potential were followed. Short and uniform T_2 values were obtained for the water molecules in the Nafion membrane in the absence of the potential. This revealed that most or all of the water molecules are confined to the hydrophilic regions, the clusters, of the polymer, and that in these regions their rotational motion was restricted by the strong electrostatic interactions with the ionic groups and also other water molecules. On the application of a continuous 5 V d.c. potential a noticeable increase in T_2 over the whole sample and particularly near the cathode occurred. From the *PD* maps it was deduced that hydrated Li^+ ions diffused towards the cathode under the influence of the potential gradient. The direction of this diffusion was

reversed by reversal of the potential. Longest T_2 relaxation times were observed in the region of the cathode and the shortest near the anode, representing an inverse correlation between the mobility of water molecules and the strength of their interactions with the surroundings. The application of the potential caused measurable displacement of approximately 10% of all water in the sample, within the timescale of the experiment. The majority of water molecules, however, appear to be unable to move large distances, perhaps because they are not associated with cations or because they are associated with cations which are trapped in the ionic regions or locked in local boundaries in the structure of the polymer.

5.6. References

-
- [1]. W. Kuhn, *Angewandte Chemie, Int. Ed. Engl.* 1990, 29, 1.
 - [2]. P. T. Callaghan, "Principles of Nuclear Magnetic Resonance Microscopy", *Clarendon Press . Oxford*, New York, 1991.
 - [3]. T. D. Gierke, *The electrochemical Society Extended Abstracts*, 1977, 77(2), 438, 1139.
 - [4]. T. D. Gierke, W. Y. Hsu, Eds A. Eisenberg, H. L. Yeager, *Am. Chem. Soc. Symp. Ser.*, 1982, 180, ch. 13.
 - [5]. C. Heinter-Wirguin, *J. Membr. Sci.*, 1996, 120(1), 1.
 - [6]. S. Nemat-Nasser, J. Y. Li , *J. Applied Physics*, 2000, 87(7), 3321.
 - [7]. H. J. Yeager, A. Eisenberg, *American Chem. Soc.*, 1982, 180(1), 41.
 - [8]. G. Meresi, Y. Wang, A. Bandis, P. T. Inglefield, A. A. Jones, W. Y. Wen, *Polymer*, 2001, 42, 6153.
 - [9]. R. T. Baker, L. Naji, J. A. Chudek, K. Lochhead, *Chem. Commun.*, 2003, 962.

Chapter Six

MRI Study of IPMCs

6.1. Introduction

As the results presented in the previous chapter confirmed, multi-echo MRI imaging, based on the CPMG pulse sequence, can be employed as a powerful, non-destructive and non-invasive technique to probe the interaction of water molecules with their immediate surroundings to follow the changes occurring in Nafion membrane. In the work presented in this Chapter, this technique was exploited once more to obtain T_2 (spin-spin relaxation time) and PD (proton density) images of an IPMC sample during application of a continuous potential across its thickness. As mentioned earlier, the bending response of an IPMC is observed when an electrical potential gradient is applied across its thickness and hydrated cations start to migrate towards the negatively charged face (cathode) of the polymer. Thus, it is required to image electrically-induced diffusion of water molecules through the thickness of the Nafion membrane to learn more about the process involved. The small thickness of commercial Nafion-based IPMC samples (~ 0.2 mm) prevents clear observation of the changes occur in T_2 and PD images of the sample once a continuous potential is applied, because of the limited spatial resolution of the MRI technique. Thus, a cast Nafion-based IPMC sample with approximate thickness of 2 mm was used for this experiment. The AuPt₁Cast sample was chosen since it contained the least amount of platinum required to observe the bending deformation in an IPMC sample. Samples with a higher number of plating cycles possessed lower resistance and also higher surface conductivity which can lead to faster and larger bending deformation of the sample under influence of the applied electric field (see Chapter Eight). This may therefore occur too quickly to allow the phenomenon to be recorded in the MRI images. AuPt₁Cast was also preferred to the Pt₁Cast sample since experiments with Pt₁Cast showed little measurable

change in T_2 and PD images, possibly due to its lower surface conductivity.^{1,2} The presence of deposited gold particles at the surfaces of AuPt₁Cast increases the surface conductivity,^{1,2} and so improves the actuation performance of this sample (see also Chapters Four and Eight).¹

6.2. Experimental

8×8 mm square samples of AuPt₁Cast with a thickness of ~2 mm were prepared and soaked in a saturated solution of LiOH at room temperature for a month before experiment (to exchange all the protons on the sulfonate group of Nafion membrane for Li⁺ ions). To enable a suitable potential to be applied to the samples once they were inside the MRI scanner a sample holder was designed (Figure 6.1) so that electrical contact could be made to each electroded face of the AuPt₁Cast square sample. This sample holder consisted of two gold-coated glass plates which were completely covered with aluminium foil at their outer surfaces and made contact with the gold coating at opposite edges at their inner surfaces. Silver paint was applied to attach the foil cover to these plates. The square AuPt₁Cast sample was washed with DI water to remove the residual of LiOH a few minutes before the experiment, and was carefully placed in the sample holder. To ensure the electrical current would pass totally through the thickness of the AuPt₁Cast square sample rather than its length, any contact with the aluminium foil cover at the edges of the sample was avoided. Wires were attached to the foil and the assembly was placed into an adapted 25 mm o.d. quartz NMR tube, which had two holes at the bottom to allow the wires to pass through. As described in Section 5.2, the holes were sealed with quick-drying epoxy resin

adhesive and a constant saturated water vapour pressure was maintained inside the tube by enclosing a water-soaked paper plug within it and using a gas-tight cap.

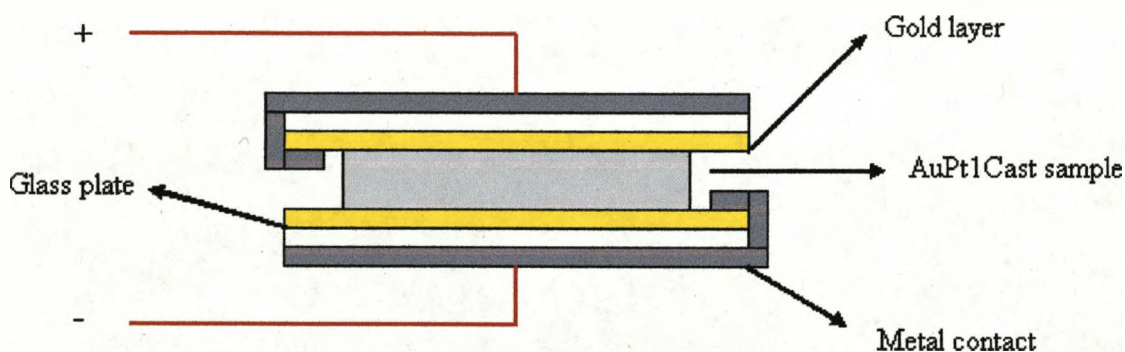


Figure 6.1. Electrochemical assembly used in the *in situ* MRI studies.

After inserting the NMR tube into the resonator probe of the Bruker MRI scanner, wires from the sample holder were connected to a variable 0-10 V d.c. power supply. The multi-echo pulse sequence, MSME from the Bruker Paravision[®] library, with a train of 64 echos, echo time, T_E , of 5 ms and repetition time, T_R , of 5 s was used and MRI images of the sample were collected. A long T_R was applied to reduce the effect of T_1 . Four electrical regimes, similar to those described in Chapter Five, were applied on a single sample in sequence to study the electrically-induced diffusion of water molecules within the AuPt₁Cast sample. These regimes were: (a) no potential applied; (b) application of a continuous 3V d.c. potential; (c) application of a continuous 3V d.c. potential of reversed polarity and (d) application of a continuous 3V d.c. potential after a second reversal of

polarity. T_2 and PD images and maps were extracted, as described in Section 3.7.2.3, from MRI images recorded during these four electrical regimes. The field of view in the images was 20×20 mm, the slice thickness was 1.0 mm, and the acquisition time for each dataset with matrix size of 128×128 pixels was approximately 21 min. This experimental sequence was repeated several times with similar samples and gave rise to qualitatively similar behaviour.

6.3. Results and Analysis

As was mentioned in previous Chapters, the Li^+ -exchanged Nafion membrane contains no protons itself, thus the PD and T_2 images of the AuPt_1Cast samples can be considered to relate uniquely to the protons present in the water molecules absorbed in the sample.

Figure 6.2, parts (a) and (a') present respectively T_2 and PD images extracted from the MRI image of AuPt_1Cast (Li^+ -exchanged) with no potential applied. As can be seen, the T_2 and PD images are quite bright, representing a relatively long T_2 and high concentration of protons in the sample, respectively. Since the intensity of a PD image is proportional to the concentration of protons present in the sample,³ the uniform intensity in the PD image with no potential applied (Figure 6.2(a'(i))) implies that PD was relatively constant over the whole sample. Figure 6.2(a(i)) shows the corresponding T_2 image of the sample with no potential applied. As can be seen, despite the uniform distribution of protons over the whole sample, water molecules absorbed at the centre of the sample have longer T_2 s than those present close to the faces of the sample. This is observed as a bright horizontal region at the centre and darker regions near both surfaces (top and bottom, in the images). In this image,

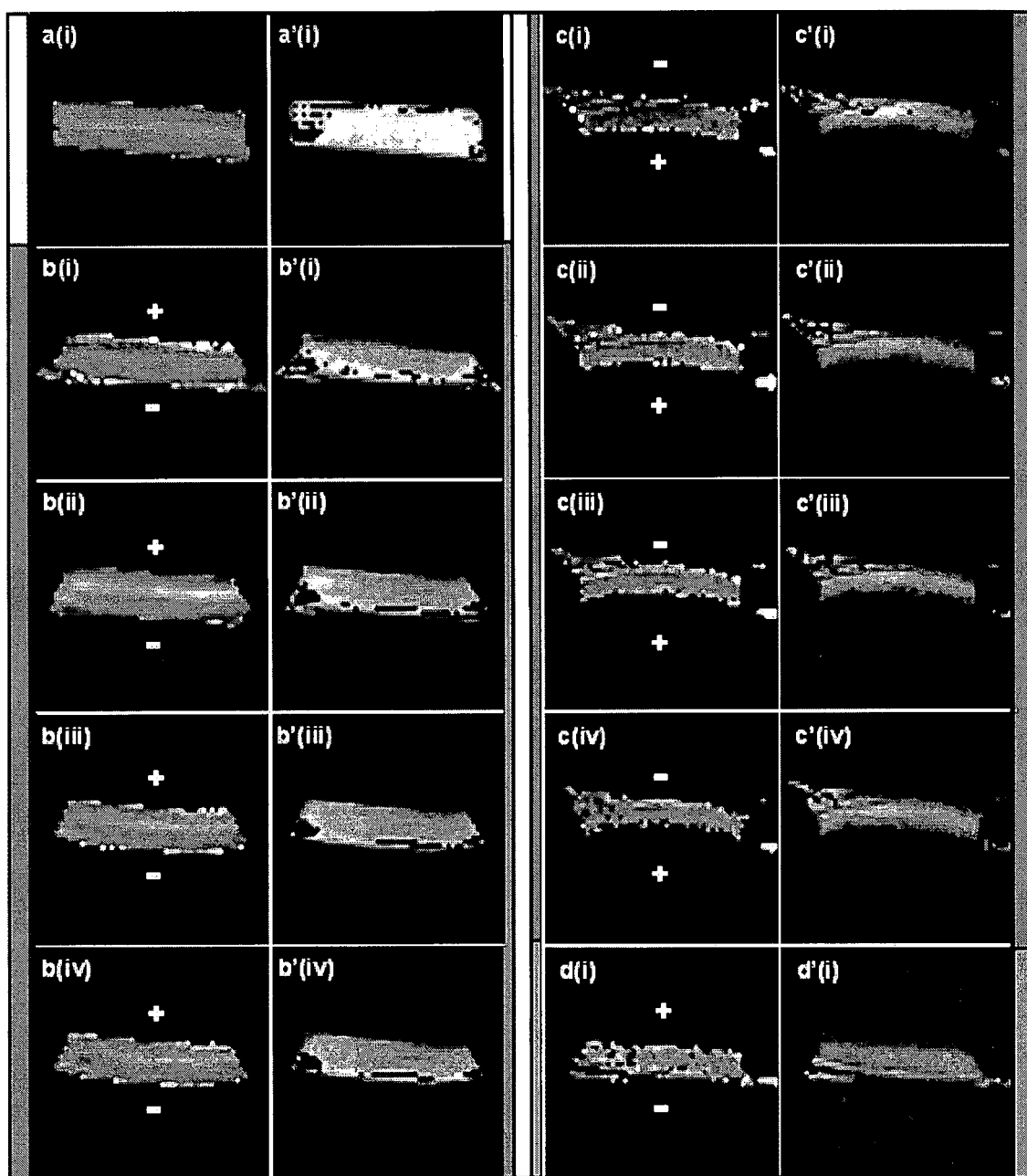


Figure 6.2. T_2 (left images) and PD (right images, primed labels) images of the $AuPt_1/Cast$ IPMC sample (a, a') with no potential applied; (b, b') (i) 0; (ii) 29; (iii) 60 and (iv) 89 min. after application of a 3V d.c. continuous potential in the sense indicated. (c, c') (i) 0; (ii) 29; (iii) 60 and (iv) 89 min. after first reversal of the polarity of the 3V d.c. potential; (d, d') (i) 0 min. after the second reversal of the polarity of the 3V d.c. potential. The negative “-” and positive “+” signs in these images show the cathode and anode side of the sample, respectively.

it can also be seen that the platinum electroded regions appear to become darker towards the outer surfaces of the sample, representing a gradual decrease in T_2 towards the sample surfaces. Since T_2 is highly motion dependent³ this reveals a difference in physical environment of the water molecules absorbed in this sample.

As the potential is applied across the thickness of the AuPt₁Cast sample, it contracts along the anode (positively charged side) and expands along the cathode (negatively charged side). Figure 6.2(b), parts (ii)-(iv) show the changes in T_2 in the sample 29, 60 and 122 min., respectively, after application of the continuous 3V d.c. potential. These images show that, over time, T_2 increases over the whole sample and that the region of high T_2 s becomes more concentrated near the cathode. These changes are also associated with the increasing bending deformation of the sample towards the anode. Since the AuPt₁Cast sample initially has longer T_2 at the centre than near to the electroded surfaces, on application of the potential the difference between long T_2 s, corresponding to mobile water molecules, and short T_2 s, corresponding to unaffected water molecules, is less clear. The simultaneous bending deformation of the sample may be another reason for the inability to observe clear changes in T_2 . Nevertheless, increases in the concentration of high T_2 s near the cathode can still be recognized against the high T_2 of water molecules at the centre. Figure 6.2(b'), parts (i)-(iv) show that the changes occurring in the T_2 images of the sample during this regime are associated with similar changes in the intensity of the accompanying *PD* images; higher proton density is seen near the cathode. This gives evidence that the high T_2 s observed near the cathode in the T_2 images are related to the accumulation of mobile water in this region during application of the continuous potential.

Figure 6.2(c, c'), parts (i)-(iv) show the changes in T_2 and PD distribution in the AuPt₁Cast sample 0, 29, 60 and 89 min., respectively, after the polarity of the applied continuous potential is reversed. These images show that by reversing the polarity of the applied potential the direction of the bending deformation of the sample and the distribution of high T_2 s – related to protons in mobile water – is reversed and T_2 near the new cathode increases over time. However, the changes in these T_2 images are less dramatic than those seen in regime (b). This is due to dehydration of the AuPt₁Cast (IPMC) sample during the application of the potential, as the lower intensity of the corresponding PD images suggests. Nevertheless, the region of high T_2 s is seen to become more localised near the new cathode at the upper surface of the sample. The localization of a high concentration of mobile water molecules near the new cathode, over time, can also be deduced by reference to the corresponding PD images.

The T_2 and PD images presented in Figure 6.2(d, d') show the effect of the second reversal of the polarity of the applied continuous potential. The area of high T_2 s again becomes concentrated near the new cathode and the AuPt₁Cast sample bends towards the new anode. It must be mentioned that 30 min after the second reversal of the polarity, the signal obtained from the sample was dramatically weakened, so very poor images were obtained from that point onwards.

In order to obtain a better understanding of the actuation mechanism of the IPMC sample and to acquire numerical data about the changes occurred in T_2 relaxation and to analyze the T_2 values as a function of location within AuPt₁Cast, three-dimensional PD and T_2 maps were prepared for the whole sample during regimes (a), (b), (c) and (d). These maps are shown in Figure 6.3 (see also Appendix 3). The negative and positive signs in these maps

indicate the cathode and anode side of the IPMC sample, respectively. In Figure 6.3 – parts (a)-(d) one can see that the intensity of the *PD* maps undergoes clear changes following the electrical regimes imposed on the sample; *i.e.* the higher concentration of protons is always observed near the cathode and the lower concentration near the anode. Comparison of these maps, from left to right, also confirms that the sample is dehydrating during this extended experiment since their total intensity, which is proportional to the proton concentration, decreases. As can be seen in Figure 6.3 – parts (a')-(d'), unlike in the *PD* maps, the changes in the corresponding T_2 maps are not very clear, due to the initial variation of T_2 over the AuPt₁Cast sample (Figure 6.3(a')). As soon as the potential is applied, the distribution of T_2 values is disturbed; T_2 decreases to some extent at the centre of the sample and sharp peaks appear at the cathode and the anode (Figure 6.3(b'(i))). As the subsequent *PD* and T_2 images (Figure 6.3(b'), parts (ii) and (iii)) reveal, on continuous application of the potential, the bending deformation of the sample towards the anode also increases. As Figure 6.3(b'(iii)) and (b'(iii)) show after 89 min. the larger bending deformation of the sample is associated with simultaneous slight increases of T_2 and *PD* near the anode and decreases of those near the cathode. As the polarity of the applied potential is reversed, sharp peaks, similar to those seen in Figure 6.3(b'(i)), appear at the new cathode and anode (Figure 6.3(c'(i))) and the sample expands along the new cathode and shrinks along the new anode. Over time, T_2 becomes higher near the new cathode and the sample bends more towards the new anode. As in regime (b), 89 min. after the first reversal of the polarity of the potential, *PD* and T_2 again decrease near the cathode and increase near the anode (Figure 6.3(c'(iii)) and (c'(iii))). These changes, however, are less marked, than those observed in regime (b). The second reversal of the polarity of the applied potential gives similar results.

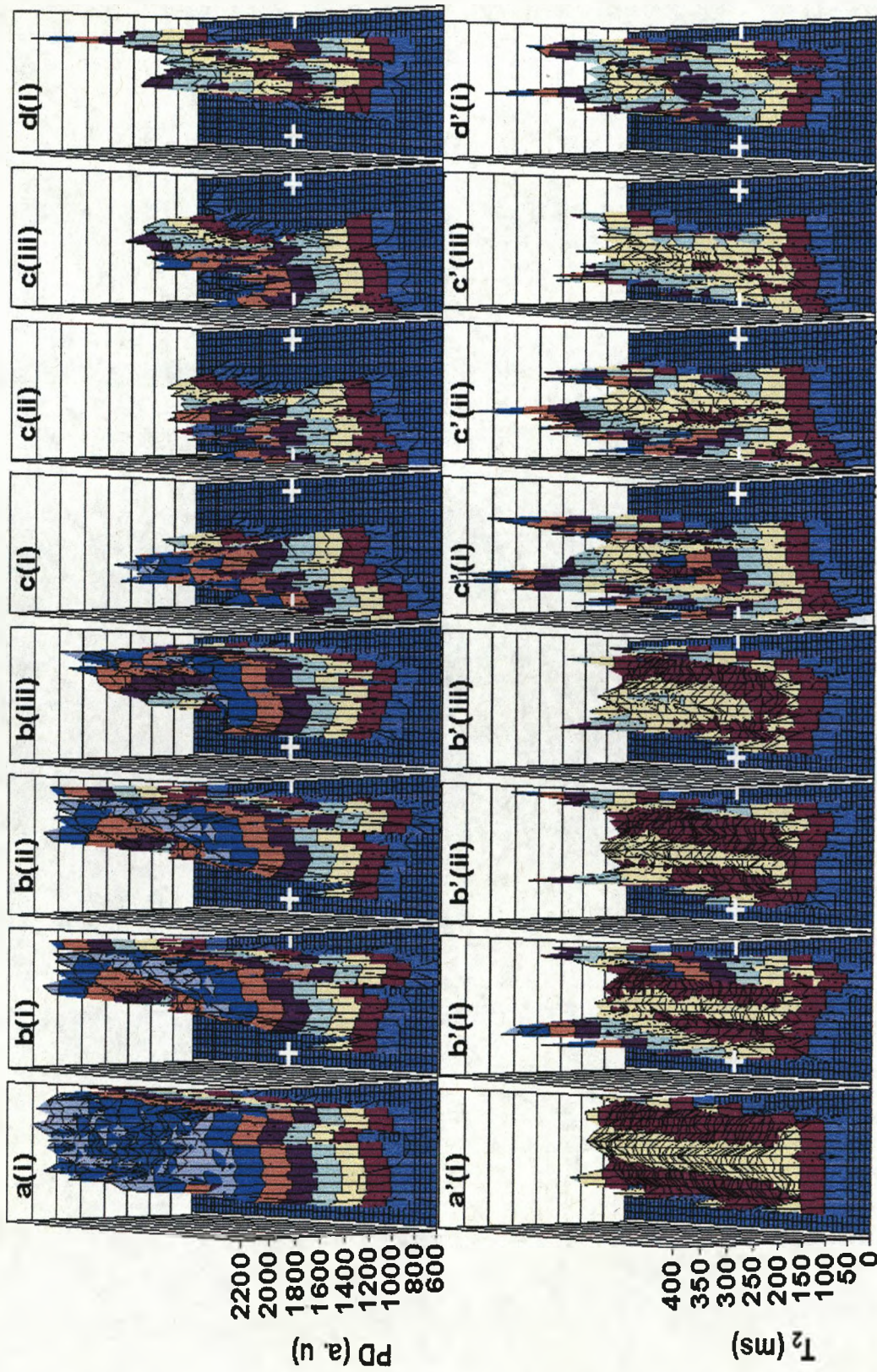


Figure 6.3. *PD* (top maps) and T_2 (lower maps, primes labelled) of the IPMC sample (a, a') with no potential applied; (b, b') (i) 0; (ii) 29; and (iii) 89 min. after application of a 3 V.d.c. continuous potential in the sense indicated. (c, c') (i) 0; (ii) 29 and (iii) 89 min. after first reversal of the polarity and (d, d') (i) 0 min. after second reversal of the polarity of the potential.

To assess the amount of water molecules which contributed to the observed bending deformation of the AuPt₁Cast sample, the percentage of water molecules that had moved after application of the continuous potential was calculated through the same procedure as described in Section 5.3: the *PD* map of the sample obtained in regime (a) was subtracted numerically from all subsequent *PD* maps in regime (b). Figure 6.4 illustrates the changes which occurred in the percentage of mobile water over the whole IPMC sample during regime (b). The percentage of mobile water molecules was estimated to be about 20%. As in Figure 5.4, the percentage of mobile water increases suddenly during the first 29 minutes and then increases slowly afterwards.

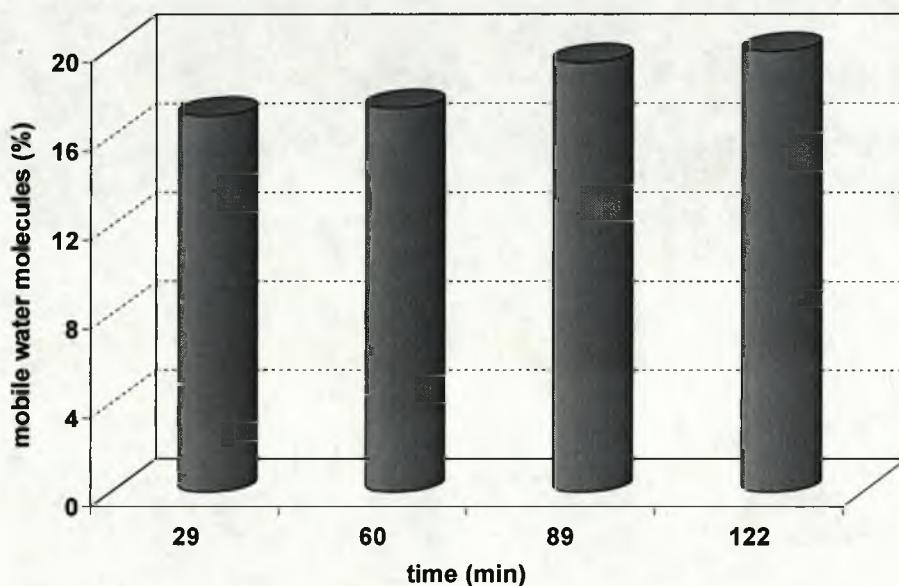


Figure 6.4. Estimation of percentage of mobile water in the IPMC sample during application of 3V d.c. potential in regime (b).

To further illustrate the changes occurring in T_2 over AuPt₁Cast, under the influence of the three imposed electrical regimes, the average T_2 values in milliseconds within three 10 pixel-wide cross-sections through the thickness of the sample at its extreme left, centre and extreme right were calculated. Figure 6.5 shows the average T_2 plots obtained for these three selected cross-sections of the sample. To decrease the noise and to obtain more comprehensible information from the area of interest in these regions, a trendline (red line) was added to all the graphs. The graphs presented in Figure 6.5 – parts (a)-(a'') - reveal that the distribution of T_2 over the three selected regions is relatively similar, indicating a uniform physical structure along the length of the sample. Figures 6.5(b) and (b'') – parts (i)-(iii) show that the application of the potential leads to a similar increase in T_2 near the cathode at both extremes, while it affects less the T_2 at the centre of the sample (Figure 6.5(b') – parts (i) to (ii)). Figure 6.5(b(iii))-(b''(iii)) show that, 89 min. after application of the potential, T_2 decreases slightly near the cathode and increases slightly near the anode. As the polarity of the applied potential is reversed (Figure 6.5(c)-(c'') – parts (i)-(iii)) the trend observed in regime (b) is quickly reversed over all three parts and T_2 increases near the new cathode. As in regime (b), 89 min. after the start of regime (c) (Figure 6.5(c(iii))-(c''(iii))), T_2 decreases near the cathode and increases slightly near the anode, but to a lesser extent. The concentration of high T_2 s near the cathode is disturbed as the polarity of the potential is reversed for the second time and T_2 starts to increase near the new cathode in Figure 6.5(d(i))-(d''(i)).

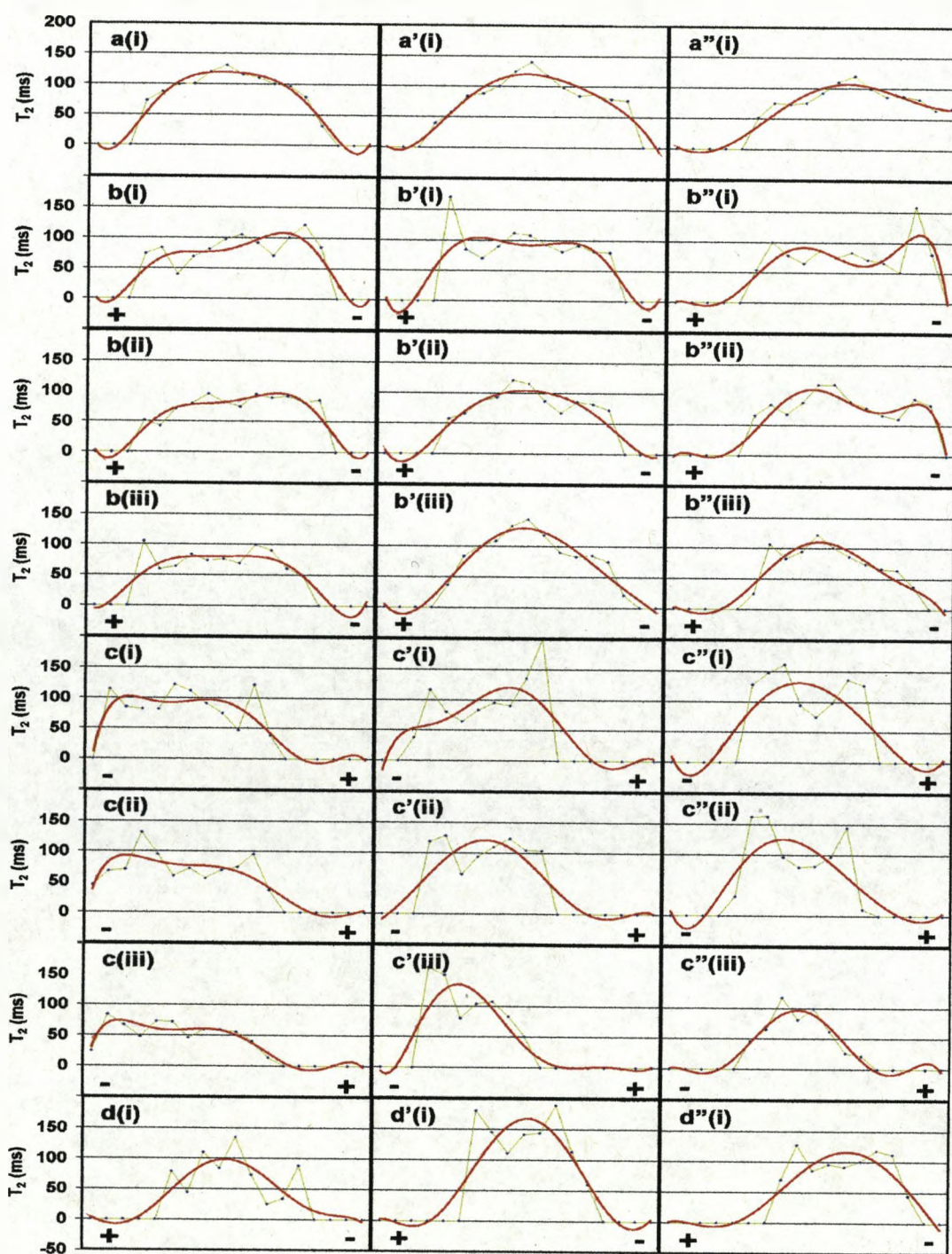


Figure 6.5. Average T_2 values across three cross-sections of the AuPt₁Cast sample at extreme left, centre (primed labels) and extreme right (double primed labels): (a, a', a'') with no potential applied; (b, b', b'') (i) 0; (ii) 29; and (iii) 89 min. after application of a 3V d.c. continuous potential in the sense indicated. (c, c', c'') (i) 0; (ii) 29 and (iii) 89 min. after first reversal of the polarity and (d, d'') (i) 0 min. after second reversal of the polarity of the 3V d.c. potential.

6.4. Discussion

As mentioned in Chapter One, several models including electrostatic, hydraulic and physicochemical models have been suggested in order to explain the actuation mechanism of IPMC materials. These models are all based on basic assumptions. They all consider the sulfonate groups to be permanently attached to the perfluorinated molecular backbones, while the counter cations are free to move through the hydrophilic regions.⁴ In these models it is also assumed that, on application of an electric field to the electrodes of an IPMC, cations (in our case, Li^+) are free to move to balance the negative charge at the cathode, while the sulfonate groups remain attached to the polymer backbone. The hydraulic model⁴ declares that the redistribution of the cations, which carry water molecules in their solvation shell, within IPMC materials contributes to volumetric swelling stresses within the membrane and consequently causes the bending deformation of these materials. The electrostatic model,⁴ however, declares that, in addition to hydration-induced stress, the redistribution of cations produces internal stresses affecting the perfluorinated backbone. This model suggests that these stresses cause the polymer chain to relax in the anion-rich region (anode) and to further extend in the cation-rich regions (cathode). The Yamagami-Tadokoro model^{5,6} considers the volume change by water content and electrostatic force generated by ionic migration in the membrane. To explain the bending deformation of IPMCs, this model uses six physicochemical phenomena: (1) ionic motion induced by electric field, (2) water motion induced by ion drag, (3) swelling and contraction of the membrane, (4) momentum effect, (5) electrostatic force and (6) conformation change. As Bar-Cohen⁴ notes, these three models can describe the contraction of the polymer near the anode and its expansion near the cathode. However, they are not able to explain the

slow relaxation motion of these materials, when they are still under application of a d.c. potential. A model presented by Nemat-Nasser and Li,⁷ which includes ion and water transport, electric field and elastic deformation, involves all aspects presented by the previous models in addition to the effect of electro-osmotic forces. This model suggests that electro-osmotic forces, the changes in the polymer stiffness and also the reorganization of cations within the hydrophilic regions (clusters) in the cathode and anode boundary layers play important roles in the actuation mechanism of IPMCs. Thus, it is able to explain the slow relaxation of IPMCs since it suggests that the redistribution of cations, which causes the volumetric swelling stresses in the polymer, is accompanied by an osmotic pressure differential within the membrane. According to this model Bar-Cohen⁴ suggests that the osmotic forces cause the slow diffusion of water molecules into the elastically softened anode boundary layer, and out of the stiffened cathode boundary layer, when the osmotic forces overcome the electrostatic forces.

In the following sections the variation of T_2 and PD over the AuPt₁Cast (IPMC) sample during imposition of the four electrical regimes ((a) to (d)) are discussed. The obtained results are also evaluated by reference to these models in order to investigate the actuation mechanism of IPMCs.

Regime (a): No Potential Applied

The T_2 map of the AuPt₁Cast sample with no potential (Figure 6.3(a'(i))) revealed that water molecules within this sample possess different T_2 values depending on their position within this sample; water molecules at the centre of the sample have longer T_2 than those

present closes to the faces of the sample. This difference can not be attributed to differences in concentration of water molecules at the surfaces and at the centre of the sample since the *PD* map of this sample in Figure 6.3(a(i)) showed that the concentration of protons (water molecules) is constant over the whole sample.

As was seen previously in Figure 4.4(b), water molecules within the cast Nafion sample (without platinum electrodes) possessed uniform T_2 values. Therefore, the variation of T_2 over the AuPt₁Cast sample can be attributed to the presence of platinum particles in the electrode structures of the sample. The BSE images and EDX results presented in Chapter Four (Section 4.5) showed that the Pt₁Cast sample is platinum-impregnated to a depth of approximately 10-20 μm at the electroded surfaces and that it contains no platinum particles at the centre. These images also showed that there was a gradient in concentration of platinum particles in the electrode region, *i.e.* the concentration of platinum is very high at the outer surfaces and decreases gradually towards the centre of the sample. Therefore, it can be said that T_2 of protons (water molecules) is inversely related to the concentration of platinum; higher concentrations of platinum leads to lower T_2 . This can be considered as a result of an increase in the stiffness⁸ of the membrane in these regions. This is thought to cause greater restriction of the rotational motion of the water molecules and so would give rise to shorter T_2 in these regions.⁹ At the centre, however, the absence of platinum particles leads to less restriction of the rotational motion of water molecules and therefore gives rise to longer T_2 , approximately the same as seen in the T_2 image of the cast Nafion without electrodes (Figure 4.4(b)).

Regime (b): Application of a Continuous 3V d.c. Potential

As was seen in Figure 6.3(b'(i)), immediately after application of the continuous 3V d.c. potential, the distribution of T_2 values over the AuPt₁Cast sample was disturbed and T_2 decreased to some extent at the centre of the sample while increasing at the cathode and at the anode. These changes were then followed by localization of the high T_2 s near the cathode, over time. The increases of T_2 near the cathode and anode, as the potential was applied, can be attributed to the formation of two thin boundary layers,⁷ one enriched in hydrated Li⁺ ions and water molecules at the cathode and other depleted of hydrated Li⁺ ions and enriched in sulfonate groups (-SO₃⁻) at the anode. As discussed in Chapter Five, at the anode, as the electrical field is applied, the electrostatic repulsive force between the hydrated Li⁺ ions within the hydrophilic regions and the positively charged surface causes the forced diffusion of hydrated Li⁺ ions via the more hydrophobic regions of the polymer. The presence of the hydrated Li⁺ ions in the more hydrophobic regions of the polymer are thought to result in the initial observed increase in T_2 values at the anode. At the cathode, the hydrated Li⁺ ions are attracted from neighbouring hydrophilic regions to balance the negative surface charges, which again results in the forced diffusion of the hydrated Li⁺ ions through the more hydrophobic regions of the polymer. The presence of excess hydrated Li⁺ ions near the cathode is also thought to result in an increase in T_2 for the reasons given in Section 5.4.

The combination of the above-mentioned changes occurring at the cathode and the anode causes initial contraction of the polymer at the anode face and swelling at the cathode face along the x-axis (along the length of the sample). As the *PD* and T_2 maps in Figure 6.3(b,

b'), parts (i)-(iii) show, on continuous application of the potential, the bending deformation of the sample towards the anode increases. Since the increasing bending deformation of the sample is associated with simultaneous increases in PD and T_2 near the cathode, and decreases of those near the anode, it can be said that the larger bending deformation of the sample, over time, occurs as a result of the increasing concentration of the hydrated Li^+ ions near the cathode and the decreasing concentration of those near the anode. Figure 6.4 gives evidence that over time a higher number of hydrated Li^+ ions are influenced by the continuous application of the electrical field and diffuse towards the cathode. It is thought that as the number of the hydrated Li^+ ions increases near the cathode the size of the hydrophilic regions increases at this region and the polymer becomes more swollen.⁷ However, the polymer near the anode shrinks more as the hydrophilic regions here become more depleted of the hydrated Li^+ ions. Thus, as the sample becomes more swollen near the cathode and shrunken near the anode a larger bending deformation of the sample towards the anode is observed.

Figure 6.3(b'(iii)) showed that the large bending deformation of the sample after 89 min is associated with a simultaneous slight increase in the intensity of T_2 near the anode. This may be explained by slow back-diffusion⁴ of water molecules towards the anode since in the corresponding PD map (Figure 6.3(b(iii))) the concentration of protons at the anode was also increased. It is reasonable to expect that on continuous application of the potential the decreasing concentration of hydrated Li^+ ions within the hydrophilic regions at the anode leads to a decrease in the osmotic pressure and a decrease in the elastic energy of the polymer at the anode.⁷ At the cathode, however, the higher concentration of these ions can cause a significant increase in the osmotic pressure within the hydrophilic regions and an

increase in the elastic energy of the polymer.⁷ It is believed that to overcome the generated osmotic pressure and elastic energy differential, water molecules start to diffuse slowly into the shrunken anode boundary layer, and out of the swollen cathode boundary layer. This process, which results in slow relaxation of the displacement⁴ of the polymer towards the cathode, may be responsible for the observed slight increase in T_2 near the anode (Figure 6.3(b'(iii))).

Regime (c): Application of a Continuous 3V d.c. Potential of Reversed Polarity

As was seen in Figure 6.3(c'(i)), as the polarity of the applied potential was reversed, T_2 initially increased significantly at the new cathode and at the new anode, and the sample bent towards the new anode. As in regime (b), over time, these changes were followed by localization of high T_2 s near the new cathode and a larger bending deformation in the sample. Comparison of T_2 maps (Figures 6.3(b'(i)) and 6.3(c'(i))), however, reveals that much greater increases in T_2 occurred near the new cathode and anode as the polarity of the applied potential is reversed, than were observed when the potential was applied for the first time, at the start of regime (b). This may be explained by considering that in regime (c) the sample was in a non-equilibrium state. Throughout regime, (b), there had been a movement of hydrated Li^+ ions from the anode to the cathode. The effect of reversing the potential on this non-equilibrium distribution of ions and water was therefore stronger than that on the sample at its equilibrium state, where the hydrated Li^+ ions were evenly distributed over the whole sample.

As in regime (b), 89 min. after reversal of the polarity of the potential, T_2 and PD again increased slightly near the anode, as the sample underwent larger bending deformation (Figure 6.3(c(iii) and (c'(iii))). These increases, however, occurred to a lesser degree than in regime (b). This might be due to the dehydration of the sample. As was observed in Figure 6.3 – parts (a)-(d), the overall intensity of the PD maps decreased over time. This indicates that the sample was dehydrating during this extended experiment. As the sample is more dehydrated in regime (c) than regime (b), the regions near the cathode and anode become closer together. This may also contribute to preventing clear observation of the changes occurring in these regions (Figure 6.3(c'(iii))), and also of the slow back-diffusion of water molecules to the anode.

Regime (d): Application of a Continuous 3V d.c. Potential after a Second Reversal of Polarity

As the polarity of the applied potential was reversed for the second time, the sample quickly bent towards the new anode as a result of the expansion of the polymer along the new cathode and its shrinkage near the new anode. As was mentioned before, 30 min after the second reversal of the polarity, the signal obtained from the sample was dramatically weakened and very poor PD and T_2 images were obtained from the sample. This can be assigned to the intensive dehydration of the sample during previous regimes as was discussed above.

As shown in the previous sections, the changes occurring in T_2 and PD at the cathode and anode regions in the T_2 and PD images mostly conform to the Nemat-Nasser and Li model⁷. However, according to their model, under application of the electric field, thin boundary layers are formed at the anode and cathode which shield the remaining part of the IPMC from the influence of the applied electric field and all the processes which lead to the bending deformation of the IPMC occur at these two layers. The formation of boundary layers may have been observed as changes in T_2 near the cathode and anode as the potential was applied. These changes, however, were not limited to thin cathode and anode regions since T_2 changed over the whole sample.

6.5. Summary

The physical structure and the bending deformation of an AuPt₁Cast IPMC sample were investigated using the MRI scanner. Images of the sample during application of four different electrical regimes were collected in two forms of T_2 and PD images to study the changes that took place in the physical structure of the sample and also the distribution of absorbed water molecules over the whole sample. It was revealed that water molecules at the centre of the IPMC sample have longer T_2 than those molecules in the electrode regions, implying different physical environments in these regions. From the uniform distribution of protons seen in the corresponding PD image of the sample and also the T_2 image of the non-electroded cast Nafion membrane, it was deduced that this difference arises from the presence of platinum particles in the electrode regions. It was shown that T_2 of protons was inversely related to the concentration of platinum: the presence of higher concentrations of

platinum lead to shorter T_2 . This revealed that the rotational motion of water molecules is more restricted in the region containing more platinum. Application of the potential across the thickness of the IPMC sample resulted in the observation of contraction of the polymer along the anode and its expansion along the cathode in T_2 and PD images. This was associated with an increase in T_2 near the cathode and a decrease near the anode. Over time, as the region of high T_2 s became more concentrated near the cathode, the bending deformation of the IPMC sample towards the anode developed. As the IPMC sample initially had longer T_2 s at the centre compared to the electroded surfaces, on application of the potential the difference between high T_2 s, corresponding to mobile water molecules, and short T_2 s, corresponding to unaffected water molecules, was less clear in the corresponding T_2 images. The changes in the T_2 images of the IPMC sample during application of the potential were associated with similar changes in the intensity of the corresponding PD images: higher proton density was always seen near the cathode. This revealed that the region of high T_2 s observed near the cathode in the T_2 images was related to the accumulation of mobile water in this region, during application of the potential. Reversing the polarity of the applied potential resulted in the reversal of the direction of the bending deformation of the IPMC sample and the distribution of high T_2 s - related to protons in mobile water - was reversed. The slow back-diffusion of water molecules towards the cathode was observed approximately 90 min after application of the potential in regimes (b) and (c). This suggested that this process occurs when the potential is applied long enough to create a considerable difference in osmotic pressure and elastic energy between cathode and anode regions. Comparison of the PD maps obtained during the four electrical regimes revealed that the sample was dehydrating throughout the experiment.

6.6. References

- [1]. K. J. Kim, M. Shahinpoor, *Smart Mater. Struct.*, 2000, 9(4), 543.
- [2]. M. Shahinpoor, K. J. Kim, *Smart Mater. Struct.*, 2001, 10, 819.
- [3]. W. Kuhn, *Angewandte Chemie, Int. Ed. Engl.* 1990, 29, 1.
- [4]. Y. Bar-Cohen, "Electroactive Polymers Actuators and Artificial Muscles – Reality, Potential and Challenges", *SPIE Press*, Bellingham WA, 2001.
- [5]. S. Tadokoro, S. Yamagami, T. Takamori, K. Oguro, *Smart Structure & Materials, Proc. SPIE*, 3987, 92.
- [6]. S. Tadokoro, S. Yamagami, T. Takamori, K. Oguro, *Robotics and Automation, Proc. ICRA*, 2000, 2, 1340.
- [7]. S. Nemat-Nasser, J. Y. Li, *J. Appl. Phys.*, 2000, 87, 3321.
- [8]. S. Nemat-Nasser, Y. Wu, *J. Appl. Phys.*, 2003, 93(9), 5255.
- [9]. P. T. Callaghan, "Principles of Nuclear Magnetic Resonance Microscopy", *Clarendon Press . Oxford*, New York, 1991.

Chapter Seven

Diffusion Studies

7.1. Introduction

As was seen in Chapters Five and Six, T_2 measurement of the commercial Nafion and the working AuPt₁Cast IPMC samples could provide information about the rotational freedom, and thus the environment, of absorbed water molecules within these samples. Results obtained from these experiments also showed how this technique of imaging could be applied to monitor the electrically-induced distribution of water molecules within these samples and, consequently, obtain information about the changes occurring in the physical structure of the samples under application of an electric field. In line with the main aim of this thesis, – to achieve a better understanding of the physical structure of Nafion membrane and also of the actuation mechanism of IPMC materials – Diffusion-Weighted Imaging (DWI) was employed in a further set of experiments to visualize the spatial variation of the translational diffusion coefficient of water molecules in the cast Nafion membrane and also in an operating AuPt₁Cast IPMC sample. The DWI method allows measurement of the rate at which water molecules move through the membrane.^{1,2} As was described in Chapter Two, this method of imaging, which involves application of a pulsed gradient to the sample in addition to the spin echo pulse sequence, is sensitive to translational motion of spins. Thus, it can provide images corresponding to the distance that water molecules move over the time interval, Δ , (time between gradients) within the membrane. This technique of imaging can also probe the microstructure of the samples. This is based on the fact that water molecules have different diffusion coefficients depending on the microstructure of the object through which they are diffusing.¹ Water molecules have lower diffusion coefficients where their diffusion is interrupted by interfaces in a sample, and higher diffusion coefficients where they are freer to diffuse.

Higher and lower diffusion coefficients are observed as darker and brighter regions, respectively, in diffusion-weighted images.

7.2. Experimental

7.2.1. Diffusion Study of Cast Nafion Membranes

The self-diffusion of water molecules within square samples of cast Nafion (Li⁺-exchanged) was monitored using the DWI technique. An 8×8 mm cast Nafion sample was sandwiched between two pre-cleaned glass plates, of the same size, and mounted horizontally in a 10 mm o.d. quartz NMR tube. Constant saturated water vapor pressure was maintained inside the tube as described previously in Section 4.3.1.1. MRI images of the self-diffusion of water molecules were accumulated by applying a pair of pulsed gradients, g , on the regular spin echo imaging pulse sequence with an echo time, T_E , of 11.329 ms and repetition time, T_R , of 5 s. In order to obtain quantitative diffusion maps and also to calculate the diffusion coefficients of water molecules within the samples, according to Equation (2.30), nine diffusion-weighted images were collected which differed in the strength of the gradient, g , while the other parameters were kept the same: duration of gradient pulses, $\delta=4$ ms, and time interval of gradient pulses, $\Delta=5.109$ ms. The strength of gradient, g , was varied from 0.1 to 0.9 T/m corresponding to a b -factor range of 43.5 to 352.4 s/mm² to obtain nine different degrees of diffusion weighting. The best possible combination of the imaging parameters T_E , δ , Δ , g and b -factor was chosen through performing several similar experiments performed on a single sample to obtain the best

signal decay in nine diffusion-weighted images. To examine the dependency of the measured diffusion coefficients of water molecules on the axis of the pulsed gradient application – the diffusion anisotropy – the samples were imaged by the application of gradients in turn along the slice-selection direction (z-axis, in our experimental set up – parallel to the main magnetic field) and then along the read-out direction (x-axis, perpendicular to the main magnetic field). Therefore, with respect to the horizontal position of the sample in the MRI scanner (see Figure 7.1), the gradients were applied respectively parallel and then perpendicular to the thickness of sample. These experiments were repeated several times to study the reproducibility of the results. MRI images were generated with a matrix size of 32×32 pixels and the acquisition time for each dataset was approximately 21 min, as for the previously performed T_2 experiments. The slice thickness was 15 mm and the *FOV* was 15×15 mm, which resulted in a spatial resolution of 468 $\mu\text{m}/\text{pixel}$. Results were collected as images and used to prepare spatial maps of the coefficient of diffusion, or *D*-maps. In this work, *D*-maps obtained from the DWI with the gradient applied along the z-axis and along the x-axis are referred to D_z -maps and D_x -maps, respectively.

7.2.3. Diffusion Study of IPMCs

Self-diffusion and also electrically-induced diffusion of water molecules in 8×8 mm square samples of AuPt₁Cast (Li⁺-exchanged by pre-soaking in a saturated solution of LiOH) were also imaged using the DWI technique. The sample was held within a sample holder, as depicted in Figure 6.1, to enable a suitable potential to be applied across its thickness once

it was inside the MRI scanner. The remaining steps of the sample set-up in the MRI scanner resemble those described in Section 6.1. Diffusion-weighted images of the samples were collected consecutively throughout four electrical regimes and by application of gradients along the x-axis, and the z-axis directions. Since the sample was mounted horizontally in the MRI scanner (Figure 7.1), in the case of DWI along the x-axis and z-axis the pulsed gradients were respectively applied perpendicular and parallel to the thickness of the sample (as in the experiment described in the previous section).

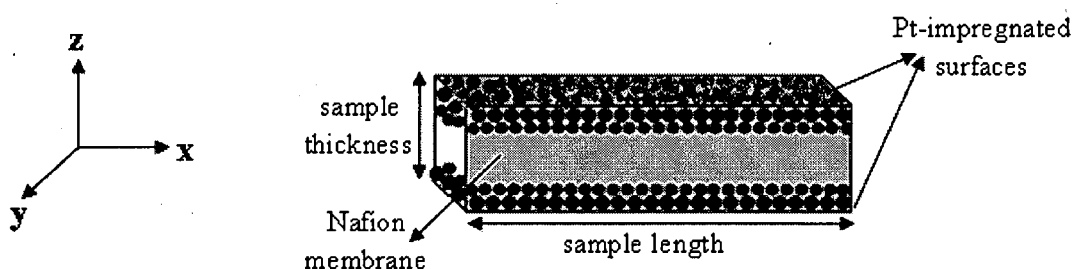


Figure 7.1. Position of AuPt₁Cast sample in MRI scanner, in relation to the x, y and z coordinates referred to in the text.

The electrical regimes were chosen so as to be similar to those applied in the T_2 experiments (Chapter Six) except for the last one. They were: (a) no potential was applied; (b) application of a continuous 3V d.c. potential; (c) application of a continuous 3V d.c. potential of reversed polarity and (d) removal of the applied potential. The sample was imaged several times in regimes (a) and (d) in order to record the changes in self-diffusion of water molecules within this sample at its equilibrium state, regime (a), and after the

potential was switched off, regime (d). It must be mentioned that the D_x and D_z images of the samples with no power applied (regime (a)) were accumulated in the same experimental run (Table 7.1, Run 1) by switching the direction of the applied pulsed gradients between the x-axis and the z-axis. Imaging parameters were chosen to be the same as were used for the DWI experiments on the cast Nafion membrane (Section 7.2.1) in order to obtain comparable results. Electrically-induced diffusion of water molecules within the sample with non-zero potentials was first imaged by applying the pulsed gradient along the x-axis (Table 7.1, Run 2), with no time interval. These experiments were performed 24 h after imaging the sample with no potential applied (regime (a)). Thus, for the purpose of comparison, prior to the performance of these experiments the sample was again imaged with no potential applied by applying the pulsed gradients along the x-axis (Table 7.1, Run 2). Imaging of the electrically-induced diffusion was repeated using the pulsed gradient along the z-axis six days later on the same sample (Table 7.1, Run 3). During this time period the sample was left in the MRI scanner in the same position to allow it to return to its equilibrium state and also to maintain all the parameters at similar values as for the previous experiment. As in Run 2, these experiments were also initiated with the imaging of the sample with no power applied (by applying the pulsed gradient along the z-axis). Results obtained from investigating the self-diffusion of water molecules within the sample at the equilibrium state, regime (a), are presented separately in Section 7.3.2 and the rest are presented in Section 7.3.3.

Table 7.1. Experimental run sequences.

No. of exp.	Run 1		Run 2 (after 24 h)		Run 3 (after 6 d)	
	Potential (Volt)	Direction of gradient	Potential (Volt)	Direction of gradient	Potential (Volt)	Direction of gradient
1	0	x-axis	0	x-axis	0	z-axis
2	0	z-axis	+3	x-axis	+3	z-axis
3	0	x-axis	+3	x-axis	+3	z-axis
4	0	z-axis	+3	x-axis	+3	z-axis
5	0	x-axis	-3	x-axis	-3	z-axis
6	0	z-axis	-3	x-axis	-3	z-axis
7	0	x-axis	-3	x-axis	-3	z-axis
8	0	z-axis	0	x-axis	0	z-axis
9	0	x-axis	0	x-axis	0	z-axis
10	0	z-axis	0	x-axis	0	z-axis
11	-	-	0	x-axis	0	z-axis
12	-	-	0	x-axis	0	z-axis
13	-	-	0	x-axis	0	z-axis
14	-	-	0	x-axis	0	z-axis
15	-	-	0	x-axis	0	z-axis
16	-	-	0	x-axis	0	z-axis
17	-	-	0	x-axis	0	z-axis
18	-	-	0	x-axis	0	z-axis

7.3. Results and Analysis

7.3.1. Self-Diffusion of Water in Cast Nafion Membrane

Figure 7.2 displays diffusion-weighted images of the cast Nafion sample recorded with increasing b -factor and with the pulsed gradient applied along (a) the x-axis and (b) the z-axis. In these figures, parts (i)-(ix) show nine images with different diffusion weighting recorded with successive increases in gradient, g , from 0.1 to 0.9 T/m, respectively. These

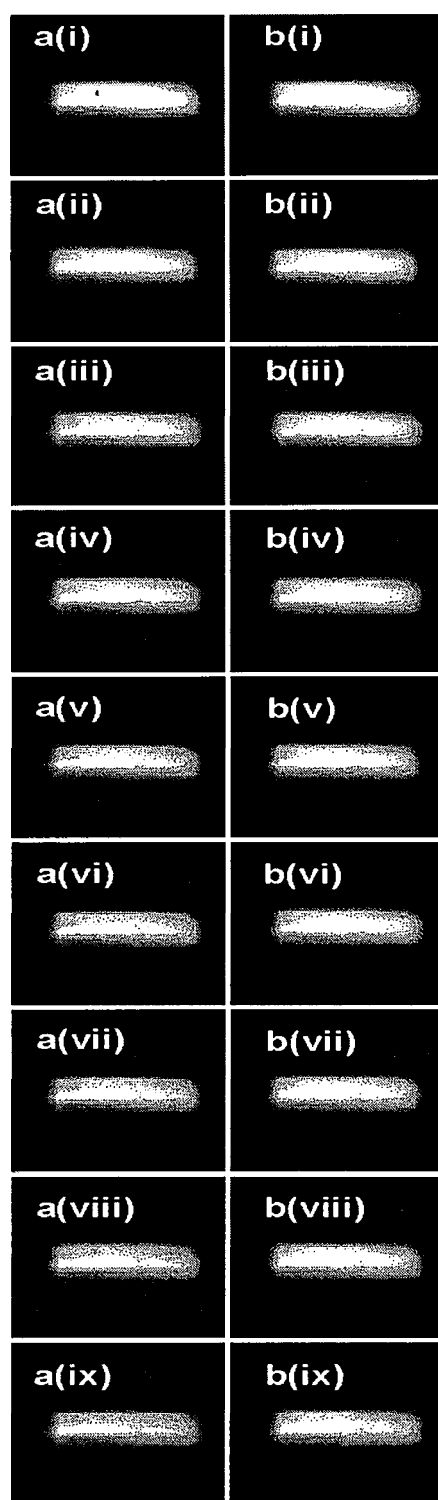


Figure 7.2. Diffusion-weighted images of cast Nafion sample recorded with increasing b -factor and using pulsed gradient along (a) x-axis and (b) z-axis. Parts (i)-(ix) show the images recorded on increasing the gradient, g , in 0.1 T/m increments from 0.1 to 0.9 T/m, respectively.

images are in general noisier than the corresponding spin echo images observed in previous chapters since the NMR signal is weakened by the application of the pulsed gradients and the very long T_E (11.329 ms). It must be mentioned that the signal intensity in these images is influenced by the choice of b -factor, T_E , diffusion coefficient, D , T_1 and T_2 relaxation.^{1,2} Therefore, the absolute intensity of these images can not be considered as a direct indicator of the diffusion coefficient at each pixel of the image; that is, that regions with high signal intensity on a diffusion-weighted image may reflect a long T_2 relaxation instead of a lower diffusion coefficient. Thus, to avoid any misinterpretation the degree of signal decay is considered more important than the absolute intensity of these images.² As can be seen, the signal intensity of the images presented in Figure 7.2(a) and (b) – parts (i)-(ix) decays as gradient strength increases and the last image (ix) in each series of (a) and (b) appears darker. This indicates that, by increasing the strength of gradient, g , sensitivity of the DWI technique increases and is able to detect much slower translational diffusion of water molecules within the sample, leading to a greater attenuation of the NMR signal.¹ For each column, comparison of the images reveals that, as the gradient strength is increased the image intensity appears to decay at the same rate over the whole sample. Figure 7.3 represents the changes that occurred in the signal intensity with changing gradient strength for images recorded by application of the pulsed gradient along the x - and z - axes. Data points in this figure correspond to the natural logarithm of average signal intensity, S , of the same three individual pixels in each set of nine diffusion-weighted images in Figure 7.2. The linear relationship between the natural logarithm of signal intensity and the square of the gradient in both plots implies that the structure of the sample along the length (x -axis) and across the thickness (z -axis) is homogenous (see Discussion section).^{1,2}

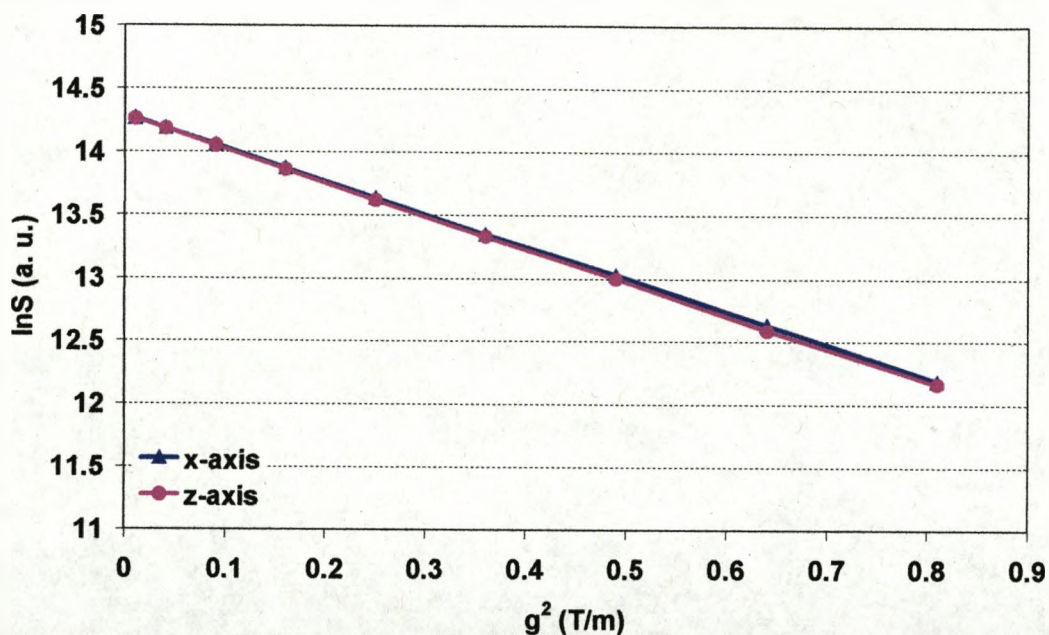


Figure 7.3. Relationship between the average intensity, S , of the nine diffusion-weighted images and the applied pulse gradient strength, g , for both axes of measurement.

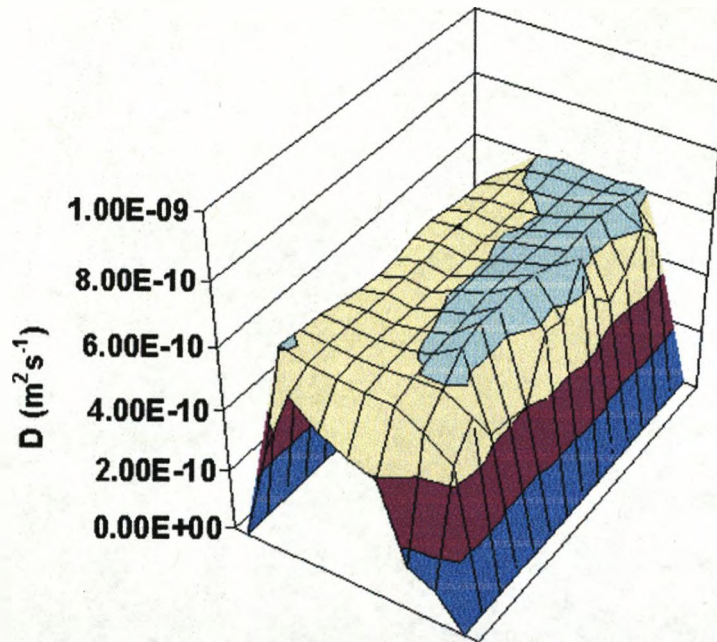
The similarity of the slopes of these plots also implies that water molecules diffuse at very similar rates along these two directions in the sample. The diffusion coefficient along the x-axis, D_x , and the z-axis, D_z , were calculated from the slope of the straight lines fitted to these data sets. The measured D relates directly to the translational molecular motion of water molecules in the sample.

Table 7.2. DWI parameters and calculated D_x and D_z for cast Nafion membrane.

Sample name	Direction of gradients	δ (ms)	Δ (ms)	b-factor range (s mm ⁻²)	lnS ₀	Diffusion coefficient (m ² s ⁻¹)
cast Nafion	x-axis	4	5.109	43.5 – 352.4	14.2	6.05×10^{-10}
cast Nafion	z-axis	4	5.109	43.5 – 352.4	14.2	6.10×10^{-10}

As the data presented in Table 7.2 show, D_x is very similar to D_z . This implies that the measured diffusion coefficients of water molecules in this sample are independent of the orientation of the gradient in the measurements. This can be seen clearly in D -maps presented in Figure 7.4(a) and (b). These maps represent the spatial variation of the measured values of D_x , and D_z , respectively, for the water molecules present across the whole sample. These maps were constructed according to the description given in Section 3.7.2.4. In each map very similar distributions of diffusion coefficients are observed. According to these maps, the average D_x ($D_x(av)$) is about $6.03 \times 10^{-10} \text{ m}^2\text{s}^{-1}$ and the average D_z ($D_z(av)$) is about $6.15 \times 10^{-10} \text{ m}^2\text{s}^{-1}$. These values are in very good agreement with D_x and D_z values estimated from the slope of the plots in Figure 7.3 (see Table 7.2). Comparison of these maps also reveals that water molecules enjoy a similar degree of freedom to diffuse along the x-axis or the z-axis, indicating a homogenous structure for the cast Nafion sample.

(a)



(b)

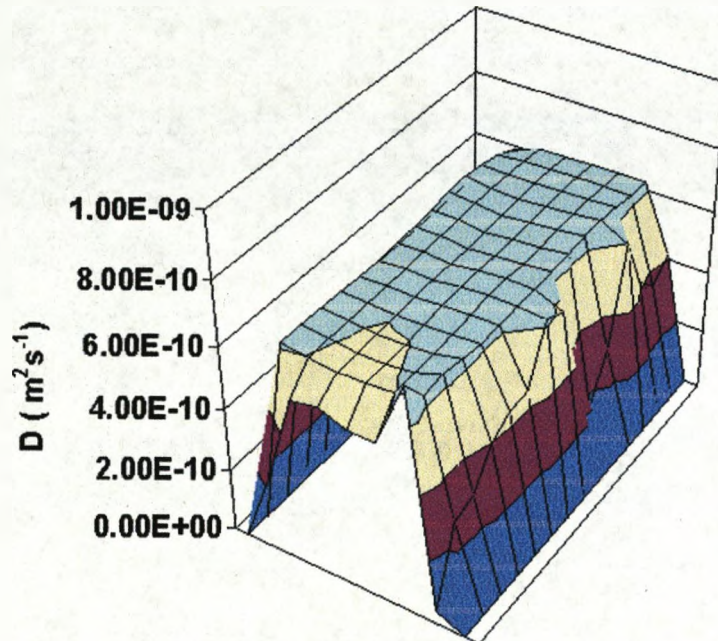


Figure 7.4. (a) D_x - and (b) D_z -map of cast Nafion sample.

7.3.2. Self-Diffusion of Water in an IPMC Actuator

Figure 7.5 shows the diffusion-weighted images accumulated for the AuPt₁Cast sample with increasing b -factor, parts (i)-(ix), and application of pulsed gradient along (a) the x - and (b) the z -axis. As can be seen, the intensity (brightness) distribution of these images appears different depending on the orientation of the measurements. Images recorded using the pulsed gradient along the z -axis (sample thickness), Figure 7.5(b), are brighter than those acquired using the pulsed gradient along the x -axis (sample length), Figure 7.5(a). This shows that the NMR signal is attenuated more strongly when the pulsed gradient is applied along the length of the sample (x -axis). Since the extent of signal attenuation depends on the diffusion coefficient of water molecules² these results indicate that D_x is higher than D_z over the whole sample. The intensity of the images presented in Figure 7.5(a) and (b) – parts (i)-(ix) also decreases as gradient strength increases. However, the extent of this decay varies over the sample, indicating that the sample has a heterogeneous structure. At the surfaces, in the platinum impregnated region, it seems the image intensity decays faster than at the centre of the sample, where there is little or no platinum. This is observed as darker regions at the surfaces and brighter regions at the centre of the images acquired by application of the stronger gradient pulses, parts (v)-(ix). This contrast between these two zones appears different in the images presented in the two columns (Figure 7.5(a) – parts (v)-(ix) and Figure 7.5(b) – parts (v)-(ix)). This shows that the spatial variation of diffusion coefficient D in the AuPt₁Cast sample depends on the orientation of the measurements.

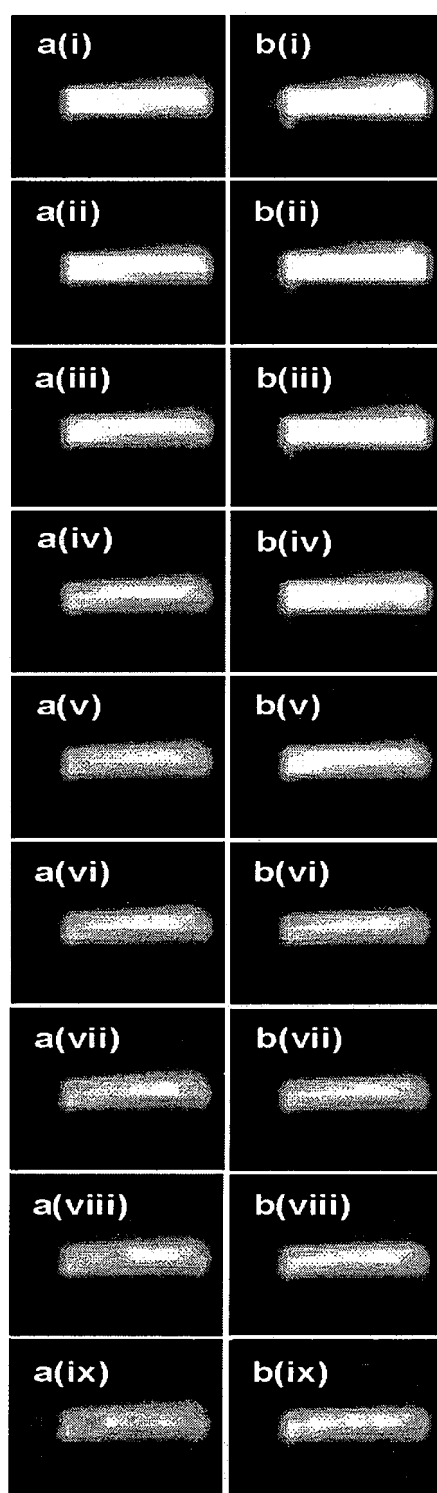


Figure 7.5. Diffusion-weighted images of AuPt₁Cast sample recorded with increasing b -factor and using pulsed gradient along (a) x-axis and (b) z-axis. Parts (i)-(ix) show the images recorded on increasing the gradient, g , in 0.1 T/m increments from 0.1 to 0.9 T/m, respectively.

The plots presented in Figure 7.6 illustrate clearly the dependency of diffusion on the orientation of the measurements. Data points in these plots were obtained in the same way as described in Section 7.3.1. As can be seen, there is a linear relationship between the natural logarithm of average intensity, $\ln S$, of the images acquired using pulsed gradients along the length of the sample (x-axis) and the square of the strength of the gradient, g^2 , indicating a homogenous structure for the sample in this direction. However, there is a non-linear relationship when the pulsed gradient was applied across the sample thickness (z-axis). This implies that the diffusion across the thickness of the sample is not homogenous (see Discussion).^{1,2}

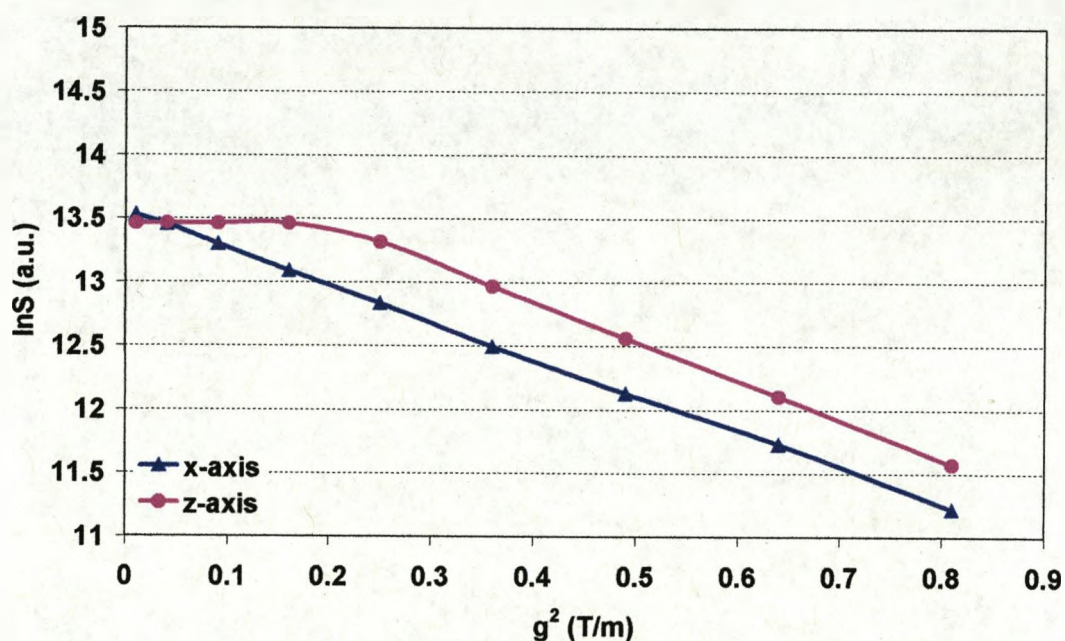


Figure 7.6. Relationship between the average intensity, S , of the nine diffusion-weighted images and the applied pulse gradient strength, g , for both axes of measurement.

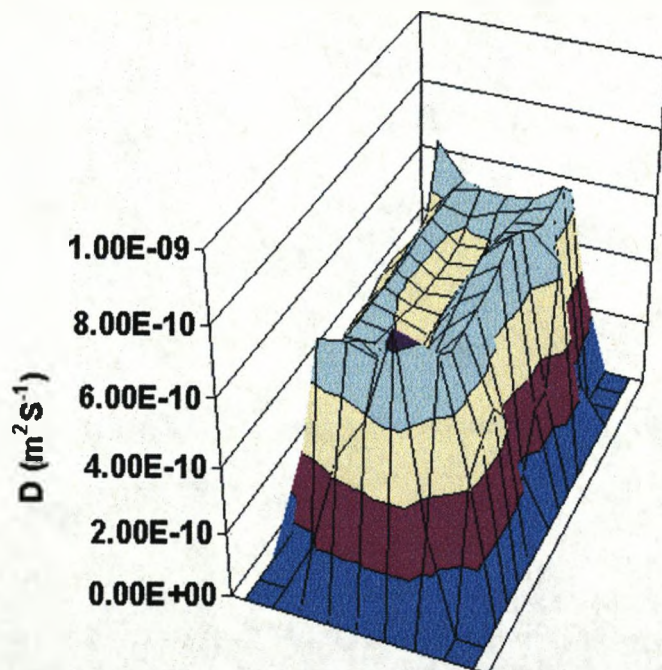
As the data presented in Table 7.3 show, the estimated value of D_x is higher than that of D_z . That is, the rate of diffusion of water molecules along the z-axis (across the sample thickness) is slower than along the x-axis (along the sample length).

Table 7.3. DWI parameters and calculated D_x and D_z for the AuPt₁Cast IPMC sample.

Sample name	Direction of gradients	δ (ms)	Δ (ms)	b -factor range (s mm ⁻²)	lnS ₀	Diffusion coefficients (m ² s ⁻¹)
AuPt ₁ Cast	x-axis	4	5.109	43.5 – 352.4	13.6	6.69×10^{-10}
AuPt ₁ Cast	z-axis	4	5.109	43.5 – 352.4	13.7	5.66×10^{-10}

The D -maps presented in Figure 7.7 also show clearly the dependence of the diffusion coefficients of water molecules in the AuPt₁Cast sample on the orientation of the measurements. In the D_x -map (Figure 7.7(a)) a shallow dip is observed, representing lower D_x (6.01×10^{-10} m²s⁻¹) for water molecules at the centre than for those near the surfaces (6.57×10^{-10} m²s⁻¹) of the sample. This dip appears much deeper in the D_z -map, shown in Figure 7.7(b), which shows that there is a larger difference between the measured D_z at the surfaces (6.72×10^{-10} m²s⁻¹) and the centre (4.44×10^{-10} m²s⁻¹) of the sample. This reveals that the rate of self-diffusion of water molecules at the surfaces where the sample is highly platinum impregnated is higher while it decreases towards the centre of the sample where the concentration of platinum is close zero.

(a)



(b)

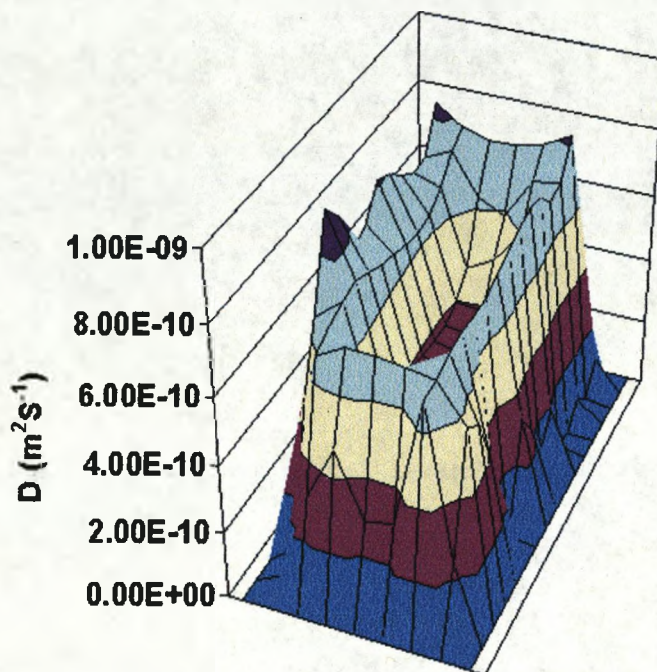


Figure 7.7. (a) D_x - and (b) D_z - maps of AuPt₁Cast sample without application of a potential

To examine the spatial variation of D_x and D_z across the sample and to observe any changes with time, the sample was successively imaged by application of pulsed gradients along the x-axis and the z-axis in turn. The results are shown as (a) D_x - and (b) D_z - maps in Figure 7.8. Parts (i)-(iv) show the changes that occurred within the sample as it was kept at equilibrium state (*i.e.* before application of an external potential) over a period of 84 min.. Comparison of the D_x - maps (Figure 7.78(a)(i)-(iv)), and the D_z -maps (Figure 7.8(b)(i)-(iv)), in each column reveal that the ratio of the measured D at the surfaces to that at the centre of the sample remains similar over time. Comparing the D - maps in each row also shows that the differences observed between the measured D_x and D_z over the whole sample remain essentially unchanged.

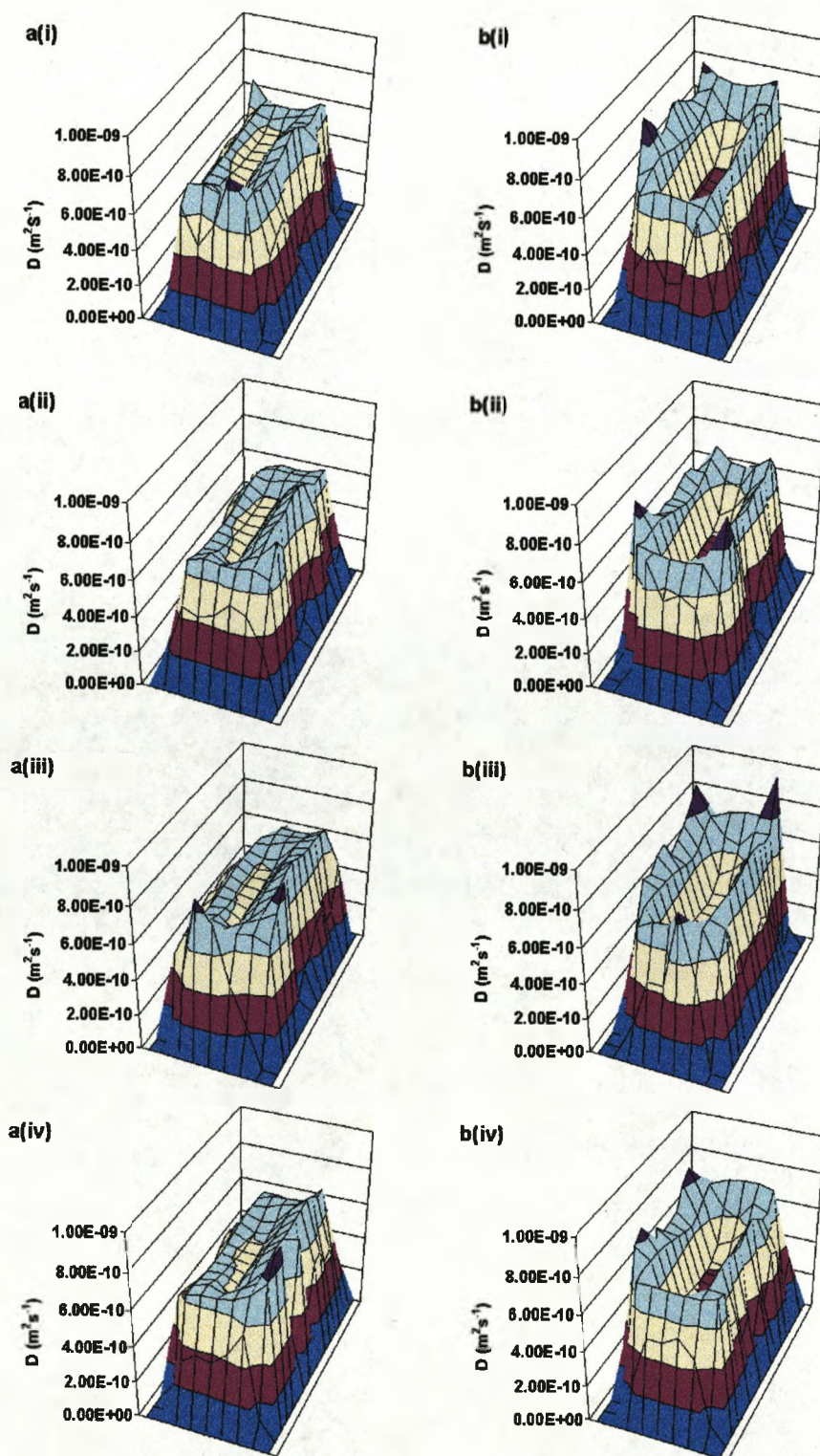


Figure 7.8. (a) D_x - and (b) D_z - maps of the AuPt₁Cast sample at its equilibrium state, with no potential applied. Parts (i)-(iv) show D -map of sample obtained after 21, 42, 63 and 84 min., respectively.

7.3.3. Electrically-Induced Diffusion of Water in an IPMC Actuator

Figure 7.9 shows diffusion-weighted images of AuPt₁Cast sample: (a) with no potential applied; 0 min; (b) after application of a 3V d.c. continuous potential; (c) after reversal of the polarity of the 3V d.c. potential; and (d) after removal of the applied potential. These images were acquired by application of a pulsed gradient along the x-axis (see Figure 7.1) and with increasing *b*-factor, parts (i)-(ix).

As can be seen in Figure 7.9(b) (i)-(ix), on application of a continuous 3V d.c. potential across the thickness of the sample the intensity of the images decrease significantly over the sample. This shows that the electrically-induced diffusion of water molecules towards the cathode causes a larger phase shift in the echo leading to higher attenuation of the NMR signal.^{2,3} Images also show clearly that by application of the continuous potential, the sample contracts along the anode (positively charged face) and expands along the cathode (negatively charged face). These changes are accompanied by a slight bending deformation of the sample towards the anode and also a significant decrease in signal intensity of the images over the whole sample, particularly near the anode and the cathode. This implies an increase in the rate of diffusion within the sample overall, and particularly near the electrodes.

Figure 7.9(c) (i)-(ix) show images of the sample acquired immediately after the polarity of the applied potential was reversed. These images appear slightly brighter than those in Figure 7.9(b). However, their intensity is still lower than in the images shown in Figure 7.9(a), illustrating a higher diffusion coefficient in the former. The effect of the reversal of the polarity of the applied potential is also observed in these images as the sample shrinks along the new anode and expands near the new cathode. The intensity of these images also

appears lower near the cathode and the anode than in the centre of the sample. In Figure 7.9(d) (i)-(ix) it can be seen that, after the applied potential is switched off, the intensity over the whole sample and particularly at the centre decreased, suggesting high diffusion coefficients in these regions. On removal of the applied potential the bending deformation of the sample also relaxes.

Comparison of the images shown in Figure 7.9 also reveals that the sample shrinks along its length and thickness during application of the potential and that the sample starts to expand along these directions, mainly thickness, after the power is switched off. As mentioned in Section 7.2, the electrically-induced diffusion of water molecules was also imaged by application of the pulsed gradients along the sample thickness (z-axis). These images are shown in Figure 7.10 and appear generally brighter and noisier than the corresponding images acquired using pulsed gradients along the x-axis (Figure 7.9). This implies that, generally, the rate of diffusion is slower along the sample thickness. Nevertheless, the intensity of these images follows essentially similar changes through the four electrical regimes, but these are generally less marked.

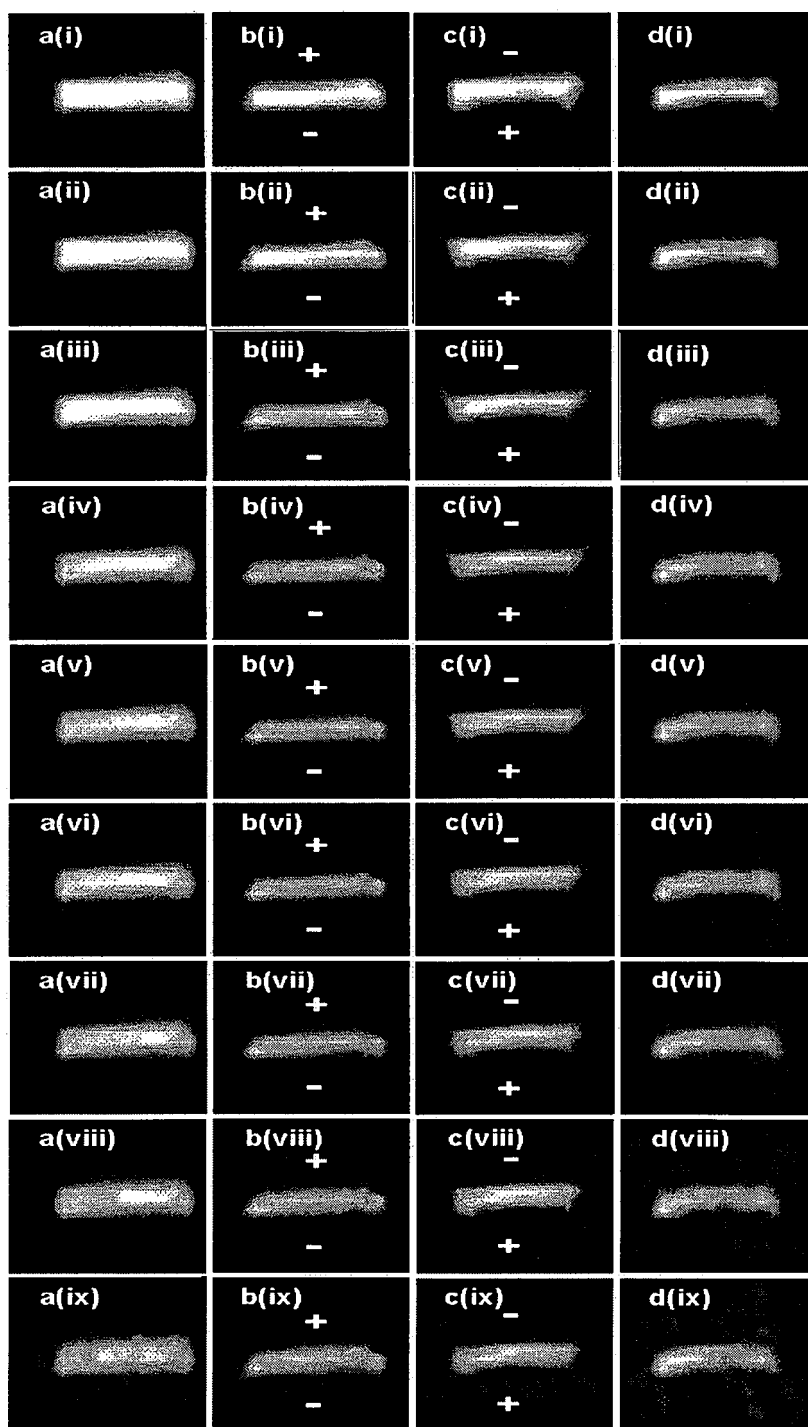


Figure 7.9. Diffusion-weighted images of AuPt₁Cast sample obtained using pulsed gradients along the length of the sample (x-axis) with: (a) no power applied; 0 min; after (b) application of 3V d.c. potential; (c) polarity of 3V d.c potential was reversed and (d) potential was turned off. Parts (i) to (ix) show the images recorded as the gradient, g , was increased in increments of 0.1 T/m from 0.1 to 0.9 T/m. The negative “-” and positive “+” signs indicate the cathode and anode sides of the sample, respectively.

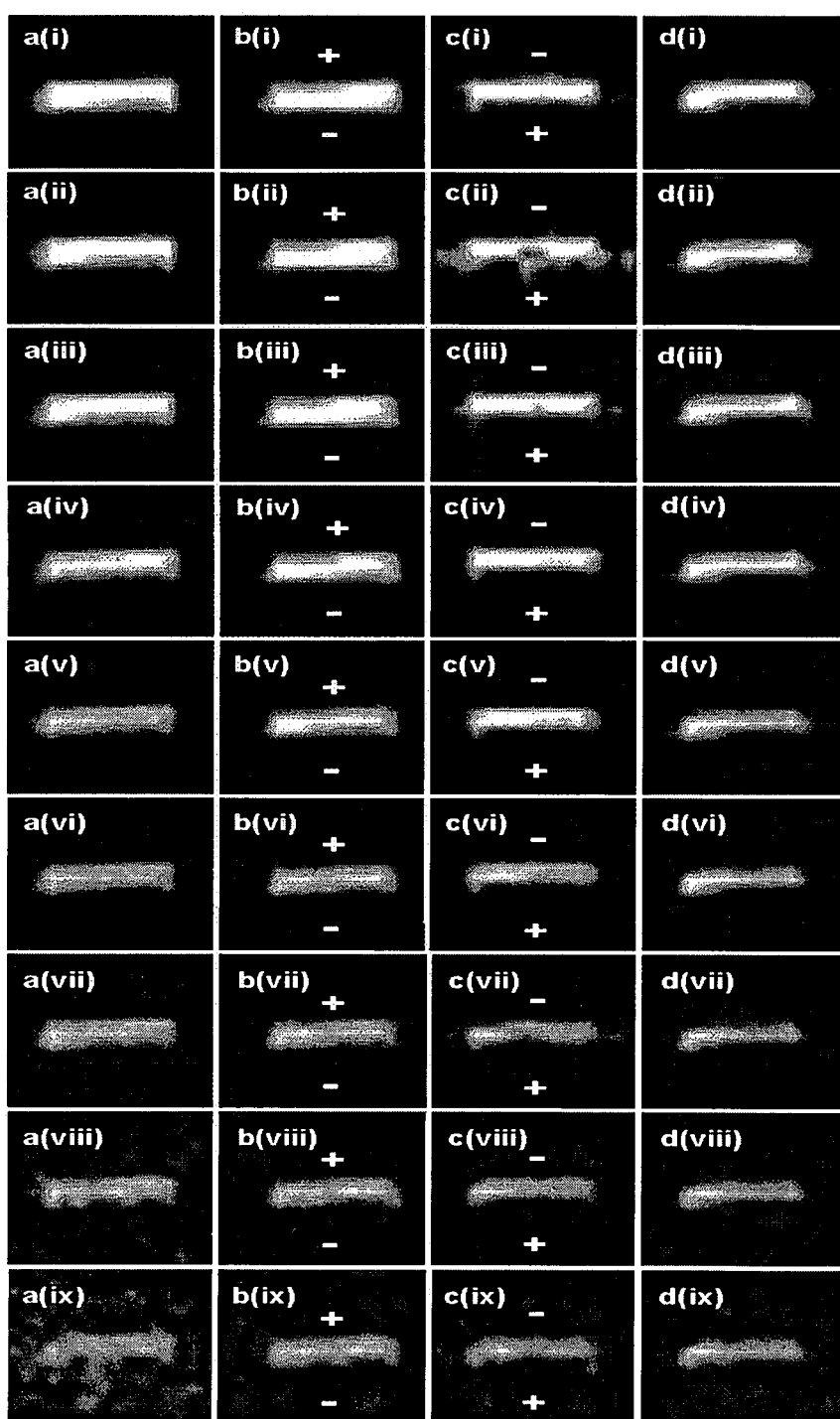
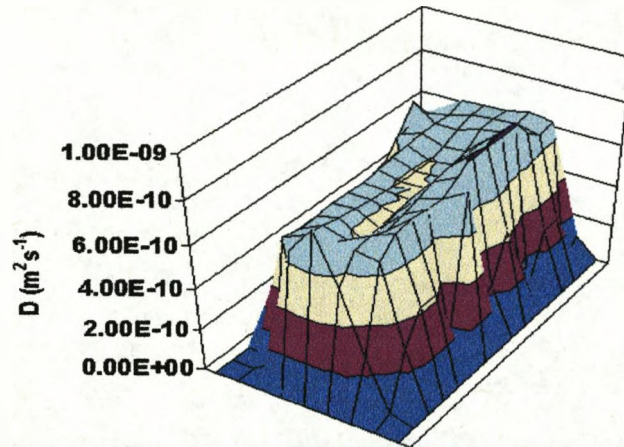


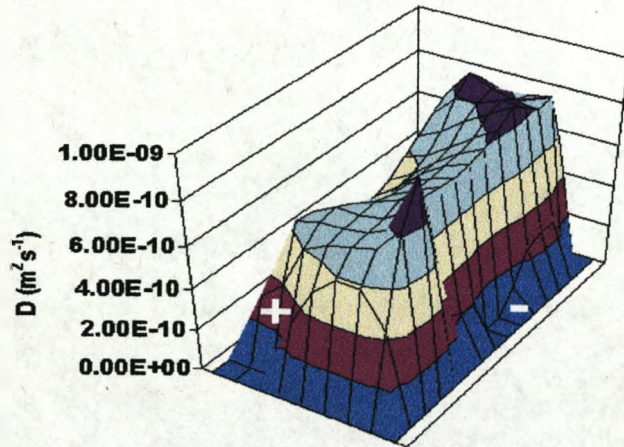
Figure 7.10. Diffusion-weighted images of AuPt₁Cast sample obtained using pulsed gradients along the length of the sample (z-axis) with: (a) no power applied; 0 min after (b) application of 3V d.c. potential; (c) polarity of 3 Vd.c potential was reversed and (d) potential was turned off. Parts (i) to (ix) shows the images recorded as the gradient, g , was increased in increments of 0.1 T/m from 0.1 to 0.9 T/m. The negative “-” and positive “+” signs indicate the cathode and anode sides of the sample, respectively.

In order to investigate further the changes that occur in diffusion coefficient of water molecules, during applied electrical regimes, and to acquire numerical data about these changes, D_x - and D_z -maps were prepared for the sample during regimes (a), (b), (c) and (d). These maps are shown respectively in Figure 7.11 and 7.12 with: (a)(i) no potential applied; (b) (i) 0; (ii) 21; (iii) 42 min. after application of the 3V d.c. continuous potential; (c) (i) 0; (ii) 21; (iii) 42 min. after reversal of the polarity of the 3 V d.c. potential. (d) (i) 0; (ii) 21; (iii) 84; (iv) 147 min; and (v) 65 h. after the power was switched off. In these maps the measured D of water molecules can be analyzed as a function of location within the IPMC sample. Figure 7.11(b(i)) shows that, as the continuous 3V d.c. potential is applied across the thickness of the sample the dip seen in Figure 7.11(a(i)) disappears and a significant increase in the D_x is observed over the whole sample and particularly near the cathode. In Figure 7.11(b(ii)) it can be seen that after 21 min. the region of high D_x – related to fast diffusing water molecules – becomes more concentrated near the cathode and that D_x decreases significantly near the anode. After 42 min., the D_x -map has a similar shape but intensities are generally lower (Figure 7.11(b(iii))). This implies a general decrease in diffusion coefficient over the whole sample. In Figure 7.11(c) – parts (i)-(iii) – very similar changes are observed but in the opposite direction, as a result of the reversal of the polarity of the applied potential. The distribution of high diffusion coefficient, D_x , is reversed as the polarity of the applied potential is reversed, so that D_x increases near the new cathode and decreases near the new anode. The D_x -maps presented in Figure 7.11(d) – parts (i)-(v) – show the spatial variation in D_x , 0, 21, 84, 147min. and 65 h, respectively, after removal of the applied potential. After the applied electric field is switched off the values of D_x become almost equal over the sample (Figure 7.11(d(i))) implying similar diffusion coefficient

a(i)



b(i)



b(ii)

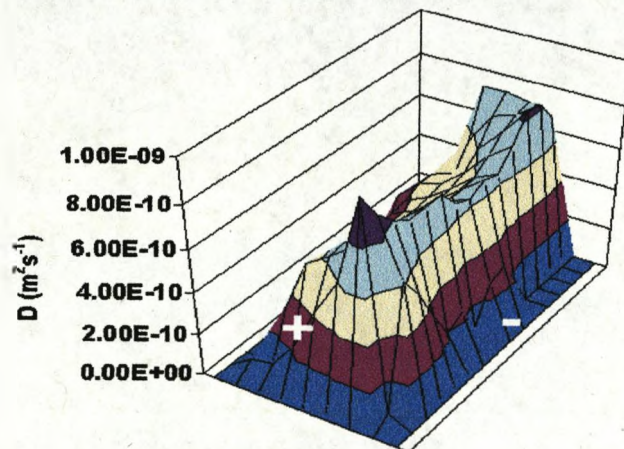
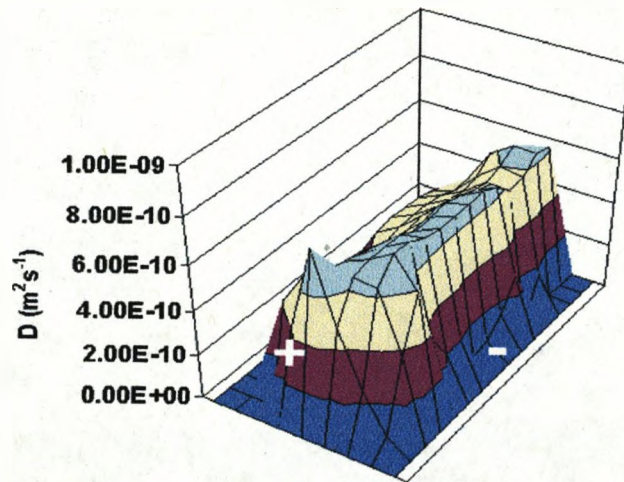
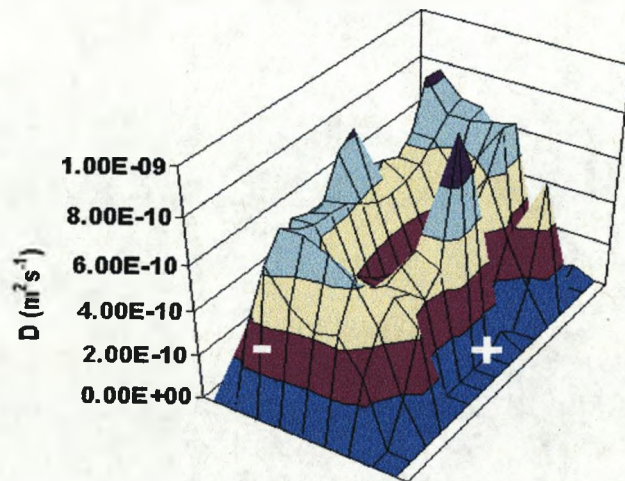


Figure 7.11. D_x -maps of AuPt₁Cast sample: (a)(i) with no potential applied; (b) (i) 0 (ii) 21 (iii) 42 min. after application of a 3V d.c. continuous potential in the sense indicated; (c) (i) 0 (ii) 21 (iii) 42 min. after reversal of the polarity of the 3V d.c. potential; (d) (i) 0 min.(ii) 21 min.(iii) 84 min.(iv) 147 min.(v) 65 h. after the potential was switched off. The negative “-”and positive “+” signs in these images indicate the cathode and anode side of the sample, respectively.

b(iii)



c(i)



c(ii)

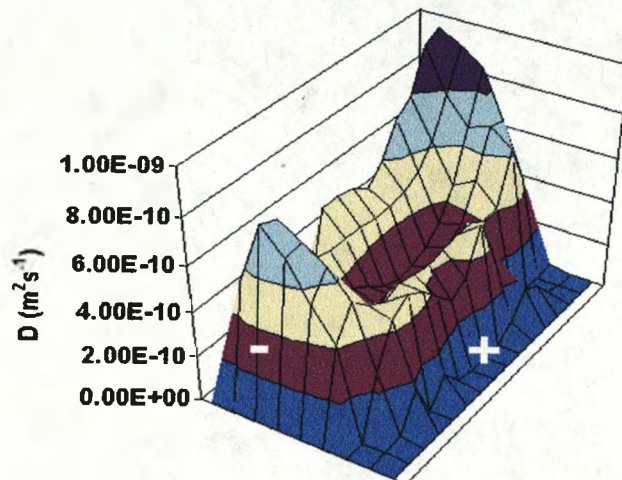
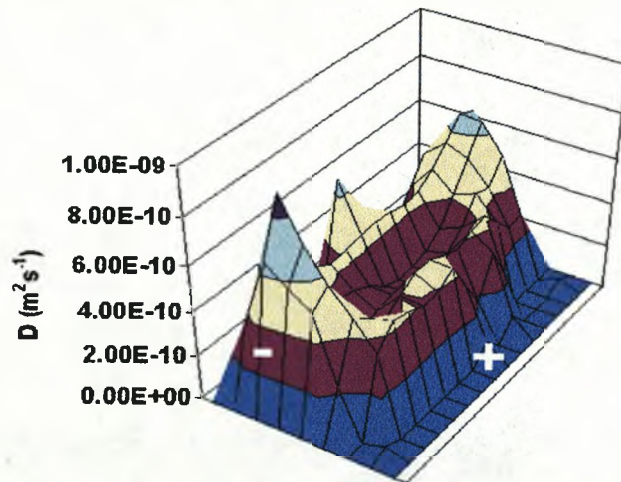
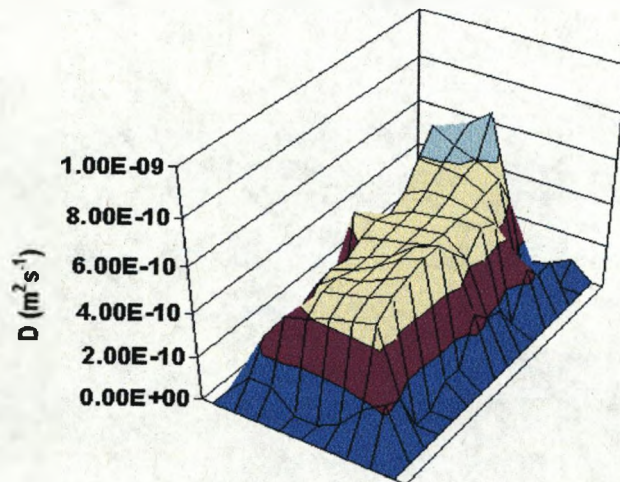


Figure 7.11. Continued.

c(iii)



d(i)



d(ii)

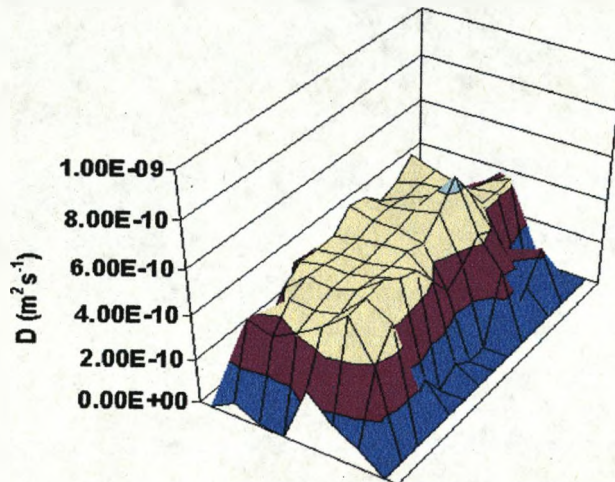
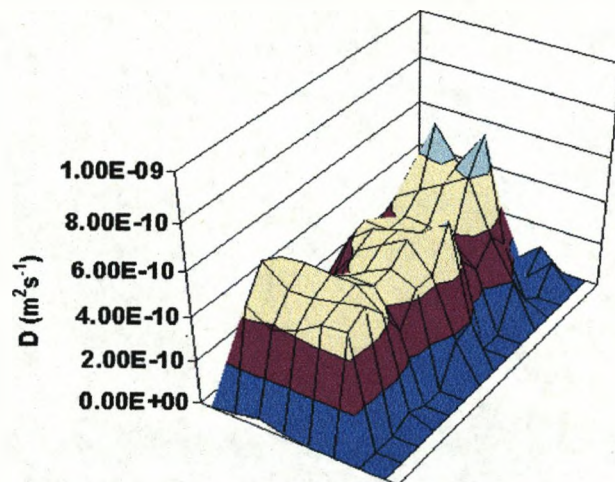
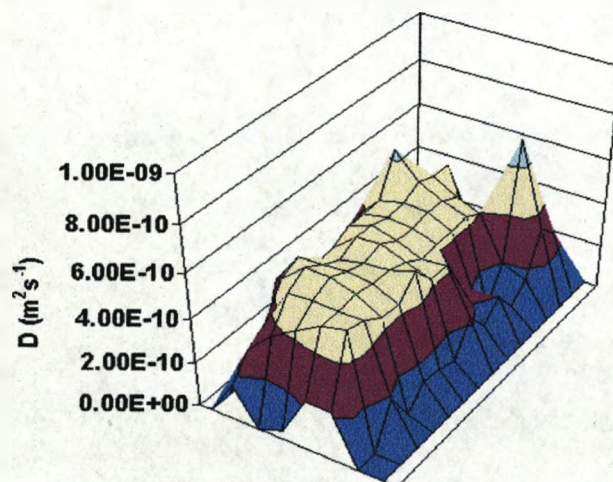


Figure 7.11. Continued.

d(iii)



d(iv)



d(v)

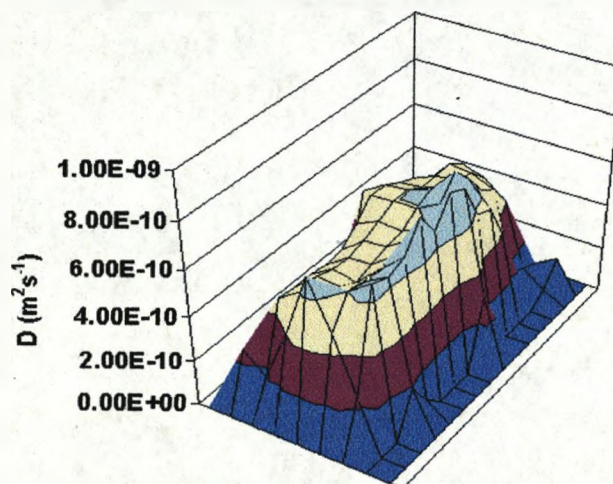


Figure 7.11. Continued.

at the surfaces and at the centre of the sample. Figure 7.11(d) (ii)-(iv) show that, over time, the values of D_x over the sample do not remain stable, but alter from map to map. It seems that water molecules continue to diffuse in different directions before the sample can re-attain its equilibrium state. After 65 h (Figure 7.11(d(v))), the spatial variation of D_x over the whole sample returns to some extent to its equilibrium state, becoming similar to the situation observed in Figure 7.11(a(i)), before the potential was applied, that is, with higher D_x at the surfaces and lower D_x at the centre of the sample. Despite the initial difference observed between the spatial variation of D in D_x - and D_z - maps of the AuPt₁Cast sample (Figure 7.7) the spatial variation of D_z in the D_z -maps (Figure 7.12(a)-(d)) also undergoes similar changes, during the consecutive electrical regimes imposed on the sample. That is, the region of high D_z is always observed near the cathode and the region of low D_z near the anode. It can also be observed that the spatial variation of D_z within the sample returns approximately to its equilibrium state (Figure 7.12(a(i))) 65 h after removing the applied potential (Figure 7.12(d(v))). However, the intensities in the D_z -maps in Figure 7.12 appear generally lower than those in the equivalent D_x -maps shown in Figure 7.11. The lower intensity in D_z - maps might be caused by more resistance to diffusion along the thickness of the sample.

To facilitate comparison of the changes that occur in D in the D_x - and D_z - maps throughout the four imposed electrical regimes, average D_x and D_z ($D_x(av)$ and $D_z(av)$, respectively) values were calculated at all distances along the z -axis (see Figure 7.1), *i.e.* through the thickness of the sample. Plots of these averages are given in Figures 7.13 and 7.14. These figures illustrate the changes that take place in average D ($D(av)$) over time, (a) with no potential applied (b) after application of 3V d.c. continuous potential, (c) after the polarity

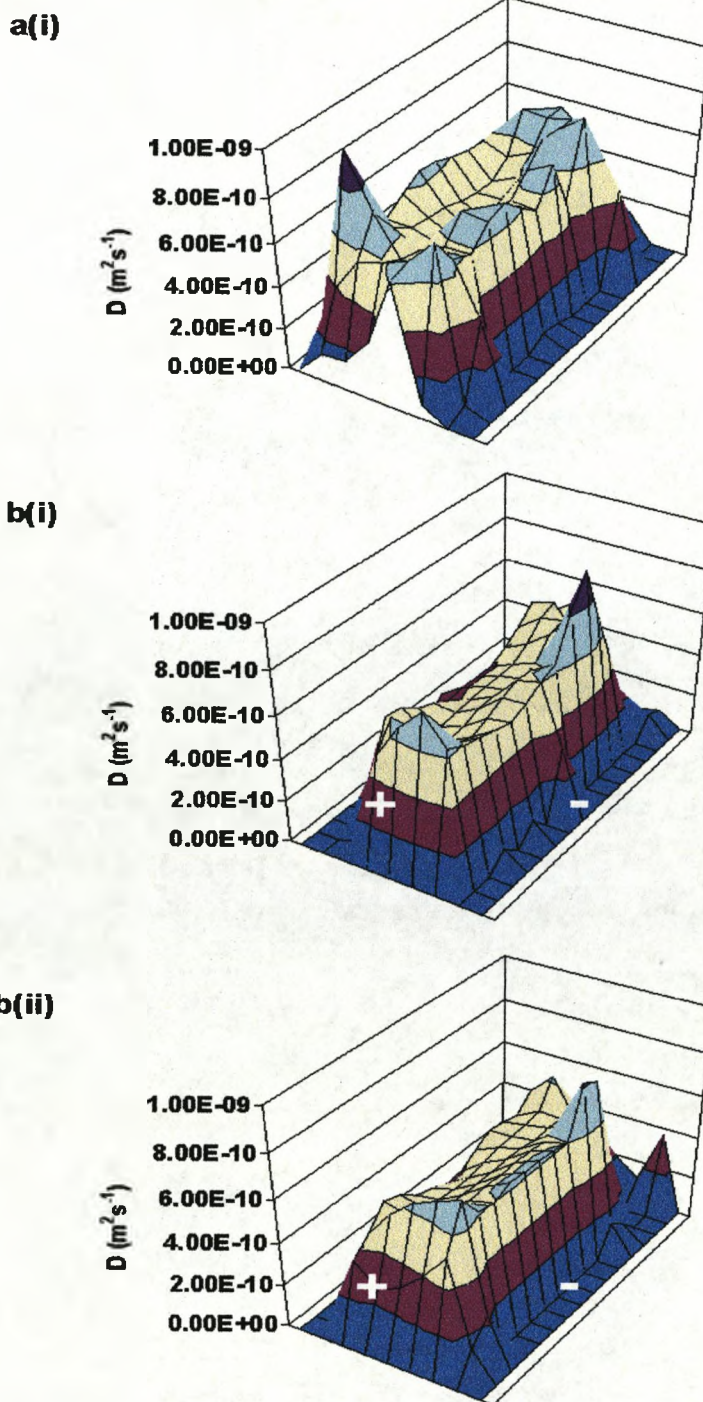
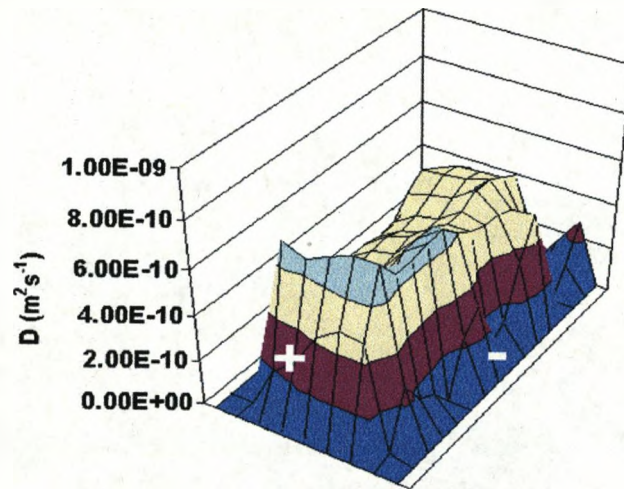
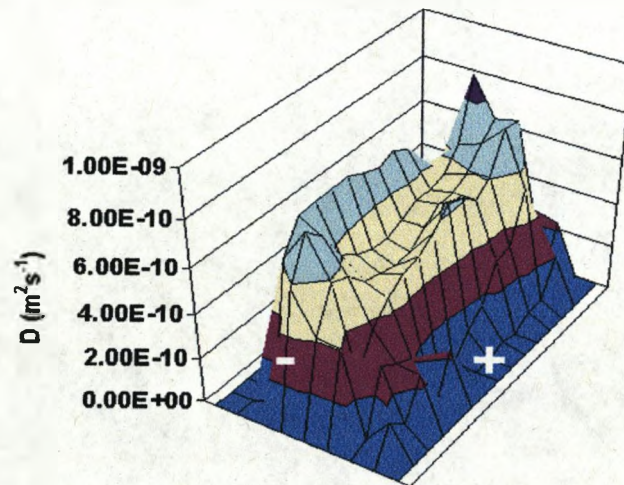


Figure 7.12. D_z -maps of AuPt₁Cast sample: (a)(i) with no potential applied; (b) (i) 0 (ii) 21 (iii) 42 min. after application of a 3V d.c. continuous potential in the sense indicated; (c) (i) 0 (ii) 21 (iii) 42 min. after reversal of the polarity of the 3V d.c. potential; (d) (i) 0 min. (ii) 21 min. (iii) 84 min. (iv) 147 min. (v) 65 h. after the potential was switched off. The negative “-” and positive “+” signs in these images indicate the cathode and anode side of the sample, respectively.

b(iii)



c(i)



c(ii)

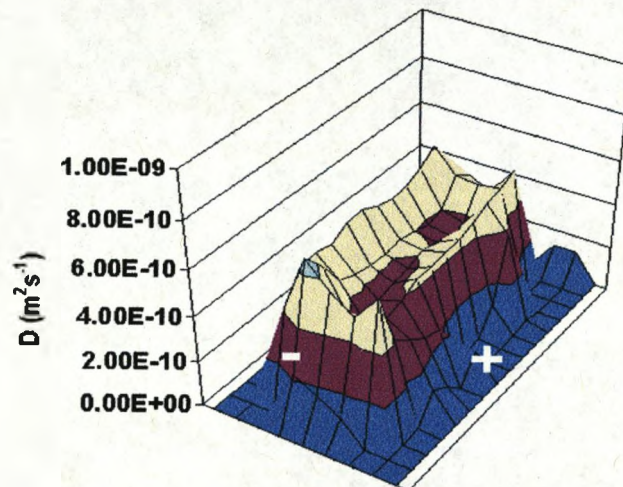
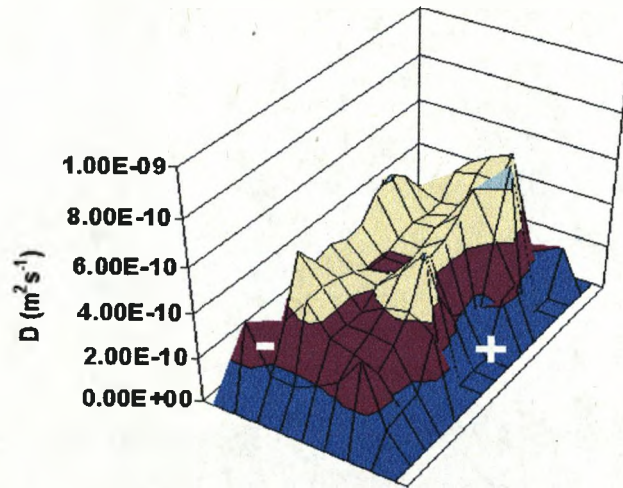
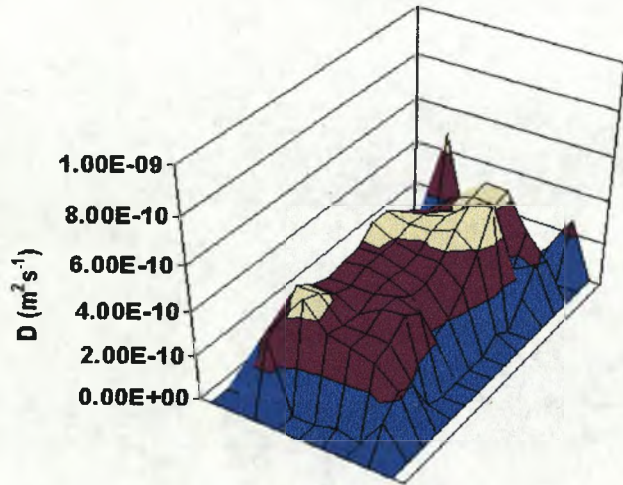


Figure 7.12. Continued.

c(iii)



d(i)



d(ii)

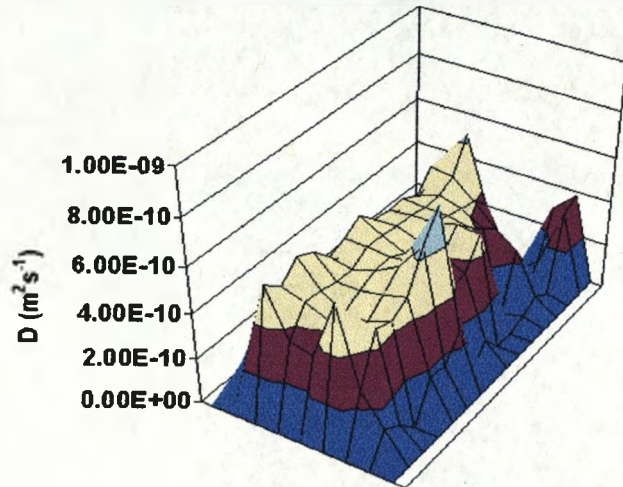
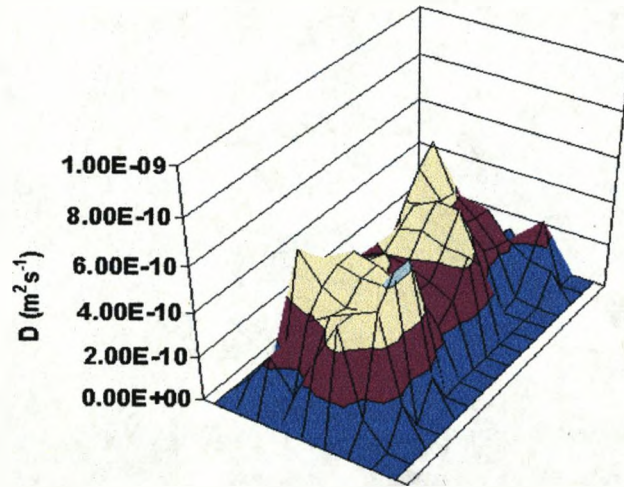
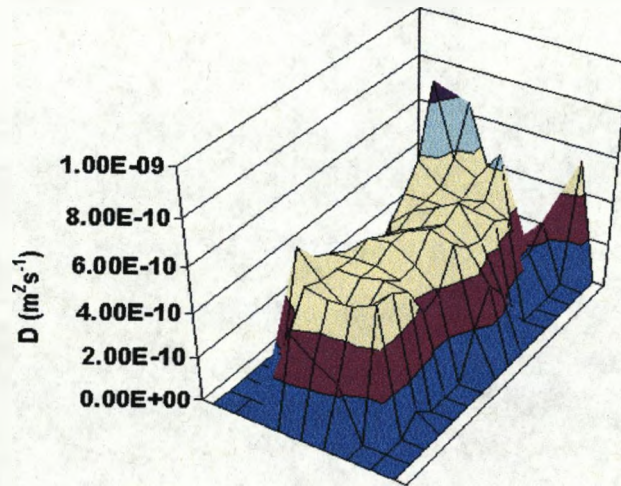


Figure 7.12. Continued.

d(iii)



d(iv)



d(v)

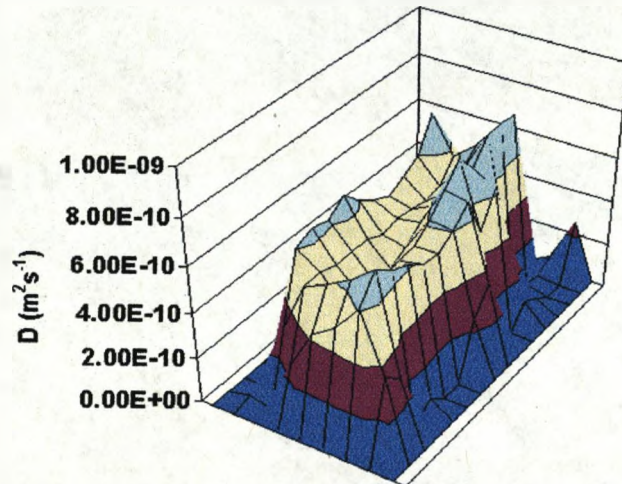


Figure 7.12. Continued.

of the applied potential was reversed, and (d) when power was switched off. Figures 7.13 and 7.14(b)-(d) include a plot of $D(av)$ with no potential applied as a reference. As was observed before in Figure 7.8, $D(av)$ remains similar across the whole sample, over time, when no potential is applied (Figure 7.12(a) and 7.13(a)). As soon as the potential is applied, $D_x(av)$ increases significantly over the sample and mainly near the cathode (Figure 7.13(b)). Figure 7.14(b) shows that the application of potential has a qualitatively similar but lesser effect on the spatial variation of $D_z(av)$. A very similar scenario is observed for $D_x(av)$ and $D_z(av)$ after the polarity of the applied potential is reversed (Figures 7.13(c) and 7.14(c)). These figures also show that after 42 min., $D_x(av)$ and $D_z(av)$ start to decrease over the whole sample while retaining their differences near the cathode and anode. Once the applied potential is removed (Figure 7.13(d) and 7.14(d)), the spatial variation in $D_x(av)$ and $D_z(av)$ become almost flat over the whole sample. When the potential is switched off, there is no significant change in the level of the $D_x(av)$ while a large decrease in the level of $D_z(av)$ over the sample is observed. Over time at zero potential, the $D_x(av)$ and $D_z(av)$ values increase over the whole sample, becoming more similar to those seen in the sample before the potential was applied. These differences are summarized in the plots shown in Figure 7.15 where the changes that occurred in $D_x(av)$ and $D_z(av)$ are compared exactly at the time the electrical regimes were changed.

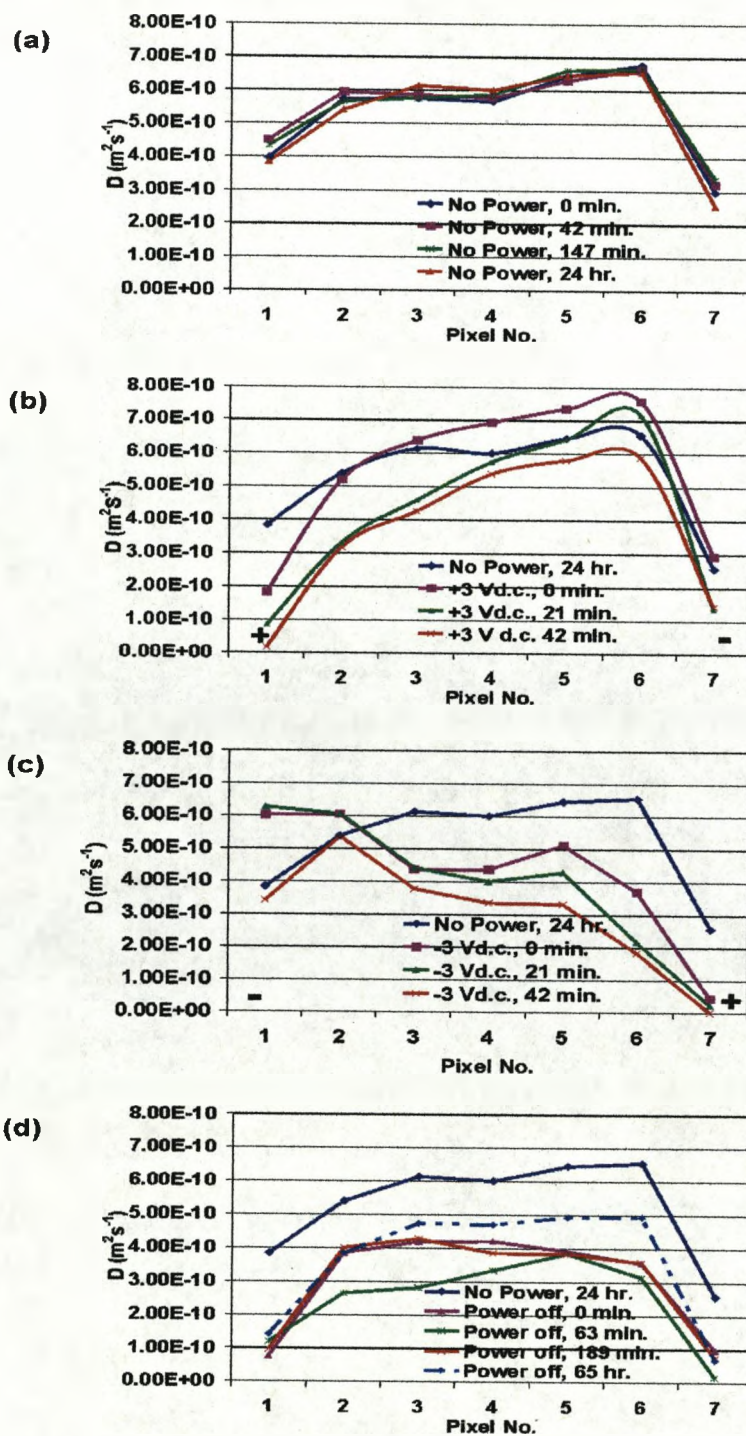


Figure 7.13. Changes occurring over time in $D_x(av)$: (a) with no potential applied; (b) after application of 3V d.c. continuous potential; (c) after the polarity of the applied 3V d.c. potential was reversed; and (d) after removal of the applied potential. The negative “-” and positive “+” signs in these images indicate the cathode and anode side of the sample, respectively.

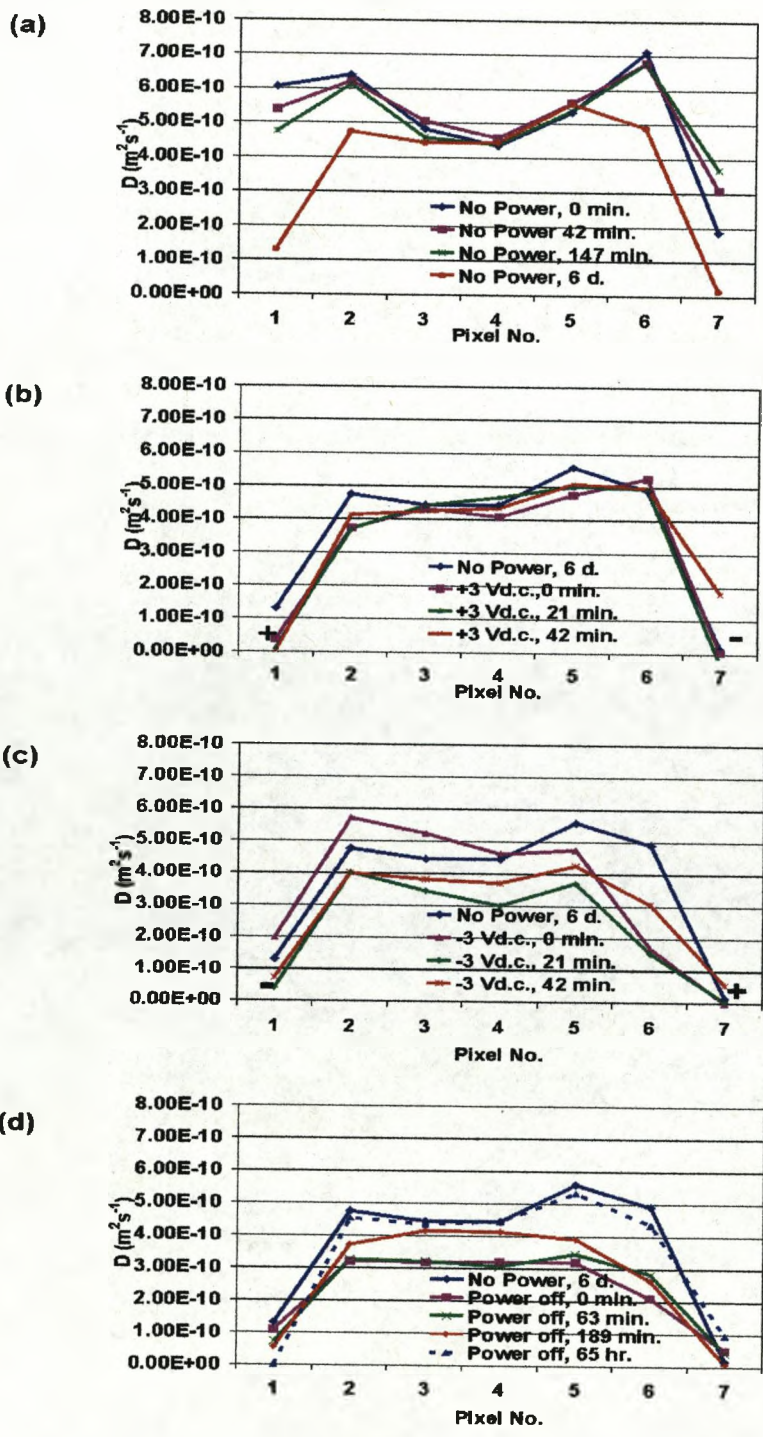


Figure 7.14. Changes occurring over time in $D_z(av)$: (a) with no potential applied; (b) after application of 3V d.c. continuous potential; (c) after the polarity of the applied 3V d.c. potential was reversed; and (d) after removal of the applied potential. The negative “-” and positive “+” signs in these images indicate the cathode and anode side of the sample, respectively.

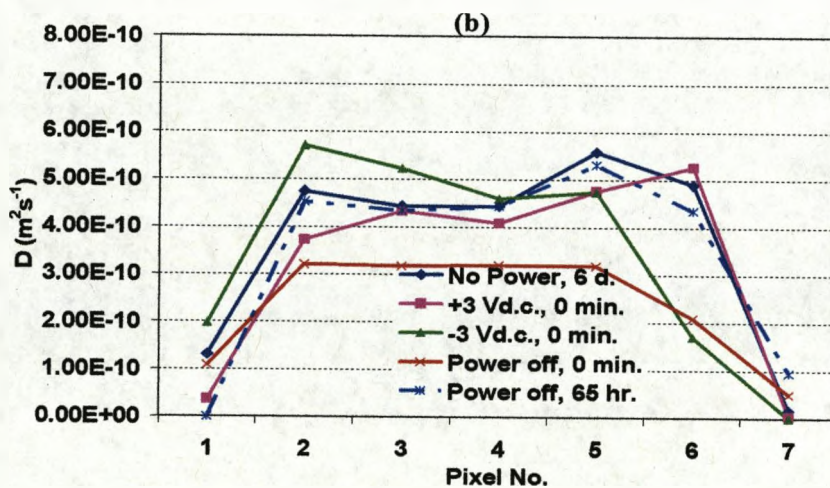
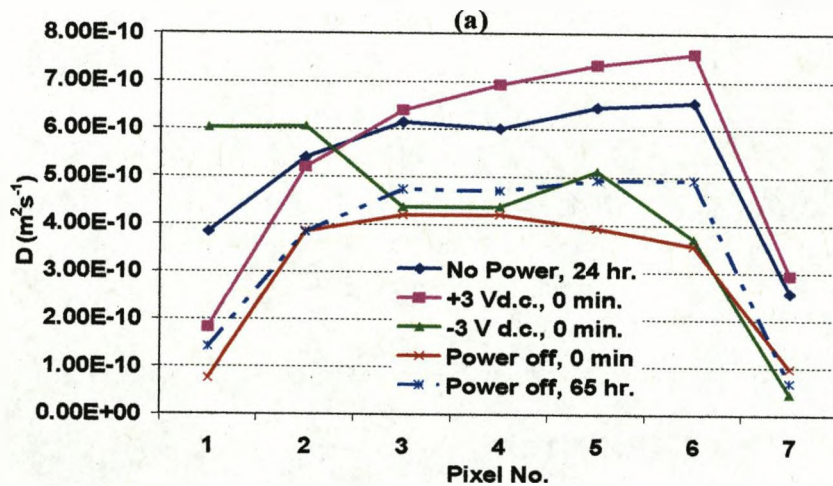


Figure 7.15. Changes occurring in (a) $D_x(av)$ and (b) $D_z(av)$, over the four imposed electrical regimes.

Values of $D(av)$ were also extracted from the same small regions of the D_x - and D_z maps in each of the four different potential regimes. These values are shown in Table 7.4 and 7.5, respectively. In the both tables, in the absence of an applied potential the $D(av)$ is similar at the surfaces while it is lower at the centre. On application of the potential, $D(av)$ increases

over the whole sample and mainly near the cathode, and decreases at the anode. On reversal of the polarity of the applied potential, this trend is reversed and the $D(av)$ becomes higher near the new cathode, and lower near the new anode. When the potential is removed, $D(av)$ increases near the anode and decreases near the cathode and the spatial variation of $D(av)$ becomes relatively flat over the sample. After 65 h, the $D(av)$ increases over the sample and particularly at the surfaces. The difference between the $D(av)$ at the surfaces and the centre of the sample (after 65 h) almost exactly mirrors the difference in the sample before any potential was applied. Comparison of the values presented in Tables 7.3 and 7.4 reveal that values of $D_z(av)$ are always smaller than those of $D_x(av)$ and that smaller changes occur in the $D_z(av)$ near the cathode and anode. Nevertheless, the changes in $D_z(av)$ under different electric regimes are qualitatively similar to those seen in $D_x(av)$.

Table 7.4. Selected $D_x(av)$ values for AuPt₁Cast IPMC sample.

D (m ² s ⁻¹) at:	Left surface	Centre	Right surface
No power (after 24 h)	5.74×10^{-10}	6.01×10^{-10}	6.55×10^{-10}
Power on + 0 min.	5.15×10^{-10} ^a	6.92×10^{-10}	7.57×10^{-10} ^c
Reversal of polarity + 0 min.	6.06×10^{-10} ^c (new cathode)	4.37×10^{-10}	3.84×10^{-10} ^a (new anode)
No power + 0 min.	3.94×10^{-10}	4.21×10^{-10}	3.55×10^{-10}
No power + 65 hr.	4.74×10^{-10}	4.71×10^{-10}	4.94×10^{-10}

^aactive anode; ^cactive cathode

Table 7.5 Selected $D_z(av)$ values for AuPt₁Cast IPMC sample.

D (m ² s ⁻¹) at:	Left surface	Centre	Right surface
No power (after 6 d)	4.74×10^{-10}	4.44×10^{-10}	5.10×10^{-10}
Power on + 0 min.	3.70×10^{-10} ^a	4.08×10^{-10}	5.37×10^{-10} ^c
Reversal of polarity + 0 min.	5.70×10^{-10} ^c (new cathode)	3.00×10^{-10}	1.70×10^{-10} ^a (new anode)
No power + 0 min.	3.25×10^{-10}	3.19×10^{-10}	2.09×10^{-10}
No power + 65 hr.	4.52×10^{-10}	4.43×10^{-10}	4.35×10^{-10}

^aactive anode; ^cactive cathode

7.4. Discussion

Self-Diffusion of Water in Cast Nafion Membrane

As results presented in Section 7.3.1 revealed, water molecules absorbed in the cast Nafion sample possess very similar diffusion coefficients, D , regardless of the orientation of the measurements. This can be seen in D_x - and D_z - maps of the sample presented in Figure 7.4(a) and (b), respectively. Distribution of similar values of D over these two maps suggests that this sample has a homogenous structure. The similar values of $D_x(av)$ and $D_z(av)$ also revealed that the water molecules in the cast Nafion membrane enjoy a similar degree of freedom to diffuse along the length (x-axis) and the thickness (z-axis) of the sample. Since the measured D for water molecules within the cast Nafion sample was independent of the orientation of the measurements the diffusion of water molecules in this

sample is considered to be isotropic.² In an isotropic environment the measured D does not depend on the direction of the applied gradient.²

$D(av)$ in the cast Nafion membrane was about $6.09 \times 10^{-10} \text{ m}^2 \text{ s}^{-1}$. This value is close to the measured D for water molecules within wheat grains⁴ of between 5×10^{-10} and $1 \times 10^{-9} \text{ m}^2 \text{ s}^{-1}$. However, $D(av)$ in the cast Nafion sample is about four times smaller than the D of pure bulk water,⁵ $2.5 \times 10^{-9} \text{ m}^2 \text{ s}^{-1}$. Diffusion of water molecules occurs according to Fick's first law.¹ According to this law, the fundamental physical process of transport is the random motion of the molecules in a fluid due to thermal or concentration gradients. For self-diffusion of water molecules, however, there is no net concentration gradient. A molecule which is at a location r_0 at $t=0$ can undergo an unpredictable succession of translations and reach location r at $t>0$.^{1,6} Thus, it is difficult to define the location of the molecule which has undergone the self-diffusion. According to Einstein's law, Equation (7.1), the molecule is expected to locate somewhere within a sphere of radius $(r-r_0)$ at time t .⁶

$$(r - r_0) = \sqrt{6Dt} \quad (7.1)$$

where D is the diffusion coefficient of the molecule. This equation is only applicable for diffusion of water molecules in a homogenous region. If time t in the above equation is replaced with Δ , the time between the gradients, the distance traveled by water molecules in this period can be calculated. According to this Equation, during the time scale Δ of 5.109 ms, used for the DWI of the cast Nafion sample, the distance traveled by a diffusing water molecule is about 4.31 μm , which is approximately half the distance that a water molecule can travel at this time scale in pure bulk water, 8.75 μm . This might be explained as follows. In pure bulk water each molecule is in continuous motion in every possible direction, due to random Brownian motion, initiated by thermal energy.^{1,6} Water molecules

within the polymer also undergo Brownian motion and diffuse in the period during which the pulsed gradients are applied. However, within the Nafion membrane the Brownian motion (self-diffusion) of water molecules is restricted, probably due to the presence of distinct hydrophobic and hydrophilic regions. This means that the self-diffusion of water molecules is restricted by boundaries and interfaces in the cast Nafion sample. However, since the D_x and D_z are very close it can be said that this restriction is similar along the length (x-axis) and thickness (z-axis) of the sample, and that the diffusion process is very similar.

Self-Diffusion of Water in AuPt₁Cast IPMC, Regime (a)

As results presented in Section 7.3.2 showed, unlike in the non-electroded cast Nafion sample, the spatial variation of D over the AuPt₁Cast sample was not uniform. This was observed as darker sample surfaces and brighter sample centre in the images shown in Figure 7.5 and also in the spatial variation of D_x and D_z in the corresponding D_x - and D_z -maps of the sample (Figure 7.7). This reveals that water molecules absorbed in the AuPt₁Cast sample possess dissimilar D depending on their location in the sample. Water molecules located at the surfaces, where the sample contains a high percentage of platinum particles, diffuse at a higher rate than those located at the centre of the sample, where the sample contains little or no platinum particles. The observed difference between the measured D at the surfaces and the centre of the sample cannot be attributed to the different level of hydration of the sample at these two regions since a very uniform distribution of

protons was observed in the *PD* map of the sample presented in the previous chapter, Figure 6.2(a(i)).

Anisotropic Self-Diffusion of Water in AuPt₁Cast IPMC, Regime (a)

Researchers have shown that diffusion in organs and tissues with ordered structure such as skeletal and cardiac muscles depend on the direction in which the diffusion gradients are applied. They have also reported how this dependency provides important information about the architecture of normal and pathological tissue.² As was seen in Figure 7.7, the difference between the *D* at the surfaces and the centre of the sample appears much larger when the pulsed gradients were applied across the sample thickness (*z*-axis), showing the dependency of the measured diffusion on the orientation of the measurements and, thus, implying anisotropic^{1,2} diffusion of water molecules in this sample. Similar values of *D_x* ($6.57 \times 10^{-10} \text{ m}^2\text{s}^{-1}$) and *D_z* ($6.72 \times 10^{-10} \text{ m}^2\text{s}^{-1}$) were observed at the surfaces while these values were very different at the centre of the sample. *D_x* and *D_z* at the surfaces of the AuPt₁Cast sample were also higher than was measured in the cast Nafion sample. As was described in Chapters Four and Six, platinum particles coagulate near the surfaces of the sample where the concentration of these particles is high and produce larger particles of approximately 50 nm diameter. Since the size of these particles is about 10 times larger than the size of the hydrophilic regions, 5 nm,^{7,8} water molecules trapped in or around these large particles would be expected to diffuse faster than those molecules within the hydrophilic regions of the sample. This suggestion can explain the higher diffusion coefficient of water molecules at the surfaces than at the centre of the sample and also the

similarity of D_x and D_z at the surfaces, since water molecules here would act more like free water and can diffuse almost at the same rate along both axes.

Despite the similarity of the values of D_x and D_z at the surfaces, these values were different at the centre of the AuPt₁Cast sample, D_x ($6.01 \times 10^{-10} \text{ m}^2\text{s}^{-1}$) being much higher than D_z ($4.44 \times 10^{-10} \text{ m}^2\text{s}^{-1}$) in this region. This difference suggests that the diffusion of water molecules at the centre of the sample, where the concentration of platinum particles is approximately zero, faces more barriers along the sample thickness, than along the length of the sample. Krivandin and colleagues⁹ have suggested a bilayer structure formed by pairwise association of perfluorinated molecular backbone regions and sulfonic acid side chains. In this model, bilayers of molecular backbone chains with side chains are separated by aqueous layers. Side chains terminated by ionic groups protrude into the aqueous layers and clusters are formed by ionic groups on each side of a molecular backbone bilayer.⁹ The phase containing water and the acid sites is also separate from the molecular backbone. If these layers were aligned across the thickness of the membrane, the diffusion of water molecules along the layers (along the length of the sample, in this work) should be much faster than that across the thickness of the sample, where their diffusion would be more restricted by interfaces between regions. Consequently, the measured D_x and D_z in the cast Nafion sample would also be significantly different. However, as was seen in Figure 7.4, there was no significant difference between these two values in the cast Nafion sample. This implies that the structure of the cast Nafion sample is not ordered in this way and that the diffusion of water molecules is restricted to the same degree along both directions. Thus, the difference observed between D_x and D_z at the centre of the AuPt₁Cast sample must be attributed in some way to the presence of the platinum particles. It is accepted¹⁰

that , platinum impregnation of Nafion at the surfaces leads to an increase in the stiffness of the polymer. If we consider that the presence of coagulated platinum particles act at the surfaces like “pins”, the observed difference between D_x and D_z at the centre of the AuPt₁Cast sample might be explained in terms of differential shrinkage of the sample on going from the aqueous solution to the air environment. When the sample is transferred from the saturated solution of LiOH to the sample holder in these experiments (see Section 7.2) it is exposed to the air environment. This would cause partial dehydration of the sample. It is thought that during this dehydration the platinum particles prevent contraction of the Nafion membrane in the x-axis direction but not in the z-axis direction. This gives rise to a larger number of interfaces per unit length in the z-direction than in the x-direction. Thus, it is expected that the diffusion of water molecules be more restricted along the sample thickness (z-axis) since there are more interfaces and barriers in this direction. This is observed as much smaller D_z ($4.44 \times 10^{-10} \text{ m}^2\text{s}^{-1}$) than D_x ($6.01 \times 10^{-10} \text{ m}^2\text{s}^{-1}$) at the centre of the AuPt₁Cast sample.

D_x at the centre of the AuPt₁Cast sample is very similar to the D_x in the cast Nafion which is in good agreement with the explanations given above.

Electrically-Induced Diffusion of Water in AuPt₁Cast IPMC, Regimes (b) and (c)

As was seen in Figure 7.8, before a potential was applied, the spatial variation of D_x and D_z in the AuPt₁Cast sample and the difference between these values remained the same over time. This reveals first, that the sample retains its unique ordered structure along its length

and thickness, over time, and, second, that the differences observed in the spatial variation of D_x and of D_z over the whole sample and of their values are genuine and reproducible.

As soon as the potential was applied, the spatial variations of D_x and D_z over the sample were disturbed and the rate of diffusion of water increased near the cathode. This increase appeared much larger in D_x than D_z (Figure 7.11 and 7.12). Comparison of the data presented in Tables 7.4 and 7.5, and in Figures 7.13 to 7.15 also showed that under the influence of the applied potential, much larger changes occurred in the spatial variation of D_x (Figure 7.11) than in D_z (Figure 7.12). This suggests that, as for the self-diffusion of water, the diffusion of water molecules after application of the potential is more restricted along the sample thickness (z-axis) than along its length, and that water molecules would therefore be expected to diffuse towards the cathode along rather a “zigzag” pathway.

D -maps presented in Figure 7.11 and 7.12 – parts (b) and (c) – show that, after application of the potential, the general increase in the diffusion coefficient of water molecules over the whole sample and mainly near the cathode was over time followed by an overall decrease in the average diffusion coefficient of water over the sample, while high D values were still observed near the cathode. This suggests that the diffusion becomes generally more restricted over the whole sample, over time. This might be explained by overall shrinkage of the sample through this extended experiment, due to dehydration.

Self-Diffusion of Water in AuPt₁Cast IPMC after Removal of the Applied Potential, Regime (d)

When the applied potential was removed much larger changes occurred in the spatial variation of $D_z(av)$ than $D_x(av)$ over the whole sample (Figure 7.15(a) and (b)). $D_z(av)$ quickly decreased over the whole sample, and especially near the cathode, while similar decreases happened only to a lesser extent in D_x . This suggests that, during the application of the applied potential, water molecules are forced to diffuse through high energy routes across the thickness of the sample. As the electric field, the force, is removed the water molecules generally avoid these routes and diffuse more through lower energy routes, of which there are more along the length of the sample (x-axis).

D_x - and D_z - maps shown respectively in Figure 7.11 and 7.12(d) – parts (i)-(v) – showed that, unlike the sample with no potential applied (Figure 7.8), after the removal of the applied potential the spatial variation and also the values of D_x and D_z alter over time and that the spatial variation of D became more stabilized and similar, after 65 h, to that in the sample before the potential had been applied. These changes were also observed clearly in Figures 7.15(a) and (b). The values of D_x and particularly D_z interestingly increased to approximately similar values to those seen at the beginning of the experiment. These changes indicate that the sample is able to return almost to its original state, before the potential had been applied. This might be explained by uptake of water by the sample from the moist environment maintained inside the NMR tube. The reason why D_x does not as close as get as close as D_z to its original values may be that the platinum layer is partly cracked during the bending deformation of the sample, so losing some of its rigidity,

allowing the sample to contract in the x-direction and increasing the resistance to diffusion along the sample length.

7.5. Summary

Self-diffusion of water molecules in the cast Nafion sample, and self- and electrically-induced diffusion of water in the AuPt₁Cast sample were monitored using the diffusion-weighted imaging (DWI) technique. Results of these experiments revealed that water diffusion in the cast Nafion sample was isotropic while in the AuPt₁Cast sample it was orientation-dependent, or anisotropic. This was explained in terms of the presence of platinum particles in this sample. Water molecules located at the surface, where the concentration of platinum was high, showed higher D compared to water molecules at the centre of the sample, where there was little or no platinum. Similar values of D_x and D_z were measured at the surfaces of the sample while D_x was significantly higher than D_z at the centre of the sample. This was explained in terms of differential shrinkage of the sample because of the rigid platinum layers. It is thought that this would give rise to more barriers to diffusion in the z-axis than the x-axis direction because, on going from aqueous solution to the air environment of these experiments, the Pt layer would prevent contraction in the x-direction but not in the z-direction. The difference observed between the measured D at the surfaces and at the centre of the sample remained the same, over time, when no potential was applied. This difference was disturbed once an electric field was applied across the thickness of the sample, and regardless of the axis of the measurements, higher D was always observed near the cathode. D_x was higher than D_z near the cathode. Electrically-

induced diffusion of water molecules was also more restricted across the thickness of the sample. Once the applied electric field was removed, the spatial variation of D_x and D_z , slowly came to resemble the situation observed before the potential had been applied.

7.6. References

-
- [1]. P. T. Callahan, "Principles of Nuclear Magnetic Resonance Microscopy", *Clarendon Press . Oxford*, New york, 1991.
 - [2]. S. Mori, P. B. Barker, *Anat. Rec. (New Anat.)*, 1999, 257, 102.
 - [3]. H. Van As, *Journal of Experimental Botany*, 2006, doi:10.1093/jxb/erl157.
 - [4]. C. D. Eccles, P. T. Callaghan, *Biophys. J.*, 1998, 53, 77.
 - [5]. J. A. Chudek, G. Hunter, *Progress in Nuclear Magnetic Resonance Spectroscopy*, 1997, 31, 43.
 - [6]. K. T. Yung, *Magnetic Resonance Imaging*, 2003, 21, 135.
 - [7]. H. J. Yeager, A. Eisenberg, *American Chem. Soc.*, 1982, 180(1), 41.
 - [8]. R. Dulesix, M. Escoubes, B. Rodmacq, F. Volino, E. Roche, A. Eisenberg, M. Pineri, *American Chem. Soc.*, 1980, 127, 469.
 - [9]. A. V. Krivandin, A. B. Solov'eva, N. N. Glagolev, O. V. Shatalova, S. L. Kotova, *Polymer*, 2003, 44(19), 5789.
 - [10]. S. Nemat-Nasser, Y. Wu, *J.Appl. Phys.*, 2003, 93(9), 5255.

Chapter Eight

Electromechanical Tests

8.1. Introduction

As was mentioned earlier, the development and future application of IPMC materials, as actuators, requires our best knowledge of their physical structure, actuation mechanism and factors influencing their electromechanical behavior. In previous chapters, physical structure and actuation mechanism of these materials were extensively studied, using SEM, NMR and MRI. In this chapter, the electromechanical characteristics of these materials, including their tip displacement (see also Section 3.7.3) and force output, in response to electrical stimuli is investigated.

8.2. Experimental

Samples used in these experiments were Li^+ -exchanged Pt_1Com , Pt_2Com , Pt_3Com , Pt_4Com , AuPt_2Com , AuPt_4Com (prepared based on the thin commercial Nafion membrane), and Pt_2Cast , Pt_4Cast , AuPt_2Cast , and AuPt_4Cast (prepared based on the thick cast Nafion membrane). The subscript refers to the number of electroless platinum electroding cycles. Table 3.1 provides detailed information on the processing of these samples. Samples with the same standard width of 8 mm and length of 38 mm were prepared in order to study the effect of the thickness of the Nafion membrane, electrode thickness and surface conductivity on the electromechanical behavior of IPMC materials. The tip displacement and force output of these samples were examined by applying sinusoidal alternating voltages across their thicknesses. These experiments were performed using the experimental setup described in Sections 3.7.3 and 3.7.4 for displacement and force output

measurements, respectively. To investigate the voltage- and frequency-dependence of the electromechanical characteristics of the IPMC samples sinusoidal input voltages of 2, 3, 4, 5, 6, 8 and 10 V in amplitude, alternating at frequencies of 0.1, 0.2, 0.4, 0.6, 0.8, 1, 2, 4, 6, 8, 10 Hz, were applied to the samples. In order to obtain a more precise estimate of the maximum tip displacement and force output of the samples, the amplitude of the input voltage was increased with a time interval of 24 h. During this time the samples were taken out of the sample holder (see Figure 3.4) and stored in a saturated solution of LiOH to allow them to become fully hydrated and re-activated before application of the higher amplitude alternating voltages. The frequency of each alternating voltage was decreased from 10 to 0.1 Hz with a time interval of 20 s during the application of each input voltage. In the force measurements, the generated force and current response to the applied sinusoidal voltage were simultaneously monitored as a function of time in order to study the electrical characteristics of the samples.

8.3. Results and Analysis

8.3.1. Displacement Measurements

8.3.1.1. Commercial IPMC Samples

The measured tip displacements of the samples (a) Pt₁Com, (b) Pt₂Com, (c) Pt₃Com and (d) Pt₄Com in response to the sinusoidal voltages of 2, 3, 4, 5, 6, 8 and 10 V in amplitude and over a frequency range of 0.2 to 10 Hz are shown in Figures 8.1 and 8.2. These figures represent the results obtained as a function of the amplitude of the applied sinusoidal

voltages and their frequency, respectively, in order to evaluate the voltage- and frequency-dependence of the tip displacement of the samples. As Figure 8.1 – parts (a) to (d) illustrates, these samples exhibit very similar dependency upon the amplitude and frequency of the applied sinusoidal voltages. The samples undergo increasing tip displacements as the amplitude of the sinusoidal input voltage increases. In Figure 8.1 – parts (a) to (d) – an essentially monotonic relationship between the measured tip displacement and the amplitude of the applied voltage is observed. The largest tip displacements occur when the highest amplitude input voltage is applied. It should be noted that, due to the instrumentation limitations, the highest amplitude of the sinusoidal voltage applied across the thickness of the samples Pt₃Com and Pt₄Com was 6 V. Figure 8.2 – parts (a) to (d) – shows that decreasing the frequency of the input voltages affects the tip displacement of all of the samples in similar way. The tip of the sample undergoes increasing displacements as the frequency of the input sinusoidal voltage decreases down to 0.2 Hz, while the lowest displacement is observed on the application of voltages at 10 Hz. There is a non-linear, approximately inverse relationship between tip displacement and frequency of the applied voltage. The sample Pt₁Com (part (a) in the figures) shows zero displacement at frequencies higher than 1 Hz, while the rest of the samples undergo small displacements.

To evaluate the effect of the electrode thickness on the actuation performance of IPMCs, the measured tip displacement of the samples with increasing number of electroless platinum electroding cycles, from 1 to 4 plating cycles, are plotted against the frequency of the applied voltage in Figure 8.3. Parts (a) to (f) of this figure compare the changes occurring in the tip displacement of these samples on increasing the amplitude of the applied

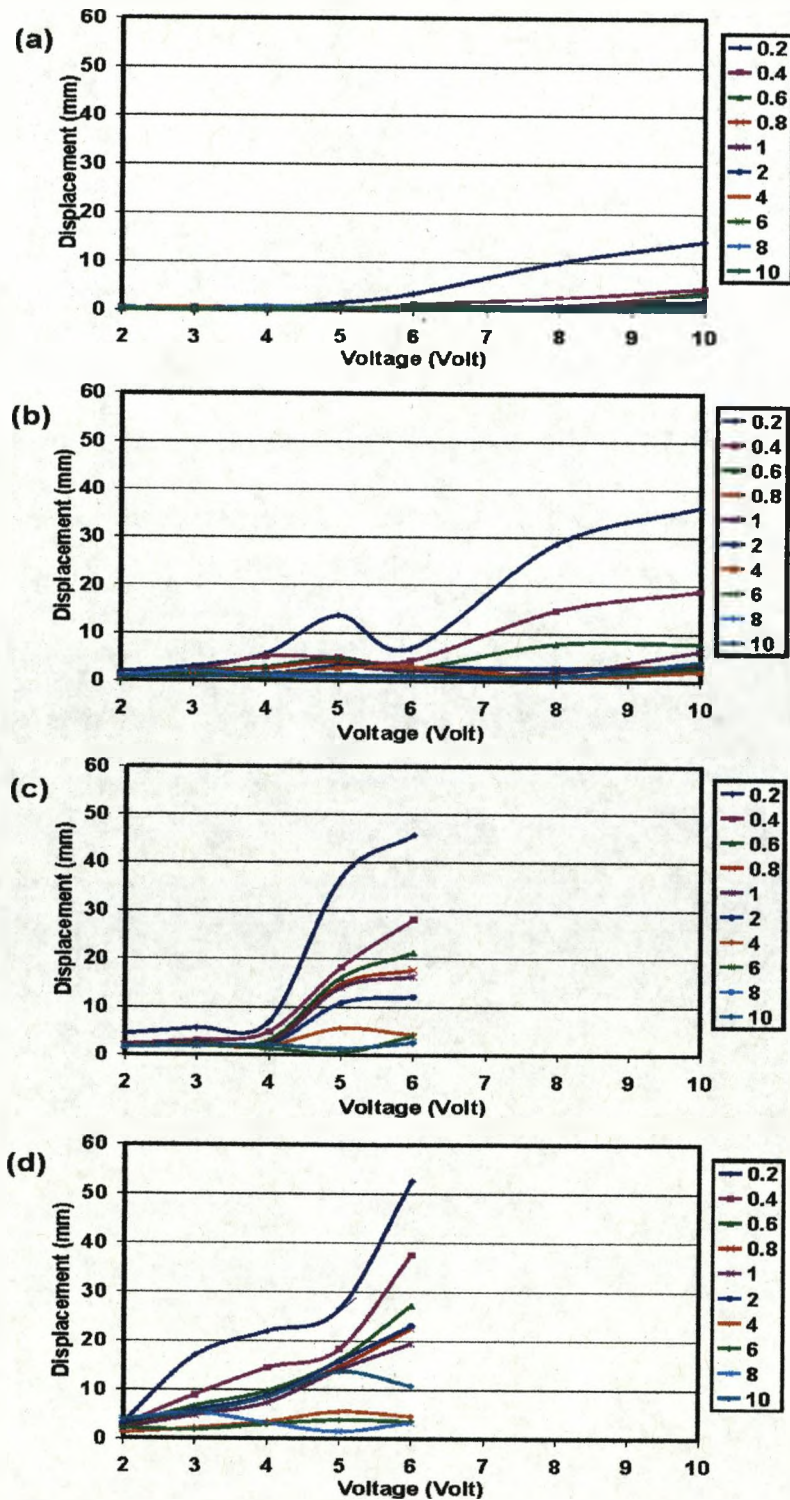


Figure 8.1. Voltage-dependence of the tip displacement of (a) Pt₁Com, (b) Pt₂Com, (c) Pt₃Com and (d) Pt₄Com IPMC samples for several applied voltage frequencies. Legends represent the frequencies of the applied voltages in Hz.

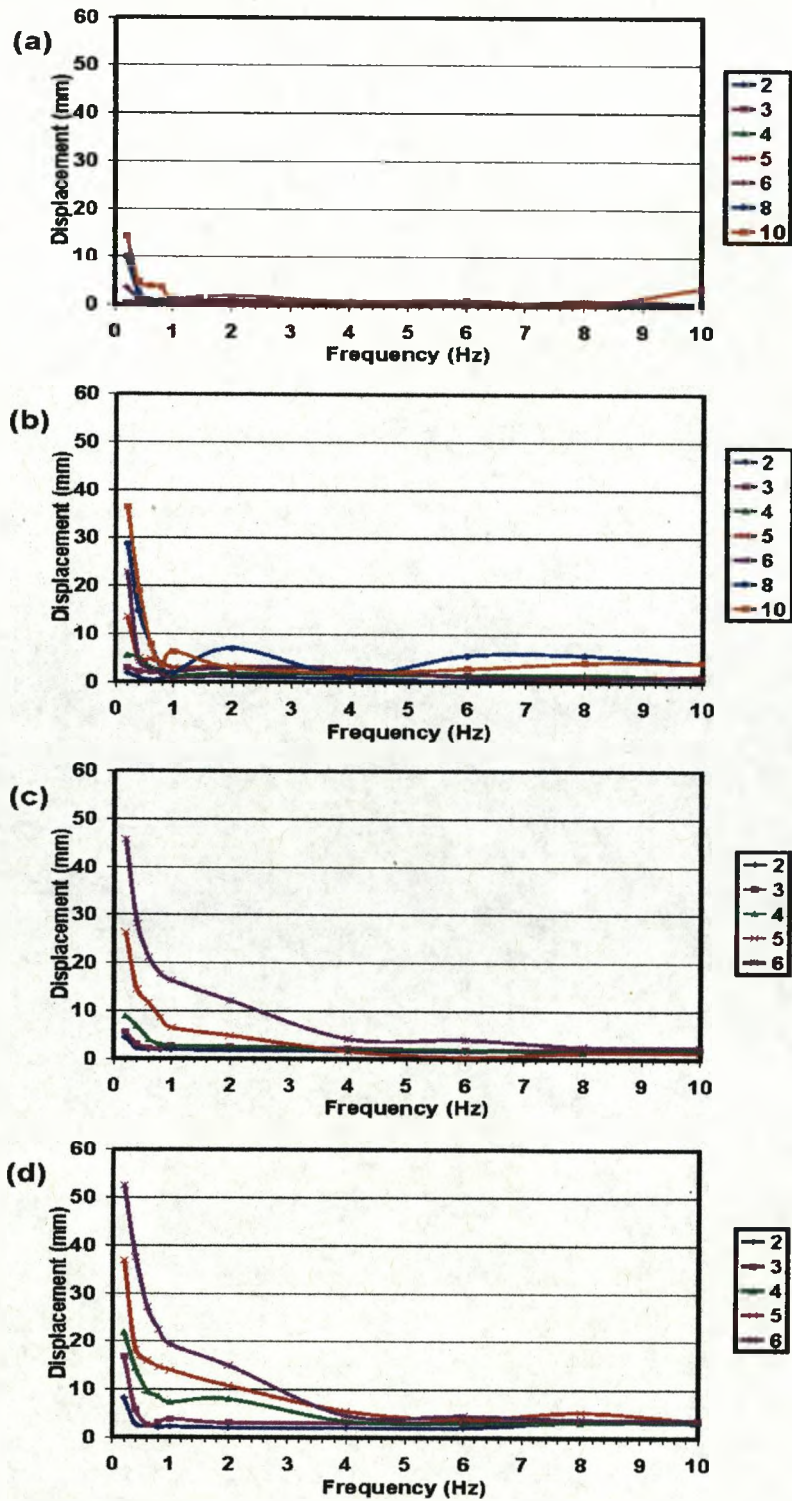


Figure 8.2. Frequency-dependence of the tip displacement of (a) Pt₁Com, (b) Pt₂Com, (c) Pt₃Com and (d) Pt₄Com IPMC samples for several applied voltages. Legends represent the amplitude of the applied voltages in V.

voltage, from 2 to 10 V. It can be seen that, at a constant frequency, as the number of plating cycles and consequently the thickness of the platinum electrodes at the surfaces of the IPMC polymer increases, the magnitude of the tip displacement increases significantly. Comparison of the tip displacement of the four samples on application of increasing applied voltages in parts (a) to (f) also reveals that the sample Pt₁Com, treated with 1 plating cycle, always underwent the lowest tip displacement in the series while Pt₄Com, treated with 4 plating cycles, exhibited the largest tip displacement. The increase in the amplitude of the applied voltage results in much larger increases in the tip displacements of Pt₄Com, which contains the thickest electrode layer. On the contrary, in the case of Pt₁Com, with the lowest electrode thickness at the surfaces, the effect of increasing the amplitude of the applied voltage, even at low frequencies (< 1 Hz), is much less significant.

In Figure 8.4 the tip displacements of the samples Pt₂Com and Pt₄Com are compared with that of the samples AuPt₂Com and AuPt₄Com when the same amplitude voltage is applied in order to study the effect of surface conductivity. The tip displacement of the samples is seen to increase in the order: Pt₂Com < AuPt₂Com < Pt₄Com < AuPt₄Com in this figure. AuPt₂Com and AuPt₄Com have the same thickness of platinum electrode as Pt₂Com and Pt₄Com, respectively. However, to improve their surface conductivity a thin gold layer was deposited by PVD on their surfaces after the platinum treatments. The tip displacements of these samples against frequency and in response to increasing amplitude of the applied voltage are shown in Figure 8.4, parts (a) to (f). In Figure 8.4(e) and (f) the displacement of Pt₂Com and AuPt₂Com only are compared since, because of instrumentation limitations, the highest input voltage applied to Pt₄Com and AuPt₄Com was 6 V in amplitude. Comparison of the four samples in this figure shows that the improvement in actuation

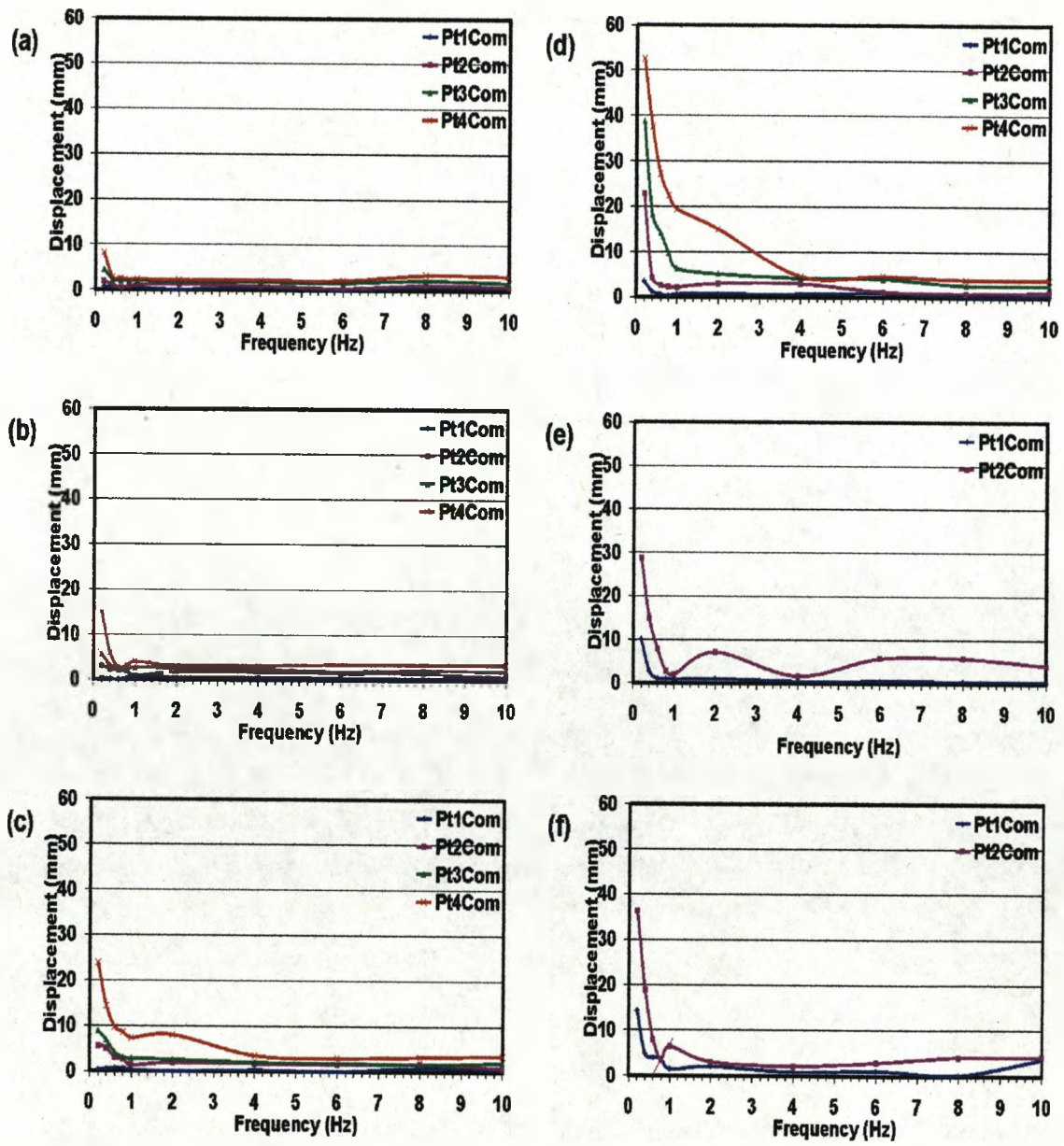


Figure 8.3. Electrode thickness-dependence of the tip displacement of commercial Nafion-based IPMC samples, under application of sinusoidal voltages of (a) 2, (b) 3, (c) 4, (d) 6, (e) 8 and (f) 10V in amplitude.

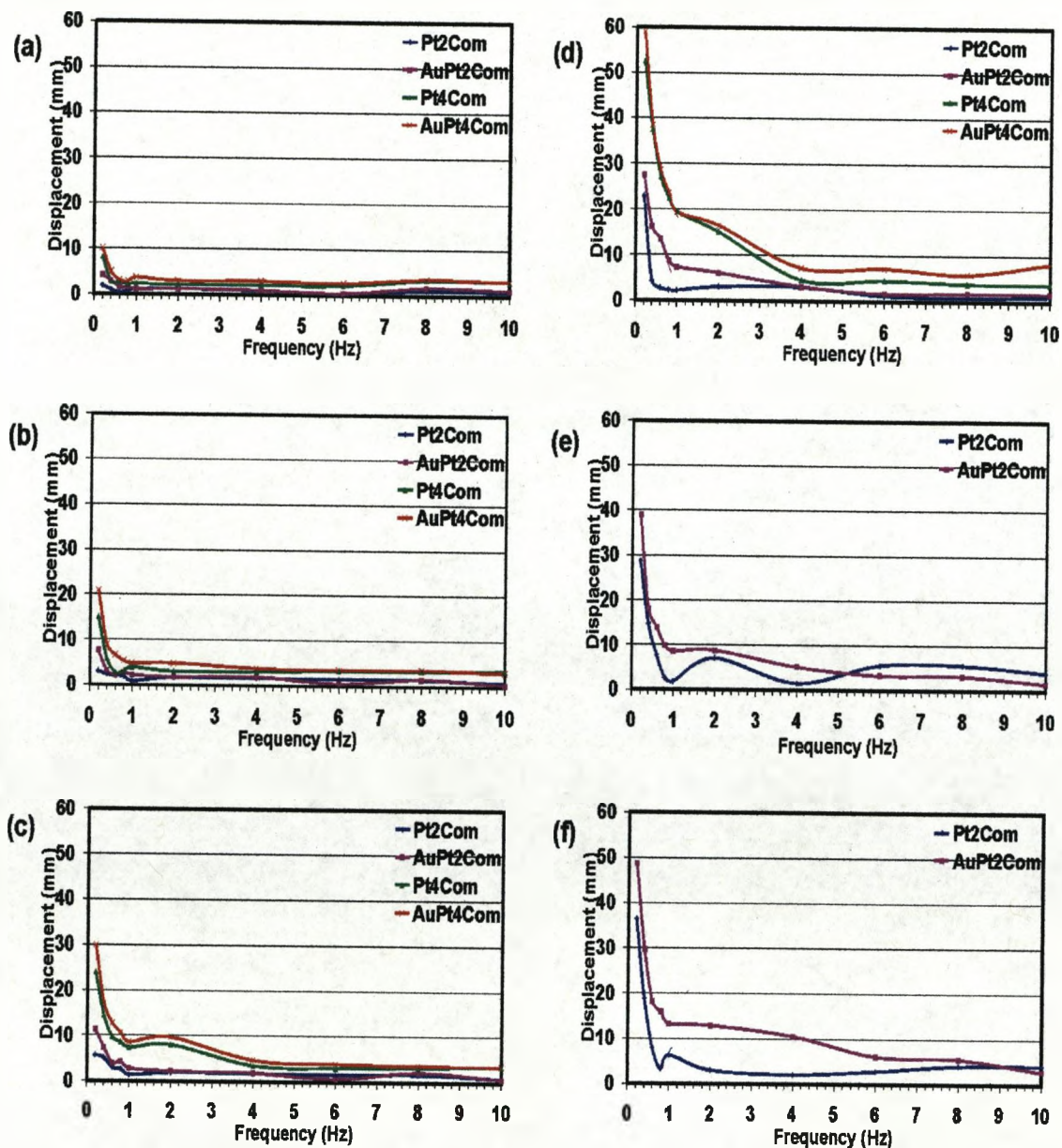


Figure 8.4. Electrode thickness- and surface conductivity-dependence of the tip displacement of commercial Nafion-based IPMC samples, under application of sinusoidal voltages of (a) 2, (b) 3, (c) 4, (d) 6, (e) 8 and (f) 10V in amplitude.

performance observed on going from Pt₂Com to AuPt₂Com was similar to that seen on going from Pt₄Com to AuPt₄Com at all applied voltages. On the application of low amplitude voltages (Figure 8.4(a) and (b)), the magnitudes of the tip displacement of these samples appear very similar. As is clear at the higher applied voltages in Figure 8.4(c) and (d), the effect of increasing the number of electroless platinum electroding cycles from 2 to 4 has a greater effect on tip displacement than the addition of the gold layer.

To study the actuation performance of IPMC materials at frequencies higher than 10 Hz the tip displacement of AuPt₄Com in response to 2, 4 and 6 V applied voltages over a frequency range of 0.2 to 100 Hz was studied. The results obtained are shown in Figure 8.5. As can be seen, this sample undergoes about 2 mm displacement at a frequency of 25 Hz, with an applied voltage of 2 V. Increasing displacement is also observed at this frequency as the amplitude of the applied voltage is increased to 4 V (~3 mm) and 6 V (~5 mm). Over the frequency range of 30 to 80 Hz, however, zero displacement is observed even where the amplitude of the applied voltage is increased up to 6 V. Surprisingly, over the frequency range of 80 to 100 Hz the sample again starts to show non-zero displacements.

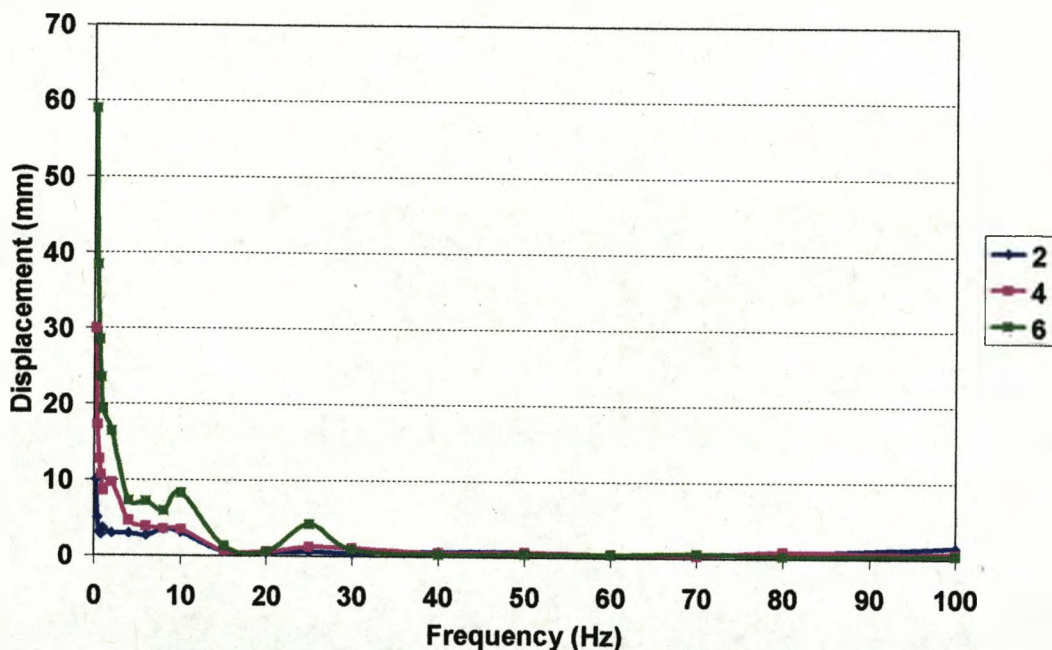


Figure 8.5. Tip displacement of the sample AuPt₄Com at high frequencies. Legend represents the amplitude of the applied voltages in V.

8.3.1.2. Cast IPMC Samples

Results obtained from the displacement measurements of the cast IPMC samples are presented in this section. The measured tip displacements of the samples (a) Pt₂Cast, (b) Pt₄Cast, (c) AuPt₂Cast and (d) AuPt₄Cast are shown in Figure 8.6 as function of the amplitude of the applied voltages, and in Figure 8.7 as a function of the frequency of the applied voltages. The displacements of these samples were measured, as for the commercial samples, on application of voltages of 2, 3, 4, 5, 6, 8 and 10 V and frequencies of 0.1 to 10 Hz across the sample thickness. As can be seen, the measured tip displacements of the samples exhibit qualitatively very similar dependency upon the amplitude and the frequency of the applied voltage as for the commercial samples. That is, the tip displacement

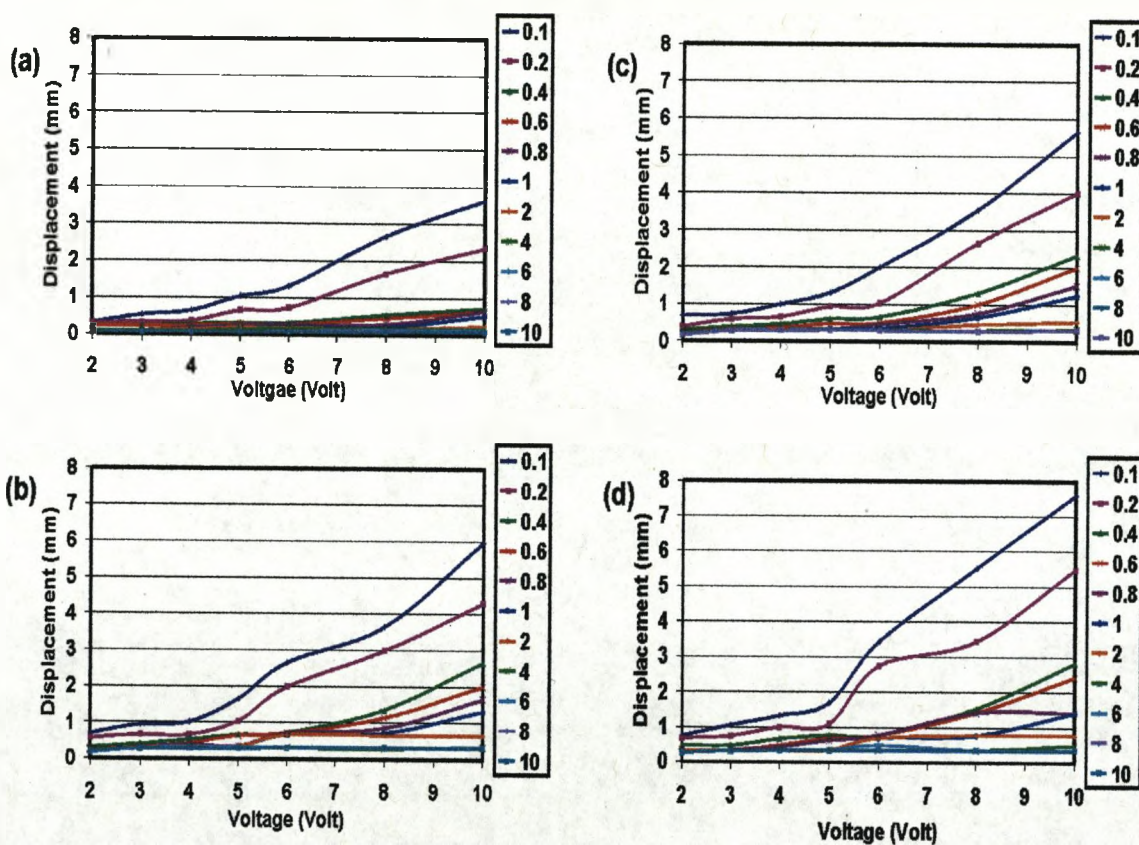


Figure 8.6. Voltage-dependence of the tip displacement of (a) Pt_2Cast , (b) Pt_4Cast , (c) AuPt_2Cast and (d) AuPt_4Cast IPMC samples for several applied voltage frequencies. Legends represent the frequency of the applied voltages in Hz.

of these samples increases almost linearly as the amplitude of the applied voltage increases, from 2 to 10 V (Figure 8.6). Their displacements also change in an inverse relationship with the frequency of the applied voltage, with the larger changes below 1 Hz. All the samples represented in the figure undergo their highest displacement at a frequency of 0.1 Hz and on application of 10 V. Except for the sample Pt_2Cast , all the samples undergo small displacements at frequencies higher than 1 Hz and the magnitude of these increases as the amplitude of the applied voltage increases. As Figure 8.7 shows, the tip displacement

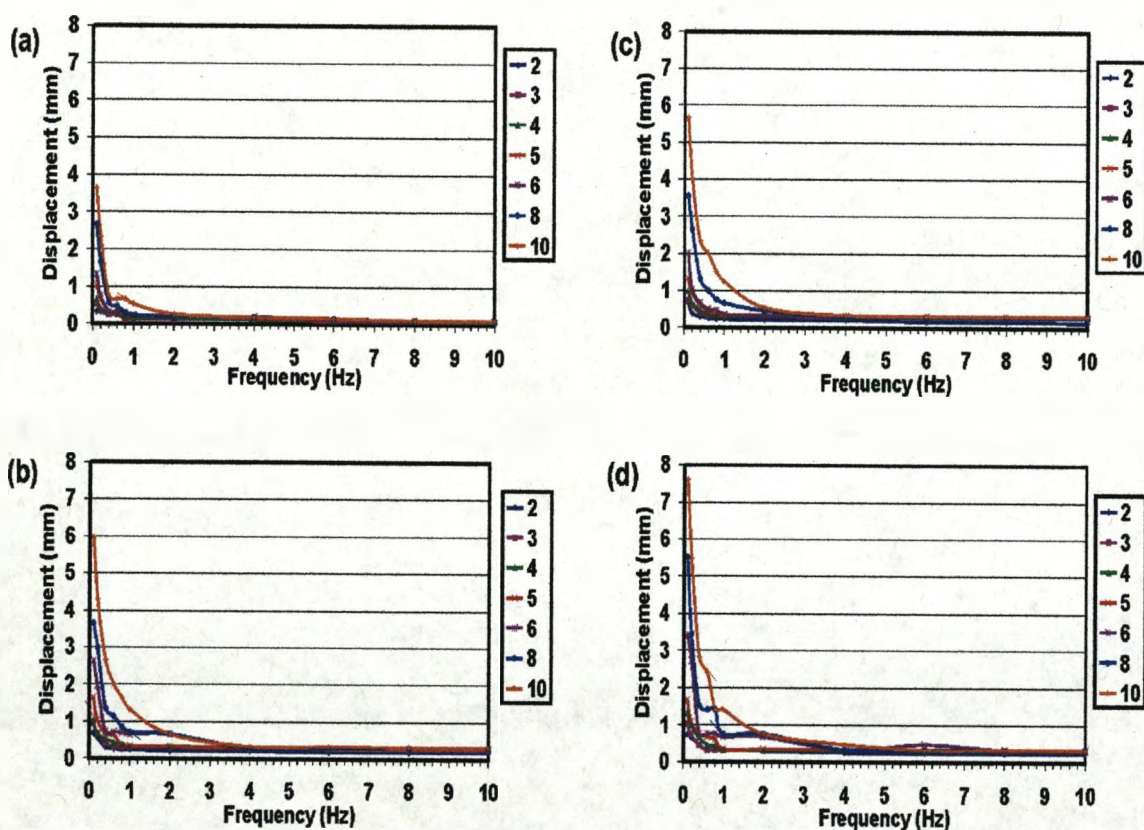


Figure 8.7. Frequency-dependence of the tip displacement of (a)Pt₂Cast, (b) Pt₄Cast, (c) AuPt₂Cast and (d) AuPt₄Cast IPMC samples for several applied voltages. Legends represent the amplitude of the applied voltages in V.

of the samples over the frequency range of 10 to 1 Hz appears relatively independent of the frequency of the applied voltages, particularly on application of low voltages (2 to 5 V). In the case of the samples AuPt₂Cast and AuPt₄Cast (shown in Figure 8.7(c) and (d)) the frequency range over which this frequency-independence is observed, is reduced in extent. The tip displacements of the samples Pt₂Cast and Pt₄Cast, versus the frequency of the applied voltage, are compared in Figure 8.8 to evaluate the effect of electrode thickness on the actuation performance of the cast IPMC samples. Pt₄Cast, which has a thicker platinum

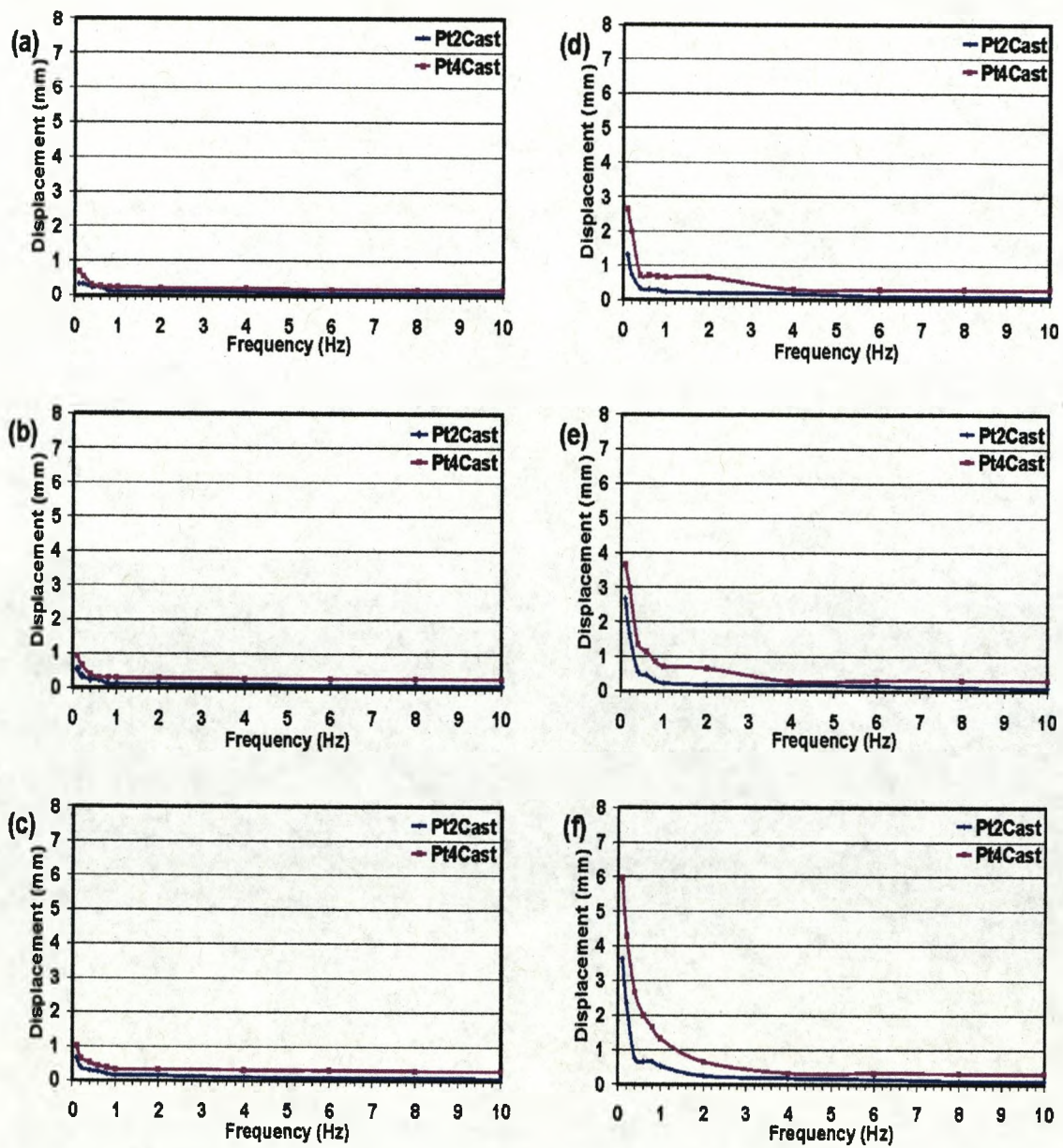


Figure 8.8. Electrode thickness-dependence of the tip displacement of cast Nafion-based IPMC samples, under application of sinusoidal voltages of (a) 2, (b) 3, (c) 4, (d) 6, (e) 8 and (f) 10 V in amplitude.

electrode layer at the surfaces than Pt₂Cast, shows the larger tip displacements at all frequencies.

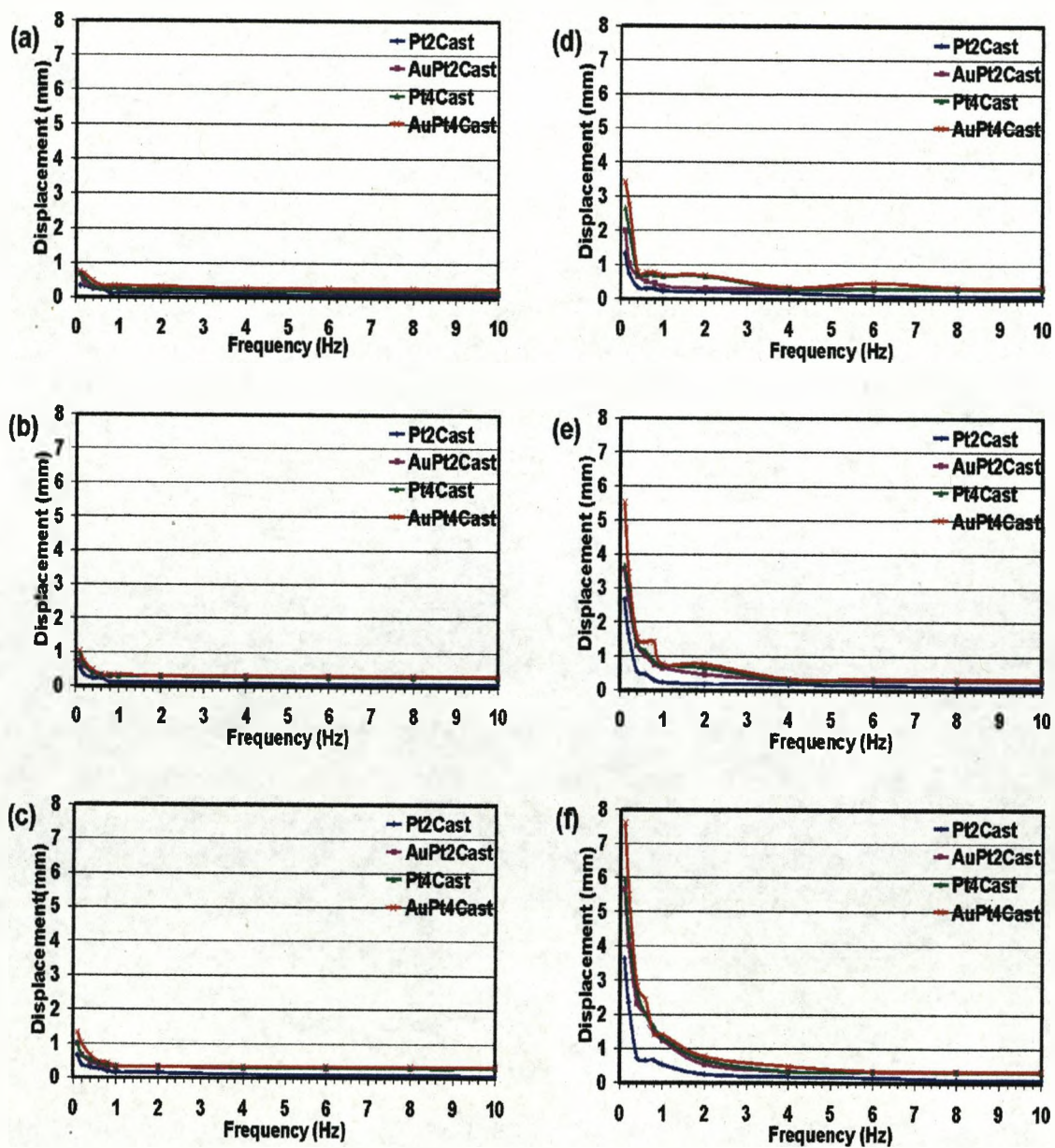


Figure 8.9. Electrode thickness- and surface conductivity-dependence of the tip displacement of cast Nafion-based IPMC samples, under application of sinusoidal voltages of (a) 2, (b) 3, (c) 4, (d) 6, (e) 8 and (f) 10V in amplitude.

Figure 8.9 shows that the displacements of the samples Pt₂Cast and Pt₄Cast can also be increased if their surface conductivity is increased by addition of a thin gold layer. The

samples AuPt₂Cast and AuPt₄Cast undergo larger displacements than the matching samples with no gold layer, Pt₂Cast and Pt₄Cast, respectively. The improved performance of these samples becomes more apparent on the application of voltages of 6, 8 and 10 V and at low frequencies (Figure 8.9 (d) to (f)).

8.3.1.3. Comparison of Commercial and Cast IPMC samples

Figure 8.10 and 8.11 compare, respectively, the voltage- and frequency-dependence of the tip displacement of the commercial, parts (a) to (d), and the matching cast, parts (a') to (d') IPMC samples. It should be mentioned that in these figures the scale used on the axis of displacement for the commercial IPMC samples is about 8 times larger than that used for the cast IPMC samples. On application of the same amplitude of applied voltage much larger displacements are induced in the samples (a) Pt₂Com, (b) AuPt₂Com, (c) Pt₄Com and (d) AuPt₄Com than in the matching cast IPMC, (a') Pt₂Cast, (b') AuPt₂Cast (c') Pt₄Cast and (d') AuPt₄Cast. Generally, there is about a 15 times difference between the commercial and cast IPMC displacement values. The effect of the increase in electrode thickness and surface conductivity also results in considerable increases in the tip displacement of the commercial and cast IPMC samples. For example, there is 36 mm difference between the tip displacements of the samples Pt₂Com (~24 mm) and AuPt₄Com (~60 mm), when applied voltage of 6 V in amplitude at frequency of 0.2 Hz is applied. Under the same electrical conditions, this difference is 2.1 mm between the samples Pt₂Cast (~1.4 mm) and AuPt₄Cast (~3.5 mm). Both changes represent an improvement of 150%. In Figure 8.10 a more linear relationship is observed between the tip displacement and amplitude of the applied voltage for the cast IPMC samples. This may be because of the increased difficulty

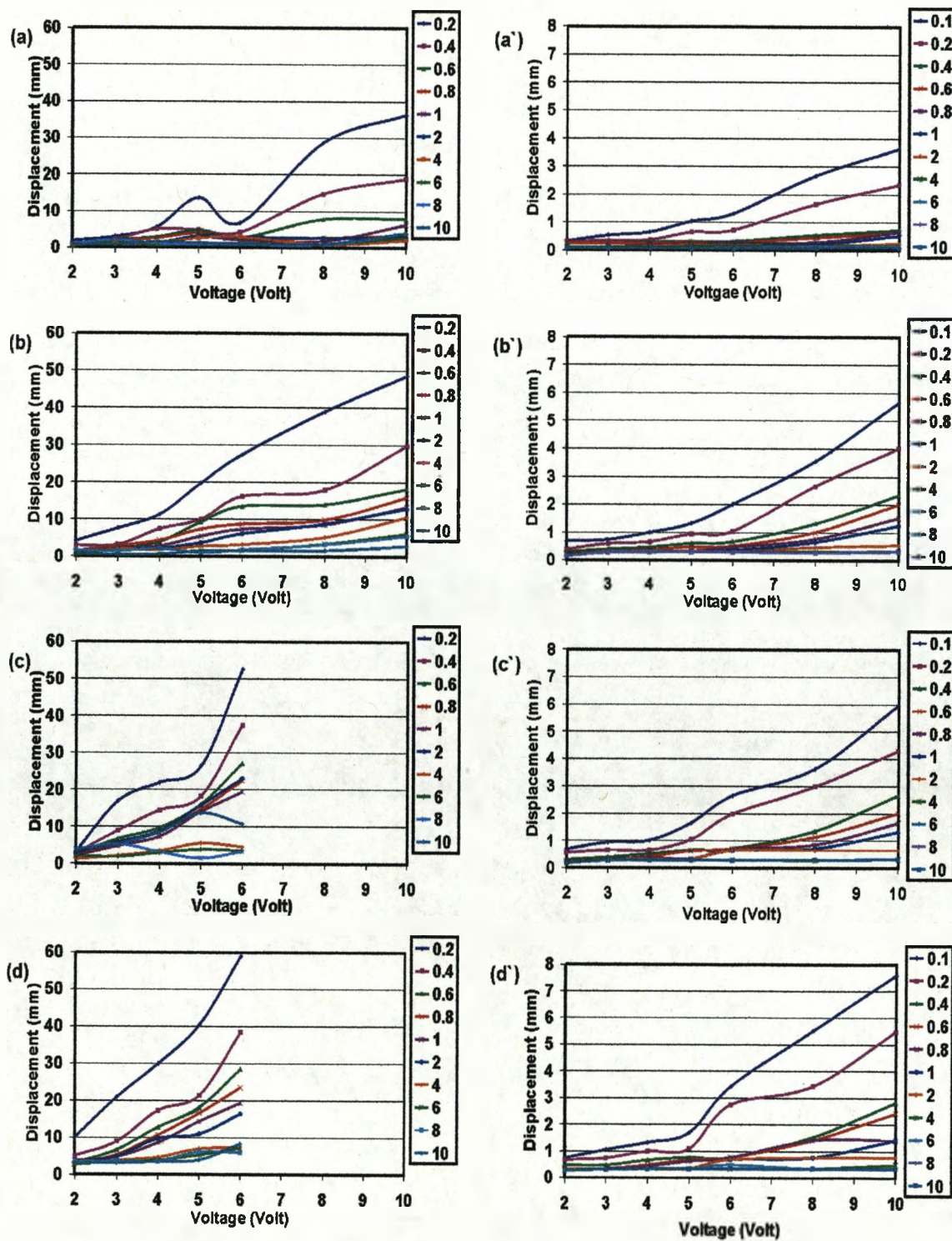


Figure 8.10. Comparison of the voltage-dependence of the tip displacement of commercial and cast Nafion-based IPMC samples; (a) Pt₂Com, (a') Pt₂Cast, (b) AuPt₂Com, (b') AuPt₂Cast, (c) Pt₄Com, (c') Pt₄Cast, (d) AuPt₄Com and (d') AuPt₄Cast. Legends represent the frequencies of the applied voltage in Hz.

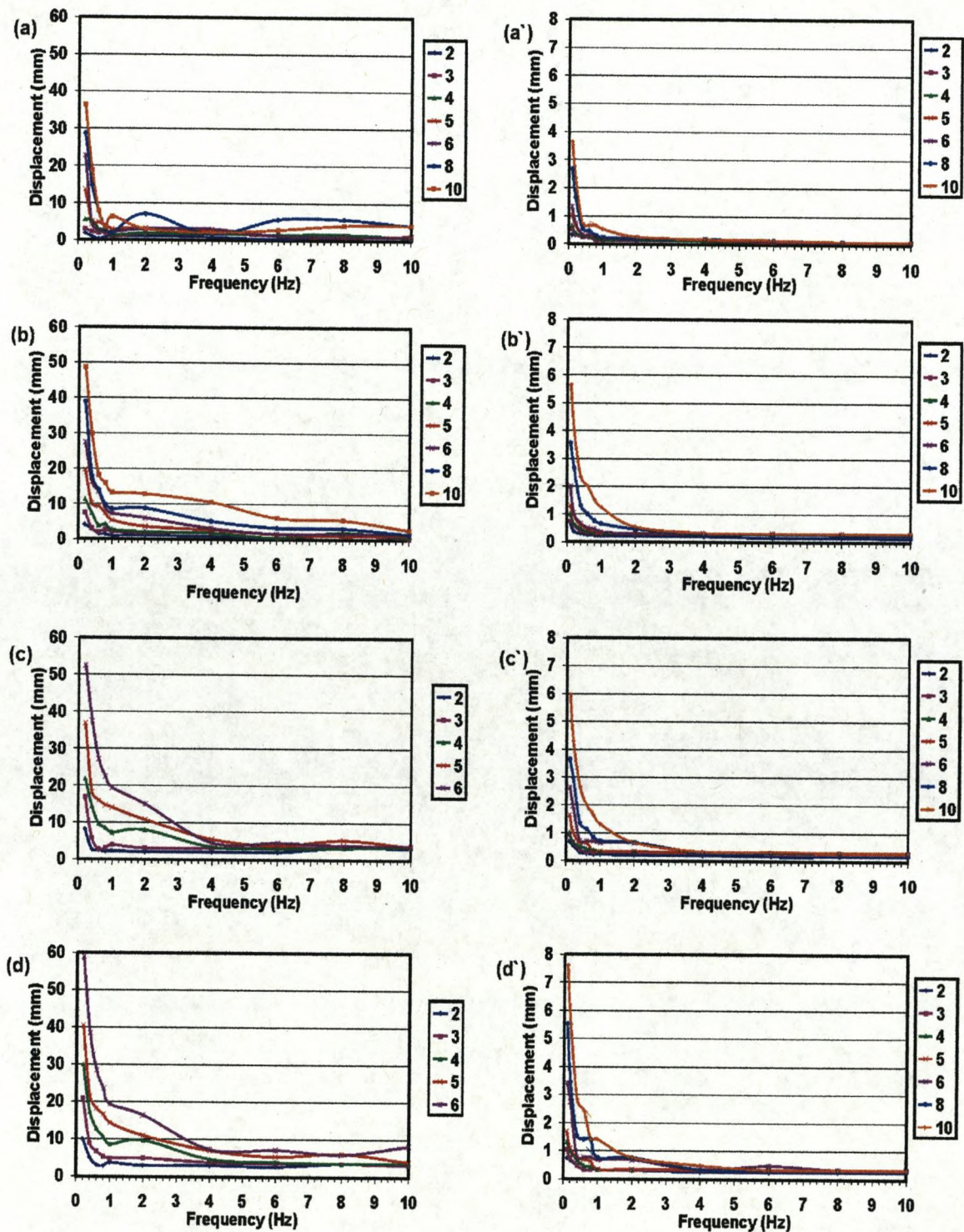


Figure 8.11. Comparison of the frequency-dependence of the tip displacement of commercial and cast Nafion-based IPMC samples; (a) Pt₂Com, (a') Pt₂Cast, (b) AuPt₂Com, (b') AuPt₂Cast, (c) Pt₄Com, (c') Pt₄Cast, (d) AuPt₄Com and (d') AuPt₄Cast. Legends represent the amplitude of the applied voltages in V.

in measuring displacement in the very light commercial IPMC samples.

8.3.2. Force Measurements

8.3.2.1. Commercial IPMC Samples

The generated force at the tip of the samples (a) Pt₂Com, (b) Pt₄Com, (c) AuPt₂Com and (d) AuPt₄Com was measured with increasing applied sinusoidal voltages of up to 10 V in amplitude, and over a frequency range of 0.1 to 10 Hz. Results are shown in Figures 8.12 and 8.13 as a function of the amplitude and frequency of the applied voltage, respectively. The generated force in these samples changes in a very similar way to their tip displacement, increasing with increasing amplitude and decreasing frequency of the applied voltage. Figure 8.12 shows that the generated force increases almost linearly with increasing amplitude of the applied voltage, reaching a maximum (for constant frequency) at 10 V. The force also increases as the frequency of the applied voltages decreases down to 0.1 Hz (Figure 8.13) and the highest force output is obtained at 10 V and 0.1 Hz. Figure 8.13 illustrates that there is an approximate inverse relationship between force output and frequency of the applied voltage. In general, force increases with the amplitude of the applied voltage.

In Figure 8.14 the effect of the thickness of the electrode and the surface conductivity on the force output of the commercial IPMC samples is presented. In parts (a) to (e) the generated force of the samples is compared as a function of applied voltage amplitude. It can be seen that, at all voltages, Pt₄Com generates a larger force than Pt₂Com, which has a thinner electrode. Furthermore, the presence of the thin gold layer at the surfaces of AuPt₂Com

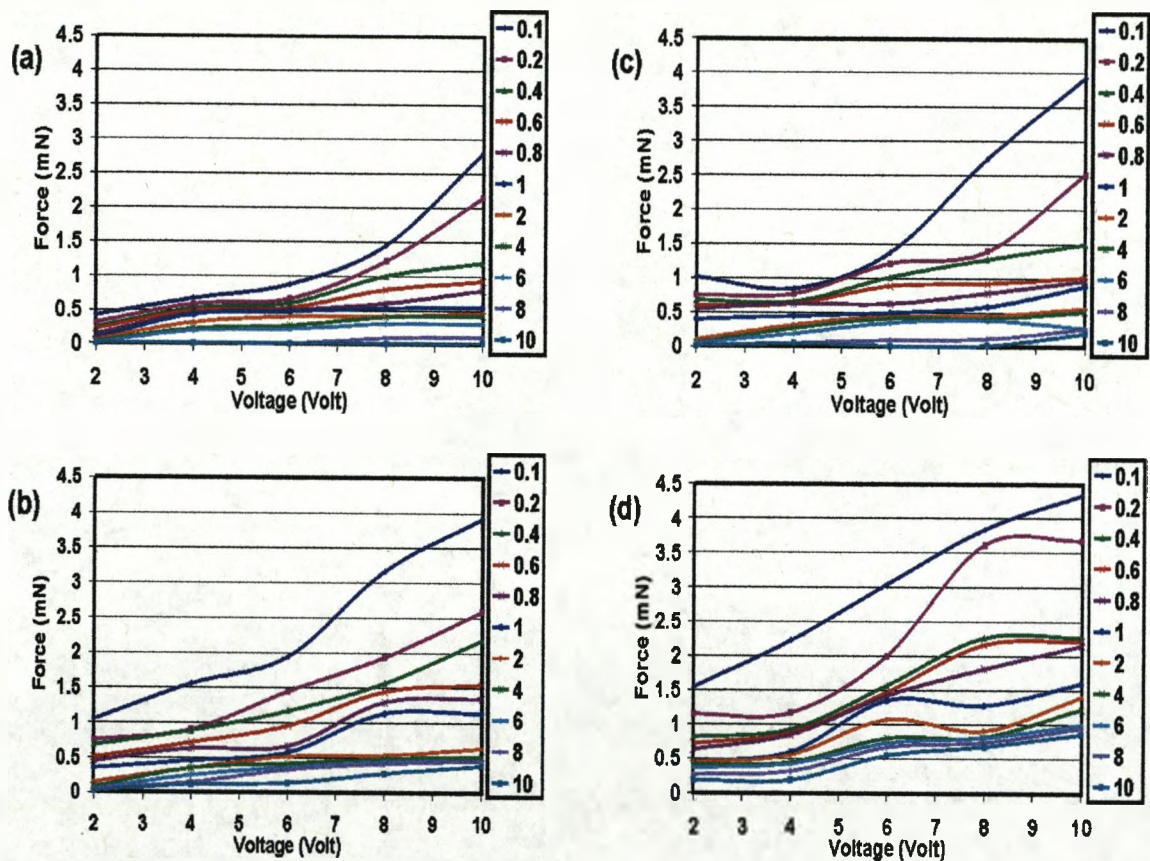


Figure 8.12. Voltage-dependence of the force generated at the tip of (a) Pt₂Com, (b) Pt₄Com, (c) AuPt₂Com and (d) AuPt₄Com IPMC samples. Legends represent the frequencies of the applied voltage in Hz.

and AuPt₄Com causes a significant increase in generated force of these samples, compared to the matching samples with no gold layer.

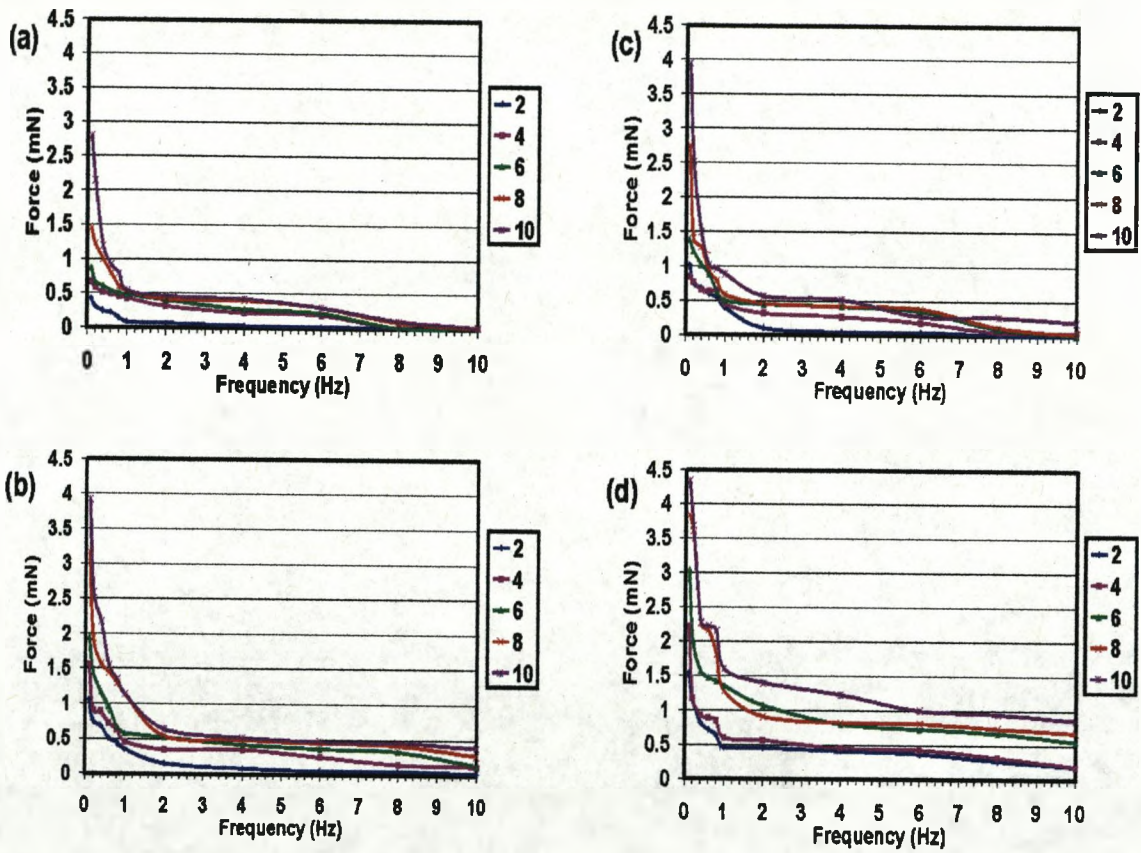


Figure 8.13. Frequency-dependence of the force generated at the tip of (a) Pt₂Com, (b) Pt₄Com, (c) AuPt₂Com and (d) AuPt₄Com IPMC samples. Legends represent the amplitude of the applied voltage in V.

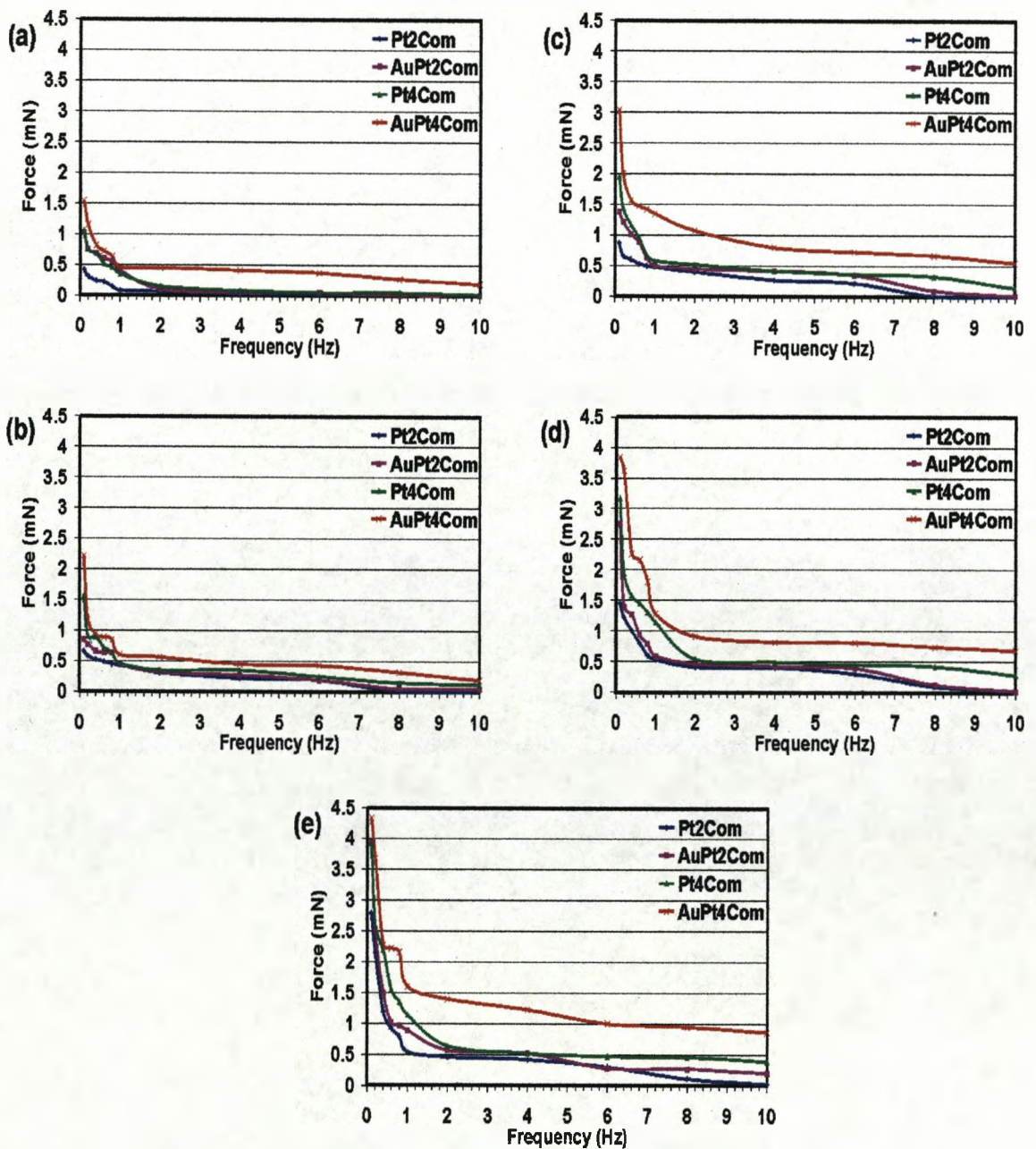


Figure 8.14. Electrode thickness- and surface conductivity-dependence of the generated force at the tip of the commercial Nafion-based IPMC samples, under application of sinusoidal voltages of (a) 2, (b) 3, (c) 4, (d) 6, (e) 8 and (f) 10V in amplitude.

8.3.2.2. Cast IPMC Samples

The measurement of the generated force of the cast IPMC samples resulted in qualitatively very similar results to those of the commercial IPMC samples. The variation in the force of the samples (a) Pt₂Cast, (b) Pt₄Cast, (c) AuPt₂Cast and (d) AuPt₄Cast shown in Figures 8.15 and 8.16, as a function of the voltage and frequency of the applied voltage, respectively.

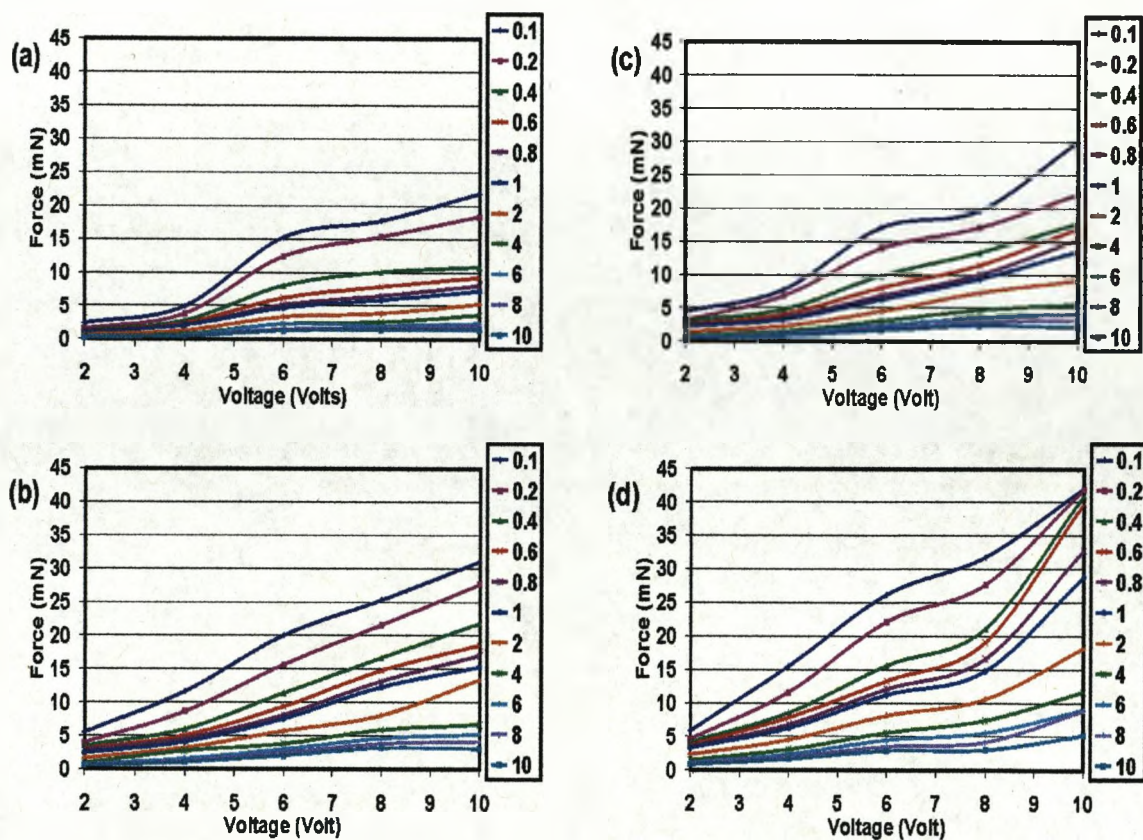


Figure 8.15. Voltage-dependence of the force generated at the tip of (a) Pt₂Cast, (b) Pt₄Cast, (c) AuPt₂Cast and (d) AuPt₄Cast IPMC samples. Legends represent the frequencies of the applied voltages in Hz.

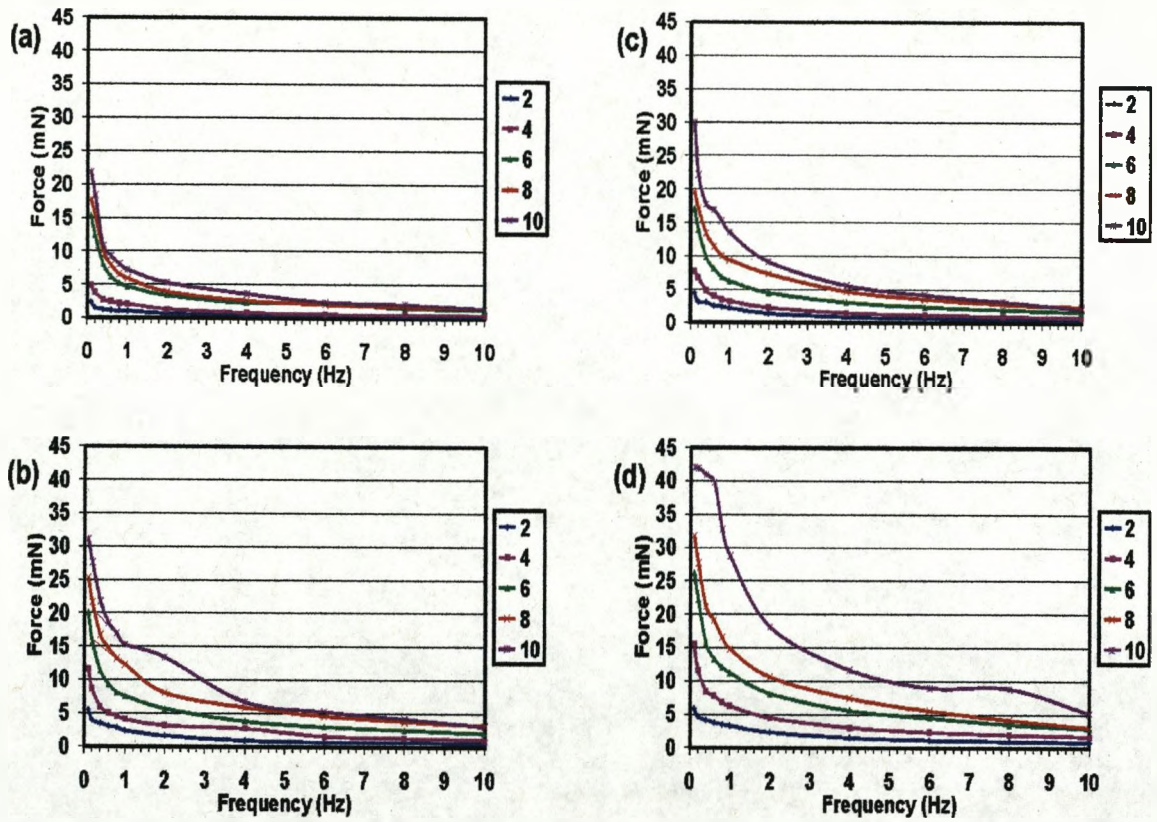


Figure 8.16. Frequency-dependence of the force generated at the tip of (a) Pt₂Cast, (b) Pt₄Cast, (c) AuPt₂Cast and (d) AuPt₄Cast IPMC samples. Legends represent the amplitude of the applied voltages in V.

Figure 8.17 shows the effect of electrode thickness and the surface conductivity on the generated force in these samples.

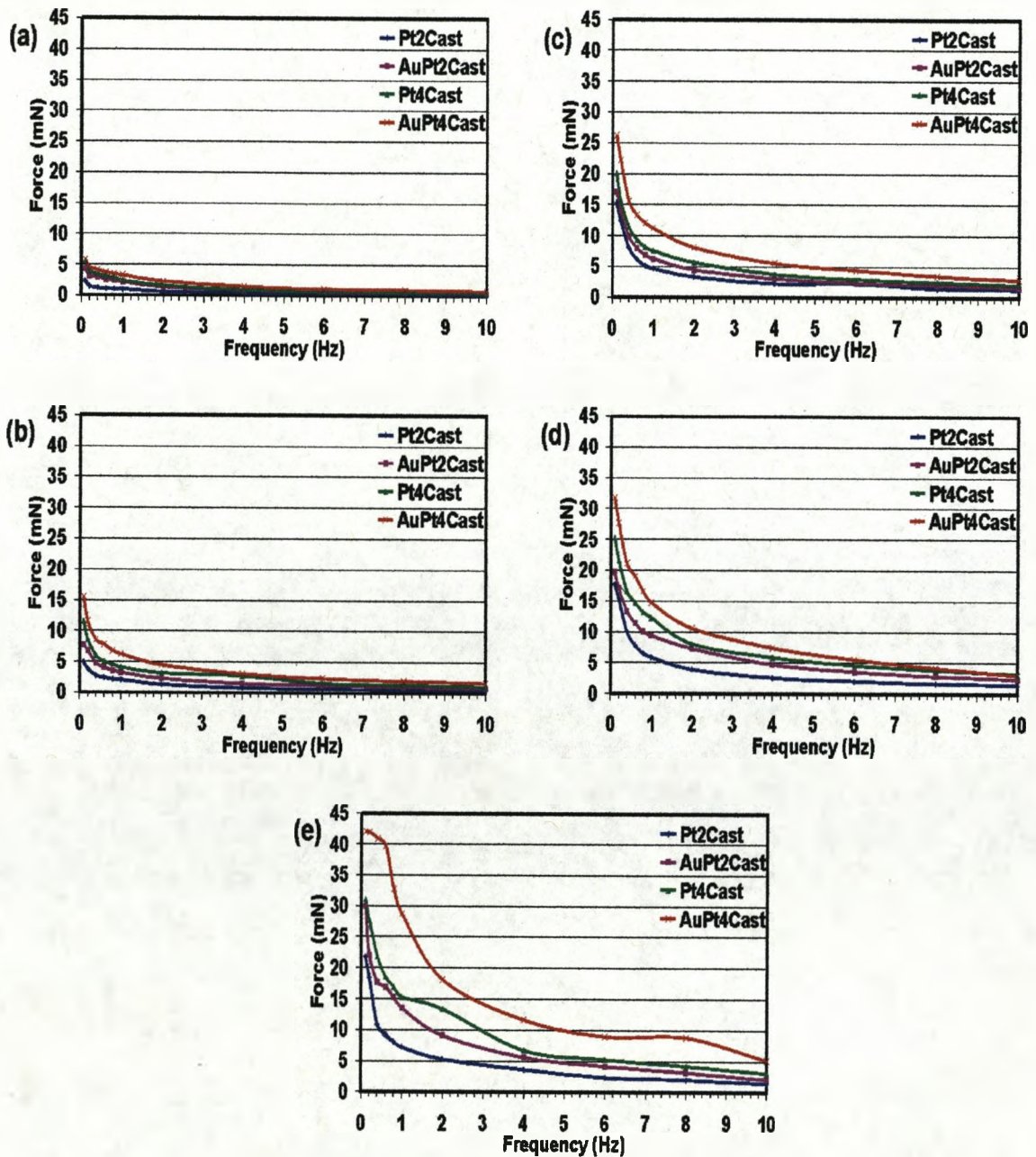


Figure 8.17. Electrode thickness- and surface conductivity-dependence of the generated force at the tip of the cast Nafion-based IPMC samples, under application of sinusoidal voltages of (a) 2, (b) 3, (c) 4, (d) 6, (e) 8 and (f) 10V in amplitude.

8.3.2.3. Comparison of Commercial and Cast IPMC samples

The force output of the commercial, parts (a) to (d), and the matching cast, parts (a') to (d'), IPMC samples are compared in Figures 8.18 and 8.19 as a function of voltage and frequency. It should be mentioned that in these figures the scale used on the force axis is 9 times larger for the cast IPMC samples than that used for the commercial IPMC samples. On application of the same voltage, as Figure 8.18 illustrates, the samples (a') Pt₂Cast, (b') AuPt₂Cast, (c') Pt₄Cast and (d') AuPt₄Cast generate much larger forces than the matching commercial IPMC samples, (a) Pt₂Com, (b) AuPt₂Com, (c) Pt₄Com and (d) AuPt₄Com. Generally, there is about a 10 times difference between the commercial and cast IPMC force values. The effect of the increase in electrode thickness and surface conductivity also results in considerable increases in the generated force of the commercial and cast IPMC samples. For example, there is a large difference (~20 mN) between the generated forces of the samples Pt₂Cast (~23 mN) and AuPt₄Cast (~43 mN), when an applied voltage of 10 V in amplitude at frequency of 0.1 Hz is applied. Under the same electrical conditions, this difference is ~1.7 mN between the matching commercial IPMC samples, Pt₂Com (~2.7 mN) and AuPt₄Com (~4.4 mN). This represents an improvement of about 100%, although forces in the cast IPMC samples are 10 times larger than in the commercial IPMC samples. In Figure 8.18 a more linear relationship between the force and amplitude of the applied voltage is observed for the cast IPMC samples. As mentioned earlier, this may be because of the increased difficulty in measuring force in the very light commercial IPMC samples.

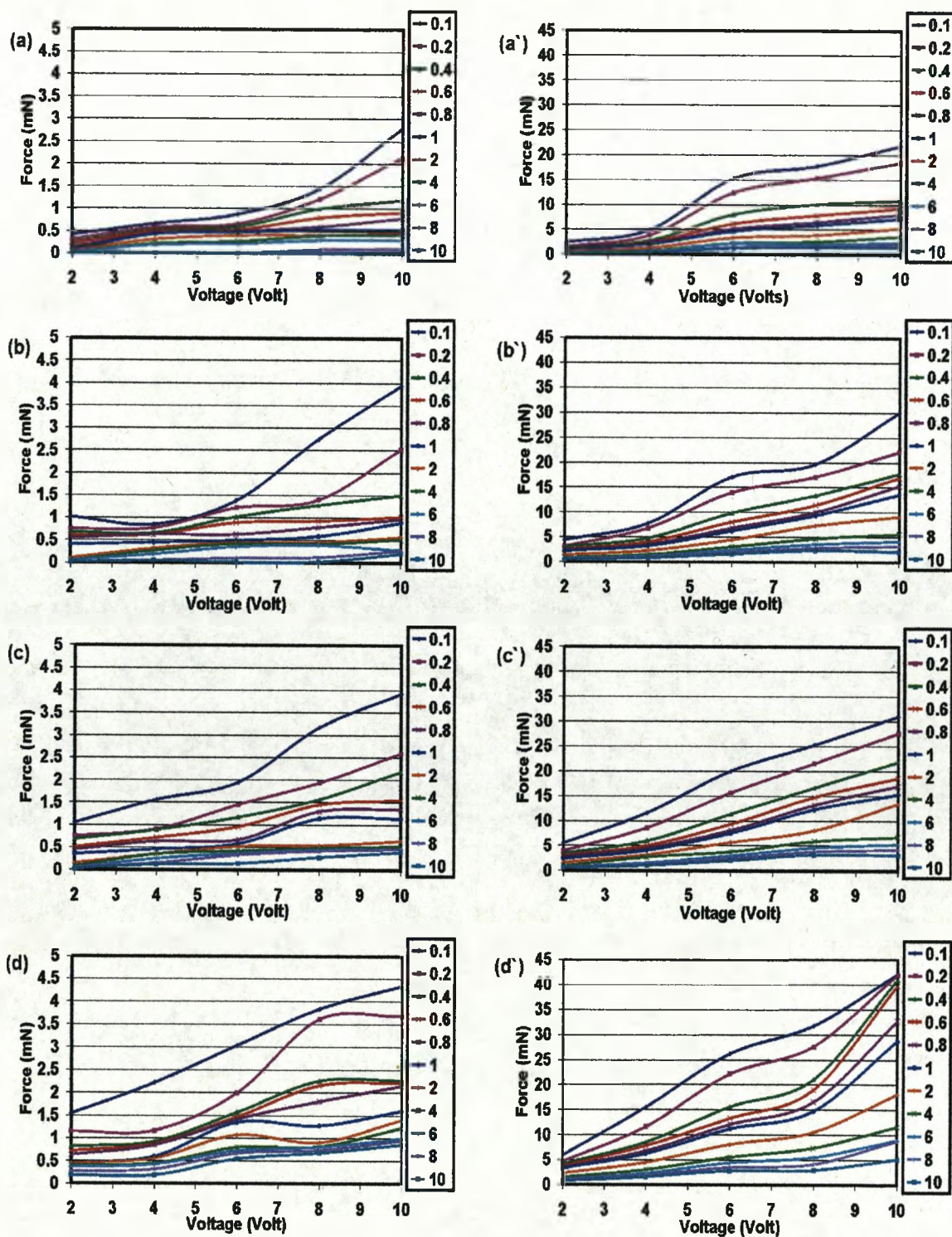


Figure 8.18. Comparison between the frequency-dependence of the generated force at the tip of the commercial and cast Nafion-based IPMC samples; (a) Pt₂Cast, (a') Pt₂Com, (b) AuPt₂Cast, (b') AuPt₂Com, (c) Pt₄Cast, (c') Pt₄Com, (d) AuPt₄Cast and (d') AuPt₄Com. Legends represent the frequencies of the applied voltages in Hz.

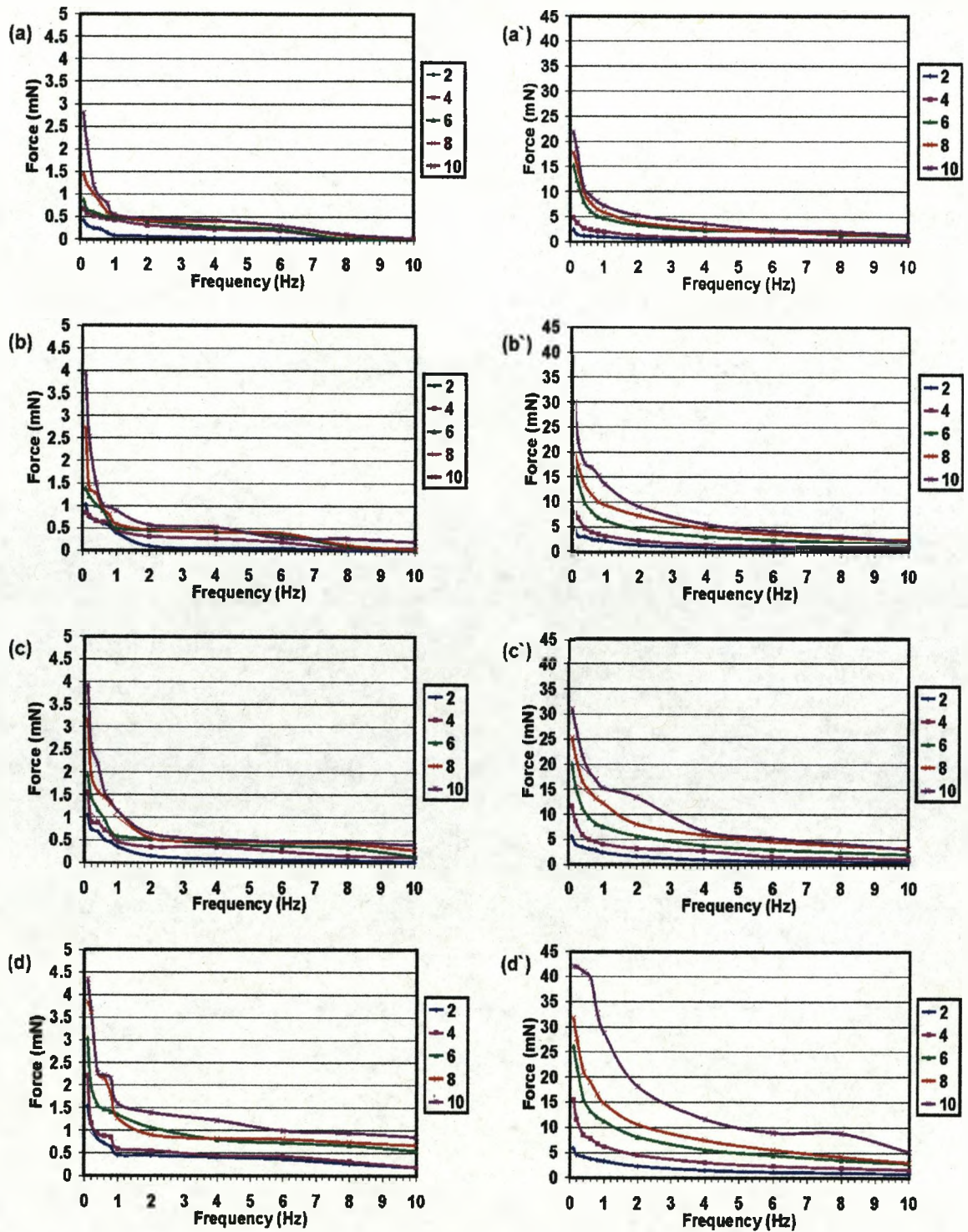


Figure 8.19. Comparison between the frequency-dependence of the generated force at the tip of the commercial and cast Nafion-based IPMC samples; (a) Pt₂Cast, (a') Pt₂Com, (b) AuPt₂Cast, (b') AuPt₂Com, (c) Pt₄Cast, (c') Pt₄Com, (d) AuPt₄Cast and (d') AuPt₄Com. Legends represent the amplitude of the applied voltage in V.

8.3.3. Waveform Analysis

In order to evaluate the effect of the thickness of Nafion polymer on the electrical characteristics of the IPMC samples the current, I , as a function of time and in response to the applied sinusoidal voltage, V , were monitored for the samples Pt₂Com and Pt₂Cast. The current, I , was recorded for these samples when voltages, V , at amplitudes of (a) 2, (b) 4, (c) 6, (d) 8 and (e) 10 V and at frequency, 0.4 Hz were applied. The waveforms obtained for the samples Pt₂Com and Pt₂Cast, respectively, are shown in Figures 8.20 and 8.21 – parts (a) to (e). Both the applied voltage and the current generated appear sinusoidal, and had constant amplitude and phase. Figure 8.20(a) shows the very small amplitude of the current, I , (-0.5 mA), for the sample Pt₂Com, as a function of time, in response to a 2V applied voltage. Increasing the amplitude of the applied voltage causes the amplitude of the current, I , to increase also (Figure 8.20(a) to (e)). At low applied voltages, there appears to be a small negative off-set in the current generated. However, this is not seen at higher voltages and so may be an artifact caused by the relatively low resolution of the current measurement. In Figure 8.20(a) there is a phase difference between the applied voltage and the current; the current, I , leading the voltage, V . This phase difference decreases gradually as the amplitude of the applied voltage increases, so that the current, I , becomes almost in-phase with the applied voltage, V , (Figure 8.20(c) and (d)).

Figure 8.21 – parts (a) to (e) presents qualitatively similar results for the sample Pt₂Cast.

Comparison of Figures 8.20 and 8.21, however, indicates several significant similarities and differences between the electrical characteristics of the samples Pt₂Com and Pt₂Cast. It can be seen that the current generated in the sample Pt₂Cast is always much greater than in the sample Pt₂Com, under the same applied voltage, the difference being approximately 5

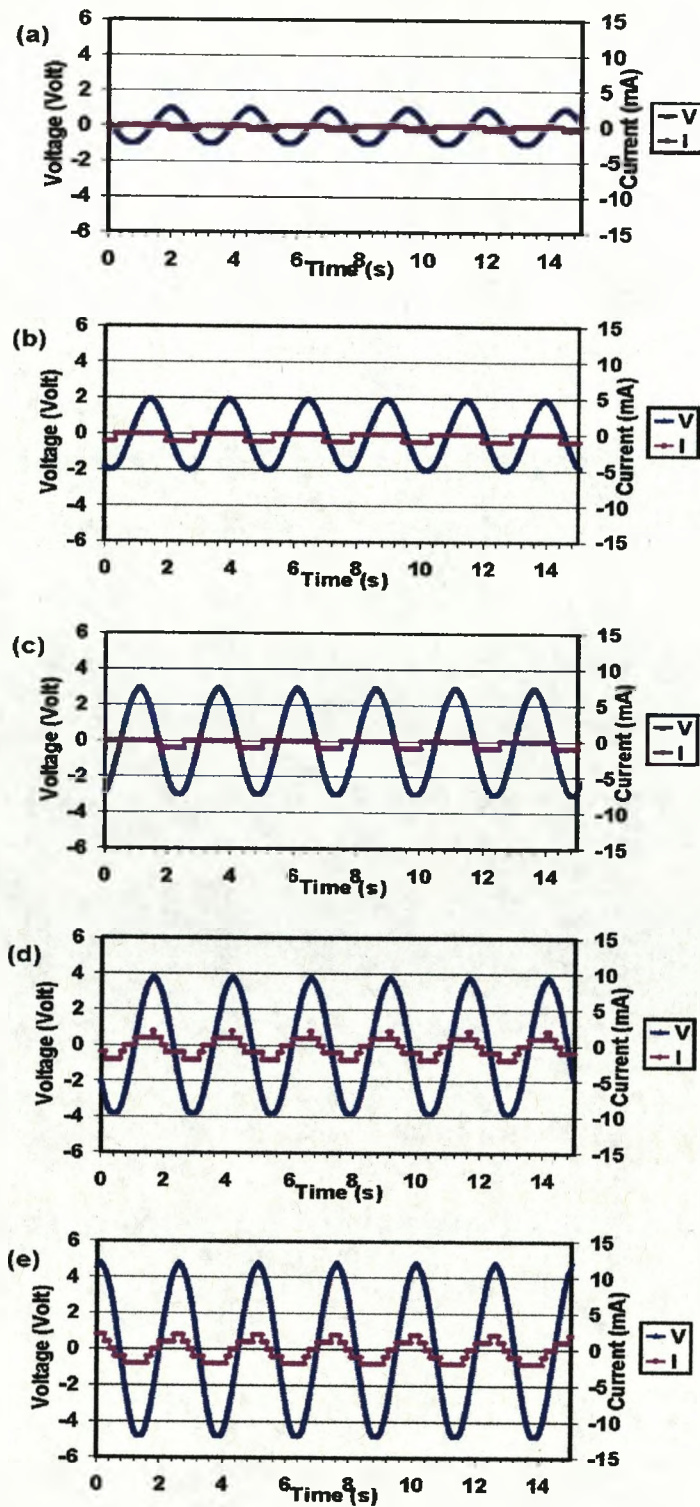


Figure 8.20. The current, I , and the applied voltage, V , versus time for the sample Pt_2Com , using sinusoidal applied voltages of (a) 2, (b) 4, (c) 6, (d) 8 and (e) 10 V in amplitude. The frequency of the applied voltage was 0.4 Hz.

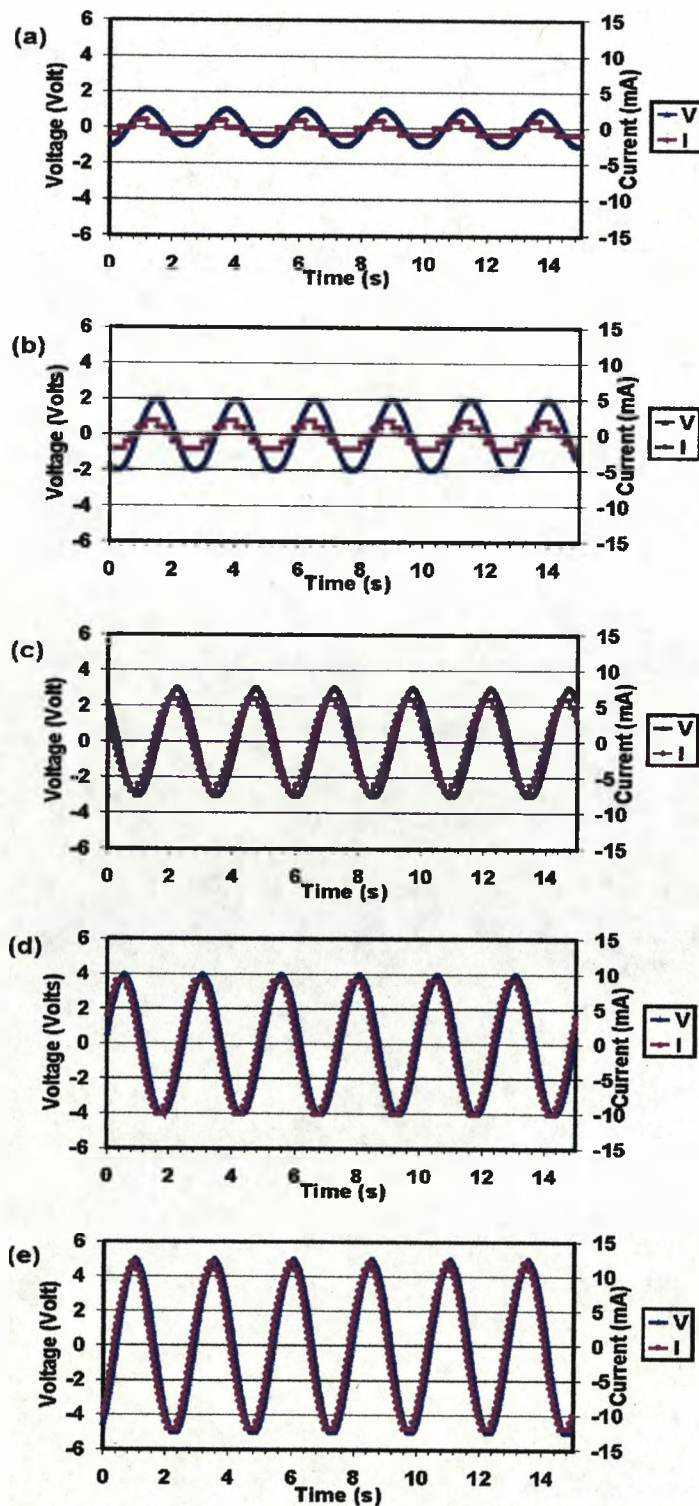


Figure 8.21. The current, I , and the applied voltage, V , versus time for the sample Pt_2Cast , using sinusoidal applied voltages of (a) 2 , (b) 4, (c) 6, (d) 8 and (e) 10 V in amplitude. The frequency of the applied voltage was 0.4 Hz.

times. A much smaller phase difference is observed between the applied voltage, V , and the current, I , for the Pt₂Cast (Figure 8.21(a)) than for Pt₂Com. As the amplitude of the applied voltage is increased this phase difference decreases until I and V are almost in-phase at 10 V (Figure 8.21(e)).

In Figure 8.22 the current, I , and the generated force, F , of the samples (a) Pt₂Cast, (b) AuPt₂Cast, (c) Pt₄Cast and (d) AuPt₄Cast as a function of time in response to 4 V applied voltage is plotted. To study the inter dependence of the frequency of the applied voltage, the current, I , and the generated force, F , these were recorded at applied voltage frequencies of 0.1 Hz (parts (a) to (d)) and 4 Hz (parts (a') to (d')). The effect of the electrode thickness and the surface conductivity on the current, I , and the generated force, F , can be examined in each column of the figure. These results show that in response to the sinusoidal input voltage, V , the force, F , is generated which also varies sinusoidally with time. The generated force, F , and the current, I , increase as the electrode thickness and the surface conductivity increase at both applied frequencies (both columns of Figure 8.22). The lowest magnitude of the generated force, F , and the current, I , are observed for Pt₂Cast, while for AuPt₄Cast, the highest magnitudes are observed. The samples generate much greater forces, F , when the 4 V sinusoidal voltages are applied at a frequency of 0.1 Hz (Figure 8.22 – parts (a) to (d)) than at 4 Hz (Figure 8.22 – parts (a') to (d')). However, comparison of the graphs in each row reveals that, for each sample, larger current amplitudes are generated at 4 Hz than at 0.1 Hz.

It is clear in Figure 8.22 that the generated force, F , lags behind the voltage, V , and that this phase difference is not influenced by increasing the electrode thickness or the surface conductivity of the samples. It even remains the same – at approximately 57° – where the

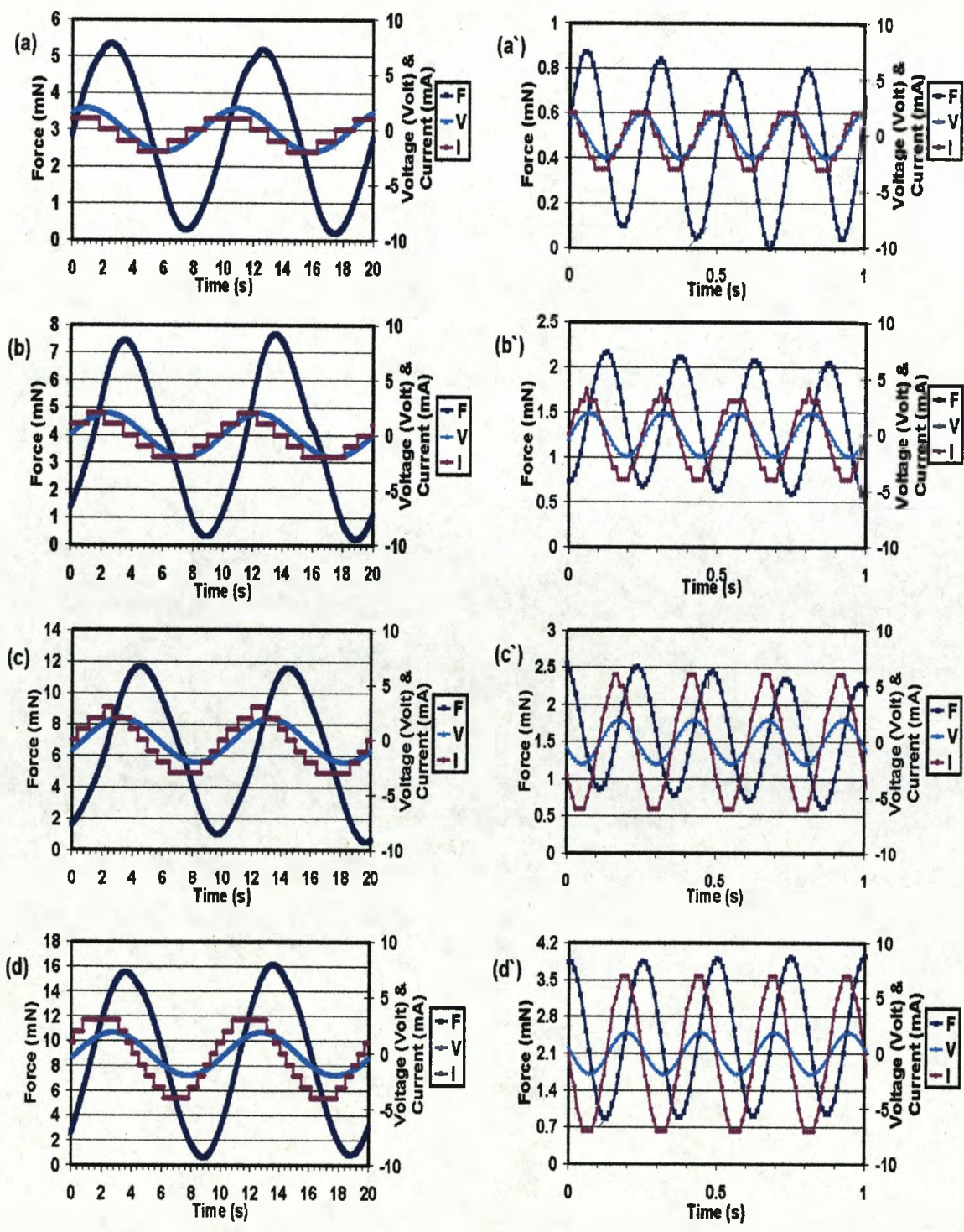


Figure 8.22. The generated force, F , current, I , and the applied voltage, V , versus time for the samples (a) Pt₂Cast, (b) AuPt₂Cast, (c) Pt₄Cast and (d) AuPt₄Cast using sinusoidal applied voltages of 4 V in amplitude. The frequency of the applied voltage is 0.1 Hz for parts (a) to (d) and 4 Hz for parts (a') to (d').

frequency of the applied voltage is changed from 0.1 Hz to 4 Hz. The current, I , however, leads the applied voltage, V . Furthermore, the phase difference between V and I varies, decreasing significantly when the frequency of the applied voltage, V , is increased.

8.4. Discussion

In the following sub-sections the effect of variables such as amplitude and frequency of the sinusoidal applied voltages, electrode thickness (number of platinum plating cycles), surface conductivity (presence or absence of gold layer) and thickness of the IPMC polymer on the electromechanical (tip displacement and generated force) and electrical characteristics of the prepared IPMC samples (see Table 3.1) are separately discussed.

Voltage-Dependence

As was seen, in response to application of sinusoidal voltages across the thickness of the commercial and the cast IPMC samples, the samples underwent bending deformations and generated force. The tip displacements and force output of the samples showed very similar dependence on the amplitude and frequency of the input sinusoidal voltages. That is, the tip displacement and generated force of these samples increased with increasing amplitude of the applied voltage up to the maximum 10 V, and with decreasing frequency, down to 0.1 Hz. The observed voltage-dependence of the electromechanical performance of the samples can be explained as follows. Each IPMC sample can be considered to behave in a similar

way to a capacitor¹ since it consists of a pair of conductive platinum electrodes sandwiching the IPMC polymer. In fact the IPMCs are not ideal capacitors since they present a resistance to the flow of current. However, we shall first consider their capacitance behaviour. We can consider an IPMC to be similar to a parallel plate capacitor. As a capacitor, the capacitance, C , of each IPMC sample can then be considered to be constant and proportional to the surface area, A , of the platinum electrodes and inversely proportional to the distance, d , between the electrodes (the thickness of IPMC polymer). The capacitance of a parallel-electrode capacitor is given by:

$$C \approx \frac{\epsilon A}{d} \quad A \gg d^2 \quad (8.1)$$

where ϵ is the permittivity of the dielectric, A is the area of the plates and d is the space between the plates. On application of an electric voltage, V , opposite charges of equal magnitude, Q , accumulate on the platinum electrodes. The charge is calculated according to Equation 8.2.²

$$Q = CV \quad (8.2)$$

In SI units, the units of Q , C and V are respectively Coulombs, Farads and Volts.

Accumulation of opposite charges on the platinum electrodes causes an electric field gradient to develop across the thickness of the IPMC samples. In this case, the hydrated Li^+ ions begin to break away from the sulfonate groups and move towards the negatively charged electrode (cathode), while the sulfonate groups remain fixed to the molecular backbone. This results in the bending deformation of the sample towards the anode (See Chapter One). According to Equation 8.2, the voltage, V , is directly proportional to the amount of accumulated charge on the electrodes. Thus, on the application of higher voltage, V , more charge, Q , accumulates on the platinum electrodes. This, in turn, causes the

electrically-induced diffusion of a greater number of hydrated ions towards the cathode, which is observed as larger tip displacements and force outputs in the IPMC samples.

In Figures 8.20 and 8.21 it was seen that the current, I , increases as a function of increasing amplitude of the applied voltage, V , at a constant frequency of 0.4 Hz. The current, I , through the IPMC sample, as a capacitor, can be considered as the rate at which charge Q forces the hydrated Li^+ ions to diffuse. This can be expressed mathematically as Equation 8.3 where I is the current (in Amperes), dV/dt is the time derivative of voltage (Vs^{-1}) and C is the capacitance (in Farads).² Thus, the current, I , increases in proportion to the rate of change of V , dV/dt .

$$I = \frac{dQ}{dt} = C \frac{dV}{dt} \quad (8.3)$$

At a constant frequency, the larger the amplitude of V , the larger dV/dt and the larger the amplitude of I would be.

In Figures 8.20 and 8.21, it was observed that the current, I , leads the voltage, V , particularly at low amplitudes of the applied voltage, V . According to Equation 8.3, the voltage, V , across a capacitor is proportional to the integral of the current, I . Thus, in the case of application of sinusoidal voltages to an ideal capacitor a phase difference of 90° should be observed, *i.e.* the current, I , would lead the voltage, V , by a quarter cycle (unlike in an inductor, where the current lags the voltage by 90°).² The phase difference in these results is approximately 31° (in Pt_2Cast) to 115° (in Pt_2Com), under application of 2 V at 0.4 Hz. Thus, these results imply that the IPMC samples possess capacitive characteristics but that they are not ideal capacitors. It also indicates that the IPMC samples, similar to capacitors, alternately absorb energy from the circuit and return the energy to the circuit.²

The mentioned phase difference, however, decreased (in the plots shown in figures 8.20 and 8.21) with increasing amplitude of applied voltage. On application of 10 V, the current and voltage appeared almost in-phase. This indicates that when 10 V is applied the samples behave more like resistors, since a resistor does not cause a phase shift between the voltage and the current.² It can be concluded, then, that the “equivalent circuit” for these IPMC devices contains both capacitive and resistive components, as would be expected.

Frequency-Dependence

The study of the frequency-dependence of the IPMC samples revealed that the electromechanical performance, in terms of tip displacement and generated force of the IPMC samples is approximately inversely related to the frequency of the applied voltage. As described, the bending deformations of the IPMC samples are thought to occur as a result of the electrically-induced diffusion of the hydrated Li^+ ions towards the cathode. Thus, the observation of lower tip displacement and force at higher frequencies can be attributed to an increase in the limitation of diffusion of Li^+ -ions within the polymer. When a sinusoidal voltage is applied the platinum electrodes are alternately charged: first in one direction and then the other. The rate at which the polarity of the electrodes changes depends on the frequency of the applied voltage. At low frequencies, this rate is low, and so a greater number of the hydrated Li^+ ions can diffuse towards the cathode. This leads to greater tip displacement and force. At high frequencies, a smaller number of ions are concentrated near the cathode before the polarity of the sinusoidal voltage is quickly reversed. This results in observation of smaller tip displacement and force. As results

obtained from the displacement measurements of the sample AuPt₄Com in Figure 8.6 revealed, at frequencies higher than 25 Hz no significant tip displacement occurs. These results are in good agreement with data obtained from a similar study, presented by Shahinpoor³ (See Section 1.2.5).

The effect of the frequency of the applied voltage, V , on the phase and amplitude of the current, I , was observed in Figure 8.22. Comparison of the results in each row of this figure revealed that the amplitude of the current, I , increases significantly as the frequency of the 4 V sinusoidal voltage is increased from 0.1 Hz to 4 Hz. The observed increase in the amplitude of the current, I , indicates a decrease in the electrical impedance, Z , of the IPMC samples at the higher frequency. The electrical impedance can be thought of as the resistance of the sample under AC conditions. The voltage, V , and the current, I , in AC circuits, as was seen, are sinusoidal and have constant amplitude, frequency and phase. The resistive component of the impedance, Z_R , of the sample is defined as the ratio of AC applied voltage, V_R , across the sample to the AC generated current, I_R , through the sample, and it is equal to the resistance, R , of the sample:⁴

$$Z_R = \frac{V_R}{I_R} = R \quad (8.4)$$

As for resistance, the unit of impedance, Z_R , is Ohms where the units of V_R and I_R are Volts and Amperes, respectively. It is important to note that, unlike for resistors (where Z_R is equal to R and it is constant), the capacitive component of impedance, Z_C , changes with frequency as Equation 8.5 shows.

$$Z_C = \frac{V_C}{I_C} = \frac{1}{j\omega C} \quad (8.5)$$

In Equation 8.5, j represents the imaginary unit ($\sqrt{-1}$), ω is equal to $2\pi f$, where f is the frequency in Hz, and C is the capacitance of the capacitor. Thus, for a sample with a constant capacitance, C , the impedance Z_C decreases as the frequency, f , increases. According to Equation 8.6, this results in a decrease in the impedance, Z , of the sample since the resistive component of impedance, Z_R , is constant, and is equal to R .

$$Z = Z_C + R \quad (8.6)$$

According to the results presented in Figure 8.22, an inverse relationship exists between the impedance of the IPMC samples and the applied frequency. This is seen as an increase in I with increasing frequency at constant V . This behavior indicates, once again, the capacitive characteristics of the IPMC samples.¹

The changes observed in phase difference between the voltage, V , and the current, I , as a result of increasing the frequency also confirms these explanations. As was seen in Figure 8.22, the current, I , leads the voltage, V , when a frequency of 0.1 Hz is applied. When an voltage frequency of 4 Hz is applied, however, the current, I , and the voltage, V , appear almost in-phase. This implies that at low frequency the IPMC samples act more like capacitors while at high frequencies they act more like resistors.⁵

Electrode Thickness

During the process of electroless platinum electroding two similar platinum electrodes are deposited at each face of the Nafion membrane. The thicknesses of these electrodes can be increased by repeating the plating process. This was extensively investigated in Chapter Four, where SEM studies of the IPMC samples were presented. It was found that the

repetition of the plating process up to 4 cycles gave rise to the thicker electrode layer at the surfaces of the IPMC samples.

In Figures 8.3 and 8.8 the effect of increasing thickness of the platinum electrodes was observed as increases in tip displacement in both the commercial and the cast IPMC samples. The force outputs of the samples also increased with increasing electrode thickness (Figures 8.14 and 8.17). Because of the dendritic structure of the platinum layers, the improvement of the electromechanical performance of the IPMC samples as a result of increasing electrode thickness might be partly attributed to increases in the area of the interface between the electrodes and the polymer (*i.e.* the surface area, A , of the electrodes).^{6,7} According to Equation 8.1, this would improve the capacitance, C , of the sample. If we consider that an IPMC sample with a higher surface area electrode would possess a higher capacitance, C , larger opposite charges, Q , would be expected to accumulate at the electrodes, according to Equation 8.2, once a voltage, V , was applied. This would produce a stronger electric field across the thickness of the sample, which would cause electrically-induced diffusion of a greater number of hydrated Li^+ ions towards the cathode. In turn, this would be observed as an improvement in the electromechanical performance of the samples. Thicker platinum layers are also likely to improve the conductivity of the electrodes themselves, so allowing more efficient application of the external voltage to the IPMC sample. There is also evidence from the SEM work that increased amount of platinum-impregnation would decrease d in Equation 8.1, and also lead to increased capacitance.

In Figure 8.22, as the result of application of 4 V at 0.1 Hz, a higher current was observed for Pt₄Cast (Figure 8.22(c)), than for Pt₂Cast (Figure 8.22(a)), which had the thinner electrode layer. This was also the case when 4 V was applied at 4 Hz. These results can be explained as a combination of decreased resistance, caused by improved surface conductivity after more platinum plating cycles, and increased capacitance because of an increase in electrode-polymer interface area and a decrease in d .

The latter point resembles the findings of the work conducted by Oguro and his coworkers.⁶ They have shown that as the concentration of platinum at the polymer surfaces is increased by using the repetitive electroless platinum electroding process, the electrical capacitance of the IPMC sample also rises. In their study, the electrical capacitance of the IPMC sample increased linearly with the number of plating cycles, only becoming constant after 8 cycles.

Surface Conductivity

It has been seen that the electromechanical behaviour of the IPMC samples can be improved by the deposition of a thin gold layer over the platinum-impregnated surfaces of the IPMC samples. This improvement is attributed to an increase in the surface conductivity of these samples.^{8,9} In Section 4.5.2, it was shown that the structure of the platinum electrodes consists of two distinct regions: a relatively broad porous layer extending into the polymer, and a thin dense layer at the external surface of this. As seen in the SEM images, this layer does contain some microcracks and is only around 0.1-0.25 μm thick, despite being generally dense. Both these factors would present resistance to electronic conductivity along the electrode layer.⁶¹ Physical vapor deposition (PVD) of a

thin gold layer, however, would be expected to improve the homogeneity of the surface structure, by filling in the microcracks¹⁰ existing in the solid platinum layer. Comparison of the BSE images of AuPt₂Com (Figure 4.13) and Pt₂Com (Figures 4.5 to 4.8 (b)) reveals the improvement of the homogeneity of the surface structure caused by the deposition of the gold layer. This is expected to increase the surface conductivity of the AuPt₂Com sample. Indeed, higher amplitudes of the current, I , are observed (Figure 8.22) for AuPt₂Cast and AuPt₄Cast, than for Pt₂Cast and Pt₄Cast, respectively. This can be explained by a decrease in the surface-resistance of the samples.

Thickness of IPMC Polymer

The electromechanical behaviour of the cast and the commercial IPMC samples showed very similar dependence on the amplitude and the frequency of the applied voltages. This implies that the electrochemical characteristics of the prepared cast Nafion (with dry thickness of 1.65 mm) were similar to those of the commercially available Nafion membrane (dry thickness of 0.2 mm). The comparison of these samples (in Figures 8.10 and 8.18) revealed that application of the same voltage at the same frequency induced much larger tip displacements in the commercial IPMC samples, while resulting in the generation of much larger forces for the cast IPMC samples. In other words the cast IPMC samples generated much larger forces but smaller displacements than the commercial IPMC samples under application of similar electrical conditions. The dissimilar behaviour of the cast and commercial IPMC could be explained simply by the large difference in thickness between the sample and possibly also by differences in the physical structure of the two

membranes. The greater thickness of the cast IPMC samples the greater it restricts the bending displacement while allowing the generation of larger forces. Subtle differences in polymer structure between the cast and commercial samples may, however, also play a role. In Chapter Four, NMR and MRI studies of these membranes indicated that the cast Nafion was less dense and so could absorb more water than the commercial polymers which have a more crystalline structure. These findings were in good agreement with the results obtained from mechanical tests performed on similar membranes by Shahinpoor and Kim.¹¹ They established that their cast membranes possessed weaker electrostatic crosslinking and lower crystallinity than the commercially available Nafion membranes. This would tend to reduce the rigidity of the cast Nafion membrane below that of the commercial Nafion membrane, if the dimension of the samples were equal. This would result in higher displacements and lower force generation in the cast sample, all else being equal.

Larger current amplitudes were recorded in Pt₂Cast (Figure 8.21) than in Pt₂Com (Figure 8.20). This implies that Pt₂Cast possessed lower impedance, Z . To explain this we must consider the difference in capacitance, C , and resistance, R , on going from the commercial to the cast IPMC sample. The cast Nafion membrane has been shown to be less dense and to absorb approximately 2-4 times more water than the commercial Nafion (Section 4.4.2) this would increase the ionic conductivity of the cast IPMC sample, decreasing impedance, Z . However, the much larger spacing between electrodes in the cast IPMC sample would act to decrease capacitance, C , and so increase impedance, Z . The less dense cast Nafion may allow a higher surface area platinum-polymer interface to form, which would tend to increase capacitance, C , and decrease impedance, Z . However, this is unlikely to compensate for the large increase in d . Therefore, the decrease in impedance on going from

the commercial to the cast IPMC sample would appear to be largely due to its improved ionic conductivity. This is demonstrated, for example, by dividing the peak to peak voltage by the peak to peak current. For the samples Pt₂Cast and Pt₂Com the values are 0.6 and 3 Ω , respectively. Taking into account the thicknesses of the samples, this implies that the conductivity is 15 times greater for the cast membrane than for the commercial membrane.

8.5. Summary

This chapter presented the results obtained from the study of the electromechanical (tip displacement and generated force) and electrical characteristics of the cast and commercial IPMC samples. The effect of variables such as the amplitude and frequency of the applied sinusoidal voltage, electrode thickness (number of plating cycles), surface conductivity and thickness of the Nafion membrane on the performances of these samples were described. All the IPMC samples underwent bending deformations and generated force, in response to application of sinusoidal voltages across their thicknesses. The application of the same amplitude of the sinusoidal voltage induced much larger tip displacements in the commercial Nafion-based IPMC samples, while it resulted in the generation of much larger forces in the cast Nafion-based IPMC samples. The tip displacements and force outputs of the samples showed qualitatively very similar dependences on the amplitude and frequency of the applied voltage. That is, they increased as the amplitude of the applied voltage increased up to 10 V and increased as frequency decreased, down to 0.1 Hz. The electromechanical characteristics of the samples improved as a result of increasing the thickness of the platinum electrodes and also of adding a gold layer to increase surface

conductivity. At a constant frequency, the effect of increasing amplitude of the applied voltage, V , was to increase the amplitude of the current, I . A phase difference between the applied voltage and the current was observed, the current, I , leading the voltage, V . This implied that the IPMC samples possessed capacitive characteristics. The phase difference decreased as a function of increasing frequency of the applied voltage and also of increasing thickness of the platinum electrode. The comparison of the electrical characteristics of the samples Pt₂Cast and Pt₂Com implied that the thick Pt₂Cast sample possessed lower resistance due to its ability to absorb larger amounts of water, increasing its ionic conductivity.

8.6. References

-
- [1]. X. Bao, Y. Bar-Cohen, S. S. Lih, *Smart Structures & Materials, Proc. of SPIE*, 2002, 4695, 220.
 - [2]. F. B.A. Früngel, "High Speed Pulse Technology", *Academic Press Inc.*, U.S, 1976.
 - [3]. M. Shahinpoor, *Smart Structures & Materials, Proc. of SPIE*, 1999, 3669, 109.
 - [4]. R. Macdonald, W. R. Kenan "Impedance Spectroscopy: Emphasizing Solid Materials and Systems", *John Wiley and Sons*, 1987.
 - [5]. F. Lufrano, P. Staiti, M. Minutoli, *Journal of Power Sources*, 2003, 124, 314.
 - [6]. K. Oguro, N. Fujiwara, K. Asak, K. Onishi, S. Sewa, *Smart Structures & Materials, Proc. of SPIE*, 1999, 3669, 64.
 - [7]. Y. Abe, A. Mochizuki, T. Kawashima, S. Yamashita, K. Asaka, K. Oguro, *Polym. Adv. Technol.*, 1998, 9(8), 520.
 - [8]. M. Shahinpoor, K.J. Kim, *Smart Mater. Struct.*, 2001, 10, 819.

[9]. M. Shahinpoor, K. J. Kim, *Smart Mater. Struct.*, 2000, 9, 543.

[10]. S. Nemat-Nasser, Y. Wu, *J. Appl. Phys.*, 2003, 93, 5255.

[11]. K. J. Kim, M. Shahinpoor, *Polymer*, 2002, 43(3), 797.

Chapter Nine

Conclusion and Future Work

9.1. Conclusion

9.1.1. Structural Characterization of Nafion Membranes

1. The results of ^1H NMR spectroscopy experiments conducted on hydrated commercial (dry thickness ~ 0.2 mm) and cast (dry thickness ~ 1.65 mm) Nafion membranes revealed that these membranes had the same chemical composition and that no proton-containing contaminant such as alcohol or DMF had been introduced to the cast membrane during the preparation process. These results also confirmed that any such contamination was removed in the cleaning procedure used in this work.
2. The results of the comparative multi-echo MRI imaging of the hydrated Li^+ -exchanged commercial and cast Nafion membranes enabled the evaluation of the physical structure of these membranes. It was found that the commercial and cast Nafion membranes were quite homogenous in structure since a uniform distribution of spin-spin relaxation time, T_2 , and proton density, PD , of the protons of the absorbed water molecules were observed in these membranes.
3. For both the cast and the commercial Nafion membranes the values of spin-spin relaxation time, T_2 , obtained were found to be significantly less than the values for bulk deionized water and even a saturated solution of LiOH . The observed difference was attributed to the confinement of most or all of the water molecules within the hydrophilic regions of the Nafion membrane, where their rotational mobility was restricted by the strong electrostatic interactions with the ionic groups and also with the other water molecules.

4. After an initial result found by NMR measurements, suggesting that the commercial Nafion membrane had a more ordered and crystalline structure than the cast Nafion membrane, the very different values of spin-spin relaxation time, T_2 , of water absorbed in these membranes also implied that the rotational mobility of the water molecules was more restricted in the commercial membrane, confirming that this membrane had a more dense and crystalline structure. The protons in water molecules absorbed in the cast Nafion had T_2 of approximately 250 ms while they possessed much shorter T_2 of approximately 40 ms in the commercial Nafion.
5. Proton density, PD , maps obtained for the hydrated Li^+ -exchanged commercial and cast Nafion membranes showed that the cast membrane contained a higher concentration of protons (of the absorbed water molecules) than the commercial membrane. This finding was in good agreement with the values of the water content determined for both the membranes. The difference in water content was attributed to the less crystalline physical structure of the cast membrane, which allows a larger amount of water molecules to be absorbed.
6. The failure of multi-echo MRI imaging to image features in the fully dehydrated Li^+ -exchanged cast and commercial Nafion membranes revealed that the protons observed in the MRI images of the hydrated membranes were uniquely related to the water molecules absorbed within the Nafion membranes. This also confirmed the results obtained from ^1H NMR spectroscopy of these membranes, that it is unlikely that mobile H-containing contaminants are present.
7. Diffusion-weighted imaging (DWI) of the self-diffusion of water molecules absorbed in the Li^+ -exchanged cast Nafion membrane showed that the water

diffusion coefficients were not dependent on the direction in which the measurements were made. This revealed that the diffusion of water molecules was isotropic in the cast Nafion membrane and that this membrane had a homogenous structure.

8. Diffusion coefficient, D , of water molecules absorbed in the Li^+ -exchanged cast Nafion membrane ($6.09 \times 10^{-10} \text{ m}^2\text{s}^{-1}$) was also found to be much smaller than the D of pure bulk water ($2.5 \times 10^{-9} \text{ m}^2\text{s}^{-1}$).
9. Very similar values of D_x and D_z of water molecules in the cast membrane were obtained. This revealed that the self-diffusion of water molecules was restricted to the same degree, by boundaries and interfaces, along the length (x-axis) and thickness (z-axis) of the membrane. It also gave evidence that the structure of the cast Nafion membranes was not specifically ordered along one direction, *i.e.* hydrophobic and hydrophilic regions were evenly distributed throughout the Nafion polymer.

9.1.2. Structural Characterization of IPMCs

10. SEM study and EDX analysis of the fabricated commercial and cast Nafion-based IPMCs revealed that the thickness, structure and morphology of the plated surfaces of these samples varied depending on the preparative method of the Nafion membrane and also on the number of repeat cycles of the electroless platinum electroding process.

11. Platinum electrode regions of IPMCs were found to be formed of two distinct layers: a thin dense layer at the outer surface and a broader porous layer extending into the Nafion membrane where platinum particles had been impregnated into the polymer. A gradient in concentration of platinum particles in the electrode region was also observed, *i.e.* the concentration of platinum was very high at the outer surfaces and decreased gradually towards the centre of the sample.
12. The effect of varying the number of repetitions of the platinum electroding process (number of plating cycles) on the thickness of the platinum electrode regions of IPMCs was also considered. It was found that increasing the number of the plating cycles affected the thickness of the platinum-impregnated regions in the commercial and cast Nafion-based IPMCs in the same way: the thinnest electrode region was observed in the samples with one plating cycle and this thickness increased according to the increase in the number of repetitions of the plating cycle.
13. It was found that application of the same number of plating cycles resulted in a much thinner electrode region in the commercial IPMCs compared to the matching cast IPMCs.
14. In the commercial IPMCs, repetition of the plating process increased the thickness of the outer dense layer at the surface more than that of the porous layer in the sub-surface regions.
15. In the cast IPMCs, repetitive platinum electroding increased the thickness of the porous impregnated layer in the sub-surface regions much more than the outer dense layer at the surfaces.

16. The dissimilarity of the effect of the platinum electroding process on the commercial and cast Nafion membranes was attributed to the difference in the density and crystallinity of these membranes, the commercial product being the denser and more crystalline.
17. The penetration of a higher concentration of platinum into the cast IPMCs also lead to the formation of larger agglomerates of platinum particles in the sub-surface region of these samples, than in the corresponding part of the commercial IPMCs.
18. Multi-echo MRI imaging of the hydrated Li^+ -exchanged AuPt_1Cast (IPMC) sample showed that despite the presence of the platinum particles in the sub-surface regions of the sample, the PD was relatively constant over this sample, as in the cast Nafion without electrodes.
19. Comparison of the PD maps of AuPt_1Cast and cast Nafion without electrode revealed that the latter contained a higher concentration of protons than AuPt_1Cast . This was attributed to the greater rigidity and stiffness of the AuPt_1Cast than the cast Nafion, caused by the presence of the platinum particles.
20. T_2 values of water molecules absorbed in AuPt_1Cast were found to decrease from the centre towards the platinum-impregnated surfaces of the sample. This suggested that T_2 of water molecules was inversely related to the concentration of platinum; higher concentrations of platinum leading to lower T_2 values. This was considered to occur as a result of the increasing stiffness of the membrane from the centre towards the surfaces, due to the increasing concentration of platinum particles towards the surfaces.

21. Diffusion-weighted imaging (DWI) of the self-diffusion of water molecules in AuPt₁Cast revealed that the spatial variation of diffusion coefficient, D , over this sample was not uniform and that water molecules in this sample possessed different diffusion coefficients depending on their location in the sample. Water molecules located at the surfaces, where the sample contained a high percentage of platinum particles, diffused at a higher rate than those located at the centre of the sample, where the sample contained few or no platinum particles.
22. The diffusion coefficients of the water molecules in AuPt₁Cast were also dependent on the orientation of the measurements. The rate of diffusion of water molecules was generally higher along the length of the sample than across the sample thickness. This implied that diffusion of water molecules in this sample was anisotropic and that this sample was not homogenous in structure.
23. It was found that in AuPt₁Cast the difference between the D at the surfaces and at the centre of the sample was much larger when the pulsed gradients were applied across the sample thickness, than along the length.
24. Similar values of D_x and D_z were observed at the surfaces of AuPt₁Cast while the values of D_x and D_z were different at the centre of the sample.
25. The measured D_x and D_z at the surfaces of AuPt₁Cast were slightly higher than those measured in the cast Nafion sample without electrodes. This was attributed to the faster diffusion of water molecules in or around the agglomerates of platinum particles near the surfaces of the sample where the concentration of these particles was high.

26. D_z at the centre of AuPt₁Cast was much smaller than D_z at the cast Nafion without electrode, while D_x at the centre of AuPt₁Cast was very similar to the D_x in the cast Nafion without electrode.
27. The dissimilarity of D_x and D_z at the centre of AuPt₁Cast suggested that the diffusion of water molecules at the centre of this sample, where the concentration of platinum particles was approximately zero, faced more resistance along the sample thickness (z-axis), than along the length (x-axis) of the sample. This was attributed to the differential shrinkage of the sample along the length and the thickness, due to the partial dehydration caused on going from storage in aqueous solution to testing in an air environment.

9.1.3. MRI Study of Electrically-Induced Distribution of Water in the Commercial Nafion Membrane and IPMC Actuator

28. The electrically-induced distribution of water molecules in the commercial Nafion (without electrode) and AuPt₁Cast (IPMC) samples were investigated by placing a functioning electrochemical cell inside the MRI scanner and performing multi-echo imaging of the water distribution in real time during application of a continuous d.c. potential. *To our Knowledge, this is the first time such an electrochemistry experiment had been performed in situ inside an MRI scanner.*
29. It was found that immediately after application of the continuous potential, as a result of the migration of the hydrated Li⁺ ions in the electric field, two thin boundary layers were formed; one enriched in hydrated Li⁺ ions and water

- molecules at the cathode (cathode boundary layer) and the other depleted of hydrated Li^+ ions at the anode (anode boundary layer). This was deduced from the increases occurred in T_2 of water molecules in the areas near the cathode and anode.
30. The increase in T_2 was attributed to a significant increase in the amount of water molecules present in the more hydrophobic regions of the Nafion, between the hydrophilic regions, where there would be much less restriction of the molecular rotation of the water molecules, due to the much weaker interaction of the chemical environment in the hydrophobic regions with the water molecules.
 31. On continuous application of the potential, the migration of hydrated Li^+ ions from the anode towards the cathode was found to be continued in the commercial Nafion and AuPt₁Cast samples since, over time, T_2 and PD increased significantly near the cathode, while they decreased significantly near the anode. A secondary contribution to the increase in T_2 near the cathode and decrease near the anode, over time, might also be caused by the respective increases and decreases in the size of the hydrophilic regions (clusters) in these areas.
 32. The direction of the migration of the hydrated Li^+ ions was reversed by reversal of the polarity of the applied potential and this was seen in the reversal of the variations in T_2 , PD and D across the sample.
 33. It was found that, on application of a continuous d.c. potential, only a small percentage of water molecules absorbed in the commercial membrane (~10%) and IPMC sample (~20%) had moved toward the cathode and that the majority of water molecules remained unaffected by the application of the potential.

34. DWI of AuPt₁Cast in real time, during application of a continuous d.c. potential revealed that as soon as the potential was applied across the thickness of the sample, the diffusion coefficient of water increased over the whole sample and particularly near the cathode. This was then followed by an overall decrease in the average diffusion coefficient of water over the whole sample while high D values continued to be observed near the cathode and low D values near the anode.
35. The increase in D near the cathode and decrease near the anode on application of the potential was attributed to the freer diffusion of the water molecules in the swollen cathode boundary layer and the restricted diffusion of these molecules in the contracted anode boundary layer.
36. In the AuPt₁Cast, but not in the commercial Nafion sample, the formation of the cathode and anode boundary layers, under application of the potential, was associated with a slight bending deformation of AuPt₁Cast (IPMC) towards the anode. This was observed in the T_2 , PD and D maps of this sample. On continuous application of the potential, the bending deformation of AuPt₁Cast towards the anode increased. This was associated with simultaneous increases in PD and T_2 and D near the cathode, and decreases of these near the anode.
37. The bending deformation of AuPt₁Cast, under application of the potential, was attributed to the elastic energy differential between the cathode and anode regions due to the increasing concentration of the hydrated Li^+ ions near the cathode and the decreasing concentration of those near the anode. This is the accepted mechanism of actuation of such IPMC actuators.

38. The direction of the bending deformation of AuPt₁Cast was reversed as the polarity of the applied potential was reversed, representing the reversal of the direction of the migration of the hydrated Li⁺ ions.
39. It was found that, as for the self-diffusion of water, the electrically-induced diffusion of water molecules was more restricted along the thickness of AuPt₁Cast than along the length of this sample. This was observed as more significant changes in the spatial variation of D_x than D_z over the whole sample, after application of the potential.
40. From DWI results it was deduced that, under application of the potential water molecules would diffuse towards the cathode along rather a “zigzag” pathway, and that during their movement their diffusion would be easier along the length of the sample than across the thickness.
41. It was found that the increase in the bending deformation of AuPt₁Cast towards the anode with time was associated with the prolonged application of the potential and the slow back-diffusion of water molecules from the cathode towards the anode (in order to overcome the generated osmotic pressure and elastic energy differential between the cathode and anode regions).
42. From the *PD* maps it was deduced that, on the continuous application of the potential, AuPt₁Cast was dehydrated much faster than the commercial Nafion membrane. This was attributed to the enhanced evaporation of the water from the porous platinum electrode surfaces of AuPt₁Cast (not present in the commercial sample) and also to the higher electrical conductivity of this sample.

43. From DWI results it was found that the removal of the applied potential resulted in relaxation of the bending deformation of AuPt₁Cast and also expansion of the sample, mainly along its thickness, but to some extent, also along its length.
44. Unlike when the potential was applied, the removal of the applied potential resulted in much larger changes in the spatial variation of D_z than D_x over AuPt₁Cast. This suggested that, during the application of the potential, water molecules were forced to diffuse through high activation energy routes across the thickness of the sample (z-direction), and that as the electric field, the force, was removed, they avoid these high activation energy routes and diffused more readily through lower activation energy routes along the length of the sample (x-direction). That is, diffusion along the length of the sample offers less resistance than diffusion across the thickness.
45. Removal of the applied potential, over time, resulted in the return of the values of D_x and particularly D_z in AuPt₁Cast to approximately similar values to those observed at the beginning of the experiment (before the potential was applied). This suggested that the sample was able to return almost to its original (equilibrium) state over a long time period through water uptake from the humidified atmosphere maintained in the experimental set up.

9.1.4. Modeling of the Structure of Nafion Membrane and Electrically-Induced Diffusion of Hydrated Li⁺ Ions within the Membrane

46. A model was proposed for the structure of Nafion membrane and electrically-induced diffusion of water molecules within the membrane. Models proposed by

Gierke¹, Yeager² and Meresi³ were considered. In the proposed model, highly hydrophilic regions would be expected to exist within a highly hydrophobic major domain but they would be connected to each other by regions of a range of thicknesses and a range of intermediate hydrophilicities.

47. Self-diffusion of water in the absence of an applied potential would be expected to take place via low activation energy routes through hydrophilic regions of the polymer.
48. Electrically-induced diffusion of water, on application of the continuous potential, would be expected to occur through higher activation energy routes. That is, the hydrated Li^+ ions would move towards the cathode by jumping consecutively from one to another hydrophilic region, but to do this it would need to pass through the more hydrophobic regions of the polymer.

9.1.5. Characterization of Electromechanical Performance of IPMCs

49. The tip displacement and generated force of the commercial and the cast IPMC samples, in response to application of sinusoidal voltages, were investigated. It was found that the tip displacements and force output of these IPMC samples were dependent on the amplitude and frequency of the input sinusoidal voltages, *i.e.* the tip displacement and generated force of these samples increased with increasing amplitude of the applied voltage up to the maximum 10 V, and with decreasing frequency, down to 0.1 Hz.

50. The application of the same amplitude and frequency of the sinusoidal voltage induced much larger tip displacements in the commercial IPMCs, while it resulted in the generation of much larger forces in the cast IPMCs. The dissimilar behaviour of the cast and commercial IPMC was attributed to the large difference in thickness of these samples and also to the differences in the physical structure of the two membranes. The greater thickness of the cast IPMC samples more severely restricts the bending displacement while allowing the generation of larger forces.
51. The improved electromechanical behaviour of IPMCs in terms of increased generated force and increased tip displacement, resulted from increasing the thickness of the platinum electrodes (by repetitive platinum electroding).
52. The electromechanical behaviour of IPMCs was also found to be improved by the physical vapour deposition (PVD) of a thin gold layer over the platinum-impregnated surfaces of the IPMC samples. This improvement was attributed to an increase in the surface conductivity of these samples. SEM studies of IPMCs revealed that PVD of a thin gold layer improved the homogeneity of the surface structure by filling in and bridging the microcracks existing in the dense platinum layer. Higher amplitudes of current were also observed for IPMCs with improved surface conductivity, due to decreased surface-resistance of these samples.
53. At a constant frequency, the effect of increasing the amplitude of the applied voltage was to increase the amplitude of the current. A phase difference between the applied voltage and the current was observed, the current leading the voltage, implying that IPMCs possessed capacitative characteristics.

54. The phase difference between the applied voltage and the current decreased as a function of increasing amplitude and of increasing frequency of the applied voltage and also of increasing thickness of the platinum electrode.
55. It was found that on application of high voltages (~10 V) to the commercial and cast IPMCs the current and voltage appeared almost in-phase. This suggested that IPMCs behave more like resistors at high voltages. It was concluded that the “equivalent circuit” for IPMCs contained both capacitive and resistive components.
56. For both cast and commercial IPMCs, in response to the same sinusoidal voltage, the highest current was recorded in IPMCs which had the thickest platinum electrode. This was attributed to the decreased resistance, caused by more platinum plating cycles and increased capacitance because of an increase in electrode – polymer interface area, and decreased space between the electrodes.
57. The comparison of the electrical characteristics of cast and commercial IPMCs revealed that the thick cast IPMCs possessed lower resistance due to their ability to absorb larger amounts of water, so increasing their ionic conductivity.

9.2. Future Work

Since understanding the actuation mechanism of IPMC actuators requires thorough knowledge of the ions and water transport within the ion exchange IPMC polymer, it has been the purpose of the work presented in this thesis to characterize the structure of Nafion and Nafion-based IPMCs and to produce models based on experimental findings, for the

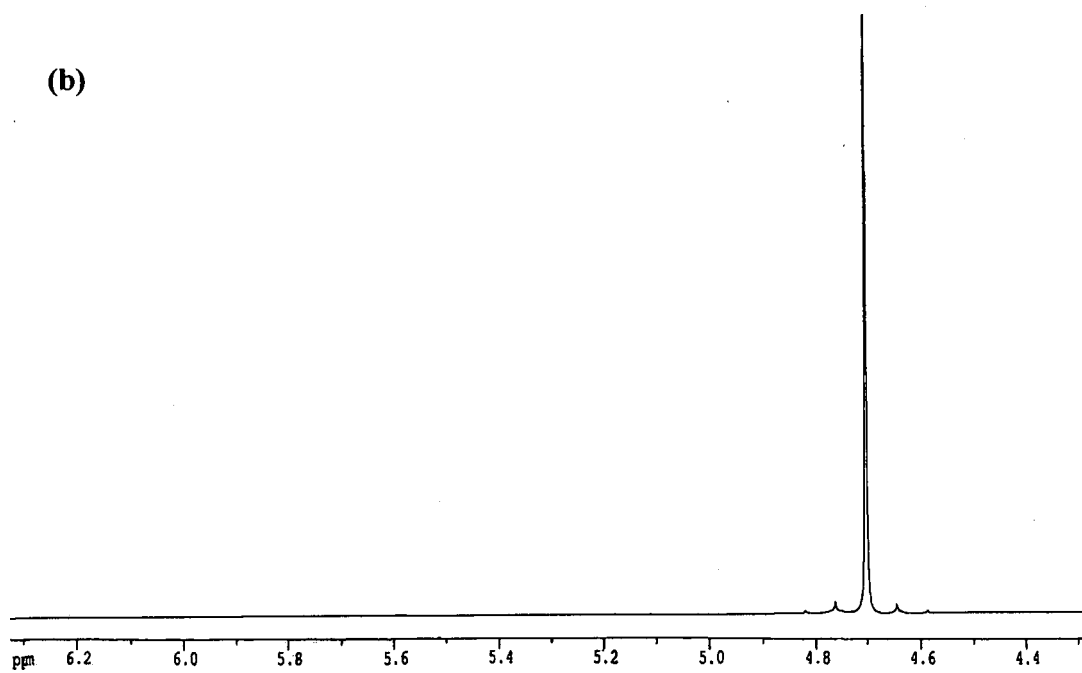
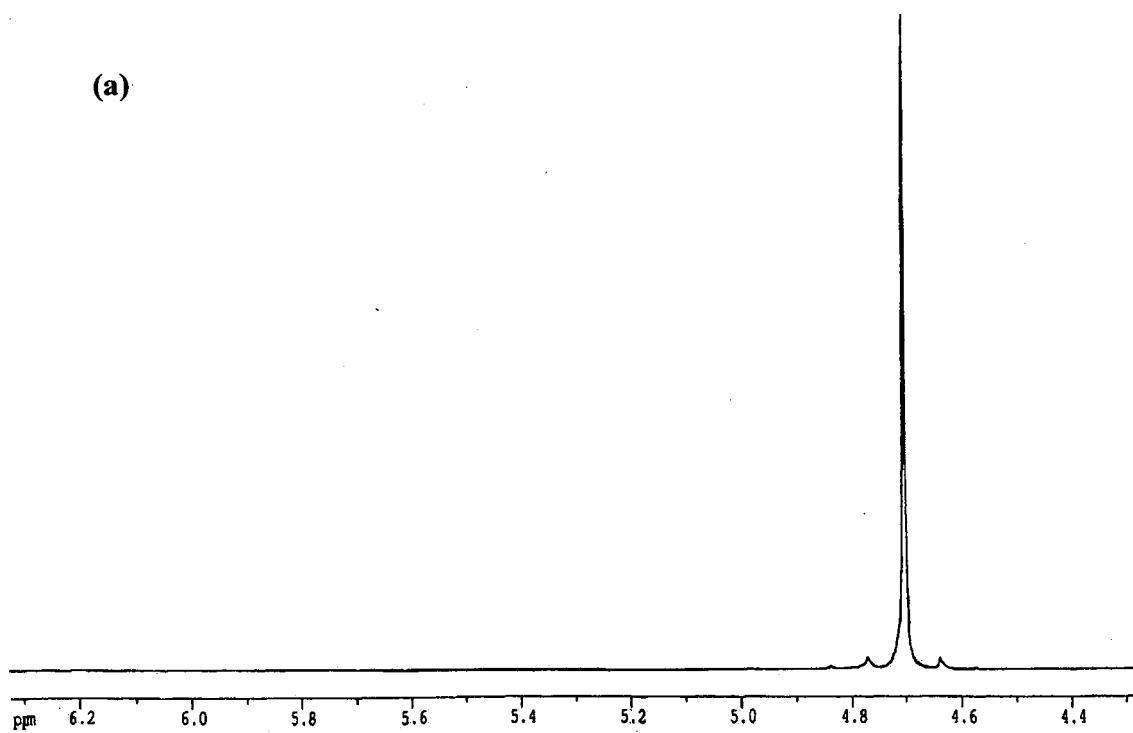
structure of these materials and also for transport processes within them. Suggestions for extensions to the work contained in this thesis are the followings:

- (1) Investigating the changes that occur in the mobility of the perfluorinated molecular backbone and side chains on application of a small d.c. potential, by ^{19}F MRI study of fluorine distribution in Nafion membranes and IPMCs, could provide additional information on the structure of these materials and water transport within them.
- (2) The effect of alternative solvents and cations on the mobility of polymer chains in Nafion membrane is also worth assessing using solid state ^{19}F NMR to obtain a better understanding of the microstructure of this polymer since these variables can affect the electromechanical performance of IPMCs.
- (3) Diffusion anisotropy in Nafion-117 membrane could be studied using diffusion-weighted imaging, and the resulting images could be compared with the results of similar experiments performed on cast Nafion in this work to evaluate the degree of ordering in these membranes.

9.3. References

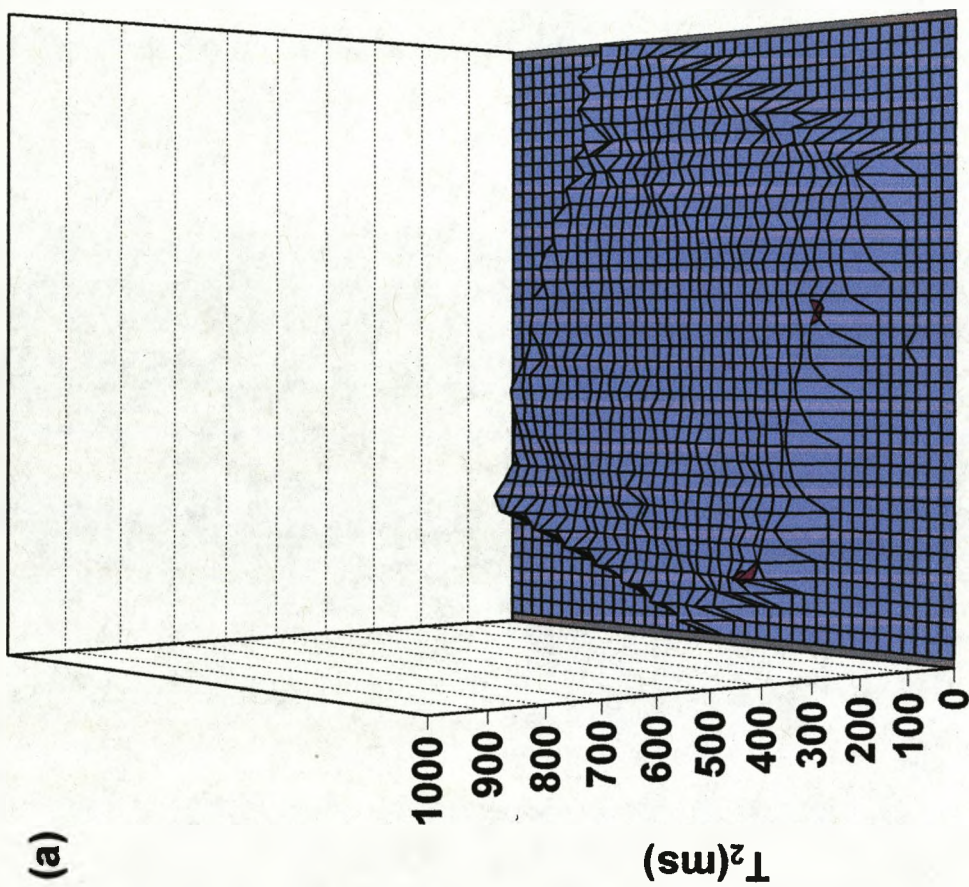
-
- [1]. T. D. Gierke, *The electrochemical Society Extended Abstracts*, 1977, 77(2), 438, 1139.
 - [2]. H. J. Yeager, A. Eisenberg, *American Chem. Soc.*, 1982, 180(1), 41.
 - [3]. G. Meresi, Y. Wang, A. Bandis, P. T. Inglefield, A. A. Jones, W. Y. Wen, *Polymer*, 2001, 42, 6153

Appendix 1

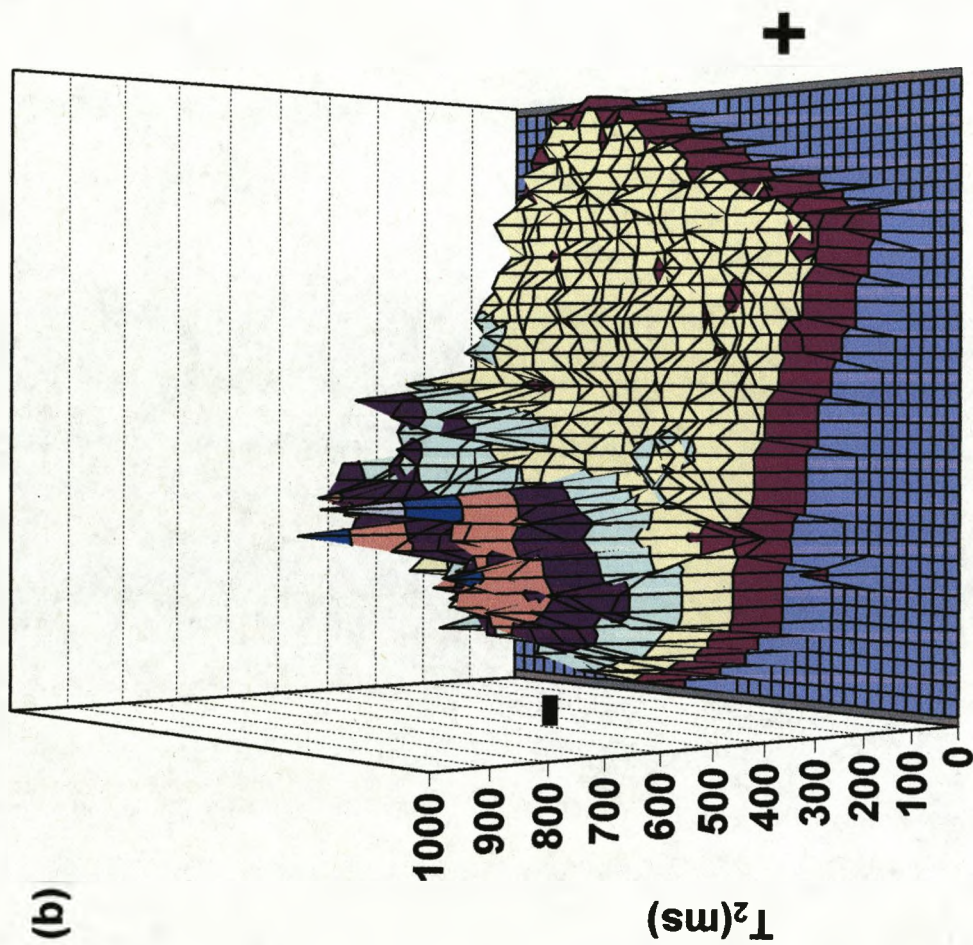


^1H NMR of DI water-swollen (a) commercial and (b) cast Nafion membranes.

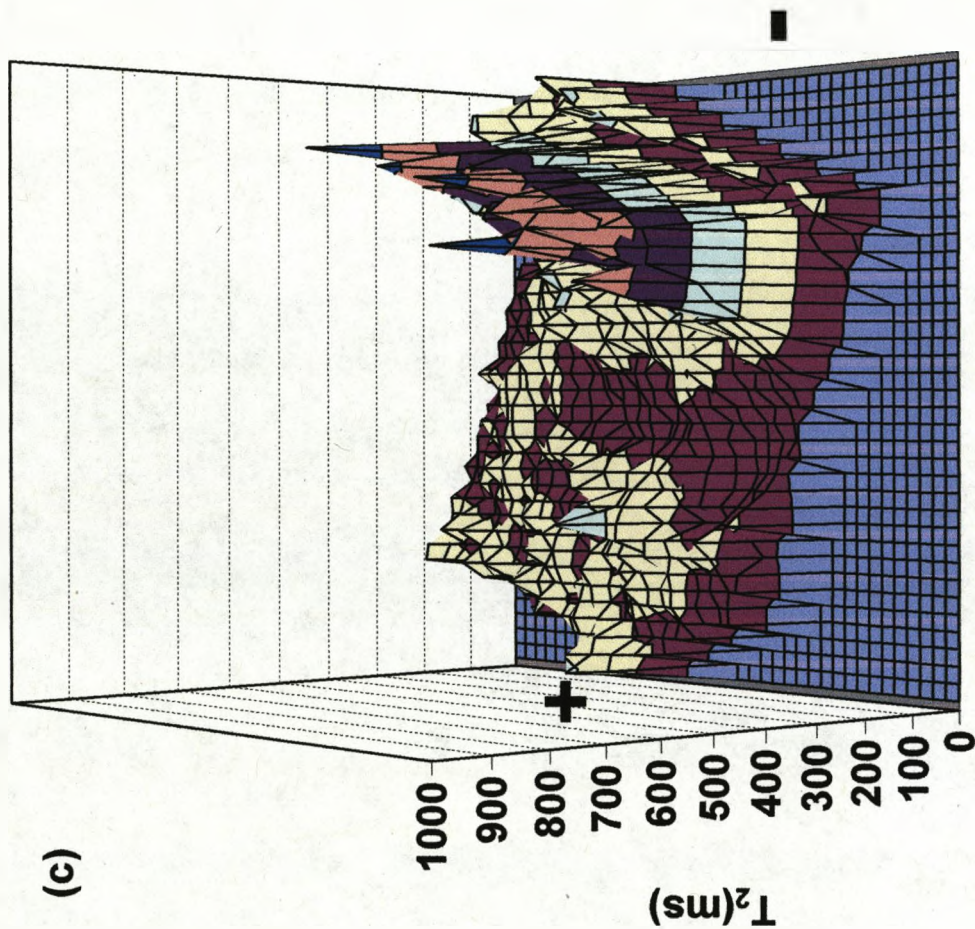
Appendix 2



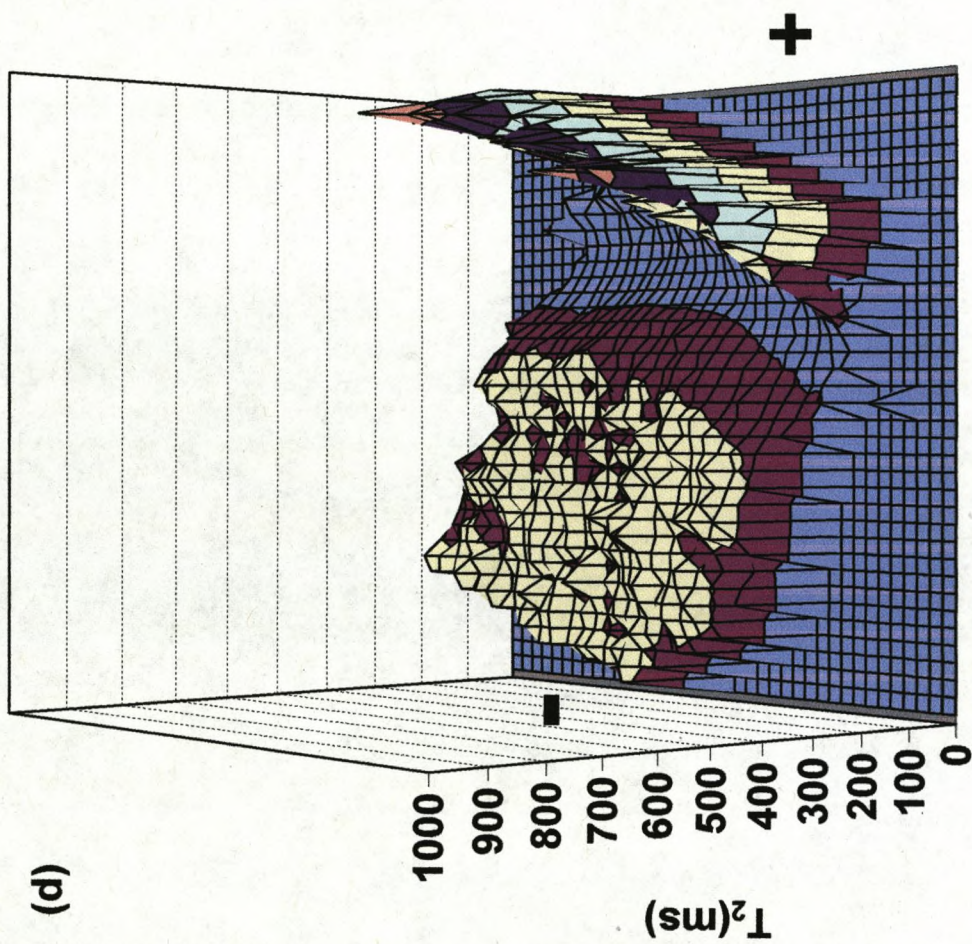
Three-dimensional plot of spin-spin relaxation time, T_2 map, across the whole Nafion sample with no potential applied.



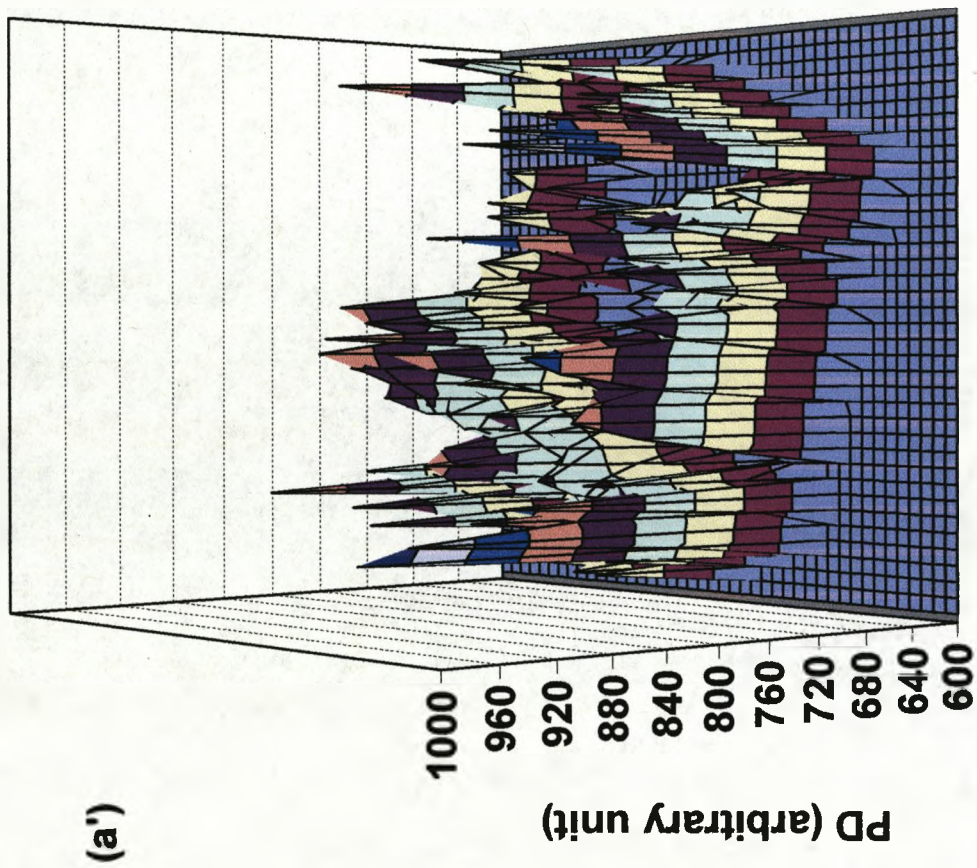
Three-dimensional plot of spin-spin relaxation time, T_2 map, across the whole Nafion sample 122 min. after application of the 5V d.c. potential. The position of the anode and cathode are indicated by "+" and "-" signs.



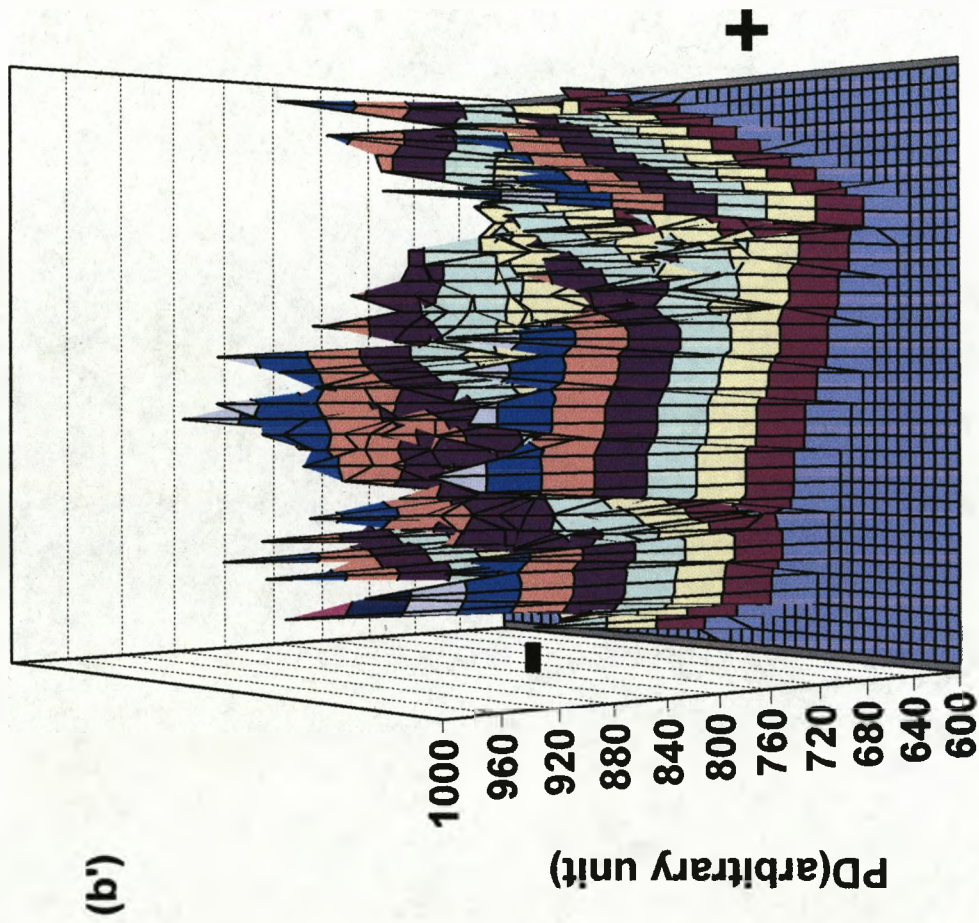
Three-dimensional plot of spin-spin relaxation time, T_2 map, across the whole Nafion sample 89 min. after first reversal of the polarity of the 5 V d.c. potential. The position of the anode and cathode are indicated by “+” and “-” signs.



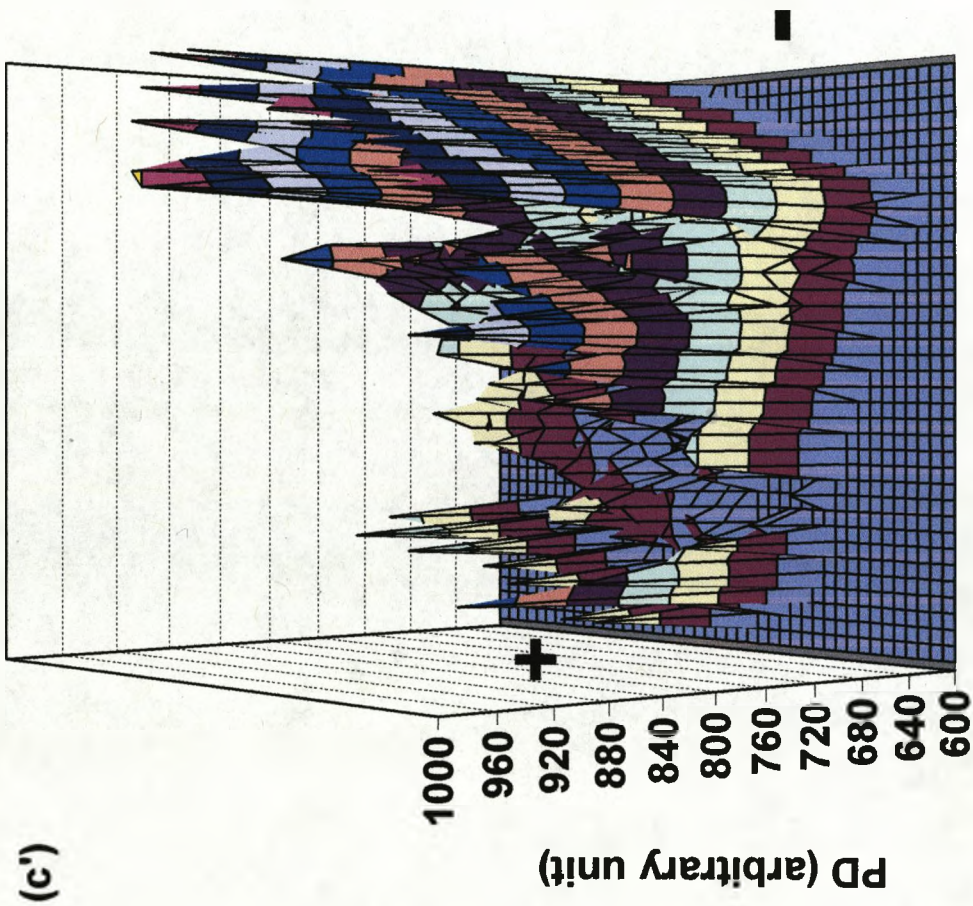
Three-dimensional plot of spin-spin relaxation time, T_2 map, across the whole Nafion sample 89 min. after second reversal of the polarity of the 5V d.c. potential. The position of the anode and cathode are indicated by “+” and “-” signs.



Three-dimensional plot of proton density, *PD* map, across the whole Nafion sample with no potential applied.

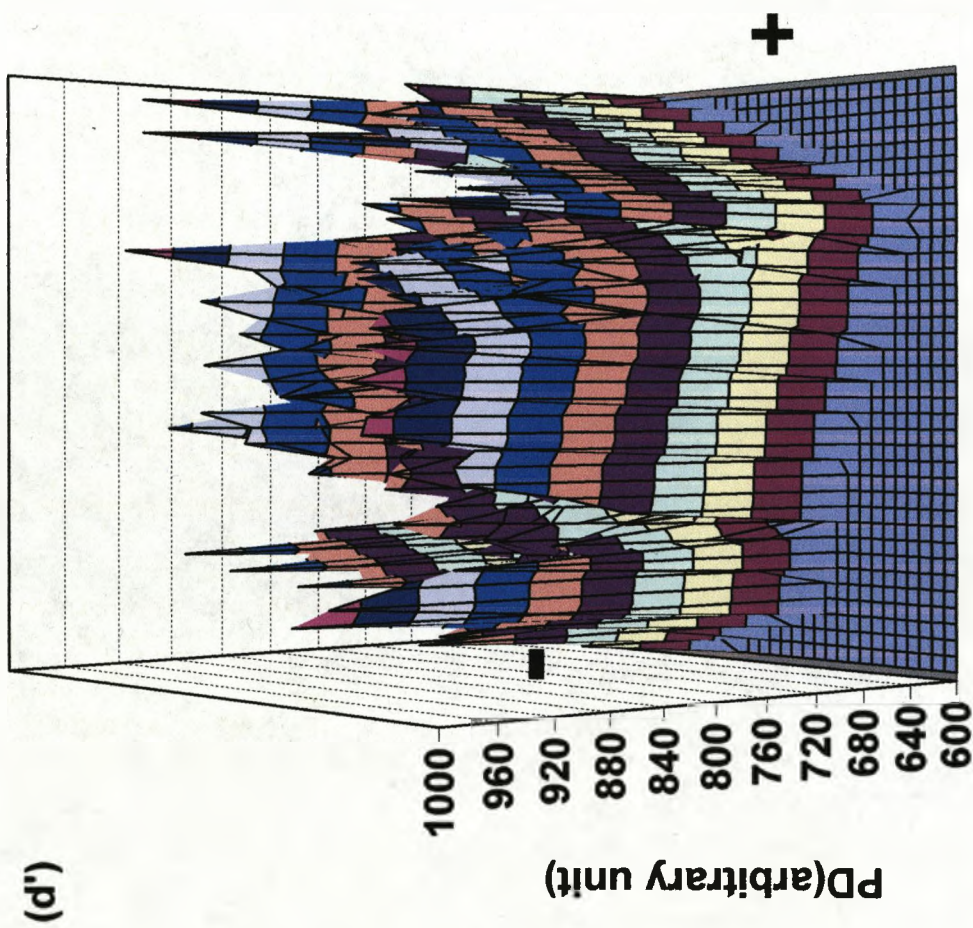


Three-dimensional plot of proton density, *PD* map, across the whole Nafion sample 122 min. after application of 5V d.c. potential. The position of the anode and cathode are indicated by “+” and “-” signs.



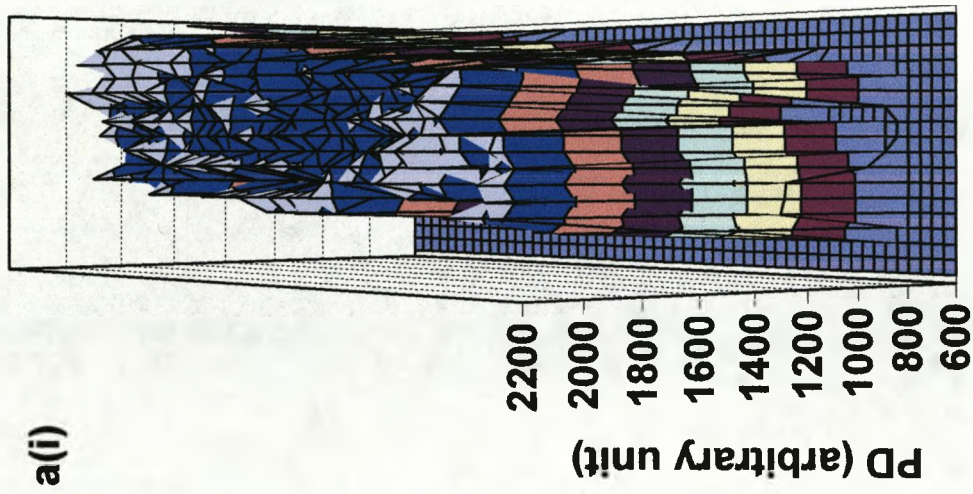
(c')

Three-dimensional plot of proton density, PD map, across the whole Nafion sample 89 min. after first reversal of the polarity of the 5V d.c. potential. The position of the anode and cathode are indicated by "+" and "-" signs.

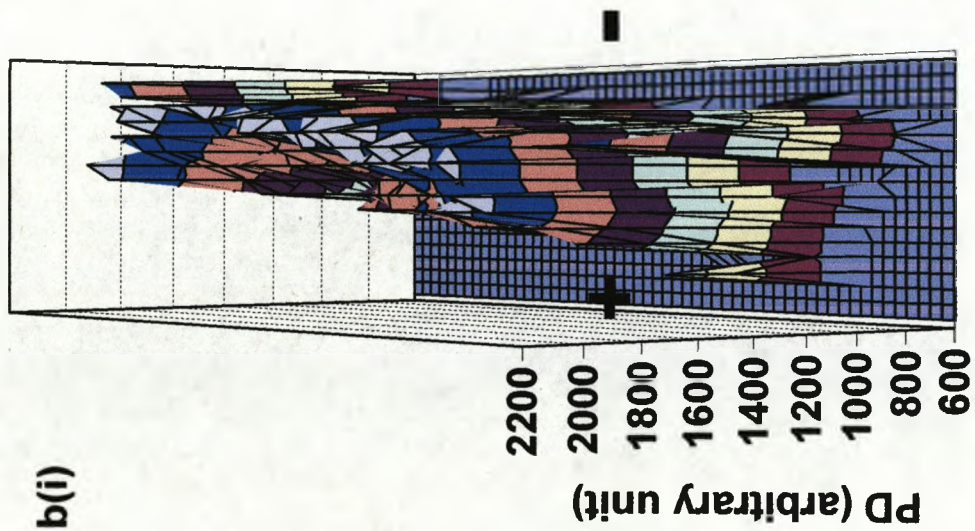


Three-dimensional plot of proton density, PD map, across the whole Nafion sample 89 min. after second reversal of the polarity of the 5V d.c. potential. The position of the anode and cathode are indicated by “+” and “-” signs.

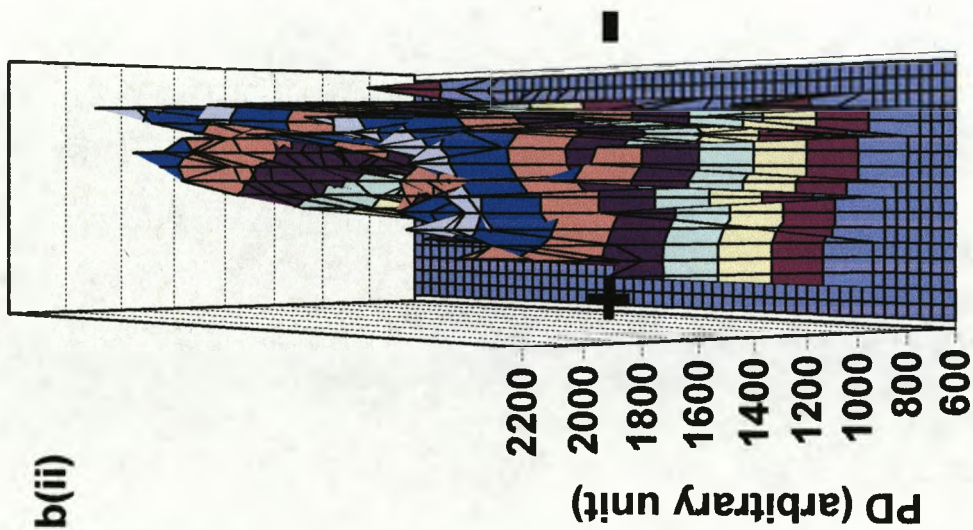
Appendix 3



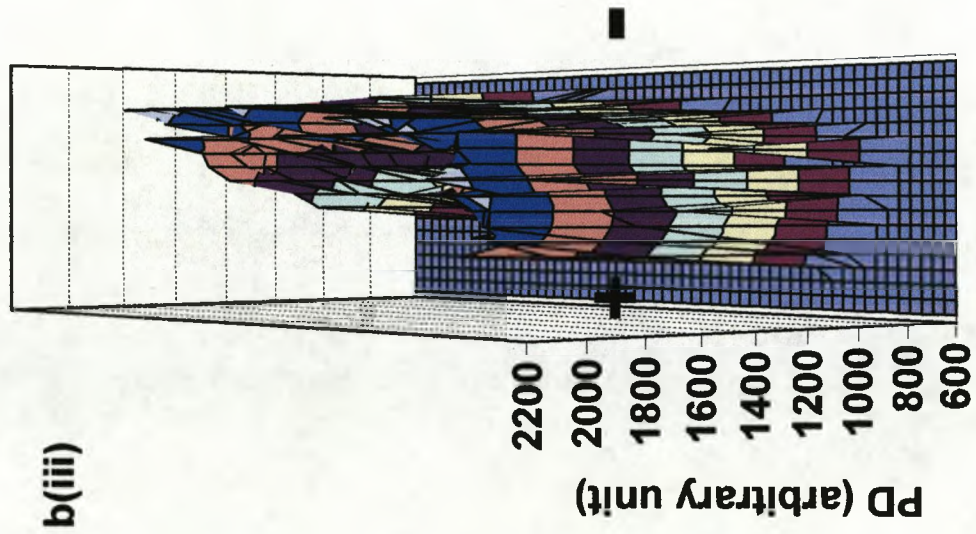
Three-dimensional plot of proton density, *PD* map, of the IPMC sample with no potential applied.



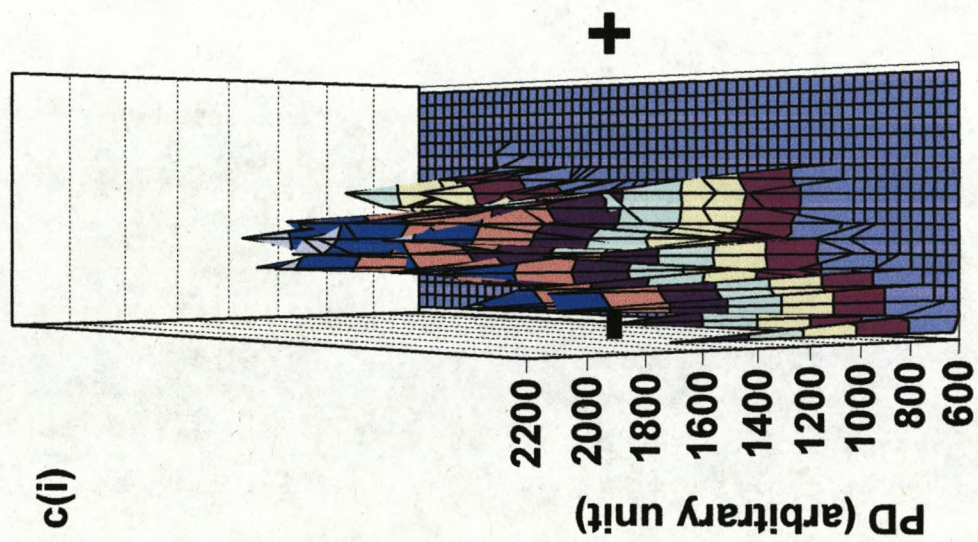
Three-dimensional plot of proton density, *PD* map, of the IPMC sample 0 min. after application of a 3V d.c. potential. The position of the anode and cathode are indicated by “+” and “-” signs.



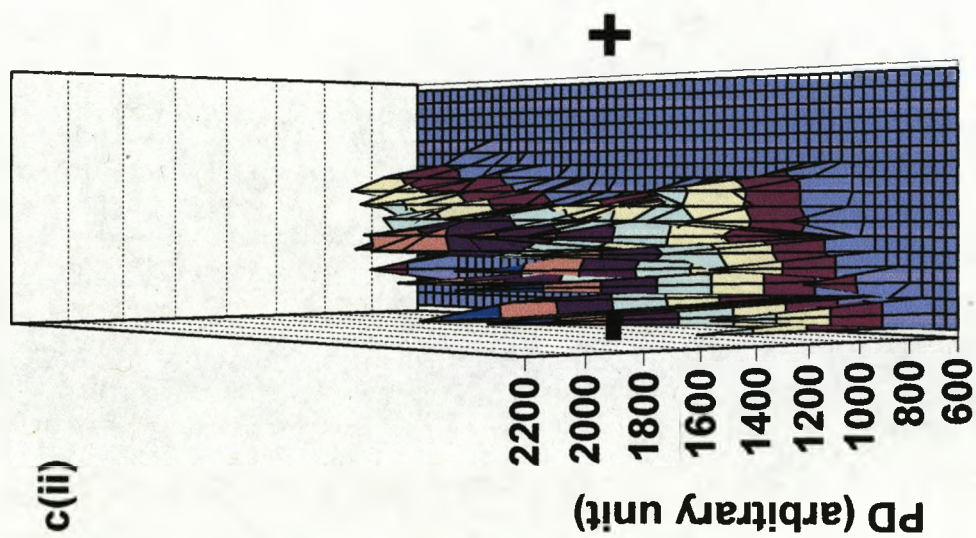
Three-dimensional plot of proton density, *PD* map, of the IPMC sample 29 min. after application of the 3V d.c. potential. The position of the anode and cathode are indicated by “+” and “-” signs.



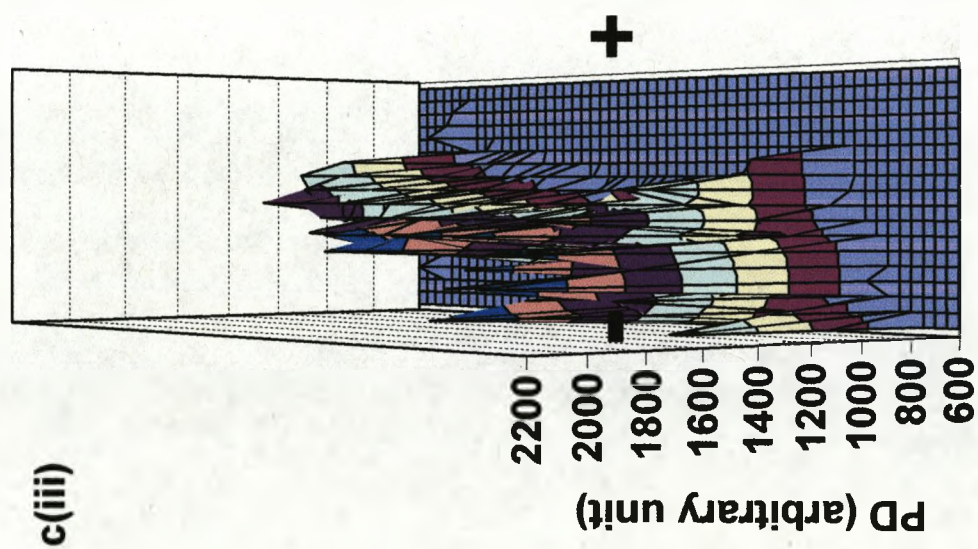
Three-dimensional plot of proton density, *PD* map, of the IPMC sample 89 min. after application of the 3 V d.c. potential. The position of the anode and cathode are indicated by “+” and “-” signs.



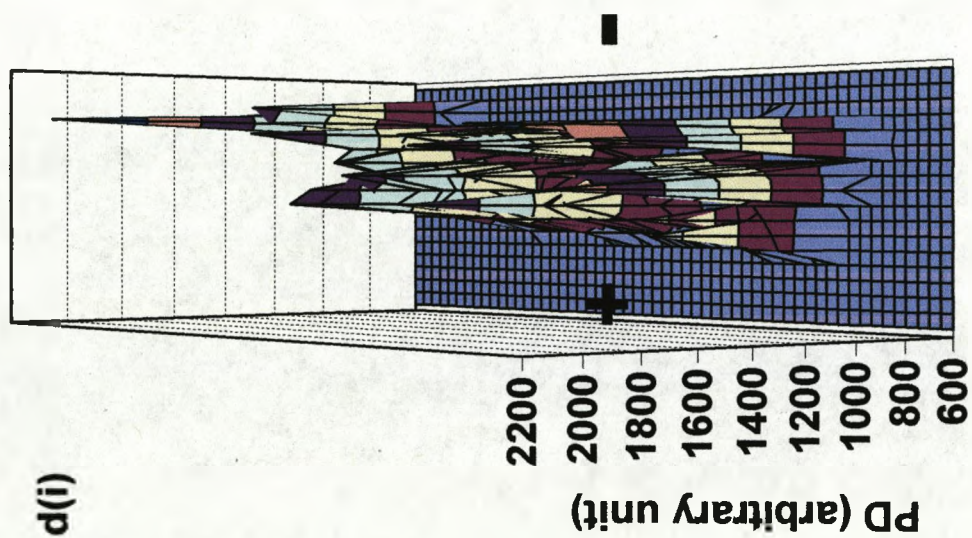
Three-dimensional plot of proton density, *PD* map, of the IPMC sample 0 min. after first reversal of the polarity of the 3V d.c. potential. The position of the anode and cathode are indicated by “+” and “-” signs.



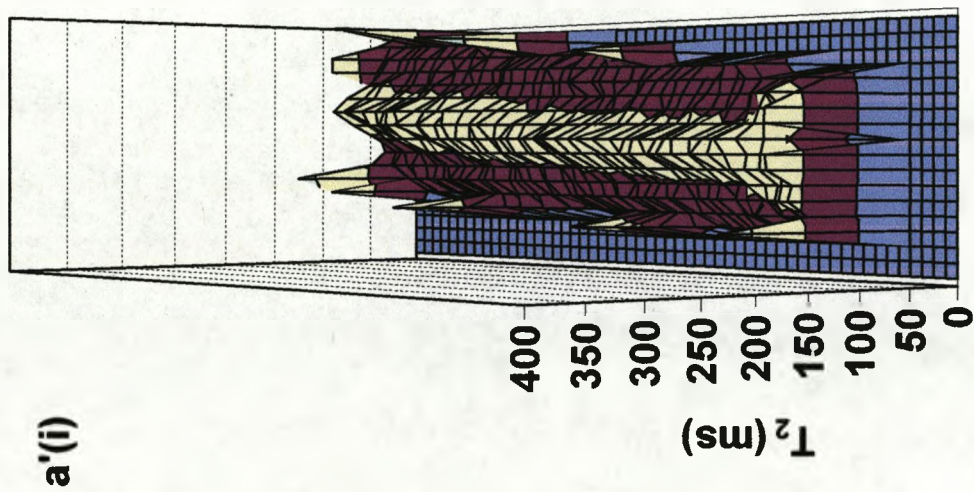
Three-dimensional plot of proton density, *PD* map, of the IPMC sample 29 min. after first reversal of the polarity of the 3V d.c. potential. The position of the anode and cathode are indicated by “+” and “-” signs.



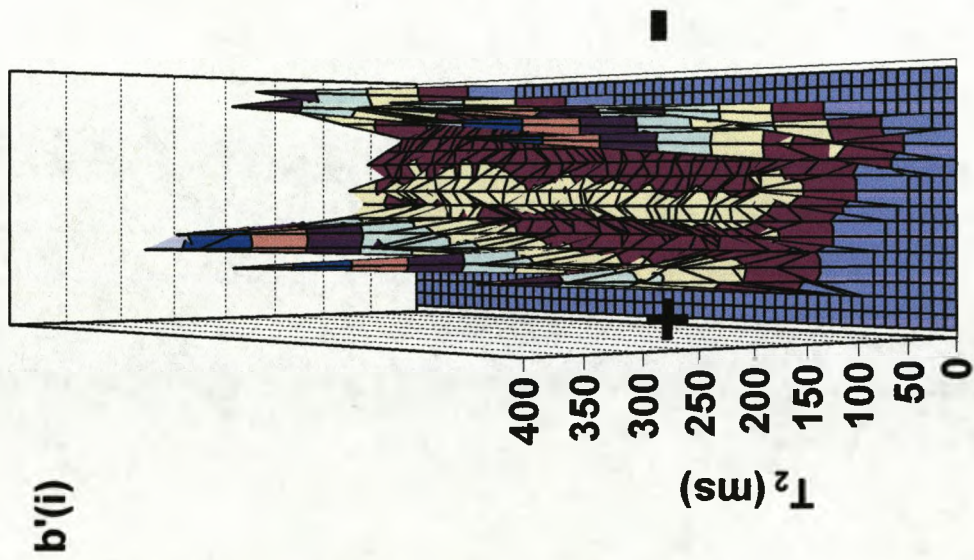
Three-dimensional plot of proton density, *PD* map, of the IPMC sample 89 min. after first reversal of the polarity of the 3V d.c. potential. The position of the anode and cathode are indicated by “+” and “-” signs.



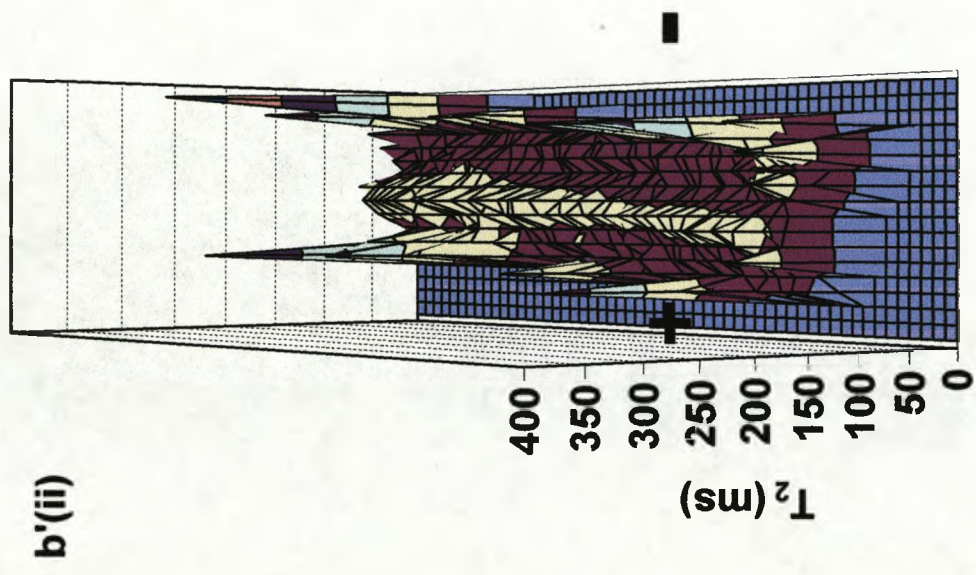
Three-dimensional plot of proton density, *PD* map, of the IPMC sample 0 min. after second reversal of the polarity of the 3V d.c. potential. The position of the anode and cathode are indicated by “+” and “-” signs.



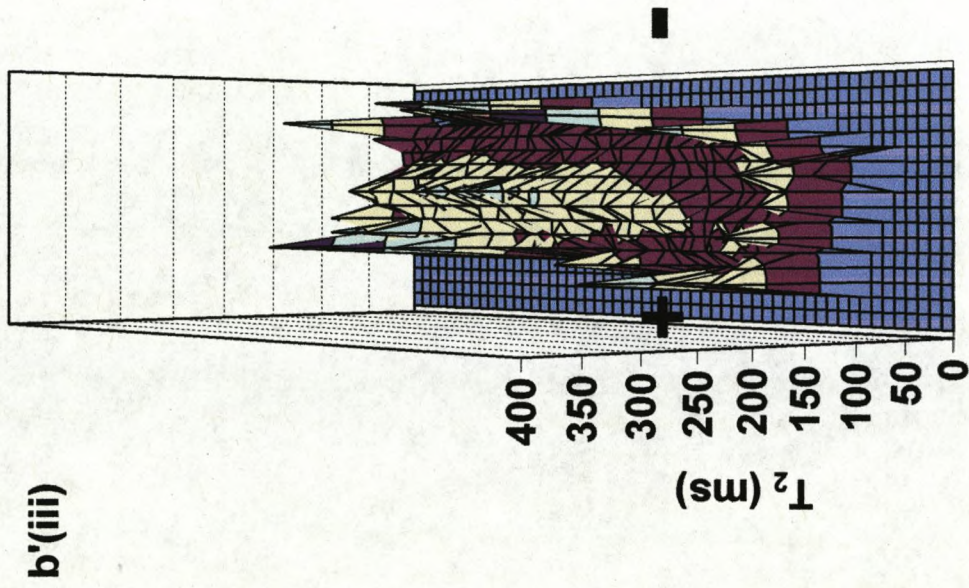
Three-dimensional plot of spin-spin relaxation time, T_2 map, of the IPMC sample with no potential applied.



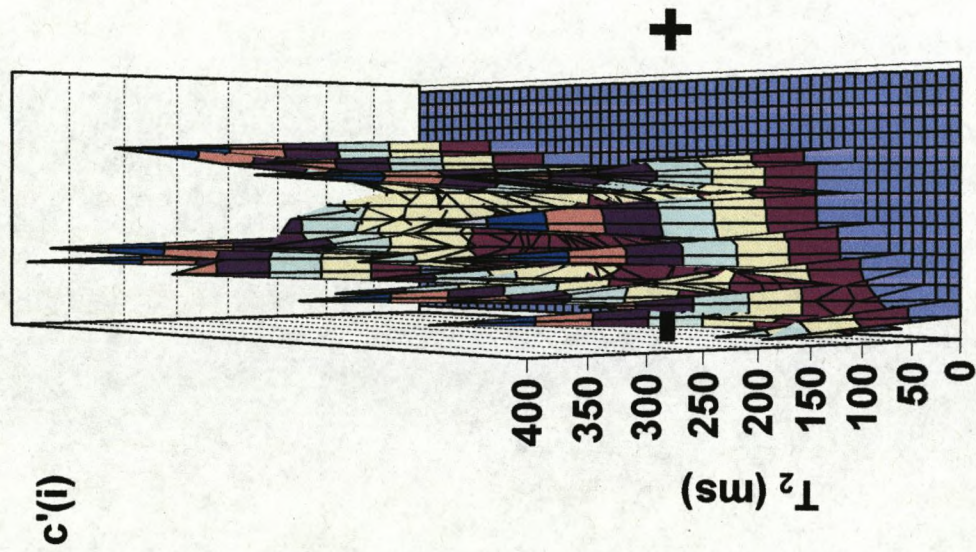
Three-dimensional plot of spin-spin relaxation time, T_2 map, of the IPMC sample 0 min. after application of a 3V d.c. potential. The position of the anode and cathode are indicated by “+” and “-” signs.



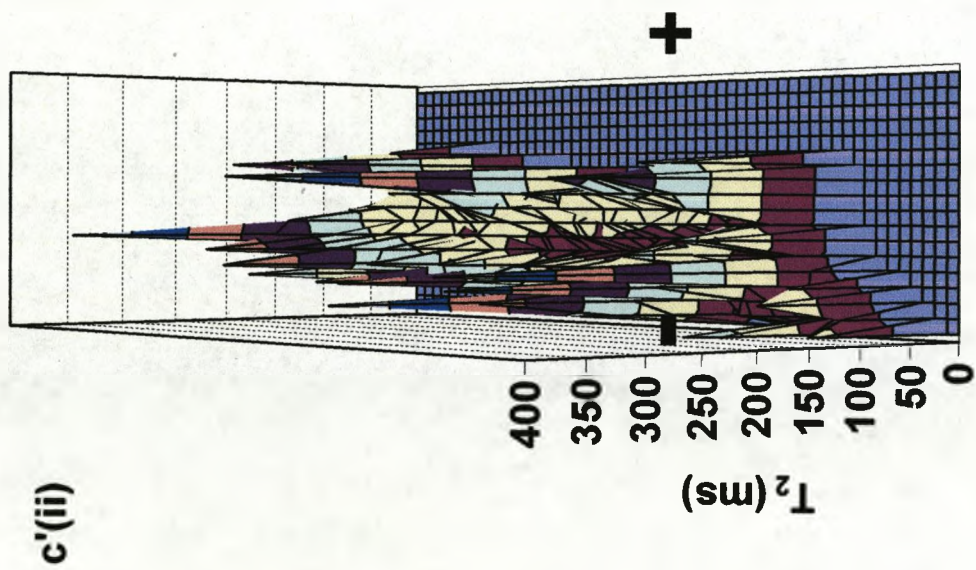
Three-dimensional plot of spin-spin relaxation time, T_2 map, of the IPMC sample 29 min. after application of the 3 V d.c. potential. The position of the anode and cathode are indicated by “+” and “-” signs.



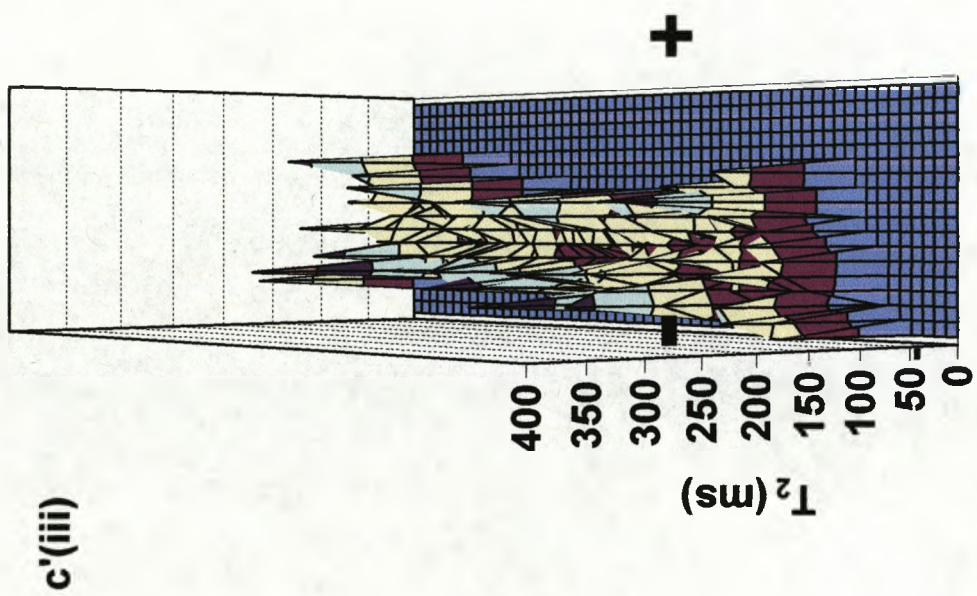
Three-dimensional plot of spin-spin relaxation time, T_2 map, of the IPMC sample 89 min. after application of the 3V d.c. potential. The position of the anode and cathode are indicated by “+” and “-” signs.



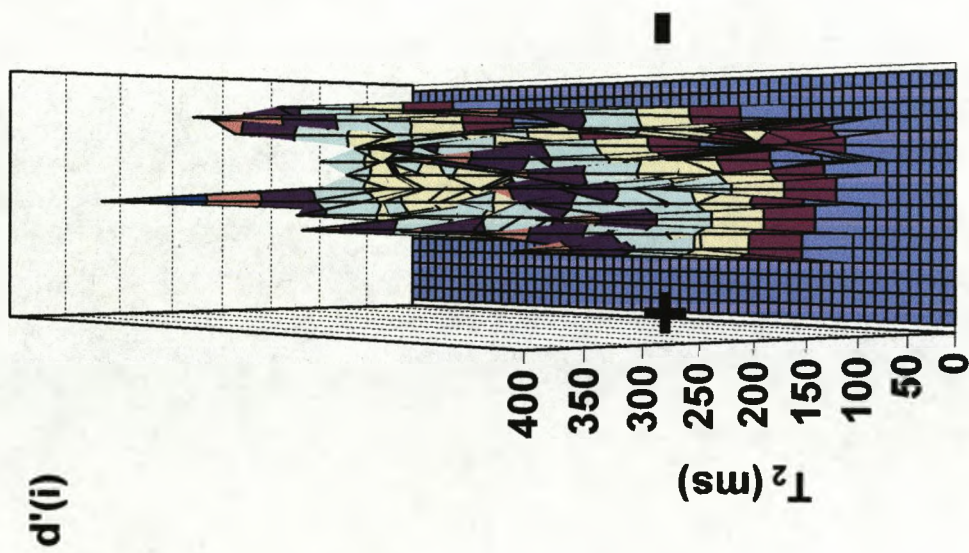
Three-dimensional plot of spin-spin relaxation time, T_2 map, of the IPMC sample 0 min. after first reversal of the polarity of the 3V d.c. potential. The position of the anode and cathode are indicated by “+” and “-” signs.



Three-dimensional plot of spin-spin relaxation time, T_2 map, of the IPMC sample 29 min. after first reversal of the polarity of the 3V d.c. potential. The position of the anode and cathode are indicated by “+” and “-” signs.



Three-dimensional plot of spin-spin relaxation time, T_2 map, of the IPMC sample 89 min. after first reversal of the polarity of the 3V d.c. potential. The position of the anode and cathode are indicated by “+” and “-” signs.



Three-dimensional plot of spin-spin relaxation time, T_2 map, of the IPMC sample 0 min. after second reversal of the polarity of the 3V d.c. potential. The position of the anode and cathode are indicated by “+” and “-” signs.